The Dissertation Committee for Yancy Leonard Shirley
certifies that this is the approved version of the following dissertation:

Tracing the Mass During Star Formation: Studies of Dust Continuum and Dense Gas

Committee:

Neal J. Evans II, Supervisor

Daniel T. Jaffe, Supervisor

Harriet L. Dinerstein

John H. Lacy

Philip C. Myers

John M. Scalo

Tracing the Mass During Star Formation: Studies of Dust Continuum and Dense Gas

by

Yancy Leonard Shirley, B.S.

Dissertation

Presented to the Faculty of the Graduate School of

The University of Texas at Austin

in Partial Fulfillment

of the Requirements

for the Degree of

Doctor of Philosophy

The University of Texas at Austin

August 2002

I dedicate this thesis to my parents, Len and Marilyn Shirley.

Acknowledgments

The past five years have been an amazing ride and I have so many people to thank for a wonderful graduate experience. Neal, my advisor, is a mentor and a friend. I cannot express enough gratitude for his patience and encouragement. I knew that I wanted to study at Texas after a brief meeting with him in the fall of 1996. Chris and Connie Walker, my undergraduate advisors, suggested that I work with Neal - the most valuable professional advice that I have received. I feel very fortunate that he was willing to take me on as a student. Neal has pushed me to be a competent and assiduous scientist, but it was not "all work and no play". I have many fond memories that are guaranteed to bring a smile to both of our faces: watching the dancing Russian cook in a restaurant in London; playing Cowboy at Hale Pohaku; eating stroopwafels in Holland; and listening to El Garbanzo at 5AM at the CSO.

Our research group has blossomed the past two years. Chad Young, Kaisa Mueller, Jeong-Eun Lee, Claudia Knez, and Katelyn Allers are an amazing group of colleagues. I learned so much about my own research with our daily interactions. I thank all of them for their extraoidinary patience and friendship.

My co-adivsor, Dan Jaffe, has always been very willing to give his time. John Lacy has been incredibly supportive, especially when I pester him with molecular Quantum questions. Harriet Dinerstein unselfishly supported my research my first year at Texas and has always encouraged me to pursue the problems in star formation that I am most interested in. I cannot thank Mark Cornell enough for his help with our computers and software (including one Sunday emergency visit). Jonathan Rawlings at University College London was a wonderful host during my visit and has been extremely helpful with my research. The staff at the CSO and JCMT are amazing; in particular, Richard Chamberlin (CSO) and Iain Coulson (JCMT) have always sent prompt replies to my questions.

Katelyn's love and support have been incredible. I am so thankful to have met such a loving person. Thank you for being apart of my life, especially during this very exciting and sometimes difficult time.

Finally, I cannot imagine my life without the undying support of my parents. They have made many sacrifices. I love them both very, very much. Nothing has made me prouder than watching the joy on my father's face during my Ph.D. defense talk. Thank you.

YANCY LEONARD SHIRLEY

The University of Texas at Austin
August 2002

Tracing the Mass During Star Formation: Studies of Dust Continuum and Dense Gas

Publication No. ____________________

Yancy Leonard Shirley, Ph.D.
The University of Texas at Austin, 2002

Supervisors: Neal J. Evans II and Daniel T. Jaffe

Currently there exists a gap in our understanding of star formation across the stellar mass spectrum. A putative evolutionary sequence exists for isolated low-mass star formation (M < few $M_\odot$) while no clear scheme exists for clustered high-mass star formation. With the advent of submillimeter bolometer arrays, observational tools are now available for pursuing statistical studies of star forming regions. Direct comparisons of the physical environments of low-mass and high-mass cores using dust continuum and dense gas emission provide important observational constraints on the theoretical picture. Two surveys of the deeply embedded phases of low-mass and high-mass star formation were recently carried out at the University of Texas: a Submillimeter Common User Bolometer Array (SCUBA) 450 and 850 μm continuum mapping survey of nearby, low-mass star forming regions and a CS $J = 5 \rightarrow 4$ spectral line mapping survey of high-mass star forming regions associated with water masers.

Since optically thin dust emission at submillimeter wavelengths traces the mass along the line-of-sight, it is a a powerful diagnostic constraining the density and temperature structure of the envelope of star forming cores. The normalized, azimuthally averaged, intensity profiles and spectral energy distributions of low-mass protostars from the SCUBA survey are modeled using a one dimensional radiative transfer code that accounts for heating from an internal source, heating from the interstellar radiation field, realistic beam effects, and chopping. The results from modeling the submillimeter continuum emission of recent low-mass and high-mass star forming regions are compared.

Similarly, the CS $J = 5 \rightarrow 4$ transition is an excellent probe of dense gas in high-mass star forming regions since the integrated intensity correlates strongly with the flux of optically thin submillimeter continuum emission. Various properties of high-mass star forming cores (such as the core size, aspect ratio, virial mass, surface density, luminosity-to-mass ratio, and mean pressure) are calculated for 63 sources mapped with the Caltech Submillimeter Observatory. This survey provides a sample from which the properties of the deeply embedded phases of high-mass star formation are determined. The conditions in low-mass and high-mass star forming regions in both surveys are directly compared.

Contents

Chapter 1

Introduction

We have begun to understand the fundamental picture of where stars are formed. There are approximately 10^{11} stars in the Milky Way with evidence for star formation throughout the history of the Galaxy (Gilmore 2001). Stars are currently forming at a rate of about 3 $M_{\odot}$/year (Scalo 1986). All stars are probably forming in molecular clouds (see Evans 1991), regions where the density of gas is high enough to convert atomic H, C, and O to molecules such as H_2 and CO and shield those molecules from the destructive effects of ultraviolet radiation from the interstellar radiation field. There is a continuum in molecular cloud size and mass from small, isolated Bok globules ($M >\sim 1$ $M_{\odot}$,Bok & Reilly 1947, Clemens & Barvainis 1988) to molecular cloud complexes ($M < 10^7$ $M_{\odot}$, Elmegreen 1985). Star formation is occurring in the solar neighborhood in the direction of Rho Ophiuchus (120 pc, de Geus et al. 1990), Lupus (130 pc, Murphy et al. 1986), and Taurus (140 pc, Elias 1978) to name a few. Globally, star formation is occurring from within the central kiloparsec of the Galaxy to the outermost portions of the galactic disk (Combes 1991). The most massive regions are most likely to be found in spiral arms (see Schweizer 1976), similar to what is observed towards other spiral galaxies (e.g., Helfer et al. 2001).

Within the molecular clouds, individual star or cluster forming cores have been identified (e.g., Myers & Benson 1983, Beichman et al. 1986) and are now the focus of intense study to understand the details of how star formation occurs. Deeply embedded phases of protostellar formation have been identified for both low-mass (e.g., André et al. 1993) and high-mass (e.g., Plume et al. 1997, Sridharan et al. 2002) star forming regions. The initial conditions of low-mass star formation are being identified with studies of cores that are thought to be precursors of protostar formation (Pre-protostellar cores, Ward-Thompson et al. 1994) while the corresponding precursors are still being sought for high-mass regions (Evans et al. 2002).

There is a dichotomy in our understanding of how stars of various masses form. A well developed, putative evolutionary sequence for low-mass protostars exists (Shu, Adams, & Lizano 1987), but there is no such sequence for high-mass stars. Low-mass stars form primarily via accretion in relative isolation (Bok globules) or in clustered environments (Lada 1991). High-mass stars always appear to form in clustered environments (Williams & McKee 1997, Carpenter 2000). It is not yet clear whether most high-mass stars form by accretion processes (e.g., Mckee & Tan 2002), by the coalescence of forming protostars (e.g. Bonnell et al. 1998), or by some other physical process. Partly, our poor understanding of massive star formation is to blame on poor observational resolution towards the high-mass star forming regions. The nearest high-mass star forming region is Orion, more than three times farther away than the Rho Ophiuchus molecular cloud. There are regions in the Galaxy that are more than an order of magnitude larger than Orion (in size and mass), but they are 15 (W51) to 30 (W49) times farther away (Sievers et al. 1991). Since high-mass stars are forming in clustered environments from very turbulent gas, the theoretical problem is more complicated than for low-mass stars.

Gravity plays a central role in determining how a star is formed (see Jeans

1928, Spitzer 1978); however, turbulence (see Myers & Lazarian 1998; Vázques-Semadeni 2000), magnetic fields (see Mestel 1985; Galli & Shu 1993ab, Li & Shu 1996; Ciolek & Konigl 1998), and rotation (see Field 1978; Terebey, Shu, & Cassen 1984; Boss 1998) mitigate the collapse and may be just as important as gravity at various stages and on different scales during the star formation process. Theoretical models predict the evolution of density, temperature, and velocity of the star forming core with time by incorporating various aspects of the physics of star formation. There is a wide range of assumed initial conditions and subsequent predictions for the evolution of a protostar (e.g., constant density isothermal sphere, Larson 1969; singular isothermal sphere, Shu 1977; unstable Bonnor-Ebert sphere, Foster & Chevalier 1993, logatropic sphere, McLaughlin & Pudritz 1997; etc.). Observers are challenged to provide some constraints on the theoretical models. In particular, the density distribution as a function of radius is a strong discriminator between theoretical models, and it provides an essential tool for understanding the process of collapse and star formation (André et al. 2000).

This thesis investigates the physical conditions during the deeply embedded phases of low-mass and high-mass star formation. In the spirit of the modern style of a thesis, the chapters consist of three journal papers and a conference proceeding. As a result, each chapter is meant to stand alone.

The first two papers (§2 and §3; Shirley et. al. 2000, Shirley et al. 2002a) focus on constraining the physical structure of nearby, isolated, low-mass star forming cores using observations of submillimeter dust continuum emission (§2; Shirley et al. 2000). Optically thin emission from dust grains in the outer envelopes of protostars provide an excellent tracer of the mass along the line-of-sight (see Appendix A). Radiative transfer models are constructed to model the density and temperature structure of the core (§3; Shirley et al. 2002a). The third paper compares the results from dust continuum studies of low-mass and high-mass star forming regions (§4;

Shirley et al. 2002c). This paper was originally presented as a talk at the meeting, Star Formation Across the Stellar Mass Spectrum, in La Serena, Chile (March, 2002) and draws on work by Young et al. (2002) and Mueller et al. (2002) in addition to the modeling in this thesis. The final paper (§5; Shirley et al. 2002d) describes a dense gas mapping survey using the CS J = 5 $\rightarrow$ 4 transition towards high-mass star forming regions with the goal of providing a consistent sample from which to determine the physical conditions of the deeply embedded phases of high-mass star formation. Results from the low-mass and high-mass surveys are compared in the conclusions (§6).

Chapter 2

Submillimeter Continuum Observations

Abstract

We have obtained 850 and 450 μm continuum maps of 21 low mass cores with SED's ranging from pre-protostellar to Class I (18K $< T_{bol} <$ 370K), using SCUBA at the JCMT. In this paper we present the maps, radial intensity profiles, and photometry. Pre-protostellar cores do not have power-law intensity profiles, whereas the intensity profiles of Class 0 and Class I sources can be fitted with power laws over a large range of radii. A substantial number of sources have companion sources within a few arcminutes (2 out of 5 pre-protostellar cores, 9 out of 16 Class 0/I sources). The mean separation between sources is 10800 AU. The median separation is 18000 AU including sources without companions as a lower limit. The mean value of the spectral index between 450 and 850 μm is 2.8 ± 0.4, with pre-protostellar cores having slightly lower spectral indices (2.5 ± 0.4). The mean mass of the sample, based on the dust emission in a $120''$ aperture, is 1.1 ± 0.9 M$_{\odot}$. For the sources fitted by power-law intensity distributions ($I_\nu(b)/I_\nu(0) = (b/b_0)^{-m}$), the mean value of m is 1.52 ± 0.45 for Class 0 and I sources at 850 μm and 1.44 ± 0.25 at 450 μm. Based on a simple analysis, assuming the emission is in the Rayleigh-Jeans limit and that $T_d(r) \propto r^{-0.4}$, these values of m translate into power-law density distributions ($n \propto r^{-p}$) with $p \sim 2.1$. However, we show that this result may be changed by more careful consideration of effects such as beam size and shape, finite outer radii, more realistic $T_d(r)$, and failure of the Rayleigh-Jeans approximation.

2.1 Introduction

Theories of isolated, low-mass star formation predict the distribution of density, $\rho(r)$, and dust temperature, $T_d(r)$, before and during the star formation process. These can be used to predict the spectral energy distribution (SED) and the spatial intensity distribution, $I_\nu(b)$, of dust continuum emission. Up to now, the primary tool for determining the evolutionary state of a particular core has been the SED, but the relationship between the SED and the distribution of matter is not unique (Butner et al. 1991, Men'shchikov & Henning 1997). Observing the spatial intensity distribution of dust continuum emission at long wavelengths, where it becomes optically thin, provides a powerful tool for constraining the actual distribution of matter (Adams 1991, Ladd et al. 1991). New instruments have recently been developed at submillimeter wavelengths that greatly enhance our capability in this area (Hunter et al. 1996, Cunningham et al. 1994). In this paper, we present maps of dust emission around 21 cores in various evolutionary states using the Submillimetre Common User Bolometer Arrray (SCUBA) (Holland et al. 1999) at wavelengths of 1.3 mm, 850μm, and 450 μm. By mapping the extended dust emission, we can probe the density structure from 7$''$ to 100$''$ (for the nearest sources in our sample, at 125 pc, these angles correspond to 870 AU to 12500 AU).

Our conception of the evolution of a dense core, first to a protostar, an object whose luminosity is dominated by accretion, then to a pre-main sequence star has been guided by an empirical evolutionary sequence (Lada 1987). Theoretical modelling of the SED (Adams, Lada, & Shu 1987) shows a good correspondence with this classification. In this scheme, sources are classified by the shape of their SED. Thus, an infrared spectral index is defined for the wavelength range λ=2–20μm;

$$\alpha_{NIR} = \frac{d(log\lambda S_\lambda)}{d(log\lambda)}, \tag{2.1}$$

where S_λ is spectral flux density per wavelength interval. Class I sources were identified as the youngest protostars, deriving most of their luminosity from accretion. They are embedded in an envelope and have SEDs that rise ($\alpha_{NIR} \geq 0$) to a peak in the far-infrared. Class II and III sources are progressively less embedded than Class I sources. Class II SEDs peak in the near-infrared but possess a mid-infrared excess ($-1.5 < \alpha_{NIR} < 0$), and they are normally associated with star/disk systems without a significant envelope. Class III SEDs are reddened blackbodies ($-1.5 > \alpha_{NIR}$) and are associated with stars without optically thick disks. Class II and Class III sources typically correspond to classical and weak-line T-Tauri stars respectively.

Within the last decade, this classification scheme, which was defined in the context of infrared SEDs, has been modified to include more deeply embedded sources, which presumably represent a phase earlier than Class I. André et al. (1993) proposed the name Class 0 for sources that are so highly enshrouded that their SEDs peak longward of 100 μm and their near-infrared emission is very faint. Class 0 sources are defined to be cores which possess a central source, but which have $L_{smm}/L_{bol} \geq 0.005$, where L_{smm} is the luminosity at $\lambda >$350μm. This criterion corresponds approximately to the mass of the centrally condensed protostellar core being less than that of the collapsing envelope. L_{smm}/L_{bol} should decrease with time (André et al. 1993).

Starless cores provide plausible candidates for a still earlier stage. These starless cores are associated with dense gas cores (Myers & Benson 1983; Benson & Myers 1989) for which no source was detected by IRAS. Ward-Thompson et al. (1994) detected submillimeter emission from a sample of these objects, which they labelled "pre-protostellar cores" (PPCs, sometimes called Class -1 sources). Pre-protostellar cores may be in hydrostatic equilibrium, or they may be gravitationally bound, magnetically sub-critical cores that are undergoing quasi-static contraction as a result of ambipolar diffusion.

In an alternative approach, Myers & Ladd (1993) defined a continuous variable, T_{bol}, which is the temperature of a blackbody with the same mean frequency as the observed SED. Class 0 sources have $T_{bol} < 70$K while Class I sources have $70\text{K} \leq T_{bol} < 650$K (Chen et al. 1995). T_{bol} has been hard to determine for pre-protostellar cores because of an absence of data at $\lambda < 450$ μm, but a few values are available from space-based observations in the far-infrared (Ward-Thompson, André, & Motte 1998, Ward-Thompson & André 1999).

The empirical classification scheme has been compared to theoretical models of star formation. Shu and co-workers (e.g. Shu, Adams, & Lizano 1987, Shu et al. 1993) developed a detailed theory of low mass star formation from the stage of cloud core formation to an emergent pre-main-sequence star. The simplest form of the theory (not including rotation or magnetic fields) begins with collapse inside a centrally condensed isothermal sphere ($n(r) \propto r^{-2}$, Shu 1977). The inside-out collapse model predicts that a wave of infall propagates outward at the sound speed of the gas. The density inside the infall radius approaches $r^{-1.5}$ toward the center as appropriate for free fall. Core formation would then correspond to the pre-protostellar cores. Collapse would begin with the Class 0 stage and continue into the Class I stage.

This model is somewhat simplistic, and alternatives have been proposed. For instance, observational evidence exists for sharp density contrasts near the edges of cloud cores (Abergel et al. 1998). Submillimeter continuum emission from pre-protostellar cores indicates that the density distributions in the core flatten, rather than continuing to follow a single power law to small radii (Ward-Thompson et al. 1994), and line profiles consistent with infall motions have been detected in a substantial fraction of pre-protostellar cores (Lee, Myers, & Tafalla 1999, Gregersen & Evans 2000). If dynamical collapse begins before the core is fully relaxed to the isothermal sphere, there is an early stage of fast mass accretion (Basu & Mouschovias 1995, Henriksen et al. 1997), that may distinguish Class 0 from Class I sources.

Determination of the density distribution of dust in a sample including PPCs, Class 0, and Class I sources can answer some questions. Do the PPCs have density distributions predicted by theoretical models of core formation leading to inside-out collapse? Are there differences between the distributions in those with evidence for infall and those without? Are there qualitative differences in the distribution of matter around Class I sources and Class 0 sources, or is the difference only quantitative?

2.2 Observations

2.2.1 The Sample

The sample of sources (Table 2.1 & 2.2) was chosen to span a range of evolutionary states, from pre-protostellar cores to Class I sources, and to include sources with (11) and without (10) evidence of infall, based on line profile shapes in HCO^+, CS, or H_2CO (Gregersen et al. 1997, 2000; Gregersen and Evans 2000; Mardones et al. 1997). The coordinates were taken from a variety of references, including Ward-Thompson et al. (1994) (PPC), Gregersen et al. (1997) and Mardones et al. (1997), and corrected or updated in a few cases. Distances were obtained from a literature search, making extensive use of the compendia of Hilton & Lahulla (1995) and Lee & Myers (1999), but going back to the original references. We chose the newer, closer distances to the Ophiuchus complex (125 ± 25 pc) favored by de Geus et al. (1990) over the traditional choice of 160 pc, and to the Perseus clouds (220 ± 20 pc) according to Černis (1990) over the usual 350 pc.

Our original sample was selected to contain roughly equal numbers of PPCs, Class 0, and Class I sources. In the end, more Class 0 sources were observed, and several sources moved from Class I to Class 0 when we recalculated their properties, including our data. Changes in estimates of L_{bol}, T_{bol}, and L_{smm}/L_{bol} are discussed in §2.3.2. We use $T_{bol} = 70$ K as the dividing line between Class I and Class 0 (Chen et al. 1995), giving us 3 Class I sources in our final sample. André et al. (1993) required $L_{smm}/L_{bol} > 0.005$ for Class 0 status; with this criterion, SSV13 would be the only Class I source remaining in our sample. Consequently, we often discuss Class 0 and I sources together, referring to them as Class 0/I.

2.2.2 Observing and Calibration

The cores were mapped simultaneously at 850 and 450 μm using SCUBA during parts of 12 nights in 1998 January, April, and May with the James Clerk Maxwell Telecsope (JCMT) on Mauna Kea, Hawaii. Nine cores were also mapped at 1.3 mm using the single bolometer detector on SCUBA. A $120''$ chopper throw in azimuth was used for all the cores. Using the 64-point jiggle map mode, each SCUBA map fully samples a $2\farcm3$ region simultaneously at 850 and 450 μm. The telescope was nodded during each map. Each jiggle map produces 4.2 minutes of integration time on the source. Because we are interested in mapping extended low brightness emission, we made 5-point maps (each a 64-point jiggle map) with a spacing of $30''$. Such maps also mitigate the effects of bad bolometers. The inner $2'$ of the final image was mapped in each of the 5-point maps with a total integration time of 21 minutes. The signal-to-noise ratio varied between 5 and 97 for our images (see Table 2.15); these estimates are conservative because the main part of the image had 5 times as much integration as the outer parts, where the noise was determined. In some cases, extra positions were observed to cover additional sources in the field.

Pointings and skydips were performed between 5-point maps. The pointing varied by less than $2''$ between objects. We measured τ_{850} and τ_{450} during each skydip. The CSO radiometer was monitored simultaneously to obtain τ_{cso} (measured at 225 GHz). Our observations confirm the correlation between this opacity and those obtained from the JCMT skydips (Chapin 1998). We used the skydips at

TABLE 2.1

OBSERVED SOURCES

Source	α (1950.0) ($^{h\ m\ s}$)	δ (1950.0) ($^{\circ\ \prime\ \prime\prime}$)	Observed	Class[a]
L1512	05 00 54.4	32 39 37	1/25/98	PPC
L1544	05 01 13.1	25 06 36	1/25/98	PPC
L1689A	16 29 10.5	−24 57 22	4/18/98	PPC
L1689B	16 31 47	−24 31 45	4/18/98	PPC
B133	19 03 27.3	−06 57 00	4/14/98	PPC
L1448NW	03 22 31.1	30 35 04	1/24/98	0
L1448N	03 22 31.8	30 34 45	1/24/98	0
L1448C	03 22 34.3	30 33 30	1/24/98	0
L1455	03 24 34.9	30 02 36	1/24/98	0
IRAS03282+3035	03 28 15.2	30 35 14	1/24/98	0
L1527	04 36 49.6	25 57 21	1/25/98	0
B228	15 39 50.4	−33 59 42	4/15/98	0
L483	18 14 50.6	−04 40 49	4/17/98	0
L723	19 15 41.3	19 06 47	4/20/98	0
B335	19 34 35.4	07 27 24	4/17/98	0
L1157	20 38 39.6	67 51 33	4/19/98	0
L1172	21 01 44.2	67 42 24	4/18/98	0
CB244	23 23 48.7	74 01 08	4/20/98	0
SSV13	03 25 57.9	31 05 50	1/24/98	I
IRAS04166+2706	04 16 37.8	27 06 29	8/30/98	I
L43	16 31 37.7	−15 40 52	4/17/98	I

[a]PPC=Pre-protostellar core

[b]As indicated by studies of HCO^+ (Gregersen 1998)

[c]Red asymmetry in HCO^+, but blue in other lines

TABLE 2.2
SOURCE PROPERTIES

Source	Dist. (pc)	Dist. Ref.	Outflow Ref.	Collapse[b] Candidate?
L1512	140	1	...	N
L1544	140	1	...	Y
L1689A	125	2	...	Y
L1689B	125	2	...	Y
B133	200	3	...	Y
L1448NW	220	4	10,11	N
L1448N	220	4	10,11	N
L1448C	220	4	10,11	N
L1455	220	4	6	N
IRAS03282+3035	220	4	12	Y
L1527	140	1	13	Y
B228	130	5	14	Y
L483	200	3	15	N[c]
L723	300	6	16	N
B335	250	7	16	Y
L1157	325	8	17	Y
L1172	288	8	...	N
CB244	180	9	18	Y
SSV13	220	4	19	N
IRAS04166+2706	140	1	...	Y
L43	125	2	20	N

[a] PPC=Pre-protostellar core

[b] As indicated by studies of HCO^+ (Gregersen 1998)

[c] Red asymmetry in HCO^+, but blue in other lines

REFERENCES.—1. Taurus – Elias 1978; 2. Ophiuchus – de Geus et al. 1990; 3. Aquila Rift – Dame & Thaddeus 1985; 4. NGC1333 region – Černis 1990, (but see Herbig & Jones 1983 who get 350 pc); 5. Lupus – Murphy et al. 1986; 6. Goldsmith et al. 1984; 7. Tomita et al. 1979; 8. Straižys et al. 1992; 9. Lindblad Ring – Launhardt & Henning 1997; 10. Bachiller et al. 1990; 11. Barsony et al. 1998; 12. Bachiller et al. 1991a; 13. Zhou et al. 1996; 14. Heyer & Graham 1989; 15. Fuller et al. 1995; 16. Hirano et al. 1998; 17. Bachiller & Perez Gutierrez 1997; 18. Yun & Clemens 1994; 19. Liseau et al. 1988; 20. Bence et al. 1998

850 and 450 μm immediately preceding and following a 5-point map to interpolate the extinction correction. The average and standard deviation over the night in the opacities at 850 and 450 μm for each night are listed in Table 2.3. Opacities derived from the peak fluxes of Uranus before correction for extinction generally agreed with the opacities derived from skydips. The uncertainties in the opacity dominate the uncertainties in the total flux calibration, but they have little effect on our primary objective of imaging the sources, because the maps were obtained with a 2-D array in a short time.

To assess the effects of image smearing when we average the components of our 5-point maps taken with different pointings, we averaged all the Uranus maps on all the runs with $1''$ pixels to produce an average Uranus map. From this map, the average FWHM (θ_{mb}) at 850 and 450 μm were $15\farcs2$ and $7\farcs9$ respectively (roughly $1''$ larger than values derived from a single map). Because even this worst-case experiment produced only marginal broadening, the maps are not significantly distorted by averaging data with different offsets. The average radial profiles for Uranus observed during April are shown in Figure 2.1 for both wavelengths; the sidelobe structure is clear and consistent with other measurements (W. Holland, personal communication). Night to night variations in the sidelobes can be seen, but amplitudes of the sidelobes vary by less than a few dB and positions of the sidelobes are roughly constant. April and August observations were made during second shift (01:30 – 09:30 HST) when the dish shape and focus had stabilized. Significant variations in sidelobe structure are seen for observations taken during first shift (17:30 – 01:30 HST) (C. Chandler personal communication). Our average 850 μm beam is characterized by sidelobes at $24''(-17$dB) and at $47''(-23$dB). The average 450 μm beam is characterized by sidelobes at $13''(-12$dB), at $24''(-16.5$dB), and at $40''(-23.5$dB). Removing Uranus from the data makes a small change in the central Gaussian width ($\leq 10\%$) and negligible difference in the sidelobe structure

TABLE 2.3
OPACITY SUMMARY

Date	τ_{850}	τ_{450}	$\tau_{1.3}$
January			
01/24/98	0.17 (0.01)	0.84 (0.01)	...
01/25/98	0.12 (0.01)	0.48 (0.06)	...
April			
04/14/98	0.12 (0.01)	0.51 (0.01)	...
04/15/98	0.14 (0.01)	0.60 (0.02)	...
04/17/98	0.14 (0.01)	0.66 (0.06)	0.06 (0.01)
04/18/98	0.15 (0.01)	0.69 (0.05)	...
04/19/98	0.34 (0.03)	1.7 (0.1)	...
04/20/98	0.15 (0.03)	0.7 (0.2)	...
August			
08/28/98	0.39 (0.01)	2.7 (0.2)	0.15 (0.01)
08/29/98	0.20 (0.01)	1.2 (0.1)	...
08/30/98	0.19 (0.01)	1.0 (0.1)	...

(The diameter of Uranus during April 1998 was $3\farcs2$). We use the actual beam profile in the the modeling described in §2.4.2.

The total flux was calibrated using $120''$ and $40''$ diameter apertures in extinction corrected maps of Uranus, AFGL 618, and Mars. The observed flux densities for an aperture of diameter θ were computed from $S_\nu(\lambda, \theta) = C_\theta^\lambda V(\lambda, \theta)$, where $V(\lambda, \theta)$ was the voltage measured at wavelength λ in an aperture of diameter θ. The calibration factors, C_θ^λ, were calculated from the fluxes of Uranus and Mars. The total observed flux from previous SCUBA measurements was used for AFGL618 (SCUBA secondary flux calibrator webpage): 4.56 ± 0.17 Jy/beam at 850 μm; 11.2 ± 1.4 Jy/beam at 450 μm. The flux calibration did not vary substantially from night to night within an observing run but did vary from run to run. Therefore, we use an average flux calibration for each run (January, April, and August), listed in Table 2.4.

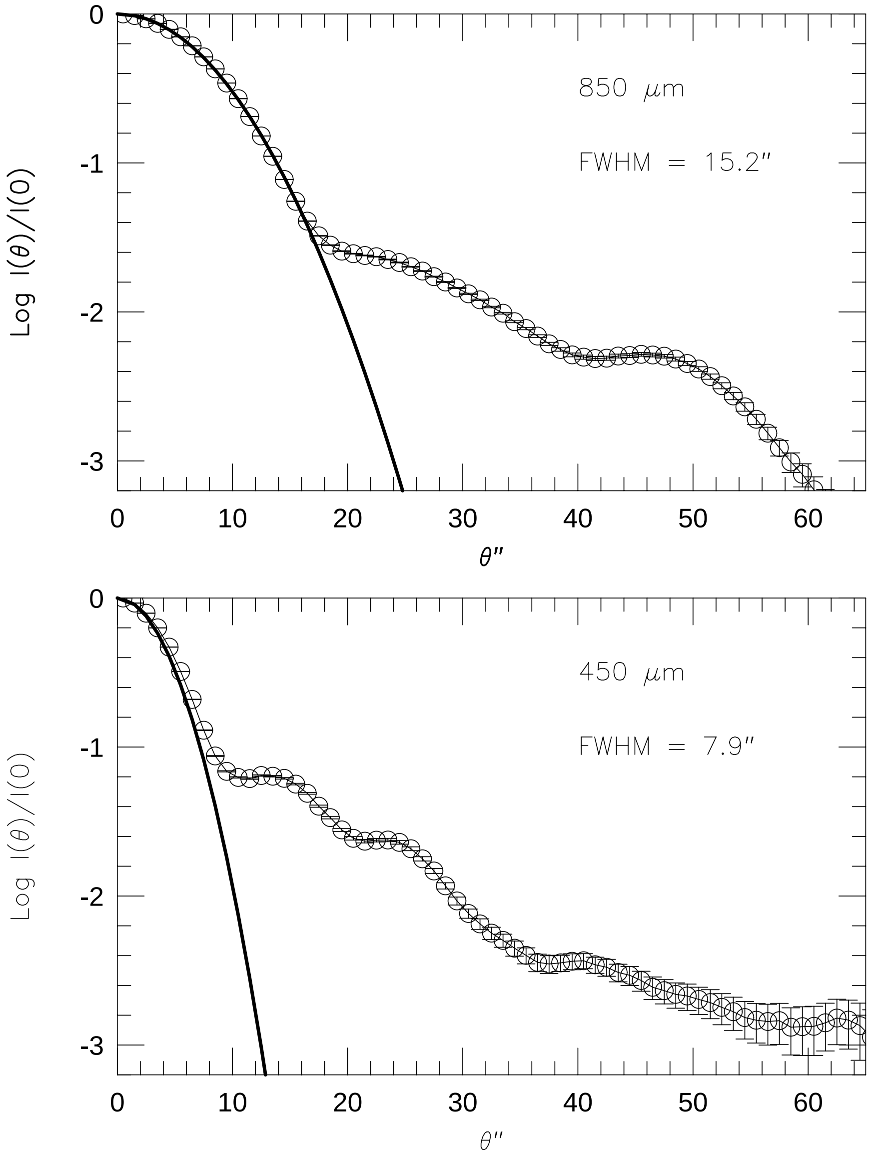

Figure 2.1 The average Uranus radial profile from the April 1998 run, based on an image with 1″ pixels. Nine maps were averaged for the 850 μm profile, and eight maps were averaged for the 450 μm profile. The normalized intensity is plotted as a function of angle from the center. The solid line shows a gaussian profile with the FWHM of the main beam.

Table 2.4

Calibration Summary

Date Jy/V[a]	C_{40}^{850} Jy/V[b]	C_{120}^{850} Jy/V[a]	C_{40}^{450} Jy/V[b]	C_{120}^{450} Jy/V[a]	$C_{40}^{1.3}$
January 1998	1.02 (0.06)	0.84 (0.04)	5.72 (0.99)	5.24 (1.97)	...
April 1998	0.94 (0.05)	0.74 (0.04)	5.76 (0.76)	4.14 (0.57)	...
August 1998	1.00 (0.05)	...	4.63 (0.99)	...	0.26(0.04)

[a]Calibration Factor for a 40″ diameter aperture

[b]Calibration Factor for a 120″ diameter aperture

2.2.3 Image Reduction

The initial reduction of each image was performed using SURF, the SCUBA User Reduction Facility software package (Jenness & Lightfoot, 1997). The raw images of 64-point jiggle maps already have removed the effects of the chopping. The raw images are further reduced by removing the telescope nod and correcting for different bolometer gains (flat-fielding). Sky variations were subtracted by averaging the response of multiple bolometers off the source. Because some of our sources are very extended, care was taken to choose bolometers that were free of significant low level emission. After sky noise subtraction, each image was rebinned to $0.5\theta_{mb}$ per pixel on a B1950.0 coordinate system. SCUBA's bolometers are subject to microphonic and 1/f noise. Excessively noisy bolometers (RMS voltage $\geq$ 60 nV in noise tests) were removed. Also, noisy sections of the integration were removed. These are most likely caused by imperfect subtraction of sky noise and are usually observed across several bolometers at the same time. The noisiest bolometers were typically found near the edge of the array, resulting in increased noise near the edge of the maps.

The final 5-point maps were rebinned by shifting the individual images by their centroid. Corners of the 5-point map occasionally chopped onto source emission, causing the negative beam to become visible. Bolometers in the negative beam were removed from the final image, resulting in irregularly shaped edges on many maps.

2.3 Results

2.3.1 Images

Contour plots of our SCUBA images are shown in Figures 2.2–2.8. Contour levels are indicated in each plot caption with the lowest contour $\geq 3\sigma$. Outflow axes are marked with a solid line. The (0,0) positions are given in Table 2.1. Typical rms noise near the edge of the maps was 20 mJy/beam at 850μm and 100 mJy/beam at 450μm. Assuming a dust temperature of 10K near the edge of the cloud, we are sensitive to $A_V = 3$mag (1σ rms) at 850μm and $A_V = 14$mag at 450μm. These correspond to column densities $N(\mathrm{H_2})$ of 2.7×10^{21} cm^{-2} and 1.3×10^{22} cm^{-2} respectively.

Pre-protostellar cores are clearly more diffuse than the Class 0/I sources. L1512 is the most extreme in this sense, showing no evidence for a centrally peaked source. L1544 is an elongated structure with a central peak. L1689B has an elongated peak at high contour levels. However, their intensities are not as strongly peaked as the Class 0/I sources. Two out of five pre-protostellar cores have companions within $2'$. L1689A has two sources visible at both wavelengths, separated by about 0.03 pc, with roughly comparable intensity. B133 has a weaker companion to the southeast. L1689B may also have multiple peaks along the east-west ridge. The maps of L1544, B133, and L1689B are consistent with maps of 1.3 mm emission toward those sources (Ward-Thompson et al. 1999; André et al. 1996).

While the pre-protostellar cores are diffuse, the Class 0/I sources are strongly

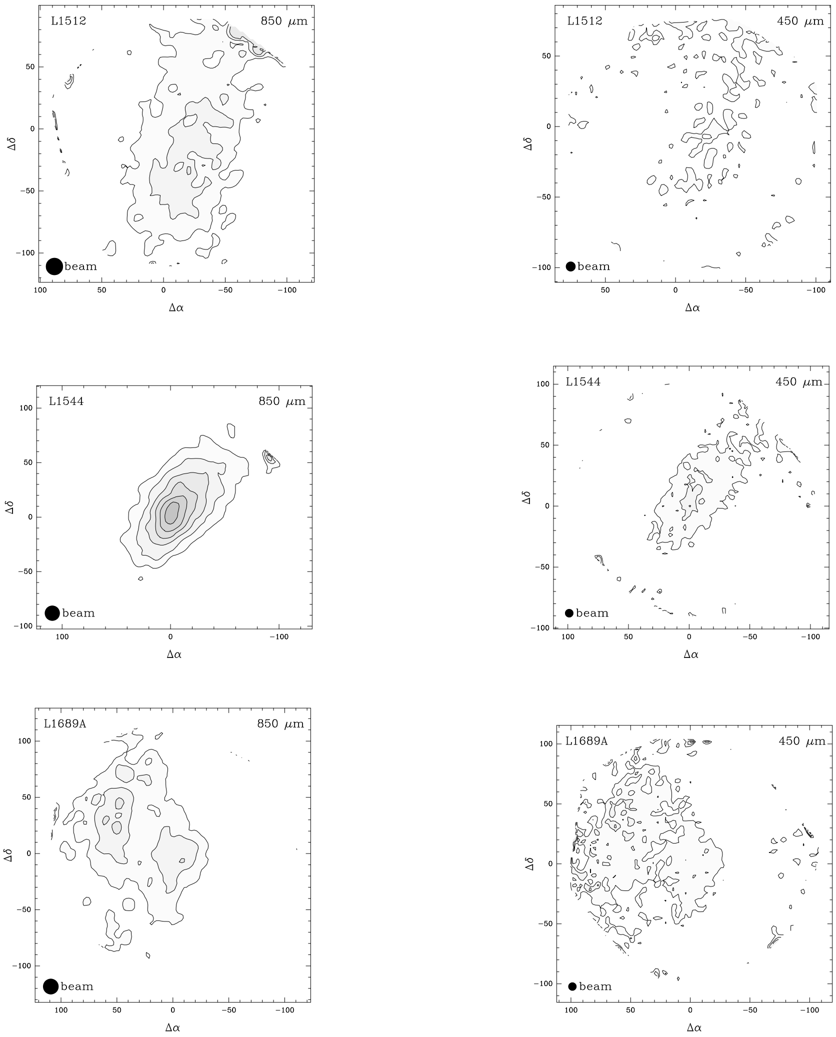

Figure 2.2 Contour maps of pre-protostellar cores. The left column is 850 μm and the right column is 450 μm. The contour levels are as follows (lowest contour and contour increment in percentage of the peak flux). L1512 (850μm) 40%(3σ) increasing by 29%(2σ). L1512 (450μm) 68%(3σ) increasing by 45%(2σ). L1544 (850μm) 20%(3σ) increasing by 13%(2σ). L1544 (450μm) 50%(3σ) increasing by 33%(2σ). L1689A (850μm) 40%(3σ) increasing by 26%(2σ). L1689A (450μm) 41%(3σ) increasing by 33%(2σ). Contours near the edge of the maps should be ignored due to noisy pixels, less integration time, and inability of the plotting package to handle irregular edges.

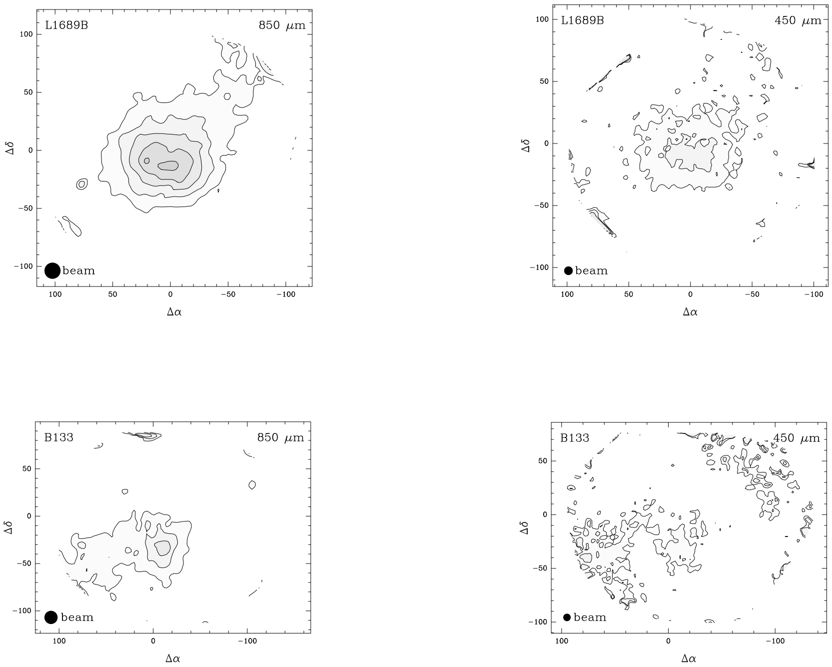

Figure 2.3 Contour maps of pre-protostellar cores. The left column is 850 μm and the right column is 450 μm. The contour levels are as follows (lowest contour and contour increment in percentage of the peak flux). L1689B (850μm) 27%(3σ) increasing by 18%(2σ). L1689B (450μm) 41%(3σ) increasing by 27%(2σ). B133 (850μm) 36%(3σ) increasing by 24%(2σ). B133 (450μm) 59%(3σ) increasing by 39%(2σ). Contours near the edge of the maps should be ignored due to noisy pixels, less integration time, and inability of the plotting package to handle irregular edges.

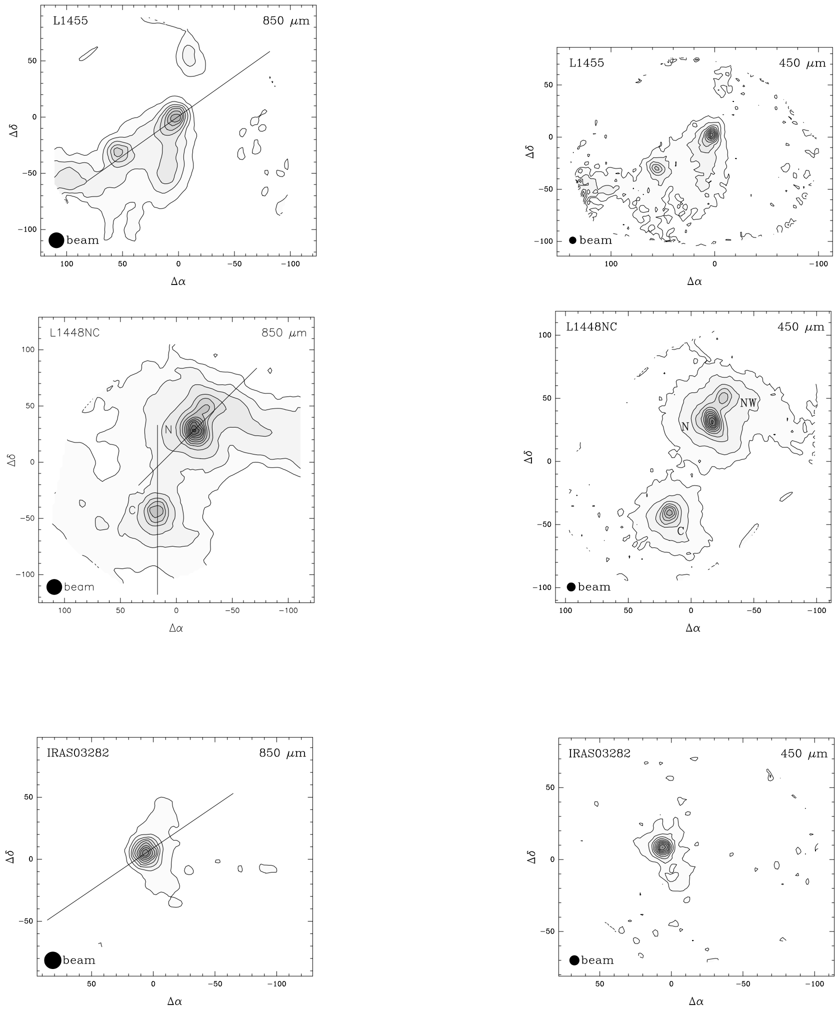

Figure 2.4 Contour maps of Class 0 sources. The left column is 850 μm and the right column is 450 μm. The solid line indicates the outflow direction. The contour levels are as follows (lowest contour and contour increment in percentage of the peak flux). L1455 (850μm) 10%(7σ) increasing by 10%. L1455 (450μm) 10%(4σ) increasing by 10%. L1448N (850μm) 2%(7σ), 5%(19σ), 10%(37σ) increasing by 10%. L1448N (450μm) 5%(5σ), 10%(10σ) increasing by 10%. IRAS03282+3035 (850μm) 10%(6σ) increasing by 10%. IRAS03282+3035 (450μm) 10%(5σ) increasing by 10%. Contours near the edge of the maps should be ignored due to noisy pixels, less integration time, and inability of the plotting package to handle irregular edges.

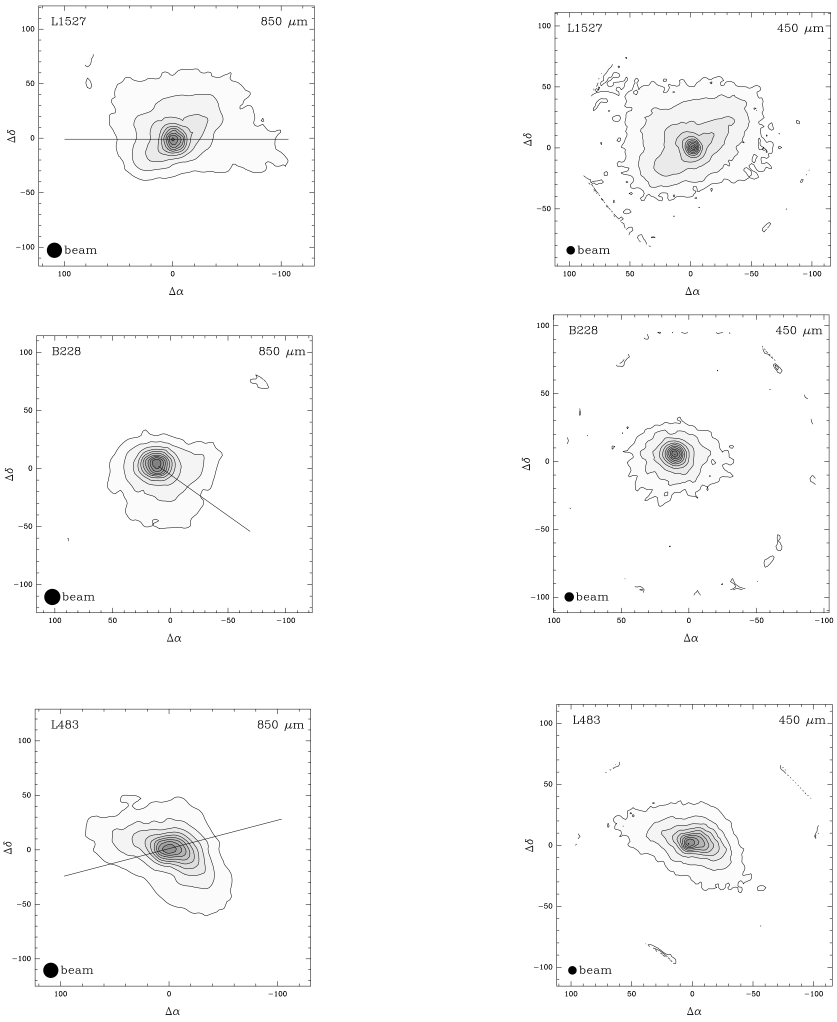

Figure 2.5 Contour maps of Class 0 sources. The left column is 850 μm and the right column is 450 μm. The solid line indicates the outflow direction. The contour levels are as follows (lowest contour and contour increment in percentage of the peak flux). L1527 (850μm) 10%(4σ) increasing by 10%. L1527 (450μm) 5%(5σ), 10%(8σ) increasing by 10%. B228 (850μm) 5%(4σ), 10%(8σ) increasing by 10%. B228 (450μm) 5%(3σ), 10%(6σ) increasing by 10%. L483 (850μm) 10%(5σ) increasing by 10%. L483 (450μm) 10%(6σ) increasing by 10%. Contours near the edge of the maps should be ignored due to noisy pixels, less integration time, and inability of the plotting package to handle irregular edges.

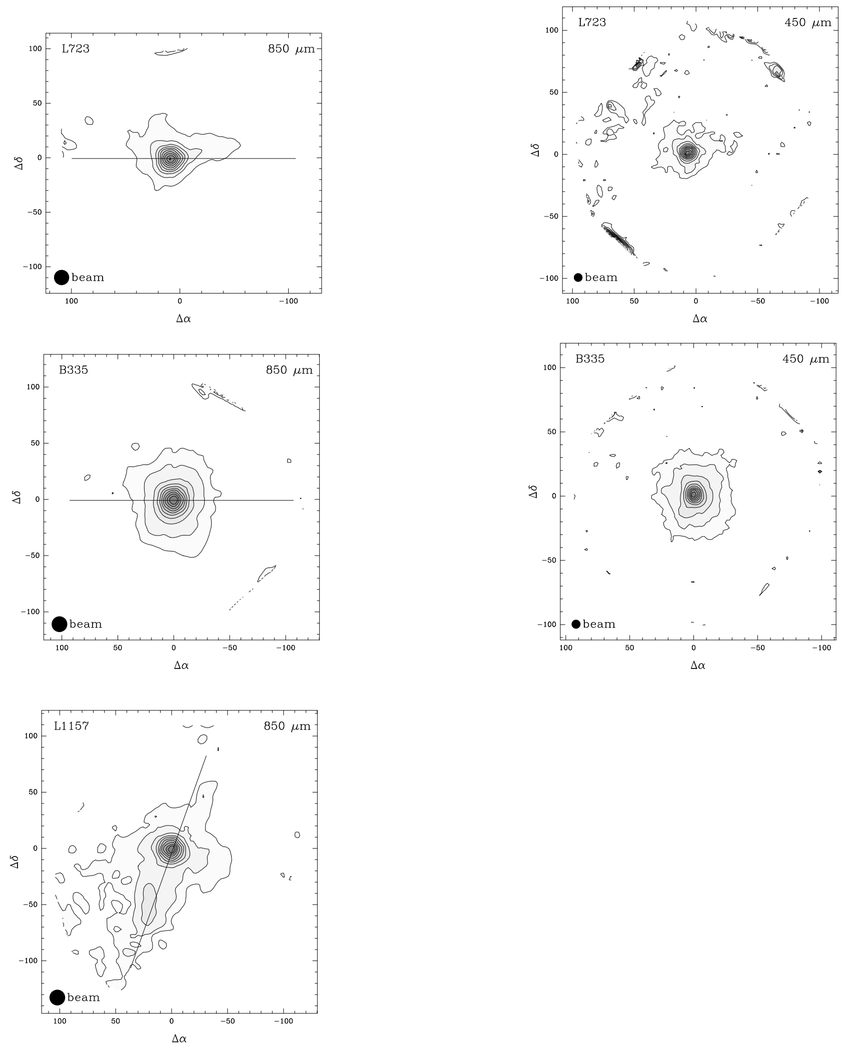

Figure 2.6 Contour maps of Class 0 sources. The left column is 850 μm and the right column is 450 μm. The solid line indicates the outflow direction. The contour levels are as follows (lowest contour and contour increment in percentage of the peak flux). L723 (850μm) 10%(4σ) increasing by 10%. L723 (450μm) 10%(3σ) increasing by 10%. B335 (850μm) 5%(5σ), 10%(9σ) increasing by 10%. B335 (450μm) 5%(3σ), 10%(6σ) increasing by 10%. L1157 (850μm) 5%(3σ), 10%(5σ) increasing by 10%. Contours near the edge of the maps should be ignored due to noisy pixels, less integration time, and inability of the plotting package to handle irregular edges.

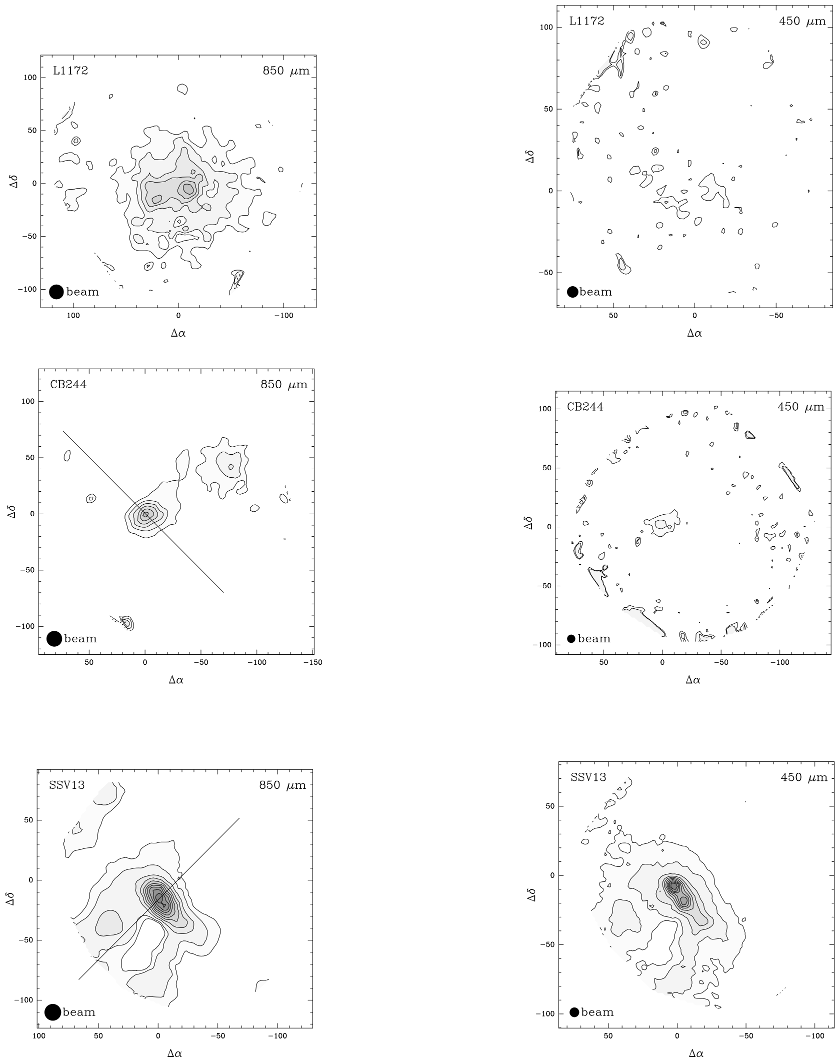

Figure 2.7 Contour maps of Class 0 sources. The left column is 850 μm and the right column is 450 μm. The solid line indicates the outflow direction. The contour levels are as follows (lowest contour and contour increment in percentage of the peak flux). L1172 (850μm) 22%(3σ) increasing by 14%(2σ). L1172 (450μm) 53%(3σ) increasing by 36%(2σ). CB244 (850μm) 22%(3σ) increasing by 15%(2σ). CB244 (450μm) 47%(3σ) increasing by 32%(2σ). SSV13 (850μm) 5%(4σ), 10%(8σ) increasing by 10%. SSV13 (450μm) 5%(6σ), 10%(12σ) increasing by 10%. Contours near the edge of the maps should be ignored due to noisy pixels, less integration time, and inability of the plotting package to handle irregular edges.

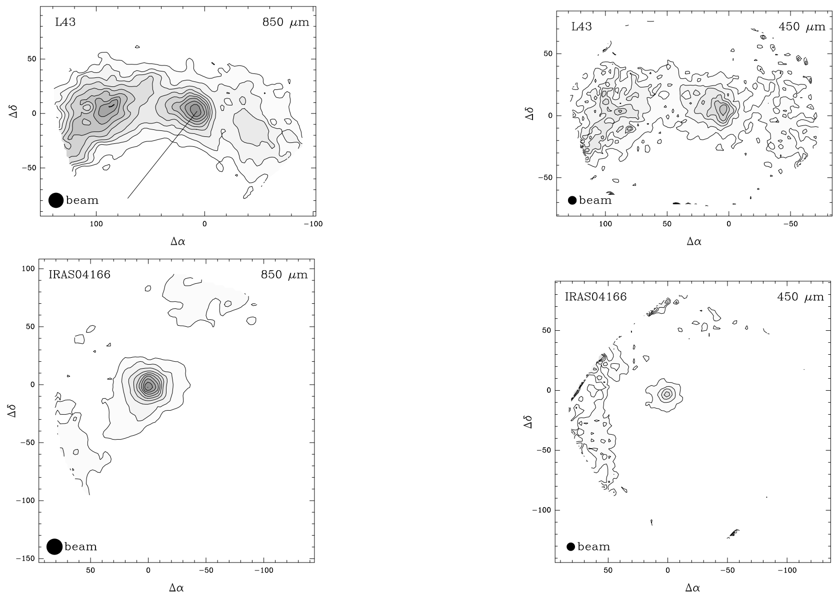

Figure 2.8 Contour maps of Class I sources. The left column is 850 μm and the right column is 450 μm. The solid line indicates the outflow direction. The contour levels are as follows (lowest contour and contour increment in percentage of the peak flux). L43 (850μm) 15%(3σ) increasing by 10%(2σ). L43 (450μm) 20%(3σ) increasing by 14%(2σ). IRAS04166+2706 (850μm) 10%(3σ) increasing by 10%. IRAS04166+2706 (450μm) 29%(3σ) increasing by 19%(2σ). Contours near the edge of the maps should be ignored due to noisy pixels, less integration time, and inability of the plotting package to handle irregular edges.

centrally peaked. All the Class 0 sources except L1172 and L1455 have one well-defined centroid. B335 and B228 appear to be quite circularly symmetric, but B335 has a slight extension to the south-east visible in the 450 μm map (cf. Huard et al. 1999) that may be associated with the outflow (Bontemps et al. 1996). The other Class 0 sources all have non-spherical extensions. These extensions correspond roughly to the outflow directions in L1527, L1157, and L1455. L1157 is a particularly good example with a sizable extension to the south along the outflow axis. Other sources (L483 and IRAS03282+3035) are extended perpendicular to the outflow direction. SSV13 is elongated perpendicular to the outflow direction at high contours, but the lower contours lie along the outflow axis. It is possible that extensions along outflow directions are caused by heating of dust by short wavelength radiation escaping along the outflow cavity, while extensions perpendicular to the outflow direction reflect the distribution of maximum column density, which most models predict to be perpendicular to the outflows. This subject will be analyzed in later papers, where two-dimensional dust radiative transport can be modeled.

Nine of our sixteen Class 0/I sources have a secondary source within $2'$. The L1448 cloud (L1448NW, N, and C) and SSV13 complex were known to contain multiple sources. In addition, the eastern source in L43 is seen in both the 450 μm map of Bence et al. (1998) and the 1.3 mm map of Ward-Thompson et al. (1999). We are not aware of previous detections of the additional sources toward CB244 and L1455 (see Table 2.5). L1455 is an extreme case with 5 sources within the SCUBA map, only one of which corresponds to a known source in this region. Continuum emission is observed to bridge between sources, making it difficult to disentangle the envelope density structure. L1172 has at least 2 peaks within a $20''$ region. For the seven Class 0/I sources without secondary sources, the lack of contamination coupled with high signal-to-noise (Table 2.15) will allow radial intensity profiles extending up to 11 beams (at 450 μm) from the central source (see section 2.3.3).

For cores with more than one source, the mean separation in the plane of the sky is 10800 AU, less than twice the fragmentation scale of 6000 AU found in the ρ Ophiuchi cores by Motte et al. (1998). A mean separation of 10^4 AU is also close to the break in the distribution of optical binaries in Taurus, which Larson (1995) associates with the Jeans length, and to the length scale inferred for dynamical collapse based on specific angular momentum arguments (Ohashi et al. 1997). Looney, Mundy, & Welch (2000) find evidence for multiplicity on still smaller scales in L1448 and SSV13. They describe sources separated by > 6000 AU as "separate envelope" multiplicity, and our data are consistent with this picture. The median separation, including the map size as a lower limit for sources with no detected companion, is 18000 AU.

2.3.2 Photometry, Classification, Spectral Index and Masses

The photometry is presented in Table 2.5, including calibration uncertainties. Fluxes are reported in $120''$ and $40''$ apertures at 1.3 mm, 850 μm, and 450 μm. Uncertainties reported include statistical uncertainties and calibration uncertainties calculated from

$$\sigma_{S_\nu}^2 = {S_\nu}^2 \left[\left(\frac{\sigma_C^2}{C^2} \right)_{Run\ Avg} + \left(\sec^2 z \, \sigma_\tau^2 \right)_{Source} \right] \tag{2.2}$$

where S_ν is the flux density (Jy) and C is the calibration factor (Jy/V). The uncertainties are σ_C and σ_τ, the standard deviation over the run in C and over the night in τ (Table 2.3) and z is the mean zenith angle of the observations of the source. Photometry is presented for each source in the map that is sufficiently strong and well-defined. The offsets of the centroids from previous infrared/submillimeter positions (Table 2.1) are reported in Table 1.5.

The spectral index $\alpha_{450/850}$, defined by

$$\alpha_{450/850} = \frac{\log\left(\frac{S_{450}}{S_{850}}\right)}{\log\left(\frac{850}{450}\right)}, \tag{2.3}$$

TABLE 2.5

OBSERVED FLUX DENSITIES OF SOURCES

Source	Centroid ($\Delta\alpha''$,$\Delta\delta''$)	1.3 mm[a]	850 μm[a]	S_ν (Jy) 850 μm[b]	450 μm[a]	450 μm[b]
L1512	(−19,−26)	...	0.35(0.02)	1.81(0.09)	1.6(0.3)	8.5(3.2)
L1544	(−1,4)	0.27(0.04)	1.12(0.07)	3.64(0.18)	4.2(0.8)	17.4(6.7)
L1689A	(−4,−9)	...	0.54(0.03)	...	3.9(0.6)	...
	(51,24)	...	0.55(0.03)	...	3.4(0.5)	...
L1689B	(−1,−12)	...	0.90(0.05)	3.18(0.18)	3.2(0.5)	10.8(1.7)
B133	(−13,−32)	...	0.60(0.03)	2.06(0.12)	3.4(0.5)	11.8(1.6)
L1448NW	(0,0)	...	6.51(0.38)	...	43.9(7.6)	...
L1448N	(−1,1)	...	8.19(0.49)	...	56.4(9.8)	...
L1448C	(0,3)	0.74(0.11)	3.95(0.24)	...	31.8(5.5)	...
L1455	(3,1)	...	1.08(0.06)	...	10.2(1.8)	...
	(55,−30)	...	0.94(0.06)	...	7.7(1.3)	...
	(−9,59)	...	0.38(0.02)	...	2.5(0.5)	...
	(10,−47)	...	0.91(0.05)	...	6.9(1.2)	...
IRAS03282	(6,8)	...	1.74(0.10)	3.59(0.17)	9.9(1.7)	25.0(9.4)
L1527	(−2,0)	0.72(0.11)	3.19(0.19)	9.41(0.46)	18.2(3.2)	55.5(20.9)
B228	(11,5)	...	2.63(0.15)	4.23(0.24)	19.6(2.7)	25.9(3.7)
L483	(1,2)	...	3.74(0.20)	9.25(0.51)	30.1(4.6)	59.2(1.7)
L723	(8,1)	...	1.79(0.11)	3.60(0.23)	8.5(2.1)	12.4(3.1)
B335	(0,1)	0.57(0.09)	2.28(0.12)	3.91(0.22)	14.6(2.2)	21.1(3.3)
L1157	(0,1)	0.58(0.09)	2.41(0.19)	5.03(0.40)	...	...
L1172	(−10,−2)	...	0.66(0.04)	2.69(0.15)	5.2(0.8)	16(3)
CB244	(0,1)	0.25(0.04)	1.04(0.08)	1.86(0.14)	5.1(1.9)	9.0(3.4)
	(−75,45)	...	0.78(0.06)	...	3.1(1.2)	...
SSV13	(1,−10)	1.83(0.28)	6.95(0.41)	...	52.4(9.1)	...
IRAS04166	(1,−4)	...	1.08(0.06)	...	4.2(1.0)	...
L43	(7,5)	...	1.60(0.09)	...	11.8(2.0)	...
	(89,6)	...	1.80(0.10)	...	11.4(1.9)	...

[a]In a 40″ aperture

[b]In a 120″ aperture

is given in Table 2.6 for both 40″ and 120″ photometry, when available. Note that this definition differs from that in Equation 2.1. The uncertainties include calibration uncertainty, which usually dominates. The values for the two aperture sizes do not differ significantly; we use the values for a 40″ aperture in the following discussion because more data are available. The mean spectral index for the collapse candidates is indistinguishable from that of sources with no evidence of collapse. The mean for the pre-protostellar cores ($\langle\alpha_{450/850}\rangle = 2.5 \pm 0.4$) is slightly less than that for Class 0 and I sources ($\langle\alpha_{450/850}\rangle = 2.9 \pm 0.4$). A lower spectral index may be an indication of lower T_d in pre-protostellar cores, resulting in failure of the Rayleigh-Jeans approximation (see §2.4.2). Because the difference is not statistically significant, we also calculated the mean and standard deviation of all the measurements ($\langle\alpha_{450/850}\rangle = 2.8 \pm 0.4$). If the emission were in the Rayleigh-Jeans limit, this result would imply that that $\kappa_\nu \propto \nu^{0.8}$ between 450 and 850 μm, but this exponent should be interpreted as a lower limit if the Rayleigh-Jeans approximation fails. The average spectral index between 850μm and 1.3mm, defined in the same manner as in Equation 2.3, is $\langle\alpha_{850/1.3}\rangle = 3.4 \pm 0.3$. A higher $\alpha_{850/1.3}$ would be expected if the Rayleigh-Jeans approximation were failing at 450 μm.

Values of L_{bol}, T_{bol}, and L_{smm}/L_{bol}, where L_{smm} includes all flux at $\lambda > 350$ μm, were newly computed (Table 1.7), including archival data and the results of our photometry. We include the archival data and references in Tables 1.8 – 1.14. For isolated sources, we chose data in the largest available apertures at long wavelengths, because our data show that much of the flux density comes from very extended regions. Two different methods were used to integrate the data. The uncertainties reflect uncertainties in the photometry and differences in the method of integration, but the uncertainties in L_{bol} do not include uncertainties in distance, since these are unavailable for many sources. Among the pre-protostellar cores, only L1544 and L1689B have the requisite far-infrared data. The L_{bol} of L1544 is comparable to

TABLE 2.6

OBSERVED SPECTRAL INDICES OF SOURCES

Source	Centroid	$\alpha_{850/1.3}$ [a]	$\alpha_{450/850}$ [a]	$\alpha_{450/850}$ [b]
L1512	(−19,−26)	...	2.4(0.7)	2.4(1.4)
L1544	(−1,4)	3.3(0.9)	2.1(0.7)	2.5(1.4)
L1689A	(−4,−9)	...	3.1(0.6)	...
	(51,24)	...	2.9(0.6)	...
L1689B	(−1,−12)	...	2.0(0.6)	1.9(0.6)
B133	(−13,−32)	...	2.7(0.5)	2.7(0.5)
L1448NW	(0,0)	...	3.0(0.7)	...
L1448N	(−1,1)	...	3.0(0.7)	...
L1448C	(0,3)	3.9(0.9)	3.3(0.7)	...
L1455	(3,1)	...	3.5(0.7)	...
	(55,−30)	...	3.3(0.7)	...
	(−9,59)	...	3.0(0.7)	...
	(10,−47)	...	3.2(0.7)	...
IRAS03282	(6,8)	...	2.7(0.7)	3.1(1.4)
L1527	(−2,0)	3.5(0.9)	2.7(0.7)	2.8(1.4)
B228	(11,5)	...	3.2(0.5)	2.8(0.6)
L483	(1,2)	...	3.3(0.6)	2.9(0.6)
L723	(8,1)	...	2.4(0.9)	1.9(0.9)
B335	(0,1)	3.3(0.9)	2.9(0.6)	2.6(0.6)
L1157	(0,1)	3.3(0.9)	...	...
L1172	(−10,−2)	...	3.3(0.6)	2.8(0.6)
CB244	(0,1)	3.4(1.0)	2.5(1.4)	2.5(1.4)
	(−75,45)	...	2.2(1.4)	...
SSV13	(1,−10)	3.1(0.9)	3.2(0.7)	...
IRAS04166	(1,−4)	...	2.1(0.9)	...
L43	(7,5)	...	3.1(0.6)	...
	(89,6)	...	2.9(0.6)	...

[a]In a 40″ aperture

[b]In a 120″ aperture

some Class 0 sources, but the origin of the relatively strong far-infrared emission is unclear.

Some sources changed classification as a result of our data or analysis. The position of IRAS04166+2706 is close to the IRAS position, but clearly displaced from the position in Mardones et al. (1997). We calculate a lower T_{bol}, but the source remains a Class I source. L1448N is clearly a Class 0 source with our photometry, whereas it was borderline for Mardones et al. (who referred to it as $03225 + 3034$). The situation is similar for L1455. We find a very low T_{bol} for IRAS03282+3035, consistent with the upper limit of Mardones et al. (1997). For L1527 and CB244, we excluded the near-infrared data, which is clearly displaced from the submillimeter source, leading to a lower T_{bol} than previous estimates (Chen et al. 1995, Mardones et al. 1997). Our value of T_{bol} for B335 is 28 K, rather than the 37 K of Mardones et al. (1997), presumably because we include the larger flux densities that we find. Adding data at submillimeter wavelengths also decreased T_{bol} for L1157 and L1172, moving the latter source to Class 0. The values of T_{bol} for SSV13 and L43 include near-infrared data, because the emission peaks on the submillimeter position. However, SSV13 has varied substantially and T_{bol} depends on the epoch; we used pre-flare near-infrared data (Harvey et al. 1998). The emission in L43 (RNO91) is polarized, hence scattered. If we exclude the near-infrared data, T_{bol} would be 83 ± 5, still a Class I source.

We have estimated the masses (gas and dust) from the dust emission and the equation

$$M_D = \frac{S_\nu D^2}{B_\nu(T_d)\kappa_\nu} = 3.69 \times 10^{-6} \mathrm{M}_\odot S_\nu(Jy) D^2(pc)(e^{16.9K/T_d} - 1), \qquad (2.4)$$

where S_ν is the flux density at 850 μm in a $120''$ beam (Table 2.7), $B_\nu(T_d)$ is the Planck function, κ_ν is the opacity per gm of gas and dust at 850 μm, and we have assumed optically thin emission in a constant density sphere. The values in Table 2.7

TABLE 2.7
SOURCE PROPERTIES

Source	Class	L_{bol} $L_\odot$	T_{bol} (K)	L_{smm}/L_{bol}	M_D(20K) $M_\odot$	M_V $M_\odot$	Ref.[a]
L1512	PPC	...	...	...	0.2	0.3	1
L1544	PPC	1.0(0.3)	18(6)	0.03(0.01)	0.4	0.4	1
L1689A	PPC	...	...	...	...	13	2
L1689B	PPC	0.2(0.03)	18(4)	0.09(0.01)	0.24	2.0	3
B133	PPC	...	...	...	...	4.7	1
L1448NW	0	2.2(0.5)	24(5)	0.09(0.02)	...	...	...
L1448N	0	8.0(1.0)	55(7)	0.028(0.007)	...	...	...
L1448C	0	6.0(0.5)	54(7)	0.020(0.005)	...	9.4	1
L1455	0	6.9(0.3)	67(3)	0.0053(0.0007)	...	6.4	4
IRAS03282+3035	0	1.2(0.3)	23(5)	0.09(0.03)	2.2	2.9	4
L1527	0	2.2(0.2)	36(5)	0.04(0.02)	0.9	0.9	4
B228	0	1.2(0.2)	48(2)	0.03(0.01)	0.4	2.6	5
L483	0	13(2)	52(8)	0.015(0.003)	1.8	2.7	4
L723	0	3.3(0.2)	47(3)	0.035(0.008)	1.6	7.3	4
B335	0	3.1(0.1)	28(1)	0.060(0.007)	1.2	3.5	4
L1157	0	5.8(0.8)	42(4)	0.009(0.003)	2.6	10	4
L1172	0	1.1(0.1)	44(4)	0.010(0.008)	...	4.9	4
CB244	0	1.0(0.1)	56(3)	0.024(0.004)	0.3	2.2	4
SSV13	I	43(2)	136(15)	0.0047(0.0012)	...	6.9	4
IRAS04166+2706	I	0.42(0.03)	91(12)	0.019(0.002)	...	1.0	4
L43	I	2.7(0.1)	370(20)	0.0054(0.0010	...	1.7	4

[a] Reference for linewidth used to calculate M_V

REFERENCES.—1. Benson et al. 1998(N_2H^+); 2. Benson & Myers 1989 (NH_3); 3. Gregersen & Evans 2000 ($H^{13}CO^+$); 4. Mardones et. al. 1997 (N_2H^+); 5. Gregersen et al. 2000 ($H^{13}CO^+$)

TABLE 2.8
SPECTRAL ENERGY DISTRIBUTIONS OF SOURCES

Source	λ (μm)	S_ν (Jy)	θ ($''$)	Ref.
L1512	450	$<$6.0(3σ)	18	1
	800	0.11(0.02)	18	1
	1100	0.045(0.009)	18	1
	1300	$<$0.016(3σ)	12	1
L1689A	450	2.20(0.30)	18	2
	850	0.29(0.045)	18	2
	1100	$<$0.10(3σ)	18	2
	1300	0.054(0.015)	24	2
B133	450	$<$1.8(3σ)	18	2
	800	0.34(0.06)	18	2
	1100	$<$0.12(3σ)	18	2
	1300	0.65(0.13)	164$\times$102	2
L1448C	12*	0.33(0.07)	35$\times$28	5
	25*	2.9(0.6)	35$\times$28	5
	60*	31.2(6.5)	36	5
	100*	70.3(14.8)	45$\times$40	5
	350	30(3.0)	19.5	5
	450	21(2.0)	18.5	5
	800	3.0(0.3)	16.5	5
	1100	1.0(0.1)	18.5	5
	1300	1.0(0.1)	12	6
	2600	0.091(0.002)	2.7	7
	3500	0.026(0.002)	2.4	6
L1448NW	12	$<$0.015(3σ)	35$\times$28	5
	25	$<$0.05(3σ)	35$\times$28	5
	60*	3.2(0.5)	36	5
	100*	23(7.5)	45$\times$40	5
	800	2.0(0.5)	16.5	5
	1300	0.4(0.1)	12	5
	2720	$<$0.021(3σ)	7.0	8

*Flux value used in calculation of L_{bol} and T_{bol}

REFERENCES.—1. Ward-Thompson et al. 1999; 2. Ward-Thompson et al. 1994; 3. IRAS PSC; 4. Ward-Thompson et al. 1998; 5. Barsony et al. 1998; 6. Bachiller et al. 1991b 7. Bachiller et al. 1995; 8. Terebey et al. 1993; 9. Ward-Thompson & André 1999

TABLE 2.9
SPECTRAL ENERGY DISTRIBUTIONS OF SOURCES

Source	λ (μm)	S_ν (Jy)	θ ($''$)	Ref.
L1544	170*	220(80)	(?)	9
	200*	280(100)	(?)	9
	450	1.3(0.24)	18	2
	800	0.45(0.06)	18	2
	1100	0.19(0.03)	18	2
	1300*	2.3(0.5)	260×140	1
L1689B	12	<0.25(3σ)	300×45	3
	25	<0.50(3σ)	300×45	3
	60	<0.63(3σ)	90×300	3
	90	<12.6(3σ)	72	4
	100	<32(3σ)	180×300	3
	160*	43(15)	72	4
	190*	46(13)	72	4
	800	0.36(0.04)	18	2
	850	4.2(0.9)	120	2
	1100	0.14(0.03)	18	2
	1100*	1.6(0.3)	120	2
	1300	0.13(0.01)	24	2
	1300*	0.8(0.17)	120	2
L1448N	12*	0.67(0.15)	35×28	5
	25*	5.7(1.2)	35×28	5
	60*	28.8(6.1)	36	5
	100*	89.0(18.7)	45×40	5
	350	45(3.0)	19.5	5
	450	28(2)	18.5	5
	800	5.8(0.4)	16.5	5
	1100	12.3(0.2)	18.5	5
	1300	2.2(0.1)	12	5
	2600	0.185(...)	2.7	7
	2720	>0.225(...)	7.0	7,8

*Flux value used in calculation of L_{bol} and T_{bol}

REFERENCES.—1. Ward-Thompson et al. 1999; 2. Ward-Thompson et al. 1994; 3. IRAS PSC; 4. Ward-Thompson et al. 1998; 5. Barsony et al. 1998; 6. Bachiller et al. 1991b 7. Bachiller et al. 1995; 8. Terebey et al. 1993; 9. Ward-Thompson & André 1999

TABLE 2.10

SPECTRAL ENERGY DISTRIBUTIONS OF SOURCES

Source	λ (μm)	S_ν (Jy)	θ ($''$)	Ref.
L1527	1.2	0.0044(0.0003)	26	10
	1.6	0.0089(0.0002)	26	10
	2.2	0.024(0.002)	26	10
	12	<0.25(3σ)	300×45	3
	25*	0.74(0.07)	300×45	3
	60*	17.8(1.6)	90×300	3
	100	89(36)	60	11
	100*	73.3(11.7)	180×300	3
	160*	94(38)	60	11
	350	22(9)	60	11
	450	14(5.6)	60	11
	800	1.4(0.56)	60	11
L483	12*	<0.25(3σ)	330×45	3
	25*	6.91(0.48)	300×45	3
	60*	89.1(11.6)	90×300	3
	100*	170(85)	60	11
	100	165.5(20.0)	180×300	3
	160*	290(145)	60	11
	190*	140(70)	60	11
	450	15(2)	19	12
	800	1.98(0.02)	19	12
	1100	0.64(0.02)	19	12
	2700	0.0072(?)	5	12

*Flux value used in calculation of L_{bol} and T_{bol}

REFERENCES.—3. IRAS PSC; 5. Barsony et al. 1998; 6. Bachiller et al. 1991b; 9. Bachiller at al. 1994 10. Kenyon et al. 1990; 11. Ladd et al. 1991; 12.Fuller et al. 1995; 13. IRAS FSC; 14. Davidson 1987; 15. Reipurth et al. 1993; 16. Keene et al. 1983; 17. Larsson 1998; 18. Gee et al. 1988; 19. Gueth et al. 1997

Table 2.11

Spectral Energy Distributions of Sources

Source	λ (μm)	S_ν (Jy)	θ ($''$)	Ref.
IRAS03282+3035	12	$<$0.18(3σ)	34$\times$29	5
	25	$<$0.29(3σ)	36	5
	60*	2.32(0.5)	33$\times$36	5
	100*	11.05(2.4)	40$\times$39	5
	350	9.1(1.0)	19.5	5
	450	5.9(1.0)	18.5	5
	800	1.4(0.1)	16.5	5
	1100*	0.58(0.05)	18.5	5
	1300	0.3(...)	12	9
B228	12*	0.19(0.03)	300$\times$45	3
	25*	1.27(0.05)	300$\times$45	3
	60*	14.7(0.59)	90$\times$300	3
	100*	41.1(2.46)	180$\times$300	3
L723	12*	0.28(0.06)	300$\times$45	13
	25*	0.38(0.05)	300$\times$45	3
	60*	6.93(0.62)	90$\times$300	3
	95	27(6)	45	14
	100*	20.7(1.7)	180$\times$300	3
	130	32(11)	33	14
	140*	23(8)	85	14
	144	33(10)	33	14
	166	40(12)	45	14
	195*	35(7)	85	14
	400	13(3)	48	14
	1000*	1.0(0.5)	102	14
	1300	0.357(0.017)	23	15
L1157	12*	0.066(0.011)	300$\times$45	13
	25*	0.226(0.016)	300$\times$45	13
	60*	9.97(0.50)	90$\times$300	13
	100	42.0(1.7)	180$\times$300	13
	1300	0.9(0.1)	(?)	19
	2700	0.04(?)	5	19

*Flux value used in calculation of L_{bol} and T_{bol}

References.—3. IRAS PSC; 5. Barsony et al. 1998; 6. Bachiller et al. 1991b; 9. Bachiller at al. 1994 10. Kenyon et al. 1990; 11. Ladd et al. 1991; 12.Fuller et al. 1995; 13. IRAS FSC; 14. Davidson 1987; 15. Reipurth et al. 1993; 16. Keene et al. 1983; 17. Larsson 1998; 19. Gueth et al. 1997

Table 2.12

Spectral Energy Distributions of Sources

Source	λ (μm)	S_ν (Jy)	θ ($''$)	Ref.
B335	12	0.32(0.08)	300×45	13
	25	0.19(0.03)	300×45	13
	60	7(2)	33	16
	60*	8.3(0.8)	90×300	3
	85*	24(2.4)	80	17
	100*	31(3.1)	80	17
	100	42.0(7.6)	180×300	3
	110	35(9)	42	16
	115	40(4)	80	17
	140	38(9)	42	16
	150*	56(5.6)	80	17
	170*	60(6.0)	80	17
	180	80(18)	90	16
	190	84(24)	102	16
	200*	67(14)	90	16
	235*	61(14)	102	16
	360*	41(8)	55	18
	750*	5.3(1.0)	58	18
CB244	12*	0.055(0.12)	300×45	13
	25*	0.775(0.039)	300×45	13
	60*	9.06(0.45)	90×300	13
	100*	15.0(0.9)	180×300	13
	350*	9.3(2.8)	19.5	20
	450	3.5(1.1)	18.5	20
	800	0.65(0.13)	16.5	20
	1100*	0.27(0.05)	18.5	20
	1300	0.12(0.02)	16.5	20

*Flux value used in calculation of L_{bol} and T_{bol}

References.—3. IRAS PSC; 13. IRAS FSC; 16. Keene et al. 1983; 17. Larsson 1998; 18. Gee et al. 1988; 20. Launhardt & Henning 1997

Table 2.13

Spectral Energy Distributions of Sources

Source	λ (μm)	S_ν (Jy)	θ ($''$)	Ref.
SSV13	1.6*	0.033(0.003)	3	22
	2.2*	0.098(0.010)	3	22
	3.4*	0.34(0.03)	3	22
	12*	13.6(3.7)	300×45	13
	25*	46.5(2.8)	300×45	13
	60*	204(20)	90×300	13
	100*	381(23)	180×300	13
	870	3.85(0.09)	18	15
	1300	1.23(0.04)	23	15
L43	0.45*	0.00064(0.00006)	12	23
	0.55*	0.0031(0.0003)	12	23
	0.70*	0.0086(0.0009)	12	23
	0.90*	0.024(0.002)	12	23
	1.25*	0.096(0.005)	12	23
	1.6*	0.25(0.01)	12	23
	2.2*	0.48(0.02)	12	23
	3.4*	0.51(0.02)	12	23
	12*	1.47(0.12)	300×45	13
	25*	6.00(0.36)	300×45	13
	60*	34.0(2.7)	90×300	13
	100*	68.0(3.4)	180×300	13
	160*	79(32)	60	11
	190*	38(15.2)	60	11

*Flux value used in calculation of L_{bol} and T_{bol}

References.—13. IRAS FSC; 15. Reipurth et al. 1993; 22. Aspin & Sandell 1994; 23. Myers et al. 1987

TABLE 2.14
SPECTRAL ENERGY DISTRIBUTIONS OF SOURCES

Source	λ (μm)	S_ν (Jy)	θ ($''$)	Ref.
L1455	12*	0.18(0.05)	300×45	13
	25*	4.24(0.21)	300×45	13
	60*	48.8(2.4)	90×300	13
	100*	82.2(4.9)	180×300	13
	160*	55(25)	49	21
	190*	40(15)	49	21
	400	20(5)	49	21
IRAS04166+2706	1.6*	0.00010(0.00002)	10(?)	10
	2.2*	0.00019(0.00009)	10(?)	10
	12*	0.07(0.007)	300×45	3
	25*	0.58(0.058)	300×45	3
	60*	5.9(0.59)	90×300	3
	100*	9.5(0.95)	180×300	3
L1172	12*	0.14(0.03)	300×45	13
	25*	0.30(0.02)	300×45	13
	60*	1.31(0.09)	90×300	13
	100	11(4.4)	60	11
	100*	4.76(1.33)	180×300	13
	160*	10(4.0)	60	11

*Flux value used in calculation of L_{bol} and T_{bol}

REFERENCES.—3. IRAS PSC; 10. Kenyon et al. 1990; 11. Ladd et al. 1991; 13. IRAS FSC; 15. Reipurth et al. 1993; 16. Keene et al. 1983; 17. Larsson 1998; 18. Gee et al. 1988; 20. Launhardt & Henning 1997; 21. Davidson & Jaffe 1984; 22. Aspin & Sandell 1994; 23. Myers et al. 1987 were computed assuming $\kappa_\nu = 2 \times 10^{-2}$ cm^2 gm^{-1} and $T_d = 20$ K. Masses computed with $T_d = 10$ K are a factor of 3.3 higher. Estimates of κ_ν vary by at least a factor of 3. We have used the value for agglomerated grains with thin ice mantles (col. 5 of Table 1 of Ossenkopf & Henning 1994, hereafter OH5 dust), a model which has reproduced other data well (van der Tak et al. 1999, 2000). For comparison, we also computed the virial mass in the same ($60''$) radius using the width of the line most likely to be optically thin (see references in Table 2.7). Both calculations assumed a uniform density cloud (no temperature or density gradients). The virial mass estimate would be decreased by a factor of 0.6 in a cloud with $n(r) \propto r^{-2}$ for example. Given the uncertainties in each calculation, the agreement is good. The mean and standard deviation of the ratio are $M_D(20K)/M_{vir} = 0.5 \pm 0.3$. This result is consistent (within reasonable uncertainties in T_d and distance) with the assumption that the sources are gravitationally bound, but the uncertainties make this assumption hard to test conclusively. The mean mass is $M_D(20K) = 1.1 \pm 0.9$ M$_\odot$.

2.3.3 Radial Profiles

To compute the average intensity distribution, we assume azimuthal symmetry. While many images are not circular, experiments with taking cuts along different axes, cutting out sectors with elongated emission, etc. indicate that the overall results are not significantly affected by deviations from azimuthal symmetry. Chandler & Richer (2000) modeled the effects of outflow cavities and found that the resulting intensity profile has only a slightly lower value of m.

Normalized, azimuthally averaged radial profiles were made for each SCUBA image. Each image was rebinned to $0.5\theta_{mb}$ spacing. The mean $I_\nu(b)$ in an annulus about impact parameter b was computed from the intensity map, weighted by A_i/σ_i^2, where A_i represents the area of the ith pixel intercepted by the annulus and σ_i is the uncertainty in the map intensity in the ith pixel. The error bars were calculated by propagating the uncertainties from the map. The radial profiles were normalized to the peak emission, and we plot $I_\nu(b)/I_\nu(0)$. The image centroids in Table 2.5 were used for the center of the radial profile. To avoid effects of chopping, we terminated the radial profiles at 98″ from the centroid; points are binned at $0.5\theta_{mb}$ spacing (7″ at 850 μm and 3.″5 at 450 μm). We have used the distances in Table 2.2 to convert angles to impact parameters (b) in units of AU. In Figures 2.9–2.12, the normalized radial profiles ($I_\nu(b)/I_\nu(0)$) are plotted versus b. The inflections in some profiles at large radii are due to contamination by secondary sources. The point-to-point fluctuations in the profile are substantially less than the errorbars because half-beam sampling was used. The radial profiles agree well with those of 1.3 mm emission presented by André et al. (1996) and Ward-Thompson et al. (1999). The radial intensity profiles of L1448-C agree well with those of Chandler & Richer (2000), but our profile of L1527 is steeper than those found by either Chandler & Richer (2000) or Hogerheijde & Sandell (2000).

Previous observations of pre-protostellar cores showed that the radial intensity profile did not follow a single power law, but a broken power law was able to fit the limited data (Ward-Thompson et al. 1994). Maps of millimeter emission (Ward-Thompson, Motte, & André 1999) have clearly shown the flattening of $I_\nu(b)/I_\nu(0)$ in the inner regions. While the outer regions can be approximated by a power law, André et al. (1996) commented that the north-south cut through L1689B would be described better by a Gaussian than by a power law. It is clear from Figure 2.9 that a power-law does not fit any portion of the pre-protostellar core radial intensity profiles in the submillimeter, confirming the result of Ward-Thompson et al. (1999). Our results for pre-protostellar cores are consistent with observations of a larger sample (André et al. 2000).

Models of core formation leading to inside-out collapse predict a flat inner

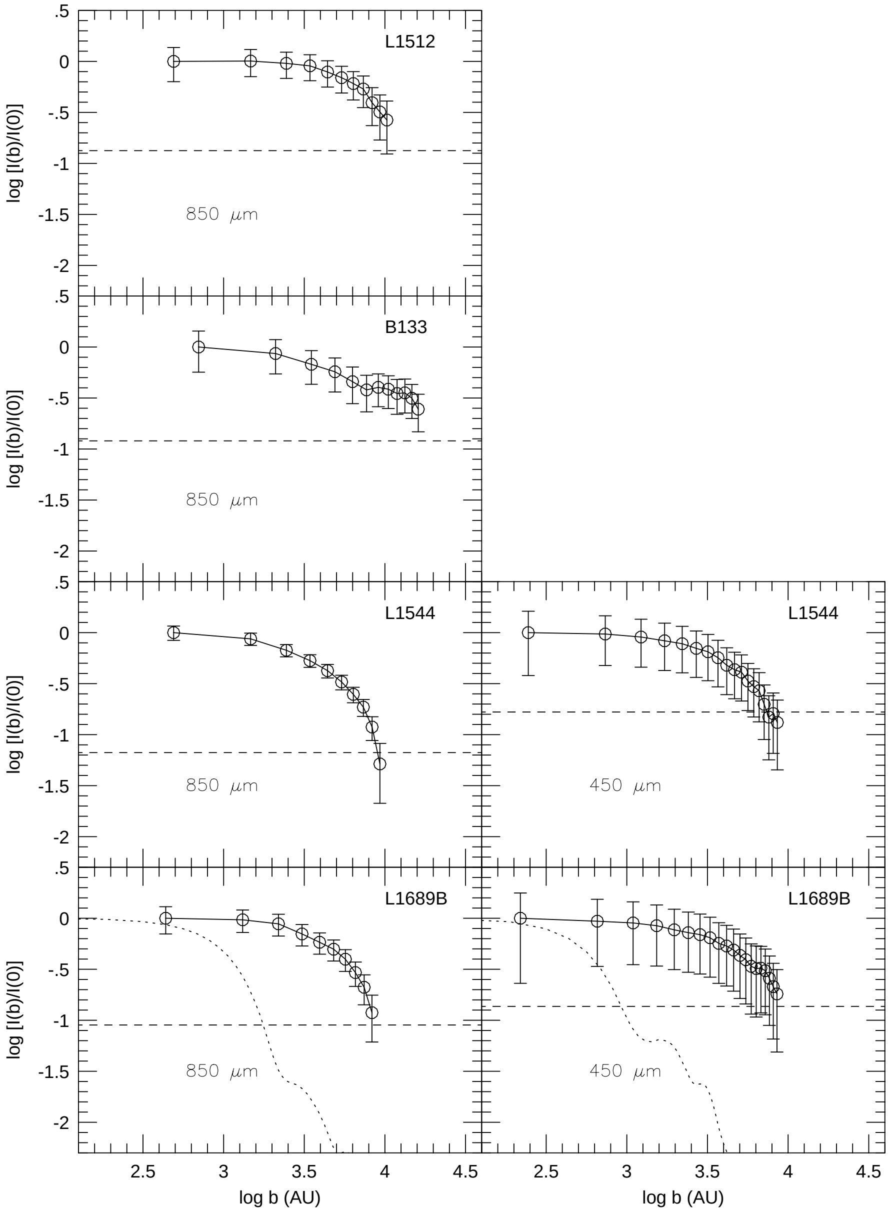

Figure 2.9 Radial profiles of pre-protostellar cores. The normalized intensity is plotted as a function of impact parameter, b(AU). The horizontal dashed lines represent the 1σ noise level at the edge of the map. Note that no section of the profile is fit by a power law. The beam profiles are shown as dashed lines in the bottom panel.

core approaching $p \sim 2$ at larger radii, and the flat core should shrink toward the center with time. While our observations do not appear to be consistent with these models, we caution that detailed modeling is still needed. If the evidence for large-scale infall in all of these cores but L1512 (Lee, Myers, & Tafalla 1999; Gregersen & Evans 2000) is correct, then infall may begin before the core has fully relaxed to a singular isothermal sphere with $n(r) \propto r^{-2}$ (e.g., Shu 1977).

In contrast, the intensity profiles of most Class 0/I sources (Figures 2.10–2.12) can be fitted with power laws, if the inner three points, which are affected by the finite beam size, and the outermost points (noisy, and possibly affected by the finite chop size or other sources) are ignored. Power law fits ($I_\nu(b)/I_\nu(0) = (b/b_0)^{-m}$, with b_0 corresponding to $0.25\theta_{mb}$) were made to 8 cores at 850 μm and 10 cores at 450 μm. The uncertainty in the value of m (Table 2.15) includes the deviations from a straight line and the standard deviation from the radial profiles, as described above. Fits used only points in the profile where the signal was greater than the noise in each bin. Fits for images with multiple sources are terminated at the intensity minimum between the sources. The slopes (m) from these fits are tabulated in Table 2.15. The average slopes are $\langle m \rangle = 1.52 \pm 0.45$ at 850 μm and $\langle m \rangle = 1.44 \pm 0.25$ at 450 μm for Class 0/I sources. Since the values of $\langle m \rangle$ determined at different wavelengths agree well, we average all values to obtain $\langle m \rangle = 1.48 \pm 0.35$. The average slope for Class I sources does not differ significantly from that for Class 0 sources, but a larger sample of Class I sources is needed. We are unable to distinguish statistically significant differences in the average slope between sources with ($\langle m \rangle = 1.60 \pm 0.38$) and without ($\langle m \rangle = 1.29 \pm 0.15$) evidence for collapse.

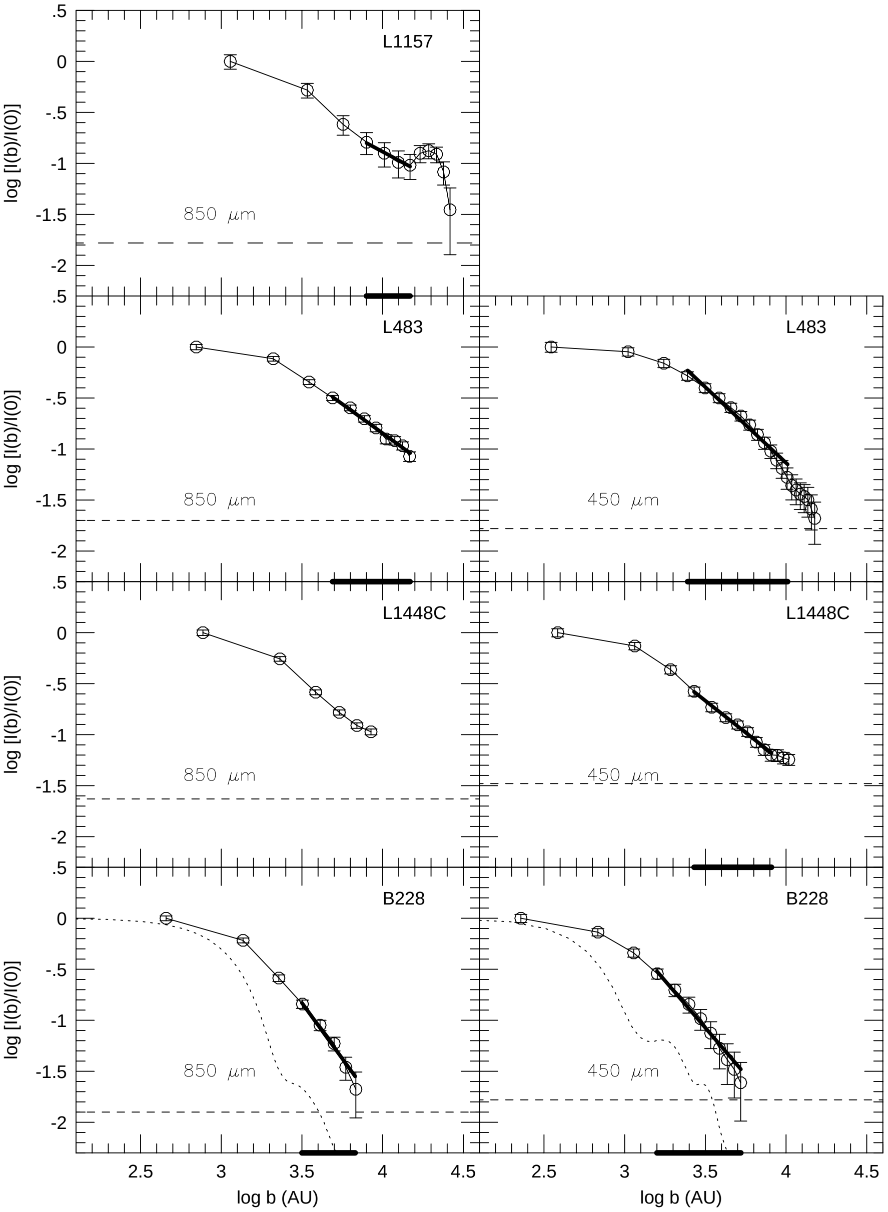

Figure 2.10 Radial profiles of Class 0 sources. The normalized intensity is plotted as a function of impact parameter, b(AU). Power law fits are shown as bold lines. The range of the fits are indicated by the bold lines on the x axis. The horizontal dashed lines represent the 1σ noise level at the edge of the map. The beam profiles are shown as dashed lines in the bottom panel.

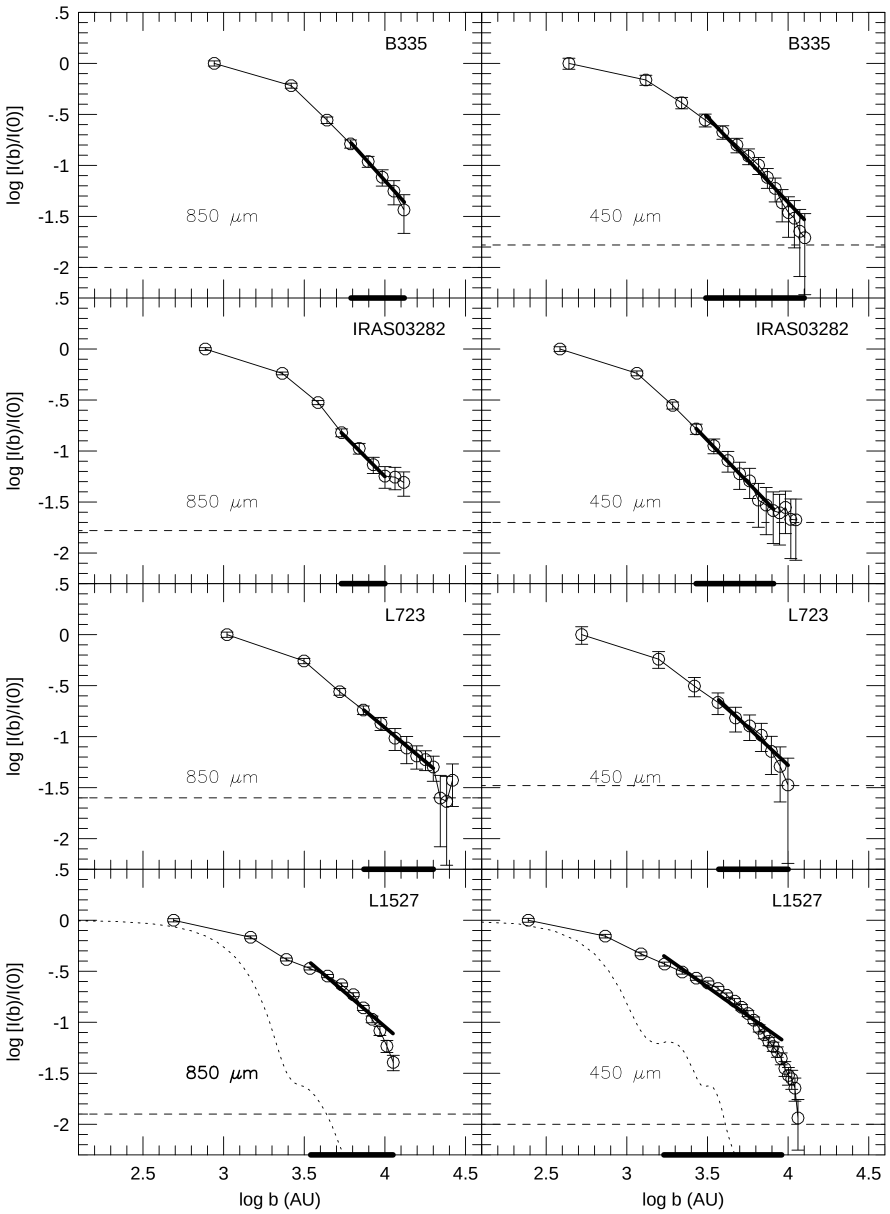

Figure 2.11 Radial profiles of Class 0 sources. The normalized intensity is plotted as a function of impact parameter, b(AU). Power law fits are shown as bold lines. The range of the fits are indicated by the bold lines on the x axis. The horizontal dashed lines represent the 1σ noise level at the edge of the map. The beam profiles are shown as dashed lines in the bottom panel.

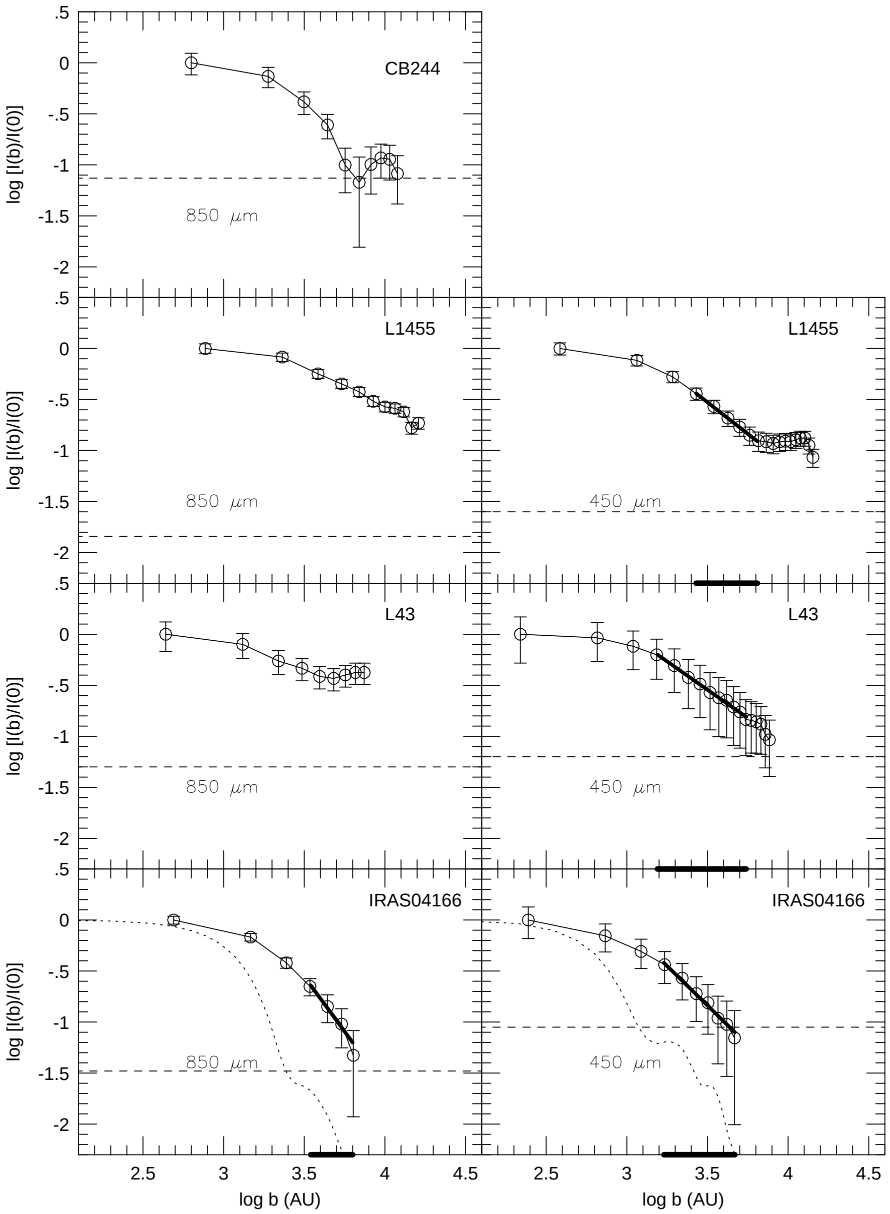

Figure 2.12 Radial profiles of Class 0/I sources. The normalized intensity is plotted as a function of impact parameter, b(AU). Power law fits are shown as bold lines. The range of the fits are indicated by the bold lines on the x axis. The horizontal dashed lines represent the 1σ noise level at the edge of the map. The beam profiles are shown as dashed lines in the bottom panel.

2.4 Analysis

2.4.1 Density Distributions: A Simple Analysis

Combining the value of the slopes in the radial intensity profiles with a knowledge of the temperature distribution of dust grains, $T_d(r)$, constrains the density distribution of dust grains, $\rho(r)$. If the emission is optically thin and the opacity (κ_ν) of the dust grains does not vary with radius, the observed intensity at an impact parameter, b, is given by

$$I_\nu(b) = 2\int_b^{r_o} B_\nu(T_d(r))\kappa_\nu\rho(r)\frac{r}{\sqrt{r^2-b^2}}dr \tag{2.5}$$

(Adams 1991), where r_o is the outer radius. If we assume power law distributions for the density and temperature,

$$\rho(r) = \rho(r_f)\left(\frac{r}{r_f}\right)^{-p} \tag{2.6}$$

$$T_d(r) = T_d(r_f)\left(\frac{r}{r_f}\right)^{-q} \tag{2.7}$$

) where r_f is a fiducial radius, then, if the emission is in the Rayleigh-Jeans limit and if $r_0 \gg b$, equation (5) simplifies to

$$I_\nu(b)/I_\nu(0) = (b/b_0)^{-m} \quad , \; m = p+q-1. \tag{2.8}$$

The dust opacity for grains in the submillimeter portion of the spectrum roughly follows a power law $Q_\nu \propto \nu^\beta$ (see Ossenkopf & Henning 1994). Using this assumption the temperature distribution around a centrally heated source follows a power law of the form

$$T_d(r) \propto L^{q/2}r^{-q} \quad , \; q = 2/(4+\beta) \tag{2.9}$$

(cf. Doty & Leung 1994). Estimates of β typically vary between 0 to 2 in the submillimeter. For $\beta = 1$, consistent with our data (§2.3.2), $T_d(r) \propto r^{-0.4}$. In

TABLE 2.15
RADIAL PROFILE POWER LAW FITS

Source	Class	T_{bol} (K)	λ (μm)	m	Range (AU)[b]	Num[a]	S/N
L1448C	0	54(7)	450	1.27 (0.11)	2700 - 8100	8	30
L1455	0	67(3)	450	1.22 (0.23)	2700 - 6550	6	40
IRAS03282+3035	0	23(5)	850	1.57 (0.31)	5400 - 10000	4	60
			450	1.66 (0.25)	2700 - 8100	8	50
L1527	0	36(5)	850	1.32 (0.05)	3450 - 11250	9	50
			450	1.13 (0.03)	1700 - 9050	16	80
B228	0	48(2)	850	2.17 (0.29)	3200 - 6800	5	80
			450	1.86 (0.21)	1600 - 5250	9	60
L483	0	52(8)	850	1.16 (0.08)	4900 - 14700	8	50
			450	1.49 (0.09)	4550 - 10150	12	60
L723	0	47(3)	850	1.30 (0.19)	7350 - 19950	7	40
			450	1.47 (0.42)	3700 - 10000	7	30
B335	0	28(1)	850	1.74 (0.30)	6100 - 13100	5	100
			450	1.65 (0.17)	3050 - 12700	12	60
L1157	0	42(4)	850	0.87 (0.56)	8000 - 14800	4	60
IRAS04166+2706	I	91(12)	850	2.07 (0.78)	3450 - 6400	4	30
			450	1.57 (0.58)	1700 - 4650	7	10
L43	I	370(20)	450	1.10 (0.39)	1550 - 5450	10	15

[a]Number of points used in fit

[b]Range (AU) over which fit was made

this case, $p = m - q + 1 = m + 0.6$, and the $\langle m \rangle$ found above translates into $\langle p \rangle = 2.08 \pm 0.35$ for Class 0/I sources. For $\beta = 2$ the slope of the density power law changes slightly to $p = m + 0.67$. These values are consistent with those found by Chandler & Richer (2000), with the exception of L1527 (see also Hogerheijde & Sandell 2000). Within the uncertainties, these values are consistent with the density distribution expected from an isothermal sphere or the outer parts of a Bonnor-Ebert sphere (Shu 1977). However, there are quite a few caveats.

2.4.2 Some Caveats

For sources without confusing secondary sources, the data often fall below the fit at large radii. This behavior could be attributed to an outer radius where the profile becomes steeper (e.g., Abergel et al. 1998). We are wary of this conclusion for several reasons. Some of the turn-down near the edge may be caused by using a finite chop. Since our sources have very extended envelopes, we may have chopped onto low level emission, decreasing the observed emission. While we tried to avoid this effect by only carrying the radial profiles out to $98''$, it still may be a problem.

To investigate the importance of various effects on the radial profiles, we constructed 5 spherically symmetric models (Fig. 13). All 5 models calculate the observed intensity, generalizing Equation 2.5 to allow finite optical depth, and convolve the result with a beam profile; they use a code generously supplied by L. Mundy. We assumed power laws for $T_d(r)$ and $\rho(r)$ ($q = 0.4$ and $p = 2$) and use OH5 opacities for coagulated dust grains with icy mantles (Ossenkopf & Henning 1994). The source was placed at a distance of 200 pc with a total mass of 1.1 $M_\odot$, equal to the mean distance (200 ± 60 pc) and mean mass of the sample. An inner radius for the dust shell of 60 AU and an outer radius of 30000 AU (corresponding to $0\farcs24$ and $120''$) were used. Model 1 assumes gaussian beams with the FWHMs of $15\farcs2$ and $7\farcs9$ at 850μm and 450μm respectively. Models 2 – 5 have been convolved with our observed beam profiles. The sidelobes clearly increase the normalized intensity throughout the profile and spread the effects of a finite outer radius back to smaller impact parameters. If very small and very large impact parameters are excluded from the fit, the effect on the fitted slope is small ($\Delta m < 0.2$).

Another important issue is Rayleigh-Jeans failure in Equation 1.5, which occurs when the dust temperature falls below $h\nu/k$ ($h\nu/k = 32$ K and 17 K at 450 and 850 μm, respectively). This is a problem for the emission at large distances from the low luminosity, highly embedded sources that we are observing because

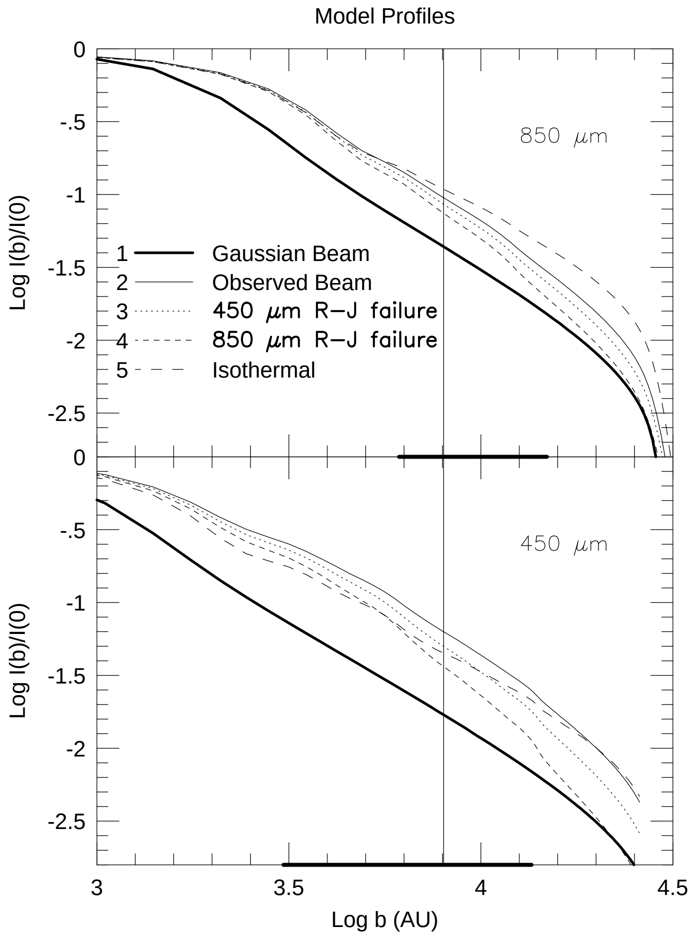

Figure 2.13 Five models of normalized intensity profiles are shown. Power laws in the density ($p = 2$) and temperature ($q = 0.4$) were assumed, and the resulting intensity was convolved with a beam profile. Model 1 (bold line) assumes a gaussian beam of FWHM 14″ and 7″ respectively. The other models use the observed beam profiles shown in Fig. 1. Model 1 and 2 assumed no R-J failure ($T_d(r) \geq 64K, 60\text{AU} \leq r \leq 30000$ AU) throughout the envelope. Model 3 allows R-J failure to occur at 450 μm at 8000 AU ($T(8000\text{AU}) = 32$K). Model 4 allows R-J failure at 850 μm at 8000 AU ($T(8000\text{AU}) = 17K$). Model 5 is isothermal ($T_d(r) = 10$ K) in the outer envelope (3000 AU $\leq r \leq$ 30000 AU). The vertical line corresponds to $b = 8000$ AU. The bold line on the x-axis represents the range over which a fit would be made.

the dust temperature does drop below $h\nu/k$. Model 2 in Fig. 13 shows the observed intensity profile for a source in which $T_d(r) > 2h\nu/k$ over the entire profile. Models 3 and 4 use the same $q = 0.4$ but were normalized to lower temperatures, such that $T_d(r)$ dropped below $h\nu/k$ at 450 μm (model 3) and 850 μm (model 4) at 8000 AU. Rayleigh-Jeans failure results in an increase in m by as much as 0.5, leading to an overestimate of p by the same amount.

The temperature is only approximated by a power-law (eq. 7). The actual $T_d(r)$ is probably steeper in the inner regions, where the radiative transfer of heating radiation is optically thick (e.g., Doty & Leung 1994). More importantly for this analysis, if the core is exposed to the interstellar radiation field, $T_d(r)$ can flatten out or even rise again in the outer regions. Figure 2.13 also shows model 5 in which the temperature distribution is isothermal ($T_d(r) = 10K$) from 3000 AU outward. A flattening of $T_d(r)$ causes a decrease in m by as much as 0.5. The typical interstellar radiation field is capable of heating dust to about 14 K at the extinctions probed by submillimeter emission. This slight rise would be expected to cause a further decrease in m. Consequently, uncertainties of about ± 0.5 are present in deducing the value of p from simple fits assuming power-laws for temperature and the Rayleigh-Jeans approximation. To correct for these effects, careful modeling of each source is needed. These models will be the subject of a later paper.

Although we have assumed spherical symmetry in the previous analysis, the actual geometry of these cores is certainly much more complex. Elongated extensions at low contour levels are seen in many sources. The slope of the intensity profile is not greatly affected by these extensions. The m at 850 and 450 μm was modified by 0.1 when sectors containing the extensions were eliminated from the azimuthal average. This appears to be a small correction compared to other uncertainties in the analysis.

We have also assumed that β is constant throughout the radial profile. Ambipolar diffusion can cause a relative drift between the gas and the dust and between the different dust grain populations. The former may lead to spatial variations in the dust-to-gas ratio, and the latter will also cause β to vary across the cores. Substantial molecular depletions and grain aggregations in the central regions of some cores can also lead to changes in β. Visser et al. (1998) interpreted decreases in spectral index toward column density peaks in NGC 2024 in terms of a decrease in β in dense cores, possibly caused by grain growth. The correction factor to β for Rayleigh-Jeans failure is

$$\gamma(T_d) = 1 + \frac{\log\left[\frac{\exp(h\nu_{850}/kT_d)-1}{\exp(h\nu_{450}/kT_d)-1}\right]}{\log\left(\frac{850}{450}\right)} \tag{2.10}$$

where the spectral index is given by $\alpha = 2 + \beta + \gamma(T_d)$ (Visser et al. 1998). If we assume $T_d = 20K$, then $\gamma(20K) \approx -0.7$. Applying this correction increases the estimate of β from 0.8 found in §2.3.2 to 1.5 for the data in a $40''$ aperture. The Rayleigh-Jeans correction factor varies quickly at low temperatures. For example, $\gamma(T_d)$ changes by 0.5 between 10 and 14 K, plausible changes in $T_d(r)$ from the center to edge of an externally heated pre-protostellar core. Chandler & Richer (2000) saw little evidence for changes in β with radius, but Hogerheijde & Sandell (2000) did observe changes in a few cases.

2.5 Conclusions

The main conclusions of our study are as follows.

Pre-protostellar cores are clearly more diffuse that Class 0/I sources. Pre-protostellar cores do not have central peaks that are as well defined as those in Class 0/I sources. Many sources had companion sources within $2'$ (2/5 pre-protostellar core, 9/16 Class 0/I sources). The presence of several sources in an IRAS beam means that previous studies of SEDs may have been distorted. Observations with higher spatial resolution in the far-infrared are needed. For the sources with companions, the mean projected separation is 10,800 AU, more than the mean separation of 6000 AU in the ρ Ophuichi cluster (Motte et al. 1998), and close to radii previously suggested to be significant for setting the scale for star formation (Larson 1995, Ohashi et al. 1997). The median separation is 18000 AU including lower limits for sources with no detected companions. These results suggests that truly isolated star formation is uncommon.

Some Class 0/I sources show extensions, sometimes along the outflow axis and sometimes perpendicular to it. Both heating and column density effects may play a role in defining the shapes at low contour levels.

The mean spectral index for all sources between 450 and 850 μm is $\langle\alpha_{450/850}\rangle = 2.8 \pm 0.4$. This value would imply an exponent in the opacity law, $\beta \sim 1$, but Rayleigh-Jeans failure could increase this value. Pre-protostellar cores have a slightly lower average spectral index ($\langle\alpha_{450/850}\rangle = 2.5 \pm 0.4$). The average spectral index measured at 850μm and 1.3mm is higher ($\langle\alpha_{850/1.3}\rangle = 3.4 \pm 0.3$).

The mean mass in the sample is $\langle M_d\rangle = 1.1 \pm 0.9\mathrm{M}_\odot$. The masses computed from the dust emission agree reasonably with those computed from the virial theorem, supporting the hypothesis that the cores are gravitationally bound and that the values used for the dust opacity are reasonable.

The radial intensity profiles of pre-protostellar cores cannot be fitted with power laws over a significant range of radii. In contrast, most Class 0/I sources can be fitted with power laws if the inner and outer points are excluded. For some sources, the fit must be truncated before emission from secondary sources affects the profile. The mean slope is $\langle m\rangle = 1.48 \pm 0.35$ for Class 0/I sources. We are unable to distinguish between Class 0 and Class I radial profiles with our limited sample. A simple analysis suggests that a density power law $\rho(r) \propto r^{-p}$, with $p \sim 2.1$ would fit the data.

Models that include more accurate $T_d(r)$, account for Rayleigh-Jeans failure, and include the actual beam shape show that the simple analysis can be misleading. These models still can be fitted by power laws in the normalized intensity, but the fitted slope may vary by ± 0.5 compared to the simple analysis.

Given the likely complexities in real cores, it is somewhat surprising that simple power-law models fit the Class 0/I sources as well as they do. Neither the mean spectral indices nor the slopes in the intensity profiles distinguish between Class 0 and Class I sources nor between candidates and non-candidates for collapse in the present sample. Firmer conclusions await a larger sample of Class I sources and detailed, source-by-source modeling.

Acknowledgments

We are grateful to T. Jenness for assistance with SURF, to L. Mundy for providing the computer code used to generate the models in Figure 2.13, and to the staff of the JCMT for crucial support while observing. We thank Claire Chandler and the referee for comments that improved the paper. The JCMT is operated by the Joint Astronomy Centre on behalf of the Particle Physics and Astronomy Research Council of the United Kingdom, The Netherlands Organization for Scientific Research and the National Research Council of Canada. We thank the State of Texas and NASA (Grant NAG5-7203) for support. NJE thanks the Fulbright Program and PPARC for support while at University College London and NWO and NOVA for support in Leiden.

Chapter 3

Models of the Submillimeter Dust Continuum Emission from Class 0 Protostars

Abstract

Seven Class 0 sources mapped with SCUBA at 850 and 450 μm are modeled using a one dimensional radiative transfer code. The modeling takes into account heating from an internal protostar, heating from the ISRF, realistic beam effects, and chopping to model the normalized intensity profile and spectral energy distribution. Power law density models, $n(r) \propto r^{-p}$, fit all of the sources; best fit values are mostly $p = 1.8 \pm 0.1$, but two sources with aspherical emission contours have lower values ($p \sim 1.1$). Including all sources, $\langle p \rangle = 1.63 \pm 0.33$. Based on studies of the sensitivity of the best-fit p to variations in other input parameters, uncertainties in p for an envelope model are $\Delta p = \pm 0.2$. If an unresolved source (e.g., a disk) contributes 70% of the flux at the peak, p is lowered in this extreme case and $\Delta p =^{+0.2}_{-0.6}$. The models allow a determination of the internal luminosity ($\langle L_{int} \rangle = 4.0$ $L_\odot$) of the central protostar as well as a characteristic dust temperature for mass determination ($\langle T_{iso} \rangle = 13.8 \pm 2.4$ K). We find that heating from the ISRF strongly affects the shape of the dust temperature profile and the normalized intensity profile, but does not contribute strongly to the overall bolometric luminosity of Class 0 sources. There is little evidence

for variation in the dust opacity as a function of distance from the central source. The data are well-fitted by dust opacities for coagulated dust grains with ice mantles (Ossenkopf & Henning 1994). The density profile from an inside-out collapse model (Shu 1977) does not fit the data well, unless the infall radius is set so small as to make the density nearly a power-law.

3.1 Introduction

Modern theories of star formation predict the evolution of the density structure, $n(\vec{r},t)$, and velocity structure, $\vec{v}(\vec{r},t)$, of the gas and dust envelope of protostars. Optically thin dust emission at submillimeter wavelengths provides an observational constraint on the density distribution of the protostellar envelope and therefore constrains theoretical models of star formation.

Class 0 protostars represent an early, highly embedded phase during the formation of low mass stars ($M <$ few $M_\odot$). The original evolutionary sequence for low mass protostars (Class I, II, and III) is based on the shape of the spectral energy distribution (SED) from observations at near and mid-infrared wavelengths (Lada 1987). Low mass protostars are thought to evolve from a thick dusty envelope where most of the energy is re-radiated by dust in the far-infrared (Class I) to progressively less embedded objects with near and mid-infrared excesses from dusty disks (Class II or classical T Tauri stars and Class III or weak-line T Tauri stars). The discovery of extremely embedded objects with submillimeter telescopes led to a new class of protostars, Class 0 objects, which are so highly enshrouded that their near infrared emission has generally not been detected and their SEDs peak longward of 100 μm. Observationally, Class 0 sources are cores that have $L_{bol}/L_{smm} \leq 200$, where L_{smm} is the total luminosity detected longward of 350 μm (André et al. 1993). Alternatively, Class 0 sources are characterized by $T_{bol} \leq 70$K, where T_{bol} is the temperature of a blackbody with the same mean frequency as the observed SED (Chen et al. 1995). Based on the relative numbers of Class 0 and Class I objects, it has been argued that the timescale for Class 0 objects is short, perhaps 10^4 years (André et al. 2000). Class 0 objects have powerful outflows, which suggest high accretion rates (Bontemps et al. 1996). As data improve, some Class I sources are being reclassified to Class 0 sources (e.g., Shirley et al. 2000, Young et al. 2001), suggesting a reexamination of this argument (see also Visser, Richer, & Chandler 2001).

It is important to understand the structure of the envelope of Class 0 objects since they are likely to be the earliest observed phase of star formation with a central accreting protostar (André et al. 2000). The emission from an optically thin dust shell observed at an impact parameter, b, with dust opacity, κ_ν, that does not vary with radius, is given by

$$I_\nu(b) = 2\kappa_\nu \int_b^{r_o} B_\nu(T_d(r))\rho(r)\frac{r}{\sqrt{r^2-b^2}}dr \tag{3.1}$$

(Adams 1991), where r_o is the outer radius. For an optically thin envelope (at all wavelengths) dominated by a central source of luminosity, L_{int}, the dust temperature distribution can be approximated by a power law:

$$T_d(r) \propto \left(\frac{L_{int}}{r^2}\right)^{\frac{1}{4+\beta}} \propto L_{int}^{q/2} r^{-q}, \tag{3.2}$$

where $q = 2/(4+\beta)$ (cf. Doty & Leung 1994) and β is the power law exponent of the dust opacity ($\kappa \propto \nu^\beta$), which typically lies between 1 and 2 in the submillimeter. If we also assume the density distribution follows a power law, $n(r) \propto r^{-p}$, then in the Rayleigh-Jeans limit ($T_d \gg h\nu/k$), the specific intensity integral simplifies to $I_\nu \propto b^{-m}$, where $m = p+q-1$. Previous studies of the density structure of Class 0 objects assumed a temperature power law of the form $T_d(r) \propto r^{-q}$ (Walker et al. 1990, Ladd et al. 1991, Chandler & Richer 2000, Hogerheijde & Sandell 2000, Shirley et al. 2000, and Motte & André 2001). However, this approach is **not** valid in the outer envelopes of low luminosity sources due to a breakdown in the Rayleigh-Jeans approximation at wavelengths shorter than 1 mm and due to external heating from the interstellar radiation field (ISRF) (Shirley et al. 2000). It then becomes necessary to calculate $T_d(r)$ self consistently in the integral in Equation (3.1) to reveal the density distribution of the envelope.

In Paper I (Shirley et al. 2000), 21 low mass cores within 325 pc were observed at 850 μm and 450 μm using the Submillimeter Common User Bolometer Array (SCUBA) (Holland et al. 1999) on the JCMT 15-m radio telescope. Thirteen sources from the original sample were classified as Class 0, three sources having been previously classified as Class I. In this paper, we present 1D dust radiative transfer models for seven of the Class 0 sources selected for spatial isolation and high signal-to-noise radial profiles ($\langle S/N \rangle_{peak} = 60$): B335, B228, L723, IRAS03282+3035, L1448C, L1527, and L483. B335, B228, IRAS03282+3035, and L1448C appear circular in the dust continuum maps down to the 20% contour, while L1527, L483, and L723 are clearly aspherical at that level. The bolometric temperature ranges from 23K (IRAS03282+3035) to 52K (L483) and the bolometric luminosity ranges from 1.2 $L_\odot$ (IRAS03282+3035 and B228) to 13 $L_\odot$ (L483). In Paper II (Evans et al. 2001), three pre-protostellar cores (L1512, L1544, and L1689B) were modeled using one-dimensional radiative transfer and a beam convolution code. In this paper, the seven Class 0 sources will be modeled using the same procedure used in Paper II, with the addition of an internal luminosity source. The modeling procedure and inputs are discussed in Section 2. We use B335 as a test object (Section 3.1) to model the sensitivity to the model input parameters. Individual sources are modeled in Sections 3 and 4, while the implications of our best fit models are discussed in Section 5.

3.2 1D Dust Radiative Transfer Modeling

The 1D dust models are calculated from a modified version of the Egan, Leung, and Spagna (1984) continuum radiative transfer code. This code iteratively calculates the equilibrium dust temperature on a 1D radial grid by simultaneously solving the combined moment radiative transport equations in quasi-diffusion form and the energy balance equations as a two-point boundary value problem. The radiation field is constructed by solving a set of ray equations along impact parameters, b, through the cloud. There are four physical inputs to the radiative transfer code: the density distribution, $n(r)$; the internal source luminosity, L_{int}; the scaling factor for the interstellar radiation field, s_{ISRF}; and the dust opacity, κ_ν. In addition, the radial grid (100 points) and impact parameters, as well as the wavelength grid (59 wavelengths) are chosen to cover the relevant range so that results are insensitive to the details of these grids. The equilibrium dust temperature distribution, $T_d(r)$, which is the output from the dust code, is used by an observation simulation code (Paper II) to calculate the normalized radial intensity profiles, $I_\nu^{norm}(b)$, by solving Equation (3.1), performing beam convolutions, and simulating chopping. The code also models the observed SED, $S_\nu(\theta_{mb})$, by convolving the model intensity with the beam (θ_{mb}) used in each observation.

The internal radiation field is assumed to be a blackbody with an effective temperature of 6000 K. Since all of the objects we are modeling are very opaque at near-infrared wavelengths, the exact shape of the spectrum of the internal radiation field is not important; only the total internal luminosity is important. The shape of the ISRF was determined from COBE results (Black 1994) plus the cosmic microwave background (CMB) and the ultraviolet component of the ISRF ($\lambda \leq 0.36\mu$m) from van Dishoeck (1988). This ISRF is considerably stronger in the infrared than the previous versions of the ISRF (Mathis, Mezger, & Panagia 1983) (see Figure 2 of Paper II for a plot of the different ISRFs). We modify the strength of the ISRF by multiplying all portions of the ISRF spectrum except the CMB with a factor denoted by s_{ISRF}. For the models discussed in this paper, we used a coarse grid with s_{ISRF} = 0.3, 1.0, and 3.0. These factors for the far-UV

(FUV) portion of the ISRF correspond to $0.45G_0$, $1.5G_0$, and $4.5G_0$ respectively, where G_0 is integrated FUV flux between 91.2 nm and 220 nm in units of 1.6×10^6 erg s^{-1} cm^{-2} (cf. Hollenbach et al. 1991). In Paper II, the best fit to the observed radial profiles and SED suggest a lower strength to the ISRF ($s_{ISRF} \sim 0.3 - 0.5$).

The dust opacity, κ_ν, was taken from the models of Ossenkopf and Henning (1994) for grains that have coagulated for 10^5 yr at a density of 10^6 cm^{-3}, both with (OH5) and without (OH2) accreted ice mantles. We assume a gas to dust ratio of 100 by mass to convert OH5 opacities (per gram of dust) to opacity per gram of gas. OH5 opacities have been successful at reproducing the SED of both high mass (van der Tak et al. 2000) and low mass star forming cores (Paper II). OH5 opacities at submillimeter wavelengths can be approximated by a power law ($\kappa_\nu \propto \nu^\beta$) with $\beta \sim 1.85$ and an opacity of 1.8×10^{-2} cm^2 per gram of gas at 850 μm. The OH2 dust opacities are lower at far-infrared wavelengths but up to 1.6 times higher at submillimeter and millimeter wavelengths than OH5 dust opacities. The cross-over point is near 350 μm (see Fig. 2 of Paper II).

The JCMT beams derived from AFGL618 and Uranus were used for the beam convolution of the model profiles at 850 and 450 μm (see Figure 3.1). It is very important to convolve the model specific intensity distribution with a realistic beam profile to derive an accurate estimate of the envelope density distribution. Using a gaussian beam shape instead of the actual beam profile can profoundly distort the interpretation of the power law index, p, by up to 0.5 (Shirley et al. 2000). Since the beam shape was stable during the second half of the night in April 1998 (see Paper I), nine Uranus profiles were added together to use an average beam profile with high signal-to-noise out to $70''$ from the center of the map. No planets were available to make beam maps for the January 1998 sources (L1527, IRAS03282, L1448C); so the secondary calibrator, AFGL618 was observed. The January 1998 observations were taken in the first half of the night when the beam shape is not so stable and changes shape continuously as the telescope cools. AFGL618 is much weaker than Uranus at 850 and 450 μm; therefore the beam maps have much lower signal-to-noise at large radii. The January beam map was produced by averaging together three AFGL618 maps observed during the same time of night that our objects were observed. Because the 450 μm profile of AFGL618 becomes too noisy beyond 34″, the average Uranus beam profile from April was used for the 450 μm January beam beyond 34″. These beam calibration difficulties introduce larger uncertainties, $\Delta p \sim 0.1$, in the best fit models for the January sources.

Many of the radial profiles from Paper I show a turn-down in the intensity profile beyond 60″ from the center of the map. This turn-down could be due to a steepening of the density profile or due to the effects of chopping. To test the possibility of a steeper density profile, we must account for the chop throw. The SCUBA observations were chopped in azimuth with a 120″ chop throw. Since the SCUBA array is 2D, all of the positions within a single annulus chop different distances from the center of the map. Therefore, our 1D model can only include an approximate simulation of the true effects of chopping. The details of how we simulate chopping has a noticeable effect on the shape of the model intensity profiles beyond 60″; consequently, we do not attempt to model normalized intensity profiles beyond this radius.

The agreement between the model and the data can be quantified in terms of the reduced chi-squared for the normalized intensity profile at wavelength λ:

$$\chi^2_\lambda \; = \; \sum_i \left[\frac{(I_\nu^{norm}(b_i))_{obs} - (I_\nu^{norm}(b_i))_{mod}}{\sigma_I(b_i)} \right]^2 \; / \; N_b \; , \qquad (3.3)$$

where $I_\nu^{norm}(b_i)$ is the azimuthally averaged, normalized intensity in a circular aperture at impact parameter b_i, $\sigma_I(b_i)$ is the uncertainty in the data, and N_b is the number of impact parameters. Only points spaced by a full beam are used in computing χ^2_λ to avoid introducing correlations. We calculate χ^2_λ for the 850 and 450 μm profiles and define χ^2_r as the sum of χ^2_{850} and χ^2_{450}. The signal-to-noise was higher

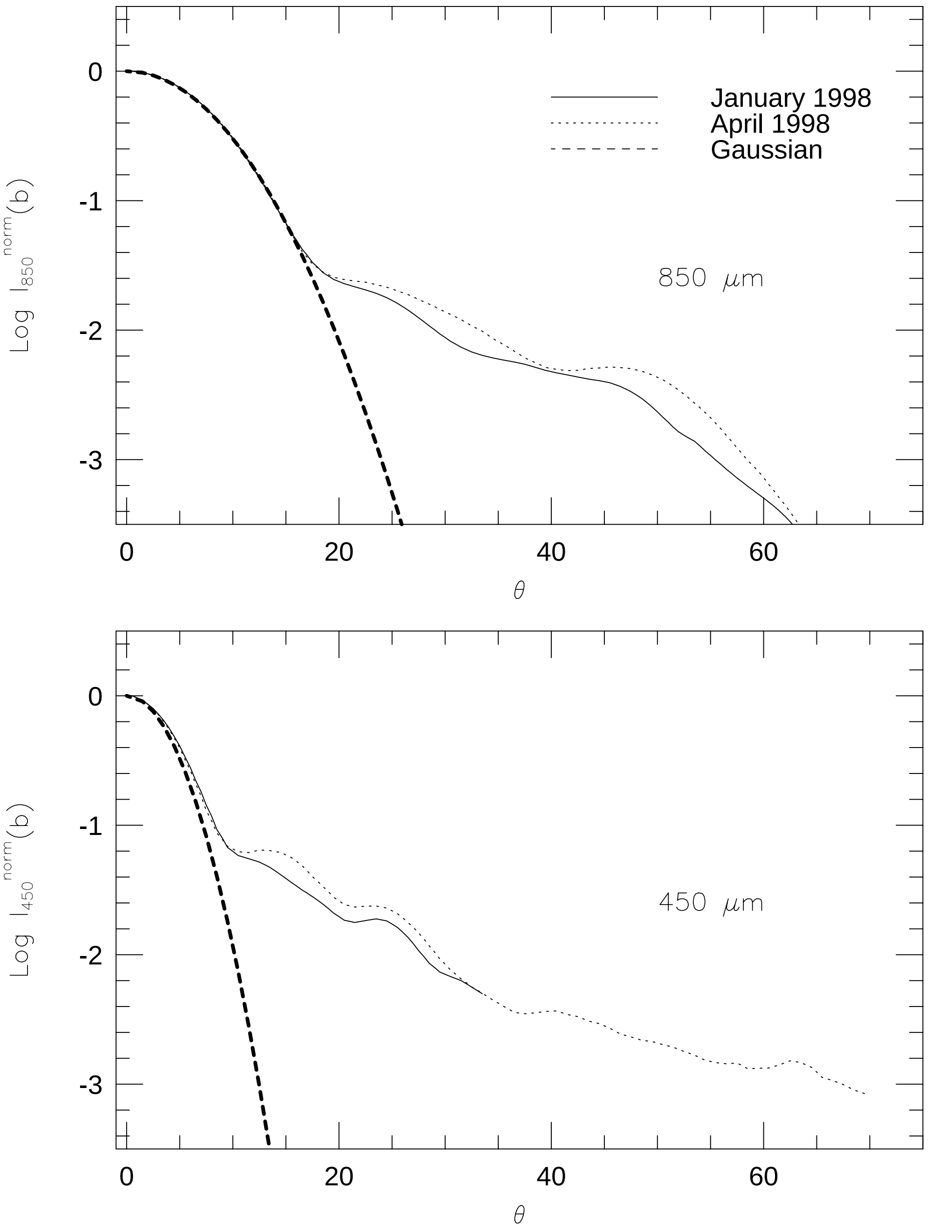

Figure 3.1 Beam profiles used for modeling Class 0 sources. The beam profile from January 1998, April 1998, and gaussian beams with the FWHMs reported in Paper I are shown. Since CRL618 is a weak calibrator, the January 1998 beam was extrapolated beyond 34$''$ using the April 1998 beam.

for the 850 μm maps and therefore the χ^2_{850} has the most weight in determining the best fit.

The agreement between the model SED and the observed one is quantified by χ^2_{SED}, calculated from a similar equation:

$$\chi^2_{SED} = \sum_i \left[\frac{S^{obs}_{\nu_i} - S^{mod}_{\nu_i}}{\sigma_S(\nu_i)} \right]^2 / N_\nu , \tag{3.4}$$

where $S^{obs}_{\nu_i}$ is the observed flux into a beam and $S^{mod}_{\nu_i}$ is the modeled flux into the same beam. When photometry at the same wavelength with different beams exists, the points are both considered in calculating χ^2_{SED}. Wavelengths shorter than 60 μm are not included because they are expected to be optically thick and therefore very sensitive to asymmetric geometries (e.g., outflow cavities, flattened envelopes), which we are currently unable to model. In addition, much of the far-infrared photometry has large and uncertain calibration errorbars, and the opacities as a function of frequency are uncertain. For all these reasons, poor fits to the SED are not considered a serious problem in constraining the density distribution; however we often find that the best χ^2_r, which considers only the profiles, occurs for the model with the best $\chi^2_{tot} = \chi^2_r + \chi^2_{SED}$.

In fact, the SED and the normalized radial intensity profiles provide nearly orthogonal constraints on model parameters (§3.3). The SED is sensitive to the strength of the ISRF and a mass$\times$opacity product (Paper II). In particular, the flux density at 850 μm constrains the mass, while the full SED provides information on the the variation of dust opacity with frequency, subject to the caveats mentioned above. Measurements of the flux density into different beams at the same wavelength provides some constraint on the density distribution, but the *shape* of the density distribution is much better constrained by the normalized radial profile ($I^{norm}_\nu(b)$).

The simplest models to test are single power laws,

$$n(r) = n_f \left(\frac{r}{r_f}\right)^{-p} \quad ; \quad r \in [r_i, r_o] \tag{3.5}$$

in cm^{-3} for the gas density. The density, n_f, is normalized to a fiducial radius, r_f, of 1000 AU and represents the total gas number density ($n = n(\mathrm{H}_2) + \mathrm{n(He)} + ... = \rho/(\mu \mathrm{m_H})$, $\mu = 2.29$). There are seven parameters in the power law models: the power law exponent, p; the density at a fiducial radius, n_f; the inner radius, r_i; the outer radius, r_o; the internal source luminosity, L_{int}; the dust opacity, κ_ν and the strength of the interstellar radiation field, s_{ISRF}. In these models, the shape of the density profile, defined by p is constrained by $I_\nu^{norm}(b)$, and only slightly affected by other parameters. In contrast, n_f and hence the mass, are constrained by the observed flux density at optically thin wavelengths; we use $S_\nu(850)$ because the calibration errors are lowest. The resulting mass depends inversely on the opacity at 850 μm ($\kappa_\nu(850)$) and weakly on other parameters.

We also test models of inside out collapse (Shu 1977), hereafter referred to as Shu77 models. These are characterized by seven parameters: a_{eff}, the effective sound speed; the radius that encloses the infalling gas, r_{inf}; r_i; r_o; L_{int}; κ_ν; and s_{ISRF}. Inside r_{inf}, the density distribution tends toward $n(r) \propto r^{-1.5}$, while $n(r) \propto r^{-2}$ outside r_{inf}. The shape of the density profile is thus set by r_{inf}, while the normalization is set by a_{eff}. We fix a_{eff} based on observations of optically thin spectral lines; thus Shu77 models have no freedom in the normalization of the density profile, unlike power law models.

The constraints on the other parameters are similar for the two types of density profiles. The internal source luminosity (L_{int}) is constrained by the integral of the SED and secondarily by s_{ISRF}. The internal luminosity dominates the bolometric luminosity over heating from the ISRF for sources with $L_{int} \geq 1 \mathrm{L}_\odot$. The model internal luminosity is tuned until the model bolometric luminosity (L_{bol}^{mod}) matches the observed bolometric luminosity (L_{obs}, Paper I), using the same method to integrate over the SED. The model bolometric luminosity is calculated using the same wavelengths and beams as the observed bolometric luminosity. L_{obs} and L_{bol}^{mod} may be greater than L_{int} for low luminosity sources because the ISRF adds energy. In some cases, especially for more luminous sources L_{obs} underestimates L_{int} because the beams used at some wavelengths do not capture all the emission (see Butner et al. 1990 for a full discussion). The choice of the overall opacity law ($\kappa_\nu(\nu)$) is constrained by the *shape* of the SED once other parameters, like p, L_{int}, and s_{ISRF} are constrained.

Models of B335 are used to test our assumptions of nearly orthogonal constraints and the effects of changing various parameters in the model (§3.3).

3.3 Testing Model Parameters – B335

B335 (IRAS 19345+0727, L663) is an extensively studied Class 0 object within the Barnard 335 dark cloud. Its submillimeter emission is very nearly circularly symmetric (Huard et al. 1999, Paper I, Motte et al. 2001). The core is the one of the best cases for a collapse candidate as deduced from models of observed asymmetric line profiles in CS and H_2CO (Zhou et al. 1993, Choi et al. 1995). Rotation, if any, is very slow (Frerking et al. 1987, Zhou, 1995), making simple spherical models reasonable. B335 has an outflow that lies nearly in the plane of the sky along an east-west direction (Goldsmith et al. 1984). There is little direct evidence in the submillimeter continuum maps of extensions or flattening along or perpendicular to the outflow direction, making this core a suitable choice for 1D modeling. Harvey et al. (2001) have recently studied B335 using a near-infrared extinction mapping technique to probe the density structure (cf. Alves, Lada, & Lada 2001). These observations provide an important check on the consistency of our submillimeter continuum models. We shall model the density structure of the outer envelope of B335 using both a single power law and the inside-out collapse model of Shu (1977).

Table 3.1

Power Law Models

Source	Model Number	p (cm^{-3})	n_f (AU)	r_i (AU)	r_o	κ_ν	L_{int} ($L_\odot$)	s_{ISRF}
B335								
	1	2.0	1.7×10^6	60	60,000	OH5	2.5	1.0
	2	2.0	1.7×10^6	30	60,000	OH5	2.5	1.0
	3	2.0	1.7×10^6	120	60,000	OH5	2.5	1.0
	4	2.0	1.2×10^6	240	60,000	OH5	2.7	1.0
	5	2.0	1.2×10^6	60	120,000	OH5	2.5	1.0
	6	2.0	2.0×10^6	60	30,000	OH5	2.5	1.0
	7	2.0	3.0×10^6	60	15,000	OH5	2.5	1.0
	8	1.8	2.5×10^6	60	15,000	OH5	2.5	1.0
	9	1.5	5.0×10^5	60	60,000	OH5	2.8	1.0
	10	2.5	2.8×10^6	60	60,000	OH5	2.5	1.0
	11	2.0	1.2×10^6	60	60,000	OH5	1.5	3.0
	12	2.2	1.7×10^6	60	60,000	OH5	1.5	3.0
	13	2.0	2.3×10^6	60	60,000	OH5	3.0	0.3
	14	1.8	1.5×10^6	60	60,000	OH5	3.3	0.3
	15	2.0	6.0×10^5	60	60,000	OH2	4.4	1.0
B228								
	16	2.1	1.2×10^6	60	30,000	OH5	1.0	1.0
	17	1.9	1.2×10^6	60	30,000	OH5	1.0	0.3
L723								
	18	2.0	2.0×10^6	60	60,000	OH5	2.0	1.0
	19	1.8	1.8×10^6	60	60,000	OH5	2.6	0.3
	20	1.8	2.4×10^6	60	30,000	OH5	2.6	0.3
IRAS03282[a]								
	21	2.1	1.9×10^6	60	45,000	OH5	1.0	1.0
	22	1.9	1.9×10^6	60	45,000	OH5	1.0	0.3
L1448C								
	23	1.7	2.6×10^6	60	45,000	OH5	5.9	1.0
	24	1.6	2.8×10^6	60	45,000	OH5	5.9	0.3
L1527								
	25	1.5	1.15×10^5	60	30,000	OH5	1.8	1.0
	26	1.0	3.5×10^5	60	30,000	OH5	2.1	1.0
	27	1.1	6.5×10^5	60	30,000	OH5	2.2	0.3
L483								
	28	1.3	6.0×10^5	60	45,000	OH5	13.0	1.0
	29	1.2	6.0×10^5	60	45,000	OH5	13.0	0.3

[a]IRAS03282+3035.

Table 3.2

Power Law Models χ^2

Source	Model Number	χ^2_{850}	χ^2_{450}	χ^2_{SED} [a]	Notes
B335					
	1	5.9	3.9	2.2	Test Model
	2	6.8	5.0	2.1	
	3	5.4	3.4	2.7	
	4	4.4	2.1	5.9	
	5	5.0	3.5	5.7	
	6	6.5	3.8	5.8	
	7	16.9	10.8	7.3	
	8	5.4	3.9	5.8	
	9	79.4	34.5	22.6	
	10	47.1	19.7	8.5	
	11	14.7	9.5	1.7	
	12	5.6	3.4	5.6	
	13	12.2	8.9	4.2	
	14	3.8	2.9	19.6	Best χ^2_r
	15	6.2	3.8	101	
B228					
	16	11.4	8.6	30.7	
	17	8.8	6.4	4.8	Best χ^2_{tot}
L723					
	18	1.1	1.3	9.6	
	19	0.8	0.5	3.4	Best χ^2_{tot}
	20	0.8	0.6	3.7	
IRAS03282[b]					
	21	13.5	3.5	4.6	
	22	10.2	1.2	5.2	Best χ^2_r
L1448C					
	23	4.7	10.4	2.0	Best χ^2_{tot}
	24	8.3	9.4	9.3	
L1527					
	25	76.7	39.6	13.7	
	26	52.3	60.3	25.6	
	27	9.2	5.4	28.3	Best χ^2_r
L483					
	28	8.9	5.1	1.2	
	29	6.1	5.2	1.0	Best χ^2_{tot}

[a] χ^2_{SED} calculated using all flux points listed in Tables 5, 6, and 7 of Shirley et al. 2000 with $\lambda \geq 60\mu$m.

[b] IRAS03282+3035.

3.3.1 Power Law Models

A $p = 2$ power law is a good starting model because it has the same density distribution as a singular isothermal sphere, until it is truncated at an inner radius. The outer radius was chosen to allow proper simulation of chopping at the distance of B335 (250 pc; Tomita et al. 1979). The chop throw for our observations was $120''$, corresponding to 30,000 AU at the distance of B335. Both the radial profile and the observed beam profile contain useful information $60''$ from the center of the map; therefore, to allow the beam to chop onto the model density distribution for radial points $60''$ from the center, the modelled density distribution must extend to twice the chop throw ($240''$) or 60,000 AU at the distance of B335. NICMOS observations of B335 indicate that reddening of background stars blend into the background noise beyond $125''$ (Harvey et al. 2001), which is within the range of the outer radii tested in our models. We initially chose the inner radius such that $r_o/r_i = 1000$ so that $r_i = 60$AU for B335. For the initial test model, we used OH5 opacities. The fiducial density, n_f, was varied to match the observed flux at 850 microns; $S_{850}^{obs} = 3.91 \pm 0.22$, and the internal luminosity, L_{int}, was varied until the model L_{bol} matched $L_{obs} = 3.1 \pm 0.1 \mathrm{L}_\odot$ (Paper I). The resulting best fit was $n_f = 1.7 \times 10^6 \mathrm{cm}^{-3}$ and $L_{int} = 2.5 \mathrm{L}_\odot$ (see Table 3.1 & 3.2). This basic model was used to test the effects of varying r_o, r_i, κ_ν, p, s_{ISRF}, and distance. The sensitivity of p and L_{int} to changes in the other parameters is summarized in Table 3.3.

Changes in r_o result in changes in the total envelope mass proportional to r_o^{3-p} for a power law; however, the column density along a line of sight, and hence the emission at long wavelengths into a fixed beam becomes insensitive to r_o for $p > 1$ ($N \propto r_i^{1-p}(1-(r_i/r_o)^{p-1})$. For the test model, the density is 4.7×10^2 cm^{-3} at 60,000 AU. This low value is probably not realistic as the dense core is embedded in an extended cloud (Frerking et al. 1987). Even if a constant density of 10^3 cm^{-3} is used for the lower limit to the density in the envelope, doubling the outer

TABLE 3.3
SENSITIVITY OF MODEL PARAMETERS[a]

Variable	Range[b]	Δp	ΔL_{int} ($L_\odot$)
r_i	30 – 240 AU	< 0.1	0
r_o	30,000 – 120,000 AU	< 0.1	0.2
n_f	$5 \times 10^5 - 3 \times 10^6$ cm^{-3}	< 0.1	0.2
L_{int}	1.5 – 3.0 $L_\odot$	< 0.1	...
κ_ν	OH5 vs. OH2	< 0.1	1.9
s_{ISRF}	0.3 – 3.0	± 0.2	1.5
$P_n(\theta)$[c]	Jan. vs. Apr.	± 0.1	0
p	1.5 – 2.5	...	0.3

[a]Tested on B335.

[b]The range of the variable tested.

[c]The beam shape.

radius to 120,000 AU only increases A_V by slightly less than 1 magnitude of visual extinction. This lower limit is used for all subsequent models. Allowing the density to fall below 10^3 cm^{-3} results in no significant change in the best fit fiducial density or internal luminosity. Factor of two changes in r_o have negligible effect on the best fit parameters. If r_o is made small enough ($r_o \leq 15000$ AU), the fit degrades (Table 3.2), but this r_o is smaller than the extent of observed emission in the SCUBA map.

While the column density increases as r_i decreases, beam dilution is more important. The SCUBA beams are much larger than the inner radii in our models (the 450 μm beamwidth of $8''$ corresponds to a radius of 520 AU for our nearest source, B228); therefore changes in the inner radius will not have substantial effects unless the inner radius gets too large. Factor of two changes in r_i have negligible effects; a factor of 4 increase in r_i begins to degrade the fit to the 60 μm point on the SED (Figure 3.2). However, 60 μm observations can be affected by deviations from spherical geometry, so the 60 μm flux should not be considered a strong constraint on one dimensional models. We do not model the effects of a disk (see Section 5.5).

The result of these tests is that the best-fit model parameters are not sensitive to changes of factors of 2 in r_o or r_i. Larger changes worsen the fit, indicating that there is no evidence in our data for either inner or outer boundaries in the power laws.

Calculations of dust opacities differ substantially between dust models, especially at long wavelengths; for example OH5 and OH2 dust models have opacities at $\lambda = 1000$ μm that are 6 and 12 times those of the model for dust in the diffuse interstellar medium (Draine & Lee 1984). With no further information, these differences would result in substantial uncertainties in n_f, or equivalently the mass since $S_\nu \propto M\kappa_\nu$. However, the SED is strongly affected by the choice of opacity law and can be used to distinguish dust models (e.g., Butner et al. 1991, van der Tak et al. 2000) if the density distribution is independently constrained. If OH2 opacities are used instead of OH5 opacities, the best fit power law remains $p = 2.0$ with n_f about one-third that of the test model. The higher $\kappa_\nu(850)$ of OH2 dust requires less column density to match the flux at 850 μm. None of the power law fits using OH2 dust produce enough emission to match the SED at 100 μm $\geq \lambda \geq$ 350 μm (Figure 3.2), yielding quite large values of χ^2_{SED}. Changing the submillimeter opacity by a factor of a few does not strongly affect the *shape* of the model density profiles, confirming our conclusions about the orthogonality of the radial profile and the SED. A dust opacity that varies with radius could in principle affect the fit to the shape of the density profile; however, we see no evidence for variation of opacity with radius (see §3.5.3).

Other models of star formation predict density distributions different from the singular isothermal sphere (e.g. McLaughlin & Pudritz 1997, Ciolek & Basu 2000). Without explaining the details of these models we note that the differences often can be approximated by variations in the power law index (p) in the bulk of

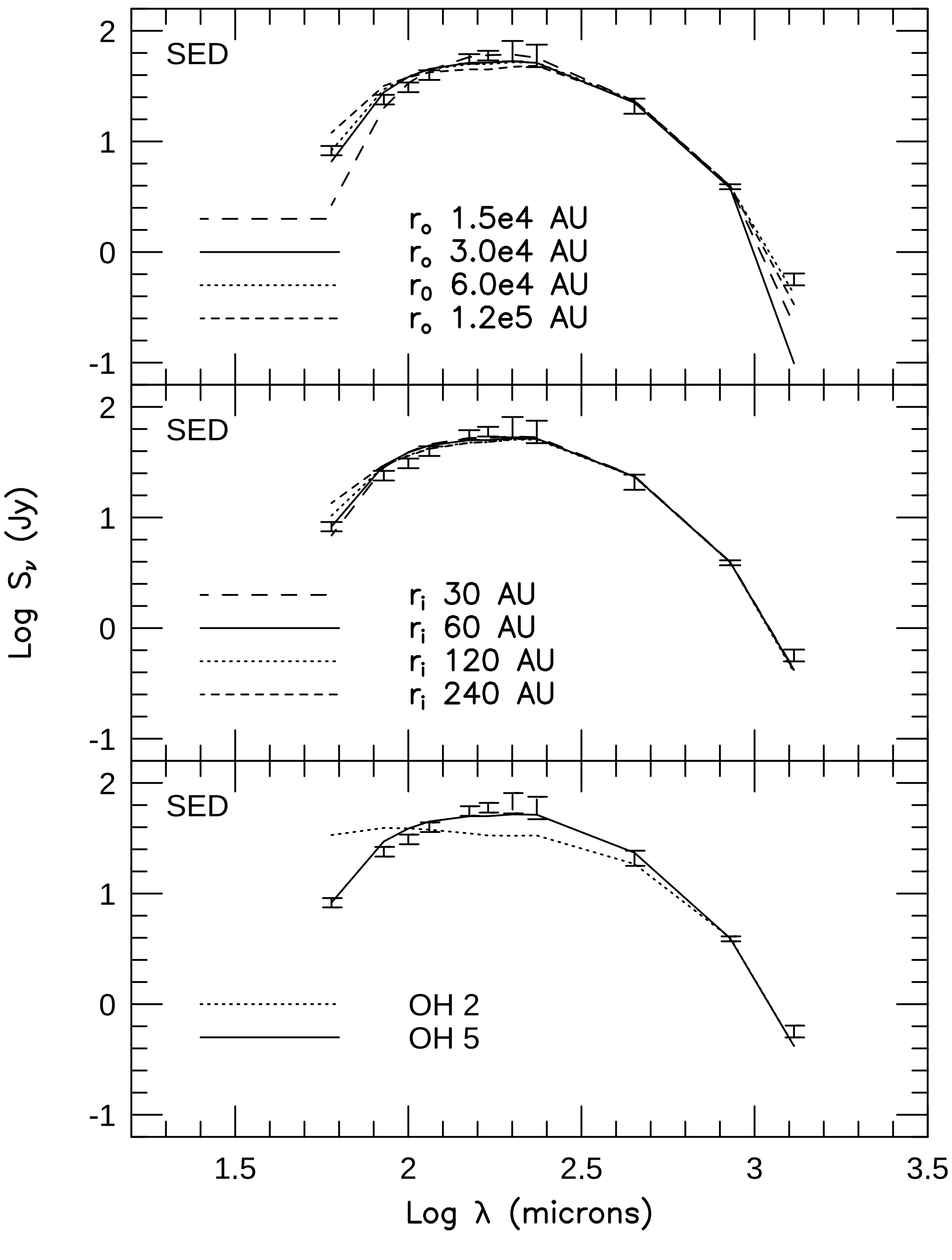

Figure 3.2 B335 Model SEDs for power laws with p=2.0 for various r_o, r_i, and κ_ν. Only the model SEDs are plotted since effects to the radial profiles are shown to be negligible.

the envelope. We therefore considered models with p = 1.5, 2.0, and 2.5 (Figure 3.3). Both the p = 1.5 and p = 2.5 models fit very poorly (Fig. 3). The p = 2.5 model shows that the predicted radial profile becomes very sensitive to the beam shape for steep power laws. Variations in p of 0.1 produce noticeable changes in the intensity profiles. In summary, we find that the $p = 2.0$ initial test model is the best fit profile for OH5 dust and $s_{ISRF} = 1.0$, and that variations in p of 0.1 can be distinguished if all other parameters are fixed.

Heating by the ISRF affects the temperature distribution in the outer envelope. The temperature levels off and eventually rises again towards the outer boundary of the cloud. The location of the minimum in the temperature is dependent on the ISRF strength and L_{int} (Figure 3.4). The strength of the ISRF could affect the intensity profiles and the SED. We tested these effects on the best fit power law by multiplying the ultraviolet to far-infrared portion of the ISRF by factors of $s_{ISRF} = 3$ and $s_{ISRF} = 0.3$. With $s_{ISRF} = 3.0$, the best fit is obtained with $p = 2.2$ and $L_{int} = 1.5$ L$_\odot$. Obviously, the greater contribution to the flux from the ISRF explains why a lower internal luminosity is appropriate. Even though χ^2_r and χ^2_{SED} are not significantly different from the standard model, the predicted SED is too bright at FIR wavelengths and severely underestimates the 60 μm flux. Using $s_{ISRF} = 0.3$, the best fit is obtained with $p = 1.8$ and $L_{int} = 3.3$L$_\odot$ (Figure 3.4 & 3.5). This model clearly yields the best fit to the intensity profiles of all of the power law models that we have considered, but the model SED has too much flux at shorter wavelengths (i.e., 60 μm). A lower strength of the ISRF is consistent with the best fit models in Paper II. A study of [CII] and [OI] emission lines with ISO towards B335 is consistent with a slightly higher strength of the ISRF, $2 - 3G_0$ (Nisini et al. 1999). Clearly, there is uncertainty in the strength of the ISRF around B335. We conclude that uncertainties of a factor of 10 in s_{ISRF} cause changes in p by ±0.2, but that the SED provides some constraints that can decrease

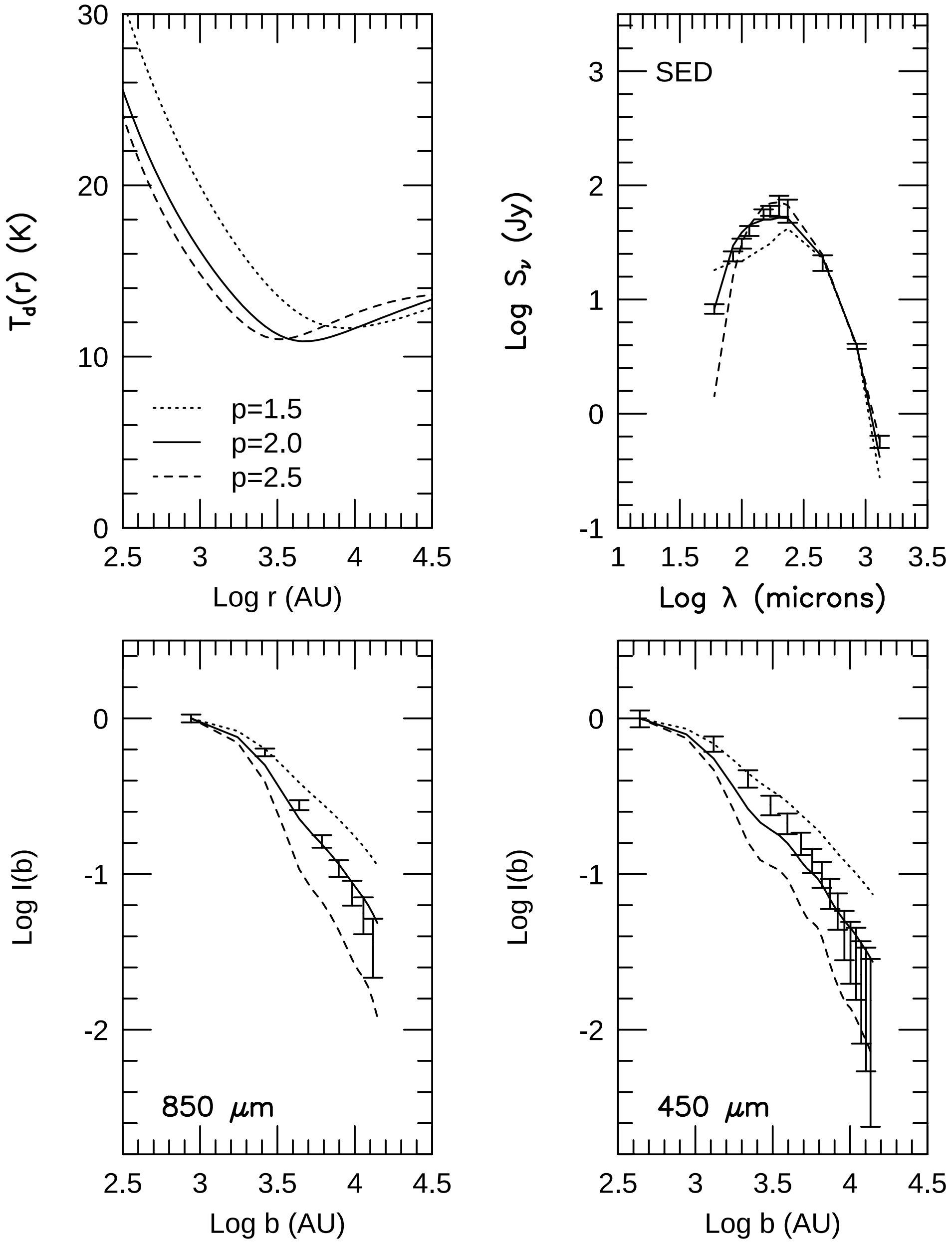

Figure 3.3 B335 power Law models with $p = 1.5$, 2.0, and 2.5. The $p = 2.0$ model is the best fit to the SED and radial profiles. The model parameters were: OH5 dust opacities, $s_{ISRF} = 1.0$, $r_i = 60$ AU, and $r_o = 60,000$AU for all models.

this uncertainty.

The effect of the uncertainty in distance was checked on the initial test power law by assuming B335 was at half the published distance (125 pc; cf. Harvey et al. 2001). Since the core is now closer, smaller inner and outer radii (30 pc and 30,000 pc) were used. The best fit power law index and shape of the model profile are very insensitive to the uncertainty in the distance (χ_r^2 increases by less than 3%). The best fit L_{int} = 0.7 L$_\odot$, and the total mass in the model decreased by a factor of 2. The mass of a power law envelope scales as $M_{env} \propto n_f r_o^{3-p}$. For factor of 2 uncertainties in the distance, L_{int} will be uncertain by factors of about 4, the mass by factors of 2 (for $p = 2$), but the best fit p is unaffected.

The effect of changing the observed beam shape was tested by substituting the January 1998 beamshape into the best fit power law model for B335. The difference in beamshape between January and April 1998 beams was greater than the difference between individual beam profiles observed during April 1998. The best fit power law was slightly lower, $p = 1.7$, indicating that uncertainties in the beam shape may effect the interpretation of the best fit model by as much as $\Delta p \sim 0.1$.

A $p = 1.8$ power law with $s_{ISRF} = 0.3$ provides the best fit to the radial profiles for B335 (Figure 3.5). However, the χ^2_{SED} is not as good for this model as for the test model. A somewhat different opacity law would fit better. The fit to the radial profiles is not perfect, with some systematic deviations as a function of impact parameter that suggest deviations from a simple power law, but given uncertainties in the beam shape, we consider this fit to be adequate.

In summary, our tests support the idea that the normalized radial profile ($I_\nu^{norm}(b)$) and the SED provide largely orthogonal constraints. $I_\nu^{norm}(b)$ constrains the shape (p) of the density profile, while $S_\nu(850)$ constrains the normalizing density, n_f, and hence the mass. The density and mass enter as a product with the opacity at 850 μm, leading to uncertainties in the mass equal to the uncertainties in the

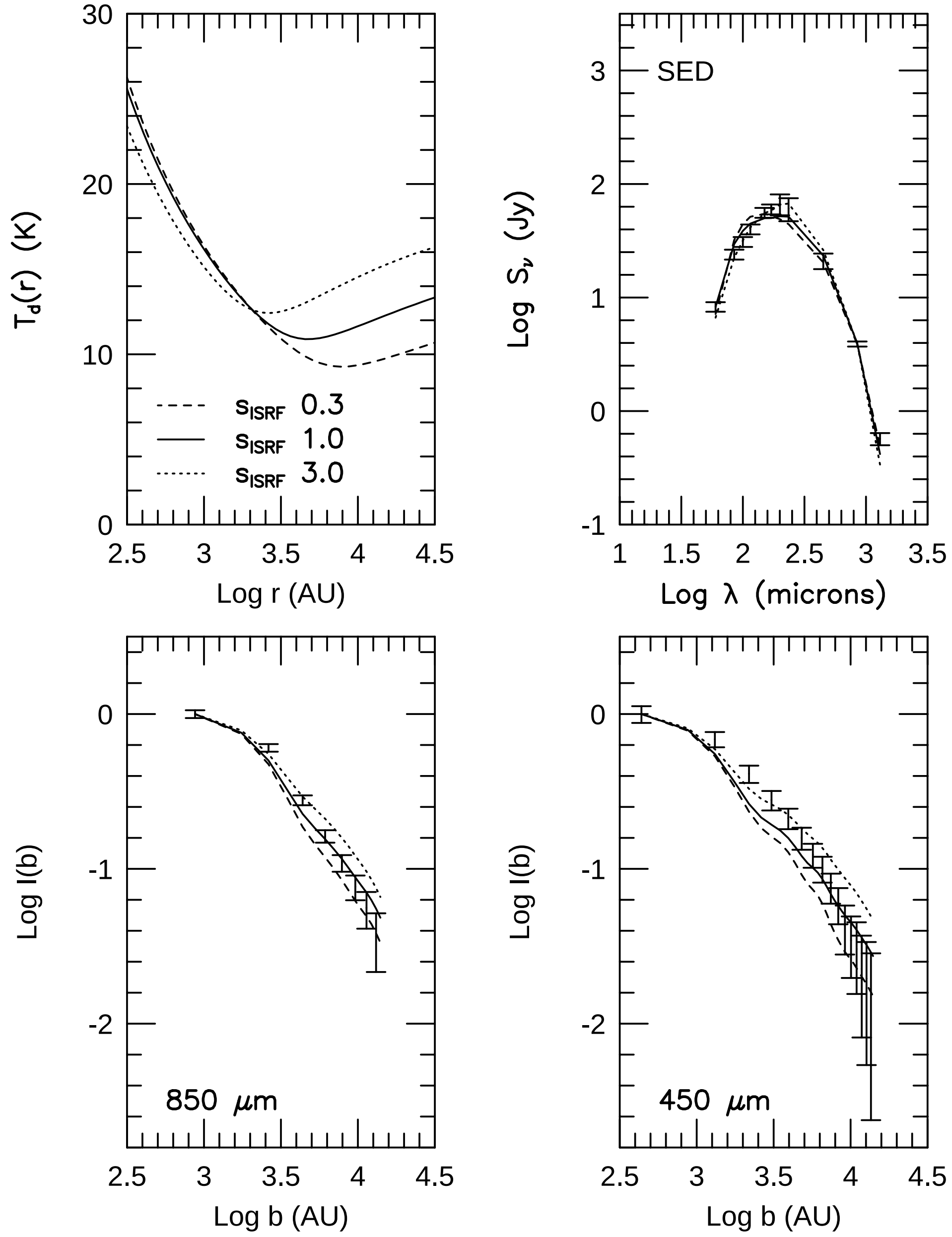

Figure 3.4 Effects of changing the strength of the ISRF. Three $p = 2$ power law models of B335 are shown with $s_{ISRF} = 0.3, 1.0$, and 3.0.

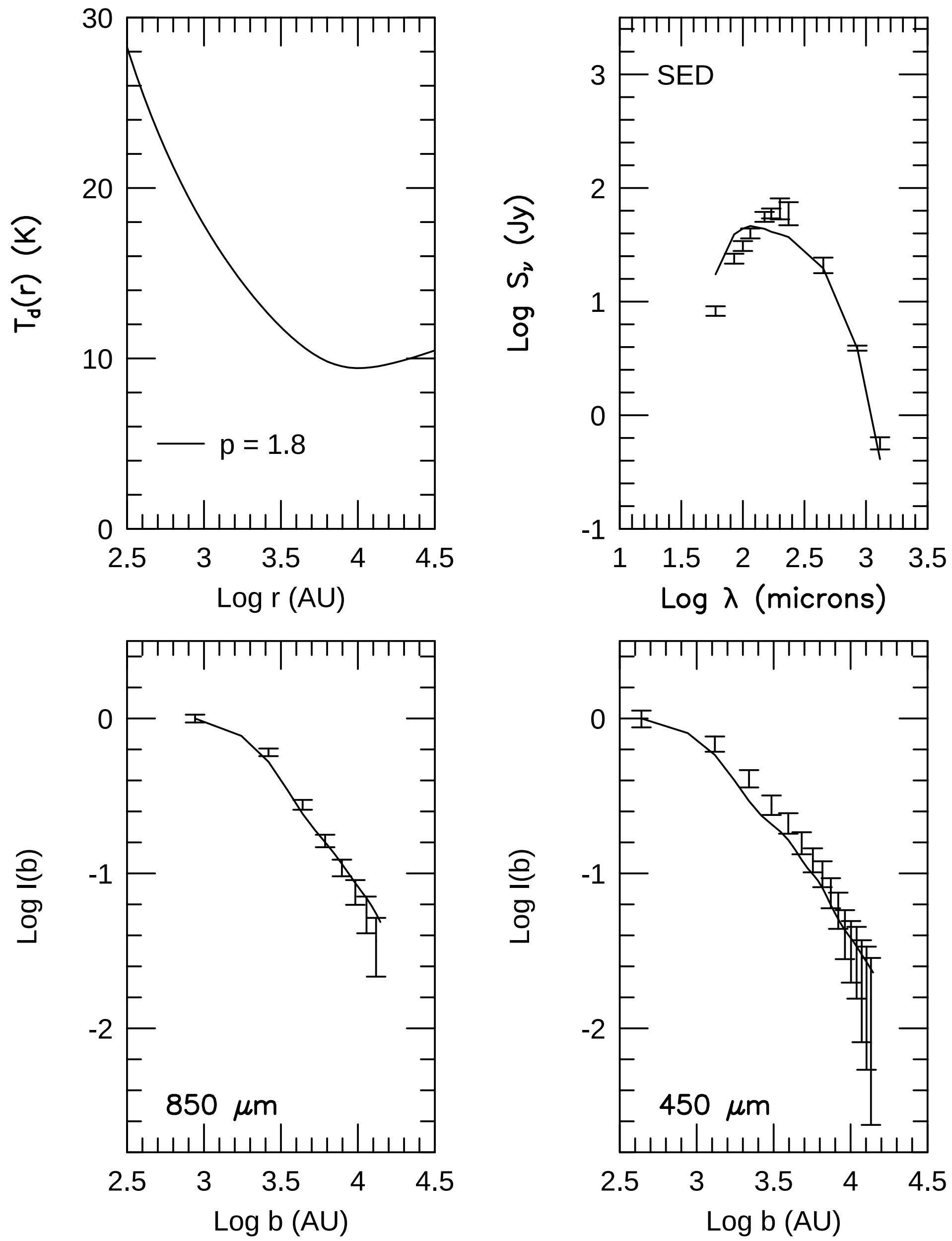

Figure 3.5 The best fit power law model for B335. The parameters of the best fit were: $p = 1.8$, $n_f = 1.5 \times 10^6$ cm^{-3}, $L_{int} = 3.3 \mathrm{L}_\odot$, and $s_{ISRF} = 0.3$.

opacities. However, the rest of the SED depends on the overall opacity law; within the limitations of spherical models, the overall SED constrains the opacity law and hence reduces the uncertainty in mass. Variations in other parameters, such as opacity, distance, and L_{int}, have negligible effect on p (Table 3.3). Variations in the ISRF have the largest effects: a factor of 3 in either direction in s_{ISRF} cause variations in p of ± 0.2. Factors of 3 in s_{ISRF} can be constrained by the SED, so larger errors are unlikely. Opacity and the strength of the ISRF strongly affect L_{int} (Table 3.3).

3.3.2 Shu77 Inside-Out Collapse Models

The Shu77 density distribution has successfully matched asymmetric line profiles seen towards Class 0 sources including B335 (Zhou et al. 1993, Choi et al. 1995, Hogerheijde et al. 2000). Based on Monte Carlo radiative transfer models of CS and H_2CO asymmetric line profiles, Choi et al. found that a Shu77 model with r_{inf} = 6200 AU and a_{eff} = 0.23 km s^{-1} was the best fit for an inside-out collapse model for B335. We mostly constrain a_{eff} to this value, unlike the procedure used by Hogerheijde & Sandell (2000), who allowed a_{eff} to be a free parameter. This lack of flexibility in the normalizing density puts Shu77 models at a disadvantage compared to the power law models with two free parameters.

The Shu77 density distribution with r_{infall} = 6200 AU was tested assuming s_{ISRF} = 1.0, and OH5 opacities. Compared to the best-fit power law model, the density in this Shu77 model is about 5 times less. There is simply not enough material to match the SED: L_{int} had to be increased to 6.5 L$_\odot$ to match L_{obs} because the lower optical depths allowed too much radiation at $\lambda < 60$ μm, which is not observed. Even with the large L_{int}, the fits to both the SED and radial profiles are extremely poor (Figure 3.6). The model radial profiles are too flat. This is not surprising since a $p = 1.5$ power law model did not fit the observed radial profiles.

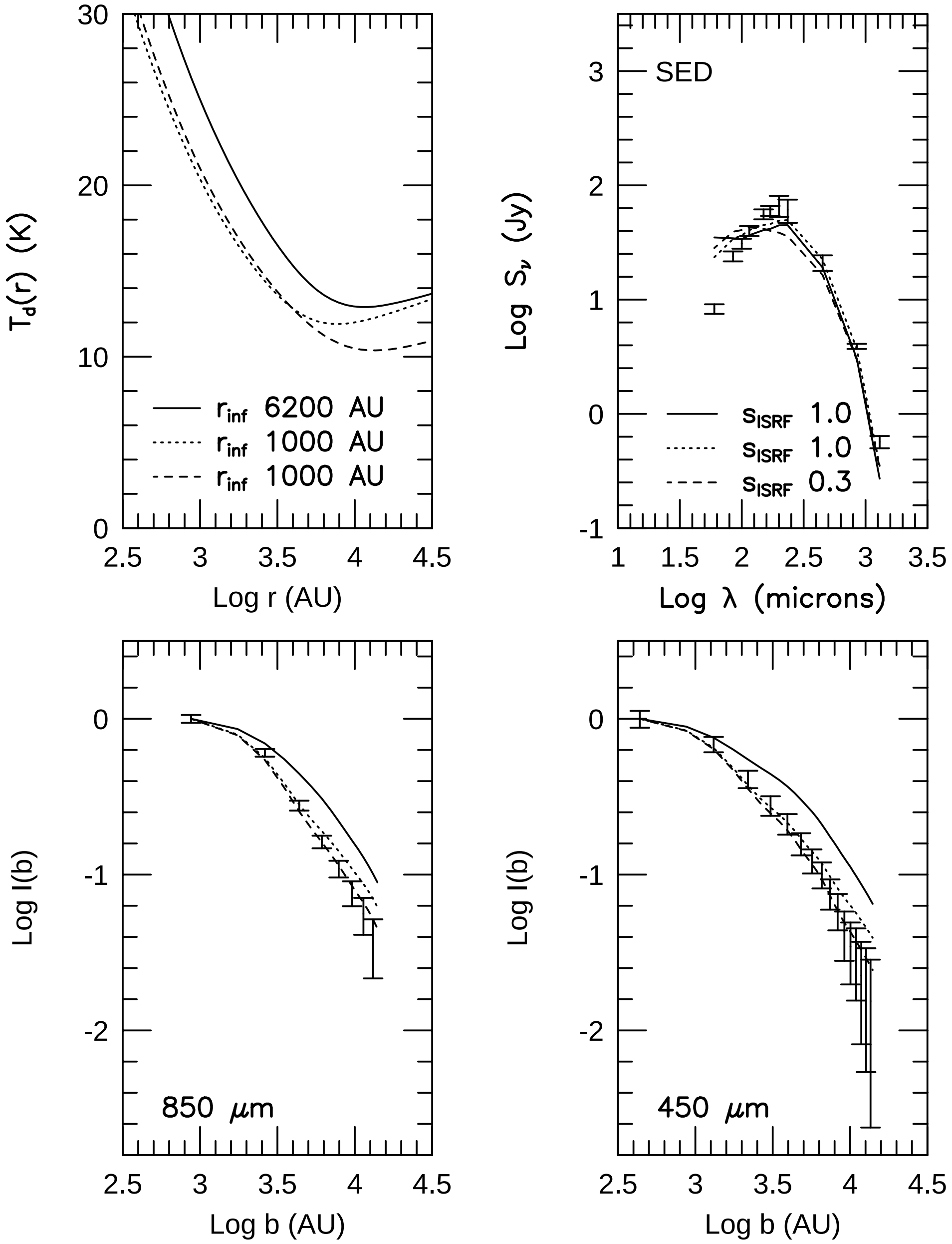

Figure 3.6 Shu77 models for B335. Three models are shown: $r_{inf} = 6200$ AU and $s_{ISRF} = 1.0$, $r_{inf} = 1000$ AU and $s_{ISRF} = 1.0$, and $r_{inf} = 1000$ AU and $s_{ISRF} = 0.3$. The smaller infall radius of 1000 AU is a better fit than the best fit from Choi et al. (1995).

TABLE 3.4

SHU77 MODELS

Source	Model Number	r_{infall} (AU)	a_{eff} (km/s)	r_i (AU)	r_o (AU)	κ_ν	L_{int} ($L_\odot$)	s_{ISRF}
B335								
	1	6200	0.23	60	60,000	OH5	6.5	1.0
	2	6200	0.26	60	60,000	OH5	5.0	1.0
	3	1000	0.23	60	60,000	OH5	3.8	1.0
	4	500	0.23	60	60,000	OH5	3.0	1.0
	5	1000	0.23	60	60,000	OH5	4.5	0.3
	6	1000	0.26	60	60,000	OH5	4.0	0.3
	7	6200	0.23	60	60,000	OH2	6.5	0.3
	8	1000	0.23	60	60,000	OH2	4.7	0.3
B228								
	9	1000	0.23	60	30,000	OH5	1.0	0.3
L723								
	10	1000	0.29	60	60,000	OH5	2.6	0.3
IRAS03282[a]								
	11	1000	0.23	60	45,000	OH5	1.0	0.3
	12	1000	0.26	60	45,000	OH5	1.0	0.3
L1448C								
	13	1500	0.38	60	45,000	OH5	5.9	1.0

[a]IRAS03282+3035.

Table 3.5
Shu77 Models χ^2

Source	Model Number	χ^2_{850}	χ^2_{450}	χ^2_{SED}	Notes
B335					
	1	79.0	53.7	108 [a]	
	2	82.1	52.8	62.2	
	3	7.6	3.6	36.7	
	4	9.0	3.5	15.8	
	5	2.3	0.8	66.8 [a]	Best χ^2_r
	6	2.4	1.0	39.1	
	7	39.6	21.9	59.0 [a]	
	8	2.6	1.1	58.8 [a]	
B228					
	9	2.9	15.6	32.2	Best χ^2_{tot}
L723					
	10	1.1	0.6	2.49	Best χ^2_{tot}
IRAS03282[b]					
	11	4.8	13.3	34.1 [a]	
	12	3.9	9.5	18.7	Best χ^2_{tot}
L1448C					
	13	10.5	3.0	2.4	

[a] Unable to simultaneously match S_{850} and L_{bol}.

[b] IRAS03282+3035.

Shu77 models would need smaller infall radii to preserve an r^{-2} density distribution throughout a greater extent of the envelope. Smaller infall radii provide better fits to the radial profile. The best of these models, with $r_{inf} = 1000$ AU and $s_{ISRF} = 0.3$, has a very good χ_r^2. However, $r_{inf} = 1000$ AU is less than the FWHM of the SCUBA beam at 450 μm. Thus, the best fit Shu77 model actually resembles a $p = 2$ power law in all portions of the profile except the central beam. A small infall radius is highly unfavored by models of profiles of molecular lines (χ^2 is 20 times worse, Choi et al 1995). Further radiative transfer modeling of the molecular line emission using the best fit density profiles from the dust models and considering possible abundance variations in the molecular tracers may resolve this discrepancy.

Thus, the Choi et al. model has two problems: the density is too low to match the observed SED, and the density distribution is not steep enough to match $I_\nu^{norm}(b)$. Because other opacity models combined with Shu77 models have fit the SED of B335 (Zhou et al. 1990), the first problem is not necessarily fatal. The bigger problem is the failure to match $I_\nu^{norm}(b)$.

The near infrared extinction study of Harvey et al. (2001) found that the Choi et al. (1995) parameters for a Shu77 model did fit the density structure of the outer envelope, but require a scaling of the density by a factor of 5. Such a large increase would require a higher a_{eff} or B335 to be much closer. A higher a_{eff} is not supported by the narrow linewidth observed towards B335 (e.g., Mardones et al. 1997). As shown in the power law models of B335, a closer distance does not strongly affect the interpretation of the best fit radial profiles; therefore, an infall radius of 6200 AU would still not fit the observed normalized intensity profile. This solution, which worked for Harvey et al., does not work for our data. A small infall radius would be required to match the SCUBA profiles with a Shu77 model. The increased density required by Harvey et al. (2001) to model their near-infrared extinction measurements makes their densities agree well with our best-fit power law model, which is based on OH5 opacities at 850 μm. The OH5 opacity at 850 μm and the extinction used by Harvey et al. in the near-infrared thus produce consistent density estimates. This agreement supports the validity of OH5 dust, as does our comparison of dust and virial masses (§3.5.2).

3.4 Sources

The other sources were modeled with less extensive exploration of parameter space, guided by the results of the B335 models.

3.4.1 B228

B228 is a deeply embedded protostar (IRAS 15398-3359) which appears very similar to B335 at 850 and 450 μm. The B228 contours are nearly circularly symmetric with extended envelope emission and a high signal-to-noise profile. Unlike B335, B228 is much less studied and therefore has less published SED information (see Paper I). B228 is an excellent candidate for 1D dust modeling of the envelope emission and should be the subject of further detailed study. We shall try both power law and Shu77 models.

A range of power law indices were tried with noticeable changes in the χ_r^2 with changes of $\Delta p = 0.1$. The best fit power law is $p = 1.9$ with a lower ISRF ($s_{ISRF} = 0.3$) and an internal luminosity of 1.0 $L_\odot$ (see Figure 3.7). Since B228 is closer than B335 (130 pc, see Paper I), the outer radius was decreased to 30,000 AU. While the $p = 1.9$ power law is a reasonable fit to both the profile and SED, it has the same problem as the B335 power law fits. The model profile is too steep in the inner portion of the envelope and too shallow in the outer portion of the profile. The deviations may be due to subtle changes in the beam shape or to departures from a single power law. Far-infrared photometry with better spatial resolution and more wavelength points would help to constrain the SED.

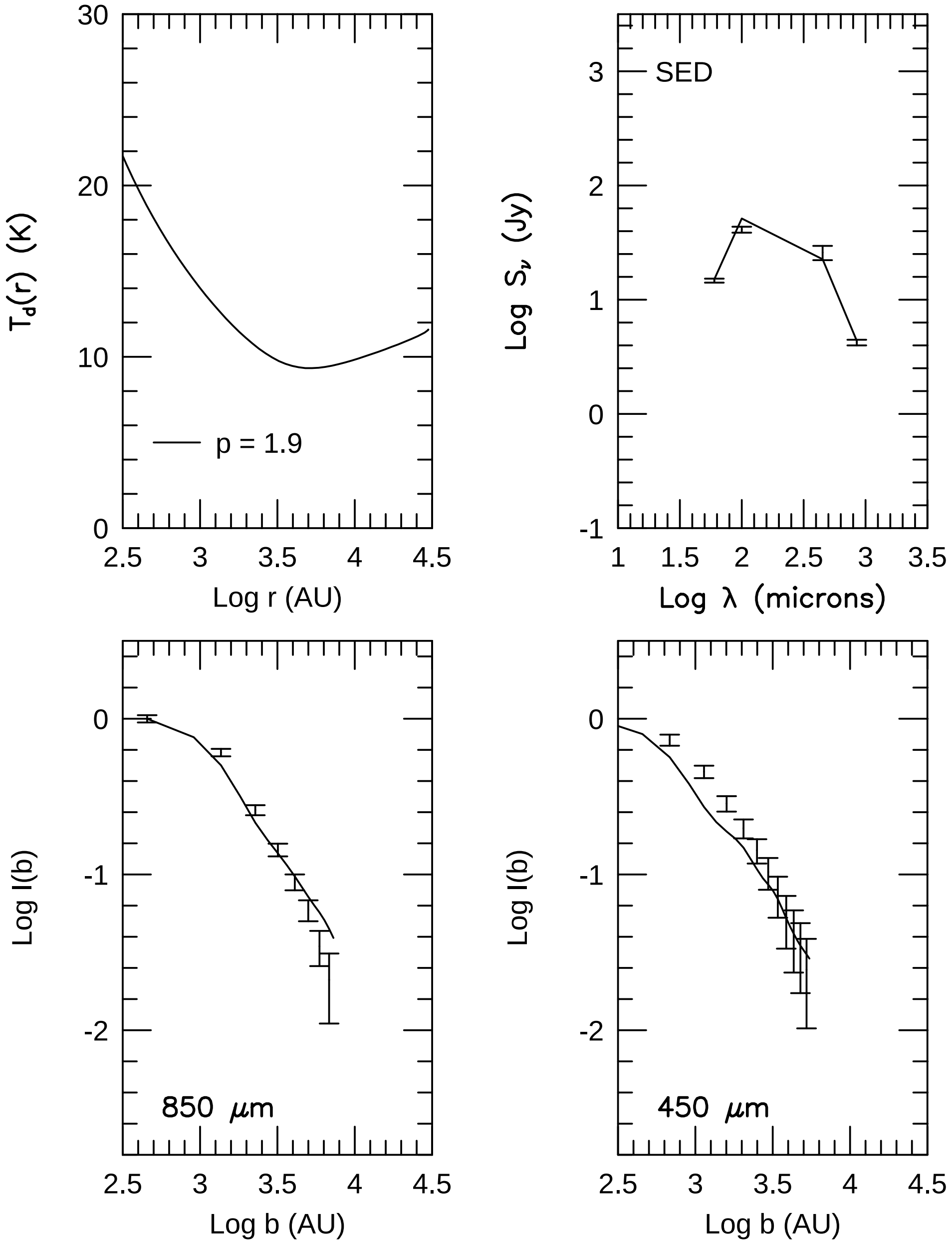

Figure 3.7 The best fit power law model for B228. The parameters of the best fit were: $p = 1.9$, $n_f = 1.2 \times 10^6$ cm^{-3}, $L_{int} = 1.0 \mathrm{L}_\odot$, and $s_{ISRF} = 0.3$.

The best fit Shu77 collapse model has an infall radius of 1000 AU and an effective sound speed of 0.23 km s^{-1}. The linewidth of optically thin lines in B228 (e.g., $\Delta v(N_2H^+)$ in Mardones et al 1997) is similar to that of lines in B335. Therefore an a_{eff} = 0.23 km s^{-1} is reasonable. As with B335, the infall radius is within the central SCUBA beam. The best fit Shu77 model was able to simultaneously match the observed bolometric luminosity and the flux at 850 μm. The fit to the profiles are not as good as the fit of the best fit power law, and χ^2_{SED} is considerably worse.

3.4.2 L723

The submillimeter emission from L723 (IRAS 19156+1906) has asymmetries only in the lowest contours of the 850 and 450 μm emission. The higher contours are very circularly symmetric. A quadrupolar outflow has been detected, indicating that L723 may contain a close binary (Palacios & Eiroa, 1999) within a common envelope. Alternatively, the outflow may be due to a single source with a very large opening angle (Hirano et al. 1998). The largest extensions in the lowest contours of the SCUBA maps are roughly aligned with an east-west outflow. The unique characteristics of the outflow structure and the possibility that L723 may be a proto-binary system warrant a detailed study of the dust continuum structure of the envelope.

L723 is best fitted by a p = 1.8 power law with s_{ISRF} = 0.3 (Figure 3.8). The fit to the profiles and SED is very good using OH5 dust. The model internal luminosity is 2.6 $L_\odot$ indicating a contribution of 0.5 $L_\odot$ to the bolometric luminosity from the ISRF. The large contribution from the ISRF may be due to the large size of model (60,000 AU) and the greater distance (300 pc; Goldsmith et al. 1984) of L723. Emission was detected beyond 65$''$ ($\sim$ 20,000 AU) in the 850μm SCUBA map, larger than the outer radius quoted by Motte & André (2001) of 14,000 AU from 1.3 mm continuum maps. As seen in the test models of B335, decreasing the outer radius to $30,000$ AU has a negligible effect on the shape of the radial profile and the interpretation of the best fit power law.

The best fit power law is very similar to the other circularly symmetric cores B335 and B228. While L723 may be a proto-binary system, there is no strong evidence for differences in the one dimensional dust models of L723 and B335 or B228. Multiple dimensional dust models are needed to probe the extended structure at low contour levels in the SCUBA maps. The envelope structure of L723 is complicated by the extensive observed outflows. The impact the outflow structure has on the overall distribution of material in the envelope cannot be effectively modeled with only one spatial dimension.

The best fit Shu77 model has a small infall radius (1000 AU) and effective sound speed of 0.29 km s^{-1}. The fit to the profile and SED is very good. As with B335 and B228, the infall radius is within the central 450 μm SCUBA beam. There is no evidence for a break in the power law density distribution in the outer envelope beyond the central beam.

3.4.3 IRAS03282+3035

IRAS 03282+3035 is a nearly circular symmetric core with slight asymmetries in the lowest contour of the 850 and 450 μm emission. There is a well studied outflow (e.g., Bachiller et al. 1994) that is nearly perpendicular to the extended submillimeter continuum emission. The signal-to-noise of the radial profiles was lower for this object (Paper I).

The best fit to IRAS 03282+3035 is a $p = 1.9$ power law with lower strength of the ISRF, $s_{ISRF} = 0.3$ (see Figure 3.9). The model fits the 850 μm profile marginally better than the 450 μm profile. Since IRAS 03282+3035 was observed during January 1998, the beam profile is much more uncertain, resulting in larger uncertainties in the best fit model. $L_{int} = 1.0$ $L_\odot$ for the best fit model, accounting

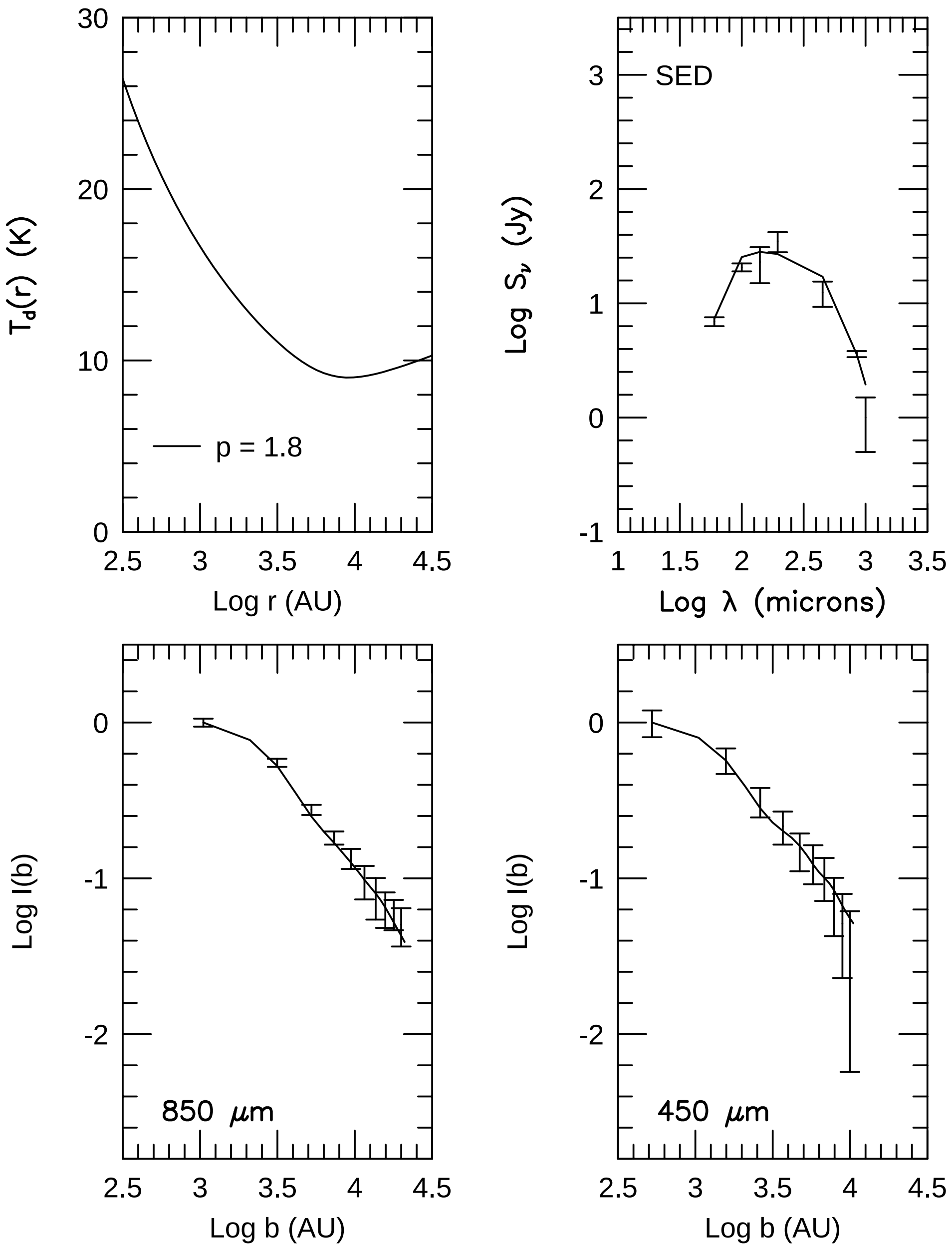

Figure 3.8 The best fit power law model for L723. The parameters of the best fit were: $p = 1.8$, $n_f = 1.8 \times 10^6$ cm^{-3}, $L_{int} = 2.6\mathrm{L}_\odot$, and $s_{ISRF} = 0.3$.

for nearly all of the bolometric luminosity.

We continue to use a distance of 220 pc (Černis 1990) for consistency with Paper I, but the recent study of de Zeeuw et al. (1999) finds a greater distance of 318 pc using Hipparcos parallaxes of the Perseus OB association. At the larger distance, the internal luminosity and mass in the envelope would increase by a factor of two. As was seen in the models of B335, the best fit power law index is not sensitive to distance and remains $p = 1.9$.

The best fit Shu77 model again has a infall radius of 1000 AU within the central SCUBA beam. Molecular line observations towards IRAS03282+3035 indicate linewidths that are similar to B228 and B335 ($\Delta v(N_2H^+) = 0.49$ km s^{-1}, Mardones et al. 1997); however, a higher effective sound speed (0.26 km s^{-1}) than used for B228 is needed to match the 850 μm flux and L_{bol} simultaneously using OH5 dust.

3.4.4 L1448C

L1448C (also called L1448-mm) is a well studied Class 0 protostar in the vicinity of 3 other deeply embedded protostars in the Perseus molecular cloud (L1448N(A & B), L1448NW; see O'Linger et al. 1999, Barsony et al. 1998). L1448C drives a powerful, highly collimated outflow (Bachiller et al. 1990) for which proper motion has been detected in extremely high velocity SiO maps (Girat & Acord 2001). H_2O maser emission has been detected (Chernin 1995) indicating the presence of very dense gas. Recently, the infrared spectrum from 6μm to 190μm has been observed with ISO and extensively studied (Giannini et al. 2001, Nisini et al. 1999). As for IRAS03282+3035, we continue to use a distance of 220 pc, but 318 pc is more likely (de Zeeuw et al. 1999); the effects on the model parameters are described in the previous section.

The submillimeter contours are circularly symmetric with a weak bridge of emission extending between L1448C and L1448N/L1448NW (Barsony et al. 1998,

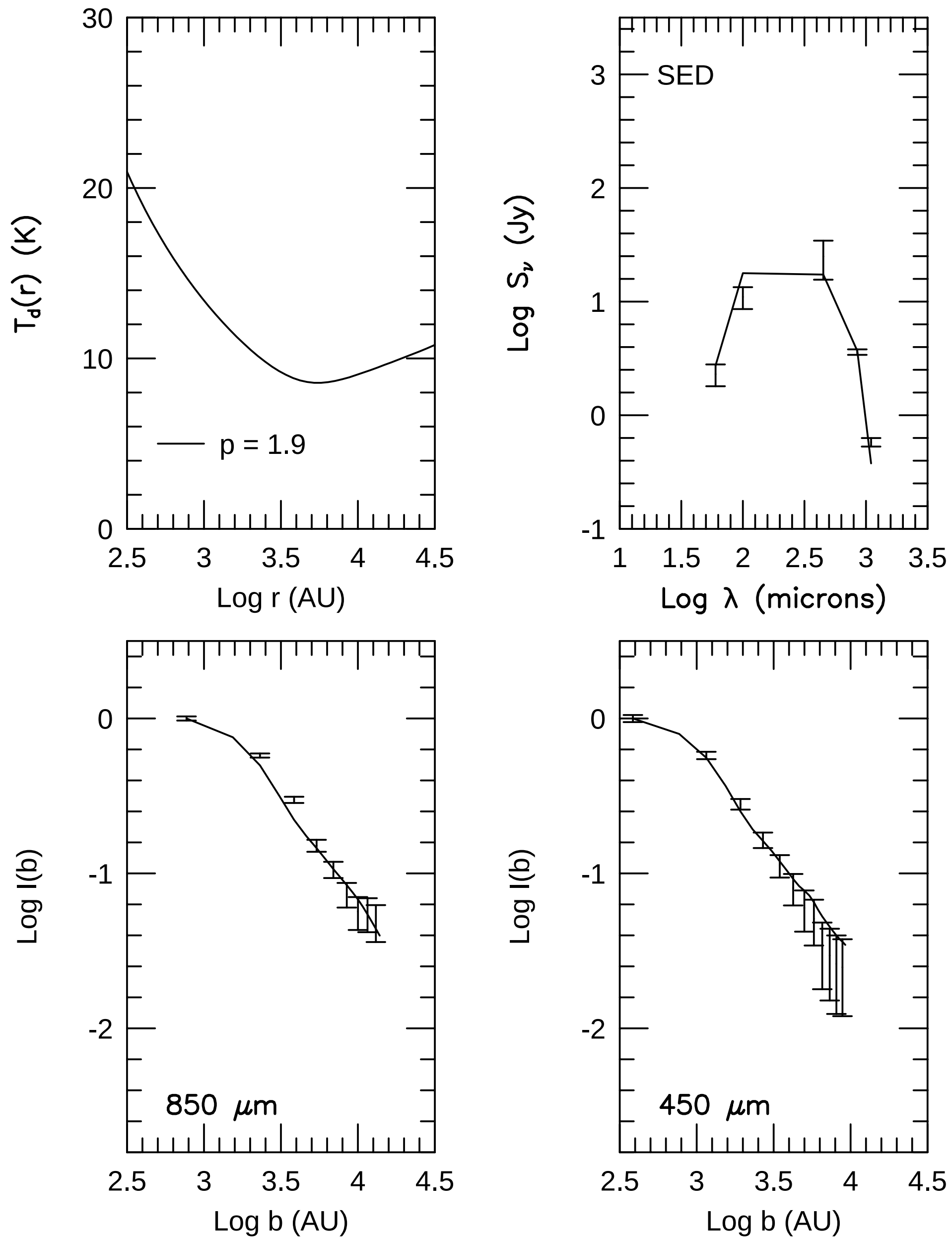

Figure 3.9 The best fit power law model for IRAS03282+3035. The parameters of the best fit were: $p = 1.9$, $n_f = 1.9 \times 10^6$ cm^{-3}, $L_{int} = 1.0\mathrm{L}_\odot$, and $s_{ISRF} = 0.3$.

Chandler & Richer 2000, Paper I). L1448C is located $82''$ from the nearest source (L1448N); therefore we shall attempt to model L1448C as an isolated source with the strong caveat that the outer portion of the observed radial profile (i.e., $> 45''$) is contaminated with emission from L1448N and L1448NW. Only points in the radial profile $\leq 45''$ from L1448C are modeled.

The best fit power law was $p = 1.7$ with $s_{ISRF} = 1.0$ (Figure 3.10). An outer radius of $45,000$ AU was used for the best fit model. This model cannot be compared directly to observations beyond half the distance between L1448C and L1448N/L1448NW (9000 AU projected on the sky). However, the large outer radius is appropriate for the model since all of the sources in the SCUBA map are clearly embedded in a diffuse envelope that extends to the edge of the map. The model of the 450 μm profile falls off too steeply for the best-fit 850 μm profile, which could be caused by a larger s_{ISRF} or uncertainties in the beam.

This power law density structure is slightly flatter than that of the other protostars with symmetric submillimeter emission. If the entire profile of L1448C is contaminated from emission from L1448N/L1448NW, then the observed intensity profile would be flatter than for an isolated source resulting in a flatter best fit p. However, it seems unlikely that the northern sources could significantly alter the conclusions of the modeling of the entire profile since they are located at least 18000 AU away.

This is the only modeled source for which $s_{ISRF} = 1$ gave the best fit. This source is also the only source modeled with multiple cores observed within the SCUBA map. It is possible that this indicates that the ISRF is indeed greater in the vicinity of L1448C; however, the overall change in the χ^2_{tot} between $s_{ISRF} = 0.3$ and $s_{ISRF} = 1.0$ is only 25%.

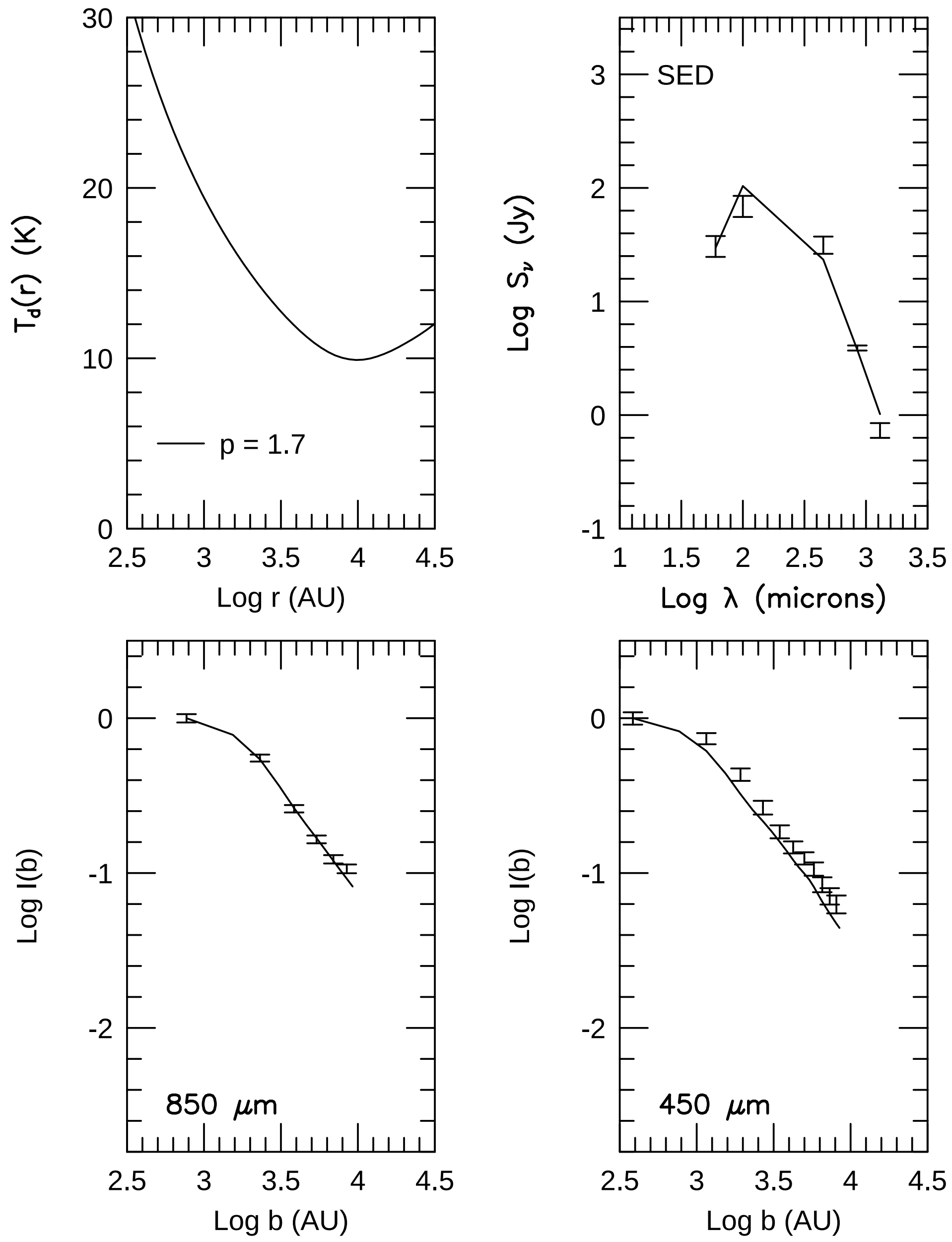

Figure 3.10 The best fit power law model for L1448C. The parameters of the best fit were: $p = 1.7$, $n_f = 2.6 \times 10^6$ cm^{-3}, $L_{int} = 5.9\mathrm{L}_\odot$, and $s_{ISRF} = 1.0$.

3.4.5 L1527

L1527 is a well studied Class 0 source (IRAS 04368+2557) in the Taurus molecular cloud complex characterized by asymmetric submillimeter and far-infrared emission extending from the southeast to northwest direction (Ladd et al. 1991, Chandler & Richer 2000, Hogerheijde & Sandell 2000, Paper I, Motte & André 2001), strong evidence for rotation (Goodman et al. 1993, Zhou et al. 1996, Ohashi et al 1997), a molecular outflow in the east-west direction (MacLeod et al. 1994, Bontemps et al. 1996), and an associated near-infrared nebula (Eiroa et al. 1994). The normalized radial intensity profile was not well fitted by a single power law in Paper I, as it shows considerable curvature. Previous studies of the dust continuum emission (Hogerheijde & Sandell 2000, Motte & André 2001) have estimated the density power law to be near $p = 1$, much lower than the best fit power laws of B335 and B228.

The best fit power law model (see Figure 3.11) is a shallow $p = 1.1$ power law with $s_{ISRF} = 0.3$, in agreement with previous dust continuum studies of L1527. The fit to the 850 μm profile is within the errorbars except for the last point. The observed profile is slightly flatter than the model $p = 1.1$ power law between 5000 and 6500 AU. The 450 μm model profile is flatter than the observed profile in the inner portion but matches extremely well in the outer envelope. These discrepancies may be explained by the inability of the one-dimensional dust code to appropriately model the observed large asymmetries in the dust continuum maps or may be explained by the problematic January 1998 beam profiles (cf. Section 2). The beam effects cannot be strong enough to change our conclusion that the density structure in L1527 is clearly flatter than the density structure of B335 or B228. The curvature in $I_\nu^{norm}(b)$ can be matched by simple power laws when $T_d(r)$ and the effects of the beam and chopping are properly simulated. The fit to the SED is poor at far-infrared wavelength as indicated by the the poor χ^2_{SED} for all of the models in

Table 3.2.

The sensitivity of the model to asymmetries can be tested by eliminating sectors in the azimuthally averaged intensity profile. L1527 is elongated in a south-east to north-west direction. If a symmetrical sector of 70° centered along the major axis is removed from the azimuthal average, then the best fit power law index changes only to $p = 1.0$. Therefore, the density distribution appears to fall off more slowly even perpendicular to the extension; thus the lower value of p appears to be real and not an artifact of azimuthally averaging an elongated intensity map. Uncertainties on the order of $\Delta p \sim \pm 0.1$ result from azimuthally averaging the L1527 continuum emission. The uncertainty in best fit p is consistent with effects seen in 1.3mm continuum maps of L1527 (Motte & André 2001).

A standard Shu collapse model was not tested since the density distribution only flattens to $p \sim 1.1$ in a small region around the infall radius and is much steeper everywhere else in the envelope. Zhou et al. (1996) were able to model molecular line emission with a Terebey-Shu-Cassen model (TSC, Terebey et al. 1984), a perturbation of the Shu collapse model to account for rotation. The one-dimensional averaged TSC profile is similar to $r^{-1.1}$ in the region inside the infall radius (5400 AU). A more detailed understanding of the density structure requires higher dimensional radiative transfer models to effectively model the asymmetric, flattened structure due to rotation and outflow cavities.

3.4.6 L483

L483 (IRAS 18148-0440) is another example of a Class 0 protostar with large asymmetries observed in the submillimeter continuum maps. The 850 and 450 μm emission is extended in the northeast to southwest direction (Paper I), nearly perpendicular to the observed outflow direction (Parker 1988). Water maser emission has been detected towards L483 (Xiang & Turner 1992) as well as an associated near-infrared

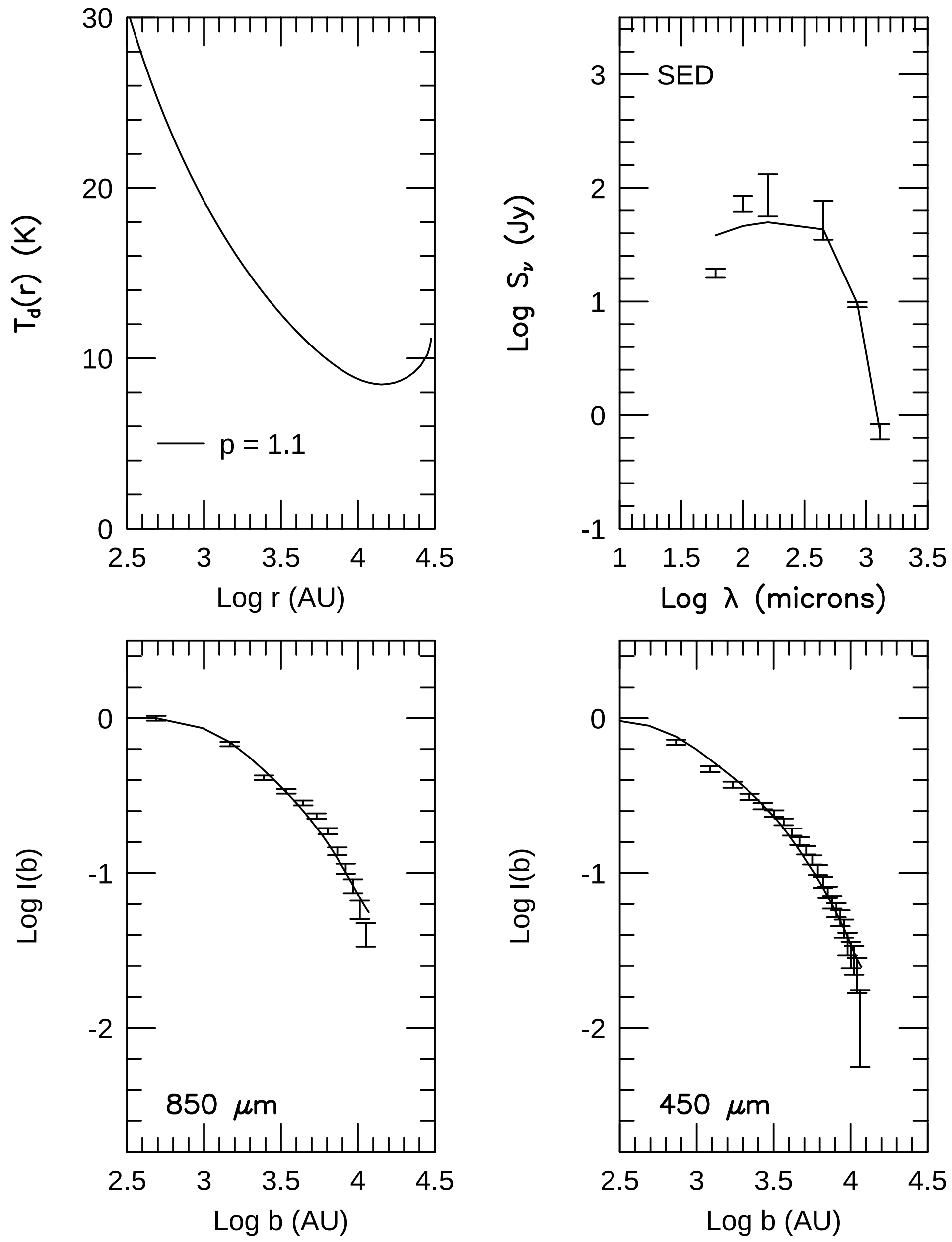

Figure 3.11 The best fit power law model for L1527. The parameters of the best fit were: $p = 1.1$, $n_f = 6.5 \times 10^5$ cm^{-3}, $L_{int} = 2.2\mathrm{L}_\odot$, and $s_{ISRF} = 0.3$.

nebula (Hodapp 1994). Molecular line studies identify this source as a possible collapse candidate (Mardones et al. 1997) but with several confusing signatures due to infall and outflow (Park et al. 2001).

The dust continuum emission from L483 is best fitted by a shallow ($p = 1.2$) power law with $s_{ISRF} = 0.3$ (Figure 3.12). The model SED and 850 μm radial profile match very well but the 450 μm model profile is not steep enough in the outer half of the envelope. This may be partially due to uncertainties in the beam profile at 450 μm, a variation in the dust opacity in the outer envelope, or a variation in the temperature structure due to geometrical effects compared to a one dimensional model. Once again, OH5 dust matches the observed SED well; however, the 160 μm point from Ladd et al. (1991) is much higher than the surrounding 100 μm and 190 μm points, perhaps indicating a larger calibration error than the published value. The internal luminosity of the model is 13.0 $L_{\odot}$. This is the most luminous source in this sample of Class 0 objects, making the contribution to the bolometric luminosity from the ISRF negligible compared to the internal luminosity, but the effects on the temperature profile are still substantial. The resulting temperature profile flattens near the outer regions probed by SCUBA observations making a single temperature power law a poor approximation. Our model is consistent with 1.3 mm continuum models of Motte & André (2001), which assume a power law temperature distribution, $T_d(r) \propto r^{-q}$, ($p = 1.2 \pm 0.6$ for $q = 0.2 \mp 0.2$). The best fit model becomes optically thick around 30 μm due to the flatter power law and higher luminosity internal source.

Like L1527, the L483 profiles were not well fitted by a single power law in Paper I, but a power law density distribution does fit well when the beam, chopping, and $T_d(r)$ are correctly modeled. The best fit power law is close to $p = 1$, for both these sources with elongated dust emission contours. Both L1527 and L483 have near-infrared nebulae associated with the core. However, both cores are not entirely

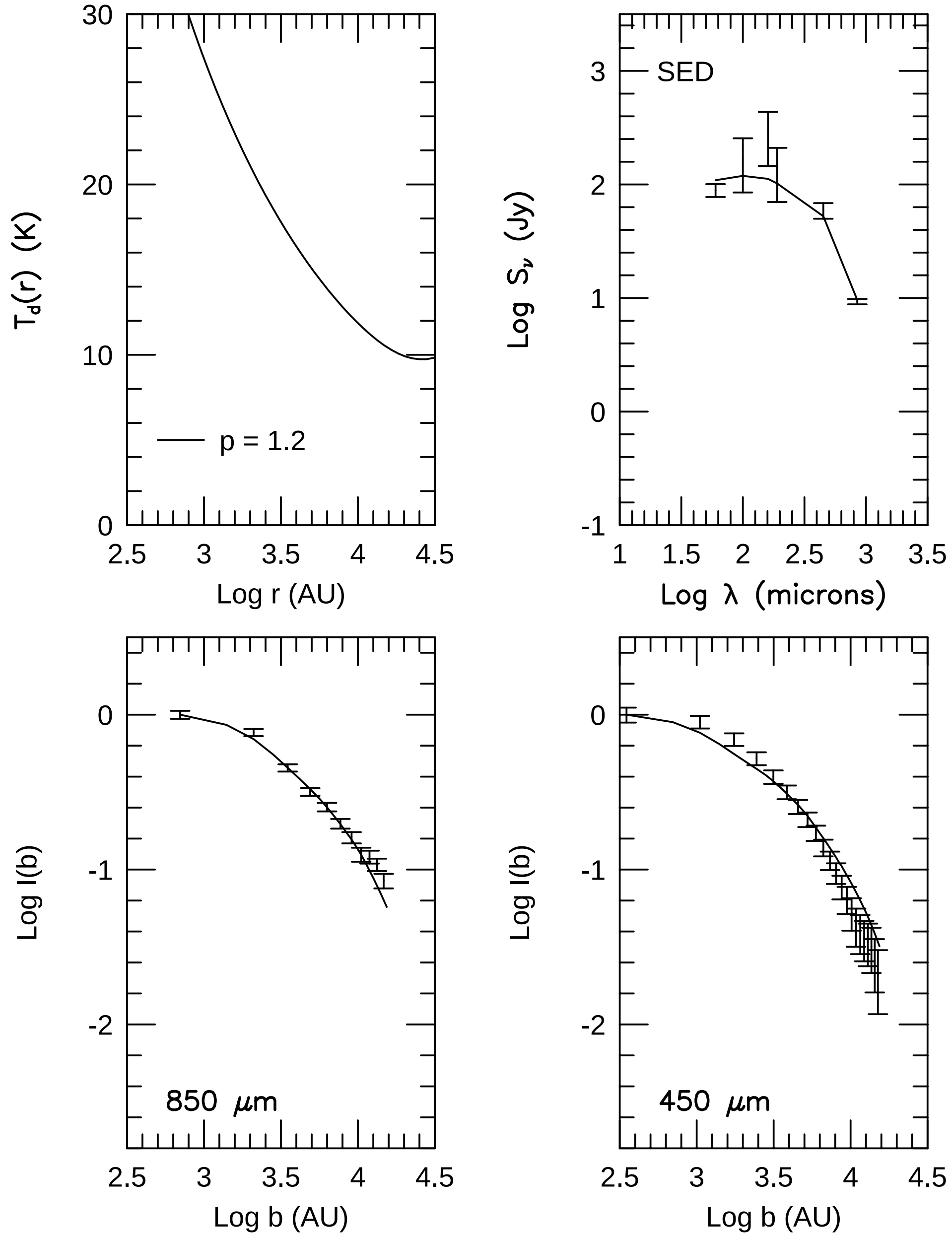

Figure 3.12 The best fit power law model for L483. The parameters of the best fit were: $p = 1.2$, $n_f = 6.0 \times 10^5$ cm^{-3}, $L_{int} = 13.0 \mathrm{L}_\odot$, and $s_{ISRF} = 0.3$.

similar since the extensions seen in the submillimeter continuum contours are in opposite directions with respect to the outflow axes. Geometrical projection effects are clearly important for these two sources. Tafalla at al. (2000) and Pezzuto et al. (2001) suggest this source is in the transitional phase between Class 0 and Class I sources based on the observed properties of its outflow and far-infrared colors. While still a Class 0, it does have the largest T_{bol} (52K) of the sources we model here. While the envelope structure is clearly different from the more symmetrical cores B335 and B228, it is not clear whether the lower p indicates a more evolved state or an intially less spherical envelope. Higher dimensional dust modeling is required to fully understand the density structure of the outer envelope.

No Shu collapse models were tested since the power law model was flatter than the Shu collapse model. However, it is possible that a higher dimensional model that includes effects of rotation (TSC) may fit the intensity profile.

3.5 Discussion

3.5.1 Density Distributions

The properties of the best fit power law for all of the Class 0 sources are listed in Tables 3.6 & 3.7. Power law models successfully fit the outer ($r > 1000$ AU) envelope structures of Class 0 protostars. Five of the Class 0 sources are well fitted by steep power laws ($p = 1.7 - 1.9$, B335, B228, L723, IRAS03282+3035, L1448C), while the two cores with elongated emission contours are fitted by shallow power laws ($p = 1.1 - 1.2$, L1527, L483). We quantify the degree of elongation in Table 4 by giving the aspect ratio (ratio of long axis to short axis) of the 20% contour. L1527 and L483 have the largest aspect ratios. Both L1527 and L483 also have near-infrared nebulae, suggestive of aspherical density distributions. The fiducial densities for all of the Class 0 cores are consistent with the central densities

TABLE 3.6
PROPERTIES OF BEST FIT MODELS

Source	p	n_f ($\mathrm{cm^{-3}}$)	L_{obs} ($\mathrm{L_\odot}$)	L_{int} ($\mathrm{L_\odot}$)	L_{bol}^{mod} ($\mathrm{L_\odot}$)
B335	1.8	1.5×10^6	3.1(0.1)	3.3	3.1
B228	1.9	1.2×10^6	1.2(0.2)	1.0	1.1
L723	1.8	1.8×10^6	3.3(0.2)	2.6	3.4
IRAS03282[a]	1.9	1.9×10^6	1.2(0.3)	1.0	1.2
L1448C[b]	1.7	2.6×10^6	6.0(0.5)	5.9	6.0
L1527	1.1	6.5×10^5	2.2(0.2)	2.2	2.2
L483	1.2	6.0×10^5	13(2)	13.0	12.9

[a]IRAS03282+3035.

[b]Quantities calculated using a 120″ aperture not shown due to confusion from nearby sources.

($n_f \sim n_c \sim 10^6$ cm^{-3}) of the denser pre-protostellar cores modeled as Bonnor-Ebert spheres in Paper II.

The best fit Shu77 models for B335, B228, L723, and IRAS03282+3035 have small infall radii (within the central SCUBA beam). The Shu77 models look very similar to the best fit power laws, but generally do not fit as well. There is no strong evidence in the radial profiles for a break in slope indicative of an infall radius in the outer portion of the envelope probed by SCUBA. This result directly contradicts the molecular line modeling results towards B335 (Choi et al. 1995), which strongly favors larger infall radii. However, the molecular line models do not take into account chemical effects and abundance gradients, which can affect the shape of the blue asymmetry profile (Rawlings & Yates 2001). Unfortunately, the best fit power laws cannot be directly used in Monte Carlo molecular line modeling without an assumption about the velocity field along the line of sight.

Table 3.7
Properties of Best Fit Models Contiunued

Source	$\alpha^{120}_{450/850}$	M^{120}_{env} (M$_\odot$)	Aspect[a]	T_{iso} (K)	M^{120}_{vir} M$_\odot$
B335	2.5	2.6	1.08	13.2	4.8
B228	2.6	0.8	1.22	12.5	2.8
L723	2.5	3.9	1.42	12.4	7.7
IRAS03282[b]	2.4	2.4	1.03	11.5	3.6
L1448C[c]	...	4.5	...	...	...
L1527	2.4	1.6	1.59	15.0	2.6
L483	2.7	2.3	1.93	18.0	5.4

[a] Ratio of major to minor axis for the 20% peak contour.

[b] IRAS03282+3035.

[c] Quantities calculated using a 120″ aperture not shown due to confusion from nearby sources.

3.5.2 Mass Determinations

The mass in the envelope within a 120″ aperture was calculated using

$$M^{120}_{env} = \int_{r_i}^{r(60'')} \mu m_H n(r) 4\pi r^2 dr. \tag{3.6}$$

The average mass is 2.6 ± 1.3 M$_\odot$ for the seven Class 0 best fit power laws, 3.5 times higher than the average pre-protostellar core mass (0.8 ± 0.1 M$_\odot$) within the same aperture (cf. Paper II). The average mass within a fixed outer radius of 30,000 AU is 9.5 ± 5.1 M$_\odot$ for Class 0 sources compared to 2.7 ± 0.3 M$_\odot$ for pre-protostellar cores. If these Class 0 sources are the next stage of evolution, they clearly have most of their mass in the envelope, as originally proposed by Andrè et al. (1993).

In the absence of a realistic model for $T_d(r)$, masses are usually determined from submillimeter observations using an isothermal approximation. To facilitate mass determinations for sources without models, we explored the most suitable temperature to use. We calculated the isothermal dust temperature that yields the same mass as the detailed model based on the measured 850 μm flux in a 120″ beam, S_{850}^{120}, using

$$T_{iso} = \frac{h\nu}{k}\left(1 + \ln\frac{2h\nu^3 M_{env}\kappa_\nu}{S_{850}^{120}c^2D^2}\right)^{-1}. \tag{3.7}$$

The results are listed in Table 3.7. Most are 11-13 K, but the most luminous source, L483, has T_{iso} = 18 K. L1448C is excluded due to confusion from the northern sources in the 120″ aperture. The mean value is 13.8 ± 2.4 K. The sources with $p \sim 1$ (L1527, L483) have higher T_{iso} (15.0K and 18.0K respectively). A similar calculation can be made for the pre-protostellar cores modeled in Paper II using the mass of a Bonnor-Ebert sphere within the 120″ aperture. For the three pre-protostellar cores, the average isothermal temperature is 11.1 ± 1.2 (12.4 K L1544, 10.9 K L1689B, 10.0K L1512), slightly lower than for Class 0 sources with an internal luminosity source.

The model dust mass can be compared to the virial mass calculated using optically thin linewidths (e.g., N_2H^+ and $H^{13}CO^+$; see Table 8 in Paper I). The virial mass estimates in Paper I assumed a constant density distribution in the envelope; however, the virial mass can be corrected for the best fit power law density distribution (cf. Bertoldi & McKee 1992) using

$$M_{virial}^{\theta_{ap}} = \frac{(5-2p)D\theta_{ap}\langle v^2\rangle}{2(3-p)G}, \quad p < 2.5\ , \tag{3.8}$$

where θ_{ap} is the FWHM size of the aperture in which the dust mass was determined, D is the distance, and $\langle v^2\rangle$ is the 3-D velocity dispersion:

$$\langle v^2\rangle = 3\left[\frac{kT_{iso}}{\mu m_H} + \left(\frac{\Delta v^2}{8ln2} - \frac{kT_{iso}}{m_{amu}m_H}\right)\right], \tag{3.9}$$

where Δv is the FWHM linewidth of an optically thin line, μ is the mean molecular mass, and m_{amu} is the molecular mass of the species whose linewidth is used.

The mean of the ratio of the virial mass to the model dust mass in a 120″ aperture is 2.1 ± 0.6. Uncertainties of up to a factor of 10 in the opacity exist between different dust models (Ossenkopf & Henning 1994). We regard this agreement as encouraging evidence that OH5 opacities describe the dust in the cores well and that the virial theorem, properly applied, gives good mass estimates. This ratio is also consistent with the ratio of virial mass to model dust mass for a sample of deeply embedded high mass star forming cores associated with water masers (2.4 ± 1.4, Evans et al. 2002). A factor of 2 decrease in $\kappa_\nu(850)$ from the OH5 value would bring the dust model mass and virial mass into agreement on average.

3.5.3 Spectral Indices

The spectral index, $\alpha^{120}_{450/850}$, was calculated from the model fluxes at 450 and 850 μm in a 120″ aperture (L1448C excluded due to confusion) using

$$\alpha^{120}_{450/850} = \frac{\log(S^{mod}_{450}/S^{mod}_{850})}{\log(850/450)}. \tag{3.10}$$

The model spectral index calculated within a 120″ aperture agrees extremely well with the observed spectral index from Paper I;

$$\left\langle \alpha^{120}_{450/850}(model)/\alpha^{120}_{450/850}(observed) \right\rangle = 0.96 \pm 0.18 \ . \tag{3.11}$$

The model spectral indices are within the observed error bars; however, the total uncertainty on the 450 μm flux ($\sim 50\%$) makes the observed spectral index fairly uncertain. OH5 opacities are also successful in reproducing the observed submillimeter spectral indices for Class 0 sources.

We also considered possible changes in the spectral index as a function of impact parameter. To avoid calibration uncertainties we compare the *normalized* specific intensity, $I^{norm}_{450}(b)/I^{norm}_{850}(b)$, for the best fit models to the observed ratios (Figure 3.13). The variations in the model ratio match those in the observed ratio. Apparent variations in the spectral index can be removed by taking into account beam effects and a realistic temperature distribution. For example, the first sidelobe at 450μm results in a large increase in the ratio. The lower signal-to-noise in outer annuli would mask any subtle variations in the dust opacity. L483 is a clear exception as the model specific intensity ratio does not decrease as fast as the observed ratio. The 450 μm model is too flat at large radii. However, this discrepancy may be caused by our use of a spherical model on an aspherical source rather than an actual variation in the dust properties. There is thus little evidence for variations of the dust opacity with radius. This result contrasts with some earlier work (e.g., Visser et al. 1998, Johnstone & Bally 1999) in regions forming more massive stars, but agrees with the conclusions of Chandler & Richer (2000), who were studying regions similar to those in this study. It is extremely important to use a realistic beam profile and $T_d(r)$ for modeling both the 850 and 450 μm SCUBA maps.

3.5.4 The ISRF and L_{int}

The contribution from the ISRF can be important to the heating of the region of the outer envelope probed by SCUBA observations of low luminosity cores. Scaling the ultraviolet to far-infrared portion of the ISRF by a factor of 3 in either direction resulted in changes of the best fit power by factors of $\Delta p = \pm 0.2$. Every source profile except L1448C was better fitted by a lower strength of the ISRF, $s_{ISRF} = 0.3$, in agreement with models of pre-protostellar cores (Paper II). Modest shielding of the ISRF by surrounding gas in the molecular cloud surrounding the dense core could account for this. L1448C is forming in a much more crowded region and may be subjected to a stronger ISRF.

Our models provide an estimate of the internal luminosity of the central protostar. For all of our sources, the internal luminosity accounts for nearly all of the observed luminosity ($\left\langle L_{int}/L_{bol}^{obs}\right\rangle = 0.95 \pm 0.12$). While the heating from the ISRF is important for the temperature structure of the outer envelope, it does not contribute significantly to the overall observed luminosity of the Class 0 sources we modeled. There is a wide range of internal luminosities modeled, from 1.0 $L_{\odot}$

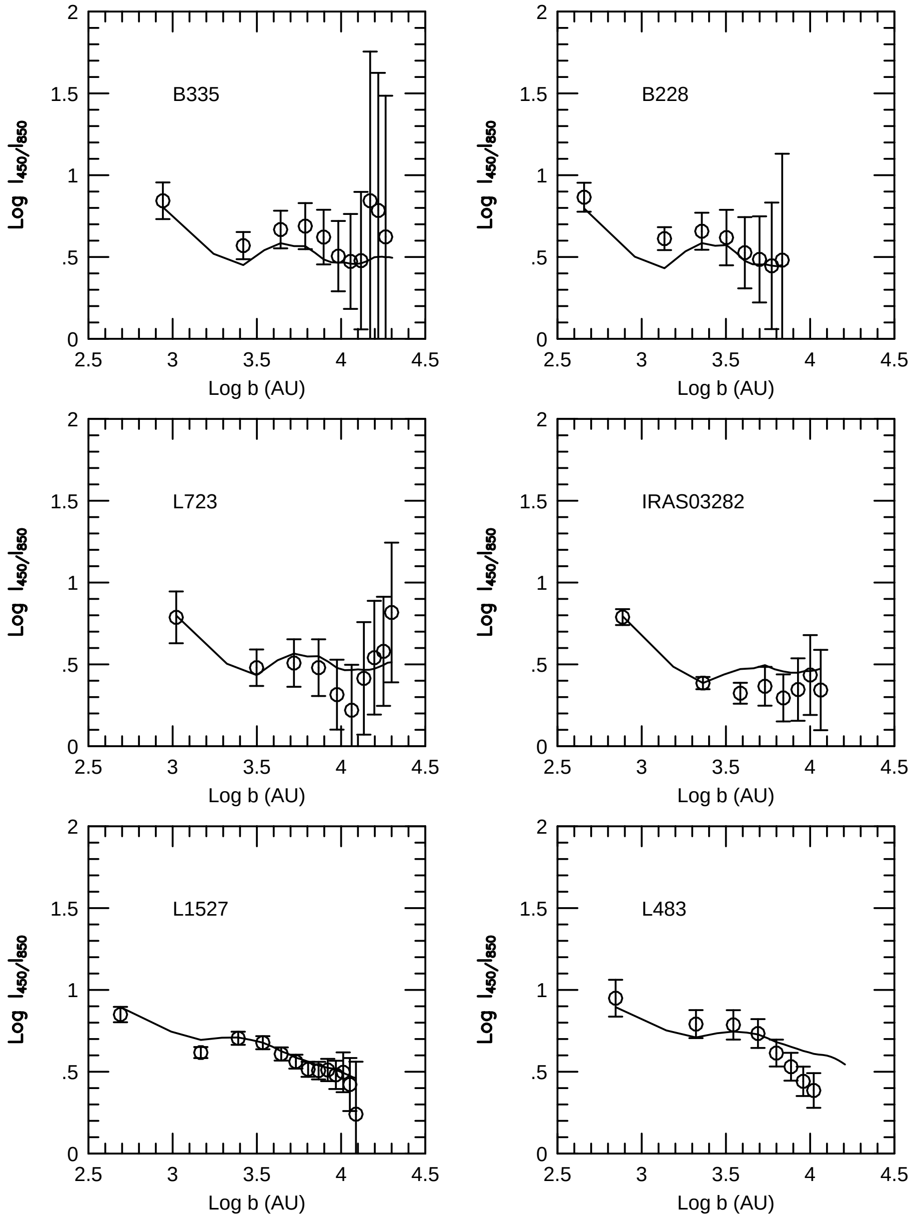

Figure 3.13 The ratio of specific intensity, $I_{450}^{norm}/I_{850}^{norm}$ for the best fit power law models of isolated Class 0 sources (solid line). Points are spaced at the half beam resolution at 850 μm.

to 13.0 $L_\odot$, with an average internal luminosity of 4.0 $L_\odot$. For each of the best fit models, the flux at 850 μm and the observed bolometric luminosity were fitted simultaneously. For sources with SEDs not observed shortward of 60 μm, the model internal luminosity is a lower limit. All of the luminosities were calculated using the distances from Paper I. Since the distance to many globules are uncertain to 50%, a true determination of the internal luminosity is uncertain to 100%; however, the model and observed internal luminosities are consistent for the distance adopted.

Interestingly, the most luminous source, L483, has about the same envelope mass as the others. The greater luminosity should reflect either a higher stellar mass or a higher accretion rate. If the former, it would imply a higher starting mass for the condensation; if the latter, it might be reflected in the linewidths. In fact, the linewidth of the N_2H^+ line is similar to that of the other sources. Alternatively, the accretion might be in a transient high state, similar to an FU Orionis event.

3.5.5 Caveats and Future Work

While our models take into account heating from a central source, heating from the ISRF, realistic beam effects, and simulated chopping, they cannot effectively model asymmetries seen in the dust continuum maps, flattening due to rotation or effects of magnetic fields, and clearing of material in outflow cavities. Five of the cores modeled (B335, B228, L723, IRAS03282+3035, L1448C) appear sufficiently symmetric that the most important effect not included would be lower densities in outflow cavities. Harvey et al. (2001) found a strong asymmetry in the $(H - K)$ colors along the outflow directions in B335, indicative of clearing of material along the outflow axes. The resulting best fit models included an outflow opening angle of 35° to 45°. While no such asymmetry is observed in the submillimeter continuum maps of B335 (Paper I), extensions along the outflow directions (e.g., L1527, L723) and perpendicular to the outflow direction (e.g., L483) are observed in submillimeter maps of Class 0 sources. The overall impact outflows have on the density structure of the envelope will become clearer with finer resolution and higher sensitivity. Future multi-dimensional modeling of the dust continuum emission should attempt to account for the effects of the outflow.

We have neglected the emission from a disk. Chandler & Richer (2002) showed that the flux from a disk is negligible compared to the the total flux from the envelope of Class 0 sources; however, Class 0 sources may have a substantial fraction of emission from a compact component within the central beam. The interpretation of the density structure of the outer envelope may be strongly affected when a centrally normalized radial profile is used. Only a few Class 0 sources have been observed at submillimeter wavelengths with interferometers (cf. Brown et al. 2000) resulting in few constraints on submillimeter disk fluxes. Observations of 2.7mm continuum towards L1527 with OVRO and BIMA find a flux of $\sim$ 40 mJy from a compact component (Terebey et al. 1994, Shirley et al. unpublished observation). Using a model for an active disk ($T(r) \sim r^{-0.5}$; Butner et al. 1994), we find an upper limit of 0.7 Jy at 850 μm. In this scenario, the disk accounts for up to 70% of the flux within the central beam, decreasing p by $\Delta p = -0.6$. If the disk has a steeper temperature power law ($T(r) \sim r^{-0.75}$), then the flux contribution drops to 0.1 Jy at 850 μm and the change in the best fit power law model is $\Delta p \sim -0.1$. As another example, the Choi et al. (1996) Shu77 model fits the B335 radial profile when the disk flux equals the envelope flux within the central beam (0.4 Jy at 850 μm). However, BIMA millimeter observations of B335 do not support such a high disk flux (Shirley et al., unpublished observation). Constraints on the disk flux and modeling of BIMA observations of the dust continuum towards Class 0 protostars will be presented in a future paper.

3.6 Conclusions

We have modeled seven Class 0 sources using single power law and Shu77 density distributions. Power law models suitably fit the 850 μm profiles and SED of all Class 0 sources. Five sources with circular contours are best fitted by a steep value of the power law index $p = 1.7 - 1.9$ (B335, B228, L723, IRAS03282+3035, L1448C), while two sources with aspherical emission are fitted by flatter power law indices $p = 1.1 - 1.2$ (L1527, L483). Uncertainties in the strength of the ISRF, s_{ISRF}, and beam shape limit the accuracy in the power law index to ± 0.2.

The Shu77 model from Choi et al. (1995) does not fit the B335 radial profiles. Smaller infall radii are able to fit the profiles (B335, B228, L723, IRAS03282+3035, L1448C), but the infall radius is within the central 450 μm beam, effectively making the density distribution appear like a single power law throughout the region of the envelope probed by SCUBA.

The average mass within a $120''$ aperture is $2.6 M_{\odot}$ and is reasonably consistent with virial mass estimates and observed mass estimates from Paper I and models of the initial conditions from Paper I. We find little evidence for variations in the dust opacity with radius. OH5 dust reproduces the observed spectral index on average and provides a good fit to many SEDs. In addition, it leads to masses determined from dust emission that are consistent with virial masses to a factor of 2. Heating from the ISRF is very important for correctly interpreting the temperature profile of the outer envelope of low mass star forming cores but does not significantly contribute to the total bolometric luminosity. The dust models constrain the internal luminosity of Class 0 protostars, but distances to isolated cores remain the largest uncertainty in determining accurate masses and luminosities.

Outflow cavities and asymmetrical density distributions should be modeled using higher dimensional dust modeling. In particular, L483 and L1527 have large asymmetries in the dust continuum emission that cannot be modeled with a one dimensional code.

The presence of a disk within the central beam may affect the interpretation of the best fit density distribution in the outer envelope, decreasing p by as much as $\Delta p = -0.6$.

We can now use a more realistic $n(r)$ and $T_d(r)$ in Monte Carlo molecular line radiative transfer models to test infall models (which provide $v(r)$) and the origin of line asymmetries, to test predictions of chemical models, to investigate amounts of depletion, and to improve estimates of the ionization fraction.

Our primary conclusion is that a simple power law for the density distribution fits all of the Class 0 sources that we have considered, while Shu77 models with substantial r_{inf} do not fit. Firmer conclusions await stronger constraints on the submillimeter flux from a possible disk and modeling of interferometric observations of Class 0 protostars.

Acknowledgments

We are grateful to L. Mundy for providing the computer code used for beam convolution and solution of Equation (3.1) and for stimulating discussions about the effects of disk. We thank Steve Doty for useful discussions and consistency checks of our 1D models. We thank Chad Young for his help simulating effects of a disk. We are grateful to the referee, Antonella Natta, who made many helpful suggestions. We thank the State of Texas and NASA (Grants NAG5-7203 and NAG5-10488) for support. NJE thanks the Fulbright Program and PPARC for support while at University College London and NWO and NOVA for support in Leiden. The JCMT is operated by the Joint Astronomy Centre on behalf of the Particle Physics and Astronomy Research Council of the United Kingdom, The Netherlands Organization for Scientific Research and the National Research Council of Canada.

Chapter 4

Submillimeter Dust Continuum Studies of Low and High Mass Star Formation

Abstract

Studying the physical environments of low mass and high mass cores using dust continuum emission provides important observational constraints on theoretical models of star formation. The motivation and procedure for modeling dust continuum emission is reviewed and the results of recent surveys towards low mass and high mass star forming regions are compared.

4.1 Introduction

Optically thin dust emission at submm and mm wavelengths is a powerful probe of the density and temperature structure of the outer envelope of protostars. Models of the dust continuum emission constrain theoretical predictions of the structure of forming protostellar cores. The resolution of current submm and mm bolometer arrays effectively image the outer envelope on scales of 10^3 to 10^5 AU. The basic procedures for understanding the density and temperature structure are reviewed as well as the need for radiative transfer modeling (§4.2). The density and temperature structure of the envelopes of low mass and high mass star forming regions are compared (§4.3) and important systematic effects are discussed (§4.4).

4.2 Dust Continuum Emission

The specific intensity, at impact parameter b, of optically thin dust continuum emission from a spherical envelope is given by

$$I_\nu(b) = \int_{los} B_\nu[T_d(s)]d\tau = \frac{4\mu m_H h\nu^3}{c^2}\int_b^{r_o} \frac{\kappa_\nu(r)n(r)}{\exp\left[\frac{h\nu}{kT_d(r)}\right]-1}\ \frac{rdr}{\sqrt{r^2-b^2}}\ , \qquad (4.1)$$

where s is a distance along the line-of-sight, μm_H is the mean molecular mass of gas in grams, r_o is the outer radius, $\kappa_\nu(r)$ is the dust opacity in cm^2/gram of gas, $n(r)$ is the gas particle density in cm^{-3}, and $T_d(r)$ is the dust temperature distribution (see Shirley et al. 2000). Generally, this integral must be solved numerically. However, several simplifying assumptions provide an analytical solution: (1) The dust emits in the Rayleigh-Jeans limit ($T_d >> h\nu/k$); (2) The temperature and density follow single power law distributions ($T_d(r) = T_f(r/r_f)^{-q}$ and $n(r) = n_f(r/r_f)^{-p}$); (3) The dust opacity is constant along the line of sight ($\kappa_\nu(r) = \kappa_\nu$); (4) $r_o \rightarrow \infty$. With these assumptions, the specific intensity can be expressed as a power law in the impact parameter ($I_\nu(b) \propto b^{-m}$) with the exponent $m = (p+q) - 1$. The density power law index, p, is found by fitting a power law to the observed intensity distribution and assuming a temperature power law index, q, to find $p = m + 1 - q$.

The analytical solution is not applicable at submm wavelengths (including 1.3mm) for several reasons. The dust temperature fails the Rayleigh-Jeans criterion in the outer envelopes of low mass and high mass protostars since the dust temperature drops below 20 K at large radii (i.e., only $2h\nu/k$ at 1.3mm). The temperature distribution departs from a single power law in the inner regions of the envelope where the radiative transfer becomes optically thick at UV to mid-IR wavelengths. In low mass protostars, heating from the interstellar radiation field (ISRF) becomes important in the outer envelope causing the dust temperature rise towards the outside edge of the core. The observed specific intensity profile has been convolved with a complicated beam pattern, containing multiple sidelobes, and is further modified by chopping and the detailed observing procedure (e.g., scanning). Therefore, to understand the density structure, we must model the radiative transfer to self-consistently calculate the temperature distribution, and then simulate the observing mode (beam convolution, chopping, etc.) to compare with observations.

4.3 Radiative Transfer Models

Two surveys of the deeply embedded phases of low and high mass star formation were recently carried out at the University of Texas: a SCUBA 850 and 450 μm survey of 39 nearby low mass star forming regions (Shirley et al. 2000, Shirley et al. 2002, Young et al. 2002) and a SHARC 350 micron survey of 51 high mass star forming regions associated with water masers (Mueller et al. 2002). Submm images are shown in Figure 4.1.

The normalized, azimuthally averaged, intensity profiles and spectral energy distributions (SED) of 19 sources from the SCUBA survey (3 Pre-Protostellar Cores, 7 Class 0, and 9 Class I) and 31 sources from the SHARC survey were modeled using a one dimensional radiative transfer code (Egan, Leung, & Spagna 1988) that takes into account heating from an internal source, heating from the ISRF, beam convolution, and chopping. The detailed testing of the model parameter space is discussed in Evans et al. (2001), Shirley et al. (2002), Young et al. (2002), and Mueller et al. (2002). The modeled normalized intensity profile is very sensitive to

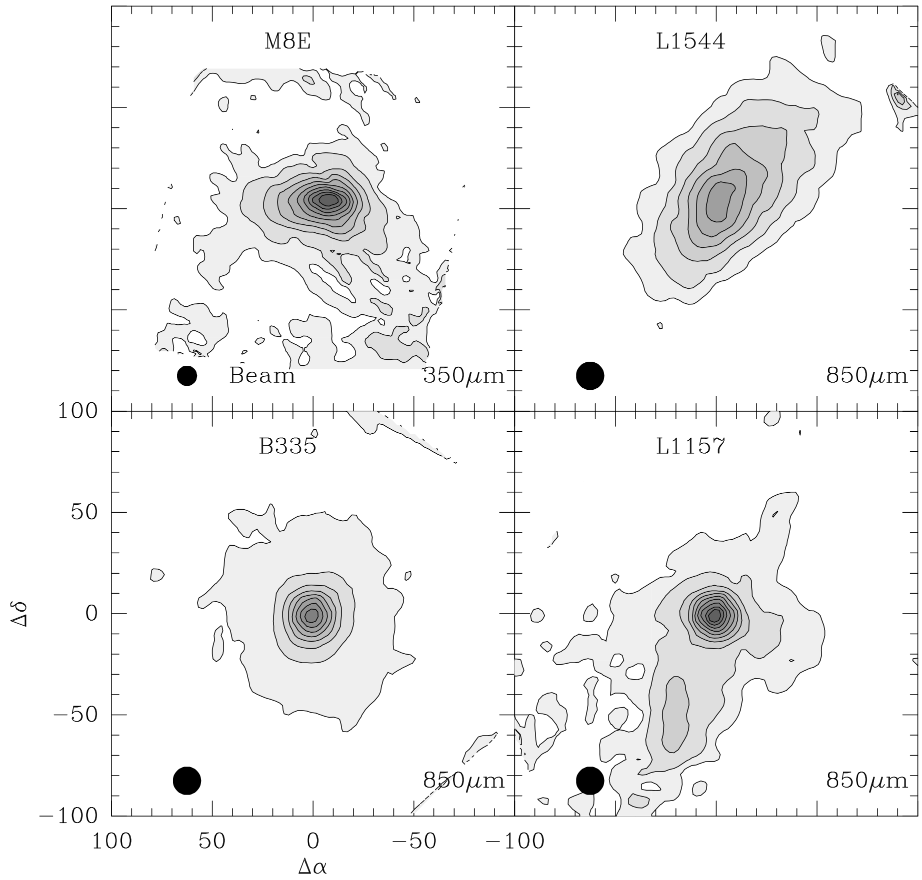

Figure 4.1 Submm images of M8E (350 μm), L1544 (850 μm), B335 (850 μm), and L1157 (850 μm) from Mueller et al. (2002) and Shirley et al. (2000).

the density structure of the core while the modeled SED is sensitive to the mass and opacity (κ_ν). Ossenkopf & Henning (1994) opacities for coagulated dust grains with thin ice mantles fit the observed SEDs of both samples well.

The temperature profile from the best fit radiative transfer models of two low mass cores (the PPC L1544 and Class 0 core B335), and a high mass core (M8E) are shown in Figure 4.2. Single power law temperature distributions do not fit the calculated profiles in the regions probed by SCUBA and SHARC. The temperature profile in a PPC (no internal luminosity source) drops towards the center as UV to near-IR radiation from the ISRF is attenuated. The temperature profile increases dramatically towards the center for sources with internal luminosity (B335, M8E). Heating from the ISRF strongly affects the shape of the temperature profile for low mass sources in the region of envelope probed by SCUBA (e.g., B335) and has some effect in regions probed by SHARC.

Sources with internal luminosity are well fitted by a single power law density profile. The histograms of best fit power-law index, p, for the low mass and high mass sample are very similar (Figure 4.3). The average p is 1.8 ± 0.4 for the high mass cores and 1.6 ± 0.4 for the low mass cores. The low mass cores may be subdivided into Class 0 and Class I objects based on the T_{bol} criterion (Class 0 typically have $T_{bol} < 70$ K, Chen et al. 1995). The average p for 10 Class 0 cores is 1.7 ± 0.30 and is 1.6 ± 0.4 for 9 Class I cores. No evidence for evolution in the shape of the density profile is seen between Class 0 and Class I cores (Young et al. 2002).

These results can be compared to other submm and mm surveys towards high mass regions (van der Tak et al. 2000 towards H_2O masers, Hatchell et al. 2000 towards UCH II regions, and Beuther et al. 2002 towards cores with IRAS colors indicative of UCH II regions) and low mass regions (Chandler & Richer 2000, Hogerheijde et al. 2000, Motte & André 2001, and Jørgensen et al. 2002). Beuther et al. (2002) observed 69 high mass cores at 1.2 mm and fit broken power laws to

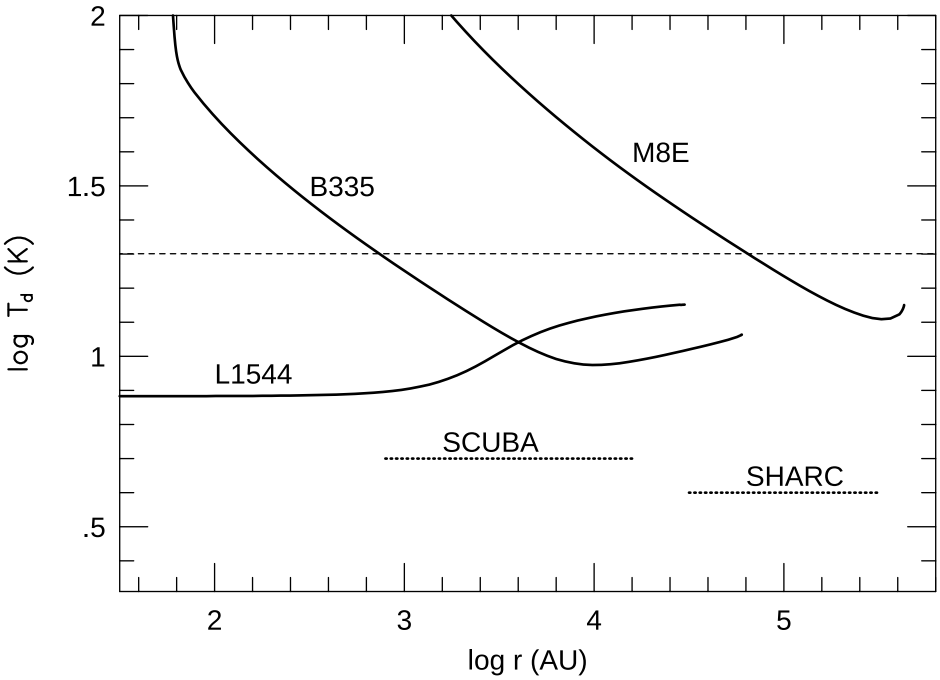

Figure 4.2 Temperature profiles from radiative transfer models of L1544 (a low mass PPC), B335 (a low mass Class 0 core), and M8E (a high mass core). The dashed lines show the range over which the SCUBA low mass survey and SHARC high mass survey probe the envelope for the median distance in each sample ($\theta_{mb}/2$ to $\theta_{chop}/2$). A dashed line marks T_d = 20 K.

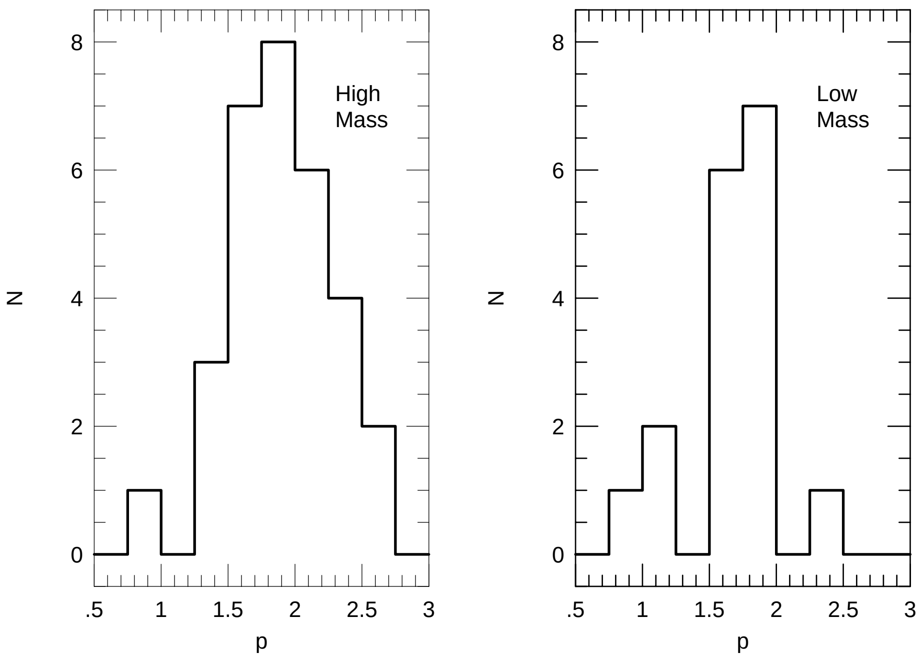

Figure 4.3 Histograms of the best fit power law model index for low mass cores (Shirley et al. 2002 & Young et al. 2002) and high mass cores (Mueller et al. 2002).

the intensity profile. The average p is 1.6 ± 0.5 in the inner regions ($\theta < 32''$), similar to the average p found by Mueller et al. There is very little overlap between high mass samples. The two sources in common agree withing uncertainties in p.

The Motte & André (2001) survey at 1.3 mm towards low mass cores gave an average p steeper by 40% for 10 sources in common. Motte & André use the analytical approximation with a single temperature power law (with q ranging from -0.2 to $+0.4$); however, detailed modeling has shown that the temperature profile changes from falling (positive q) to rising (negative q) within the regions of the envelope probed by these two surveys (Figure 4.2). Jørgensen et al. (2002) use a one dimensional model of the radiative transfer of SCUBA-observed, low mass cores, but ignore the effects of the ISRF. For 7 sources in common, their average p is flatter by 30% . If the ISRF is not included in the model, the temperature profile will continue to drop towards the outside of the core and the resulting best fit density distribution must be flatter to compensate for the colder dust grains in the outer envelope. There are significant variations between the best fit models from these surveys. The effects of the ISRF on the temperature profile can partially explain the differences and must be included in radiative transfer models (Shirley et al. 2002).

The robustness of the best fit density distribution can be tested by comparing to the density derived from near-IR extinction maps. In the case of B335, a low mass Class 0 protostar, the best fit density distribution ($n(r) \sim r^{-1.8}$, Shirley et al. 2002) agrees well with the extinction profile derived from NICMOS images (Harvey et al. 2001) for radii beyond 5000 AU. The near-IR extinction map is unable to probe regions of high extinction ($A_V > 30 - 50$ mag) due to a lack of background sources (Alves et al. 1999, Lada et al. 1999); therefore, we are unable to compare methods in the inner regions of the envelope of B335 ($r < 5000$ AU). Interferometric observations are needed at submm wavelengths to test the findings from the dust continuum models at smaller radii. Nevertheless, it is encouraging that two different methods are consistent in the outer region of the envelope. Further comparisons with NIR extinction maps are anxiously awaited.

4.4 Caveats & Future Work

There are many caveats and systematic effects that may affect the interpretation of the best fit density distribution. Several sources (e.g., L1544 and L1157) have asymmetric contours that cannot be modeled with a one dimensional radiative transfer code. Multi-dimensional radiative transfer codes are needed to model asymmetric cores.

Outflows are observed towards many of the sources in our sample. In the near-IR extinction study of B335, it was necessary to consider clearing of material in outflow cones with a $35^o - 45^o$ opening angle, while the submm emission displays no evidence of the outflow (Figure 4.1). However, several cores display emission extending along the outflow direction (e.g., L1157). A 1D radiative transfer code cannot properly model the effects of the outflow.

Pure envelope models without disks have been used in the models; however, disks may contribute a significant fraction of the flux at submm wavelengths within the central beam. Since a centrally normalized radial profile is used, the disk contribution may flatten the interpretation of the density profile (in an extreme limit) up to $\Delta p \sim -0.5$ (Shirley et al. 2002, Young et al. 2002). Strong constraints on the disk flux await observations by submm interferometers (SMA and ALMA). The potential importance the disk must not be ignored in future dust continuum studies.

The methods of modeling will become more refined with 3D radiative transport and the inclusion of asymmetries, outflows, and disks. Studies of protostellar envelopes on scales of 10 - 10^5 AU will be possible with the combination of submm interferometers and single dish bolometer cameras.

Chapter 5

A CS $J = 5 \rightarrow 4$ Mapping Survey Towards High Mass Star Forming Cores Associated with Water Masers

Abstract

We have mapped 63 regions forming high mass stars in CS $J = 5 \rightarrow 4$ using the CSO. The sample is a subset of a sample originally selected toward water masers; the selection on maser sources should favor sources in an early stage of evolution. The cores are located in the first and second galactic quadrants with an average distance of 5.3 ± 3.7 kpc and were well detected with a median peak signal-to-noise in the integrated intensity of 40. The integrated intensity of CS $J = 5 \rightarrow 4$ correlates very well with the dust continuum emission at 350 μm. For 57 sufficiently isolated cores, a well-defined angular size (FWHM) was determined. The core radius (R_{CS}), aspect ratio ($(a/b)_{obs}$), virial mass (M_{vir}), surface density (Σ), and the luminosity in the CS $J = 5 \rightarrow 4$ line (L(CS54)) are calculated. The distributions of size, virial mass, surface density, and luminosity are all peaked with a few cores skewed towards much larger values than the mean. The median values, $\mu_{1/2}$, are as follows: $\mu_{1/2}(R_{CS}) = 0.32$ pc, $\mu_{1/2}((a/b)_{obs}) = 1.20$, $\mu_{1/2}(M_{vir}) = 920$ $M_\odot$, $\mu_{1/2}(\Sigma) = 0.60$

g cm^{-2}, $\mu_{1/2}(L(\mathrm{CS54})) = 1.9 \times 10^{-2}$ L$_\odot$, and $\mu_{1/2}(L_{bol}/M_{vir}) = 165$ L$_\odot$/M$_\odot$. We find a weak correlation between CS linewidth and size, consistent with $\Delta v \sim R^{0.3}$. The linewidths are much higher than would be predicted by the usual relations between linewidth and size determined from regions of lower mass. These regions are very turbulent. The derived virial mass agrees within a factor of 2 to 3 with mass estimates from dust emission at 350 μm after corrections for the density structure are accounted for. The resulting cumulative mass spectrum of cores above 1000 M$_\odot$ can be approximated by a power law with a slope of about -0.9, steeper than that of clouds measured with tracers of lower density gas. and close to that for the total masses of stars in OB associations. The median turbulent pressures are comparable to those in UCH II regions, and the pressures at small radii are similar to those in hypercompact H II regions ($P/k \sim 10^{10}$ Kcm^{-3}). The filling factors for dense gas are substantial, and the median abundance of CS is about 10^{-9}. The ratio of bolometric luminosity to virial mass is much higher than the value found for molecular clouds as a whole, and the correlation of luminosity with mass is tighter.

5.1 Introduction

Many, possibly most, stars form in clustered environments with massive stars (see Carpenter 2000). Regions forming massive stars are the only detectable manifestations of star formation in other galaxies. Understanding the formation of massive stars is crucial to an improved understanding of galaxy formation. Despite all these motivations, our understanding of the conditions in which massive stars form is quite primitive. In contrast to the well-developed theories for isolated, low-mass star formation (e.g., Shu, Adams, & Lizano 1987), theories dealing with massive star formation are less developed. While promising theoretical work has been done (e.g., Bonnell et al. 1997, Bonnell, Bate, & Zinnecker 1998, Klessen 2001, McKee & Tan 2002a) the theoreticians are hampered by a lack of systematic information on the properties of the regions. Many detailed observational studies of individual regions have been made, but the field has lacked statistical information based on large samples analyzed with uniform methods.

One approach to this problem has been to collect a unified data base for a well-characterized sample. Most work of this kind has focused on samples selected to have ultra-compact H II regions or *IRAS* colors similar to those of cores with UCH II regions (Wood & Churchwell 1989, Sridharan et al. 2002). The sample studied by Sridharan et al. and Beuther et al. (2002) used *IRAS* colors, but then selected against H II regions by choosing sources with low emission in the radio continuum in an attempt to identify early phases. We have sought to study an early phase by selecting sources based on their water maser emission (Cesaroni et al. 1988). A survey of a large sample of water masers revealed that emission in the CS $J = 7 \rightarrow 6$ transition was common in this sample (Plume et al. 1992; hereafter Paper I). Detection of this highly excited line suggested high densities and temperatures, but additional transitions were needed to pin down the conditions. A multi-transition study of CS lines showed that the mean density, $n(\mathrm{cm}^{-3})$, of the sample of 71 sources was $\langle n \rangle = 7.9 \times 10^5$ cm^{-3} (Plume et al. 1997; hereafter Paper II). That study also made cross-scans of 25 sources to estimate sizes, masses, and star formation activities, indicated by the luminosity to mass ratio (L_{bol}/M_{vir}), where the mass referred to the dense gas probed by CS.

In the current paper, we present fully sampled maps in the CS $J = 5 \rightarrow 4$ line of a much larger sample (63 sources) than was mapped in Paper II. These data should provide a much firmer statistical foundation for determining the conditions at early stages of the formation of massive stars. That statistical data is presented here. We have made similar maps of CS $J = 7 \rightarrow 6$ and dust continuum emission for a subset of these sources. These data will allow a more detailed analysis of the density and temperature gradients, similar to that accomplished by van der Tak et al. (2000) on a small subset of these sources. The analysis of the dust continuum data (Mueller et al. 2002b) and combined models of CS excitation (Knez et al. 2002b) will be presented separately. A summary of early results of this work can be found in Evans et al. (2002), Shirley et al. (2002), Mueller et al. (2002a), Knez et al. (2002a), and Lee et al. (2002).

5.2 Sources and Observations

Sixty-three high mass star forming cores were mapped in the CS $J = 5 \rightarrow 4$ transition between September 1996 and July 1999 at the Caltech Submillimeter Telescope (CSO). Fifty-seven cores were observed in the $C^{34}S$ $J = 5 \rightarrow 4$ transition and nine cores were observed in the ^{13}CS $J = 5 \rightarrow 4$ transition towards the $C^{32}S$ peak position between July 2001 and June 2002 at the CSO. We employ the conventional notation that, unless noted otherwise, the isotope is the most common one: thus CS means $^{12}C^{32}S$.

5.2.1 The Sample

All of the objects observed are listed in Table 5.1 and 5.2. Nearly all of the cores are located in the first and second quadrant (Figure 5.1). Sources were selected from Paper I and Paper II based on the strength of their CS $J = 7 \rightarrow 6$ emission with each source detected at the 1 K T_R^* level (Paper I). Within this criterion, we made some effort to include sources with weaker emission than those in the sample mapped by Plume et al. (1997) in order to have a sample less biased toward the largest and most massive cores. The center of each map was the water maser position from the catalog of Cesaroni et al. (1988). This sample extends the sample of 25 cores mapped in Paper II by including less massive cores and fully mapping each core.

The sources were distributed from 0.7 kpc to 15.6 kpc from the sun (Figure 5.1). The distances were determined from an extensive literature search (See Table 5.3 and 5.4 for distance references). Photometric distances were used whenever possible, but distance estimates to many cores are based on kinematical distances using the rotation curve of Fich et al. (1989). The average distance of the sample of 63 cores is 5.3 ± 3.7 kpc while the median distance is 4.0 kpc. The distribution is

Table 5.1

Observed Sources

Source	α (1950.0) (^{h} ^{m} ^{s})	δ (1950.0) ($^\circ$ $'$ $''$)	Date CS Mapped
G121.30+0.66	00 33 53.3	+63 12 32	12/97
G123.07-6.31	00 49 29.2	+56 17 36	12/97
W3(OH)	02 23 17.3	+61 38 58	12/96
G135.28+2.80	02 39 31.0	+62 44 16	12/97
S231	05 35 51.3	+35 44 16	12/96
S235	05 37 31.8	+35 40 18	12/96
S241	06 00 40.9	+30 14 54	12/97
S252A	06 05 36.5	+20 39 34	12/97
S255	06 09 58.3	+18 00 12	12/96
RCW142	17 47 04.5	−28 53 42	04/97
W28A2(1)	17 57 26.8	−24 03 54	09/96
M8E	18 01 49.1	−24 26 57	04/97
G9.62+0.10	18 03 16.0	−20 32 01	09/96
G8.67-0.36	18 03 18.6	−21 37 59	04/97
W31	18 05 40.4	−19 52 21	09/96
G10.6-0.4	18 07 30.7	−19 56 28	09/96
G12.42+0.50	18 07 56.4	−17 56 37	04/97
G12.89+0.49	18 08 56.3	−17 53 09	04/97
G12.2-0.1	18 09 43.7	−18 25 09	09/96
W33cont	18 11 18.3	−17 56 21	10/96
G13.87+0.28	18 11 41.5	−16 16 34	07/98
W33A	18 11 44.0	−17 53 09	04/97
G14.33-0.64	18 16 00.8	−16 49 06	04/97
G19.61-0.23	18 24 50.1	−11 58 22	09/96
G20.08-0.13	18 25 22.6	−11 30 45	07/98
G23.95+0.16	18 31 40.8	−16 16 34	07/98
G24.49-0.04	18 33 22.8	−07 33 54	04/97
W42	18 33 30.3	−07 14 42	04/97
G28.86+0.07	18 41 07.9	−03 38 41	07/98
W43S	18 43 26.7	−02 42 40	07/98
G31.41+0.31	18 44 59.5	−01 16 07	04/97

Table 5.2

Observed Sources Continued

Source	α (1950.0) (^{h} ^{m} ^{s})	δ (1950.0) ($^{\circ}$ $'$ $''$)	Date CS Mapped
W43Main3	18 45 11.2	−01 57 57	07/98
G31.44-0.26	18 46 57.5	−01 32 33	04/97
G32.05+0.06	18 47 02.0	−00 49 19	07/98
G32.80+0.20A/B	18 47 57.3	−00 05 28	07/98
W44	18 50 46.1	+01 11 11	07/98
S76E	18 53 45.6	+07 49 16	07/98
G35.58-0.03	18 53 51.4	+02 16 29	10/96
G35.20-0.74	18 55 40.8	+01 36 30	07/98
W49N	19 07 49.8	+09 01 17	10/96
W49S	19 07 58.2	+09 00 03	07/99
OH43.80-0.13	19 09 31.2	+09 30 51	07/98
G45.07+0.13	19 11 00.3	+10 45 42	09/96
G48.61+0.02	19 18 13.1	+13 49 44	07/98
W51W	19 20 53.3	+14 20 47	07/99
W51M	19 21 26.2	+14 24 36	10/96
G59.78+0.06	19 41 04.2	+23 36 42	07/98
S87	19 44 14.0	+24 28 10	09/96
S88B	19 44 42.0	+25 05 30	07/96
K3-50	19 59 50.1	+33 24 17	06/97
ON1	20 08 09.9	+31 22 42	07/98
ON2S	20 19 48.9	+37 15 52	07/98
ON2N	20 19 51.8	+37 17 01	07/98
S106	20 25 32.8	+37 12 54	07/98
W75N	20 36 50.5	+42 27 01	07/98
DR21S	20 37 13.8	+42 08 52	07/99
W75(OH)	20 37 14.1	+42 12 12	07/99
G97.53+3.19	21 30 37.0	+55 40 36	07/98
CepA	22 54 19.2	+61 45 44	07/99
BFS11-B	21 41 57.6	+65 53 17	12/97
S158	23 11 36.1	+61 10 30	12/97
S157	23 13 53.1	+59 45 18	12/97

TABLE 5.3
KNOWN SOURCE PROPERTIES

Source	Dist. (kpc)	Dist. Ref.	D_g (kpc)	UCH II [a] R_{2cm} (pc)	UCH II Ref.
G121.30+0.66	1.2	1	9.2	...	...
G123.07-6.31	2.2	2	9.9	...	...
W3(OH)	2.4	3	10.3	0.023	19
G135.28+2.80	7.4	1	14.7	...	...
S231	2.3	2	10.8	...	...
S235	1.6	2	10.1	...	...
S241	4.7	2	13.2	...	...
S252A	1.5	2	10.0	...	...
S255	1.3	4	9.8	0.013	20
RCW142	2.0	5	6.5	...	21
W28A2(1)	2.6	5,6	5.9	0.052	14
M8E	1.8	2	6.7	...	...
G9.62+0.10	7.0	7	3.0	...	22
G8.67-0.36	8.5	8	4.1	0.033	14
W31	12.0	4	4.0	0.047	23
G10.6-0.4	6.5	9	2.4	0.060	14
G12.42+0.50	2.1	10	6.5	0.011	24
G12.89+0.49	3.5	8	5.1	...	...
G12.2-0.1	16.3	11	5.7	0.266	14
W33cont	4.1	9	4.6	...	...
G13.87+0.28	4.4	12	4.4	0.405	23
W33A	4.5	5	4.2	...	...
G14.33-0.64	2.6	8	6.0	...	...
G19.61-0.23	4.0	4	4.9	0.122	14
G20.08-0.13	3.4	7	5.4	0.053	14
G23.95+0.16	5.8	9	4.0	0.316	14
G24.49-0.04	3.5	1	5.5	...	...
W42	9.1	13	3.8	...	...
G28.86+0.07	8.5	5	4.2	...	...
W43S	8.5	4,14	4.4	0.276	14
G31.41+0.31	7.9	12	4.5	0.050	14

[a] R_{2cm} is the size of the UCH II region measured at 2 cm.

REFERENCES.—1. R_N Paper I 1992, 2. Blitz 1982, 3. Harris 1976, 4.Genzel 1977, 5. Braz 1983, 6. Chini 1986, 7. Hofner 1996, 8. Val'tts 2000, 9. Solomon 1987, 10. Zinchecnko 1994, 11. Hunter 2000, 12. Churchwell 1990, 13. Downes 1980, 14. Wood 1989, 15. Brand 1993, 16. Wink 1982, 17. Zhou 1996, 18. Plume 1997, 19. Wilner 1995, 20. Kurtz 1994, 21. Walsh 1998, 22. Olmi 1999, 23. Hatchell 2000, 24. Jaffe 1984, 25. Bronfman 1996

TABLE 5.4
KNOWN SOURCE PROPERTIES CONTINUED

Source	Dist. (kpc)	Dist. Ref.	D_g (kpc)	UCH II [a] R_{2cm} (pc)	UCH II Ref.
W43Main3	6.8	4	4.4	...	...
G31.44-0.26	10.7	9	5.6	0.036	20
G32.05+0.06	8.5	9	4.7	...	...
G32.80+0.20A/B	15.6	13	9.6	0.091	20
W44	3.7	9	5.8	0.061	14
S76E	2.1	1	7.0	...	...
G35.58-0.03	3.5	13	6.0	0.022	20
G35.20-0.74	3.3	9	6.1	...	...
W49N	14.0	4	9.7	0.010	26
W49S	14.0	4	9.7	...	...
OH43.80-0.13	2.7	13	6.8	0.008	20
G45.07+0.13	9.7	13	7.1	0.038	14
G48.61+0.02	11.8	1	8.9	...	...
W51W	7.0	17	6.6	...	...
W51M	7.0	17	6.6	0.207	27
G59.78+0.06	2.2	1	7.6	...	...
S87	1.9	15	7.6	0.010	20
S88B	2.1	2	7.7	0.008	14
K3-50	9.0	4	10.1	...	...
ON1	6.0	1	8.5	0.020	20
ON2S	5.5	1	8.9	...	...
ON2N	5.5	1	8.9	0.075	14
S106	4.1	16	8.5	0.012	20
W75N	3.0	4	8.6	...	...
DR21S	3.0	4	8.6	0.045	20
W75(OH)	3.0	4	8.6	...	...
G97.53+3.19	7.9	1	12.3	...	...
CepA	0.73	17	8.8	...	...
BFS11-B	2.0	5	9.2	...	...
S158	2.8	2	9.9	...	...
S157	2.5	2	9.7	0.099	20

[a] R_{2cm} is the size of the UCH II region measured at 2 cm.

REFERENCES.—1. R_N Paper I 1992, 2. Blitz 1982, 3. Harris 1976, 4.Genzel 1977, 5. Braz 1983, 6. Chini 1986, 7. Hofner 1996, 8. Val'tts 2000, 9. Solomon 1987, 10. Zinchecnko 1994, 11. Hunter 2000, 12. Churchwell 1990, 13. Downes 1980, 14. Wood 1989, 15. Brand 1993, 16. Wink 1982, 17. Zhou 1996, 18. Plume 1997, 19. Wilner 1995, 20. Kurtz 1994, 21. Walsh 1998, 22. Olmi 1999, 23. Hatchell 2000, 24. Jaffe 1984, 25. Bronfman 1996, 26. Dreher 1984, 27. Scott 1978 strongly peaked between 2 to 4 kpc. The sources at large distances from us are all in the first quadrant. The distances can be converted into galactocentric distances, D_g, using a distance of 8.5 kpc to the solar circle. The result is an average distance of 7.3 ± 2.6 kpc and a median distance of 6.8 kpc from the galactic center. Most (64%) of the cores are located between 5 and 10 kpc from the galactic center, 25% of the cores are less than 5 kpc from the galactic center, and 11% are beyond 10 kpc (Figure 5.1). This sample is characterized by regions near the solar galactocentric distance within the galaxy.

There is very little overlap between previous CS studies ($J_u \geq 2$) selected towards water maser positions: 3 sources in common (Zinchenko et al. 1994); 0 sources in common (Zinchenko et al. 1995); 0 sources in common (Juvela 1996); and 8 sources in common (Zinchenko et al. 1998). There is slightly more overlap of sources selected towards UCH II regions or IRAS colors indicative of UCH II regions: 24 sources in common (Bronfman et al. 1996); 6 source in common (Olmi & Cesaroni 1999); and 3 sources in common (Beuther et al. 2002). Thirty-two of our sources were included in the CS $J = 1 \rightarrow 0$ and NH_3 survey of Anglada et al. (1996); however, we trace a denser gas component with the $J = 5 \rightarrow 4$ transition.

5.2.2 Observational Method

The 230 GHz sidecab receiver with a 50 MHz AOS backend was used for all observations (Kooi et al. 1992, Kooi et al. 1998). The average velocity resolution was 0.119 km s^{-1}. The observing parameters and conditions are listed in Table 5.5. The standard chopper calibration method was used to measure T_A^* (Penzias & Burrus 1973). The beam size (θ_{mb}) at 244 GHz was 24$''$.5 for the September 1996 through July 1998 observations. The secondary edge taper was increased from -5.2 dB to -8.5 dB in August 1998 (Chamberlin, R. priv. comm. 2001; see Kooi, J. 1998) resulting in a larger beam of 30$''$.5 at 244 GHz (see Table 3). Only five sources were

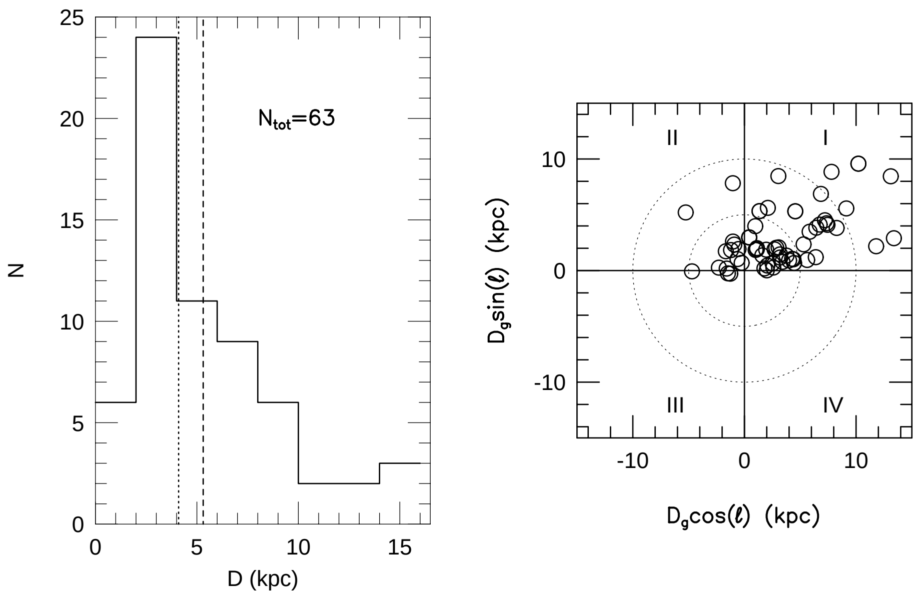

Figure 5.1 Histogram of distances and the position of the 63 mapped cores in the galactic plane. The histogram is binned at 2 kpc. The median (dotted line) and mean (dashed line) are shown. In the galactic coordinates plot, the Sun is at the center. Since the observations were performed at the CSO in the northern hemisphere, almost all of the cores are in the first and second quadrant. The circles represent distances of 5 kpc and 10 kpc from the Sun.

TABLE 5.5
CSO OBSERVATIONS 1996-2002

UT Date	Transition	ν (GHz)	θ_{MB} ($''$)	η_{MB}	Pointing (σ_{AZ}'' ,σ_{ZA}'')
09/96	CS $J = 5 \rightarrow 4$	244.9355680	24.5	0.56	(3.8,2.7)
10/96	CS $J = 5 \rightarrow 4$	244.9355680	24.5	0.56	(3.8,2.7)
12/96	CS $J = 5 \rightarrow 4$	244.9355680	24.5	0.54	(1.9,3.2)
04/97	CS $J = 5 \rightarrow 4$	244.9355680	24.5	0.56	(6.6,3.2)
06/97	CS $J = 5 \rightarrow 4$	244.9355680	24.5	0.58	(2.0,5.2)
12/97	CS $J = 5 \rightarrow 4$	244.9355680	24.5	0.55	(4.4,5.2)
07/98	CS $J = 5 \rightarrow 4$	244.9355680	24.5	0.57	(6.7,2.7)
12/98	$C^{34}S$ $J = 5 \rightarrow 4$	241.0161940	31.0	0.66	(2.4,3.4)
	^{13}CS $J = 5 \rightarrow 4$	231.2209960	32.5	0.66	
07/99	CS $J = 5 \rightarrow 4$	244.9355680	30.5	0.64	(5.6,5.4)
07/01	$C^{34}S$ $J = 5 \rightarrow 4$	241.0161940	31.0	0.73	(3.0,3.4)
	^{13}CS $J = 5 \rightarrow 4$	231.2209960	32.5	0.73	
01/02	$C^{34}S$ $J = 5 \rightarrow 4$	241.0161940	31.0	0.54	(12.7,3.8)
06/02	$C^{34}S$ $J = 5 \rightarrow 4$	241.0161940	31.0	0.61	(4.2,4.8)
	^{13}CS $J = 5 \rightarrow 4$	231.2209960	32.5	0.59	

mapped using the larger beam size (W49S, W51W, DR21S, W75(OH), and CepA).

Observations towards the peak of the CS $J = 5 \rightarrow 4$ position were made in $C^{34}S$ $J = 5 \rightarrow 4$ and ^{13}CS $J = 5 \rightarrow 4$. All of the observations were made after the secondary edge taper was increased. The beam size at 241 GHz and 231 GHz was $31\farcs0$ and $32\farcs5$ respectively.

Main beam measurements, η_{mb}, were made on planets during each observing run. The average η_{mb} increased by 20% after the secondary edge taper was increased, excluding the last two observing sessions (01/02 and 06/02) where mirror alignment problems decreased the main beam efficiency. Average system temperatures ranged from 191 K to 590 K during the observations. Pointing was checked every hour using planets. The average standard deviation in azimuth and zenith angle pointing were $5''$ and $4''$ respectively for all of the observations, resulting in a $6''$ pointing uncertainty. These errors, adding to about one-quarter beam, are upper limits to the actual pointing errors because they were mostly slow drifts over the time of a run and pointing was corrected by repeated measurements during each night.

The cores were mapped using the On-The-Fly (OTF) mapping technique (e.g., Mangum et al. 2000) with a square grid in RA-DEC coordinates, oversampled at $10''$ resolution. The scan rate was set at $2''$ per second to provide 5 s of integration time per spectrum. On some occasions, the maps were repeated for higher signal-to-noise. The map was extended until the CS $J = 5 \rightarrow 4$ line was not detected or negligible compared to the peak.

5.3 Results

While there is a wealth of information on velocity structure in this data set, we focus on the integrated intensity maps in this paper. One core, W49N, clearly shows two velocity components that were analyzed separately (see below). For an example of interesting velocity structure in the S235 region, see Lee et al. (2002).

The integrated intensity of the CS $J = 5 \rightarrow 4$ transition was calculated using,

$$I(T_A^*) = \int_{v_1}^{v_2} T_A^* dv \tag{5.1}$$

$$\sigma^2_{I(T_A^*)} = \left\langle \sqrt{\Delta v_{line} \delta v_{chan}} \sigma_{T_A^*} \right\rangle^2_{map} + \left(\frac{\Delta v_{line}}{\Delta v_{lft} + \Delta v_{rt}} \right)^2 \sigma^2_{I_{base}} \tag{5.2}$$

where $\Delta v_{line} = v_2 - v_1$ is a velocity interval that includes the entire line (as distinct from the FWHM of the line), Δv_{lft} and Δv_{rt} are the velocity intervals of the left and right baselines, δv_{chan} is spectrometer velocity resolution, and $\sigma_{I_{base}}$ is the standard deviation of the integrated intensity of the total baseline ($\Delta v_{lft} + \Delta v_{rt}$) calculated over all of the spectra in the map. The first term in the integrated intensity error is the theoretical error and assumes no deviation from a linear baseline. The second term in the integrated intensity error compensates for residual variations in the baseline after a linear baseline was removed. This average error in the integrated intensity is added in quadrature to the average of the theoretical error for the integrated intensity, calculated for each spectrum in the map. The theoretical error (first term) typically dominates. The integrated intensity is placed on the T_R^* scale (Kutner & Ulich 1981) by dividing Equation (1) by the main beam efficiency appropriate for the night the object was observed, $I(T_R^*) = I(T_A^*)/\eta_{mb}$. An assumed error in the main beam efficiency (10%) was propagated into the uncertainty in $I(T_R^*)$.

Contour maps of integrated intensity are shown in Figures 5.2–5.8. The average extent of the maps is $\pm 50''$, but larger maps were made where necessary. The lowest contour is at least $2\sigma_I$ and typical contour intervals are 10% of the peak intensity. The cores were well detected with a median peak-signal-to-noise of 40 and peak integrated intensities that range from 5.5 to 208 K km s^{-1}. The peak integrated intensity correlates well ($r = 0.85$) with the submillimeter flux at 350 μm (Figure 5.9) from the survey of Mueller et al. (2002); a fit to the logarithms indicates a relationship that is nearly linear: $\log I(T_R^*) = (-0.60 \pm 0.01) + (0.92 \pm 0.05) \log S_{350\mu\mathrm{m}}$. Objects that are bright at 350 μm are also strong emitters in the CS $J = 5 \rightarrow 4$ line. Since the 350 μm dust continuum is optically thin, it is good tracer of mass along each line-of-sight. The strong correlation between $I(T_R^*)$ and $S_{350\mu\mathrm{m}}$ confirms that high J lines of CS are excellent tracers of dense gas.

The CS centroid is generally consistent with the water maser peak with a median centroid distance of $8''$; only eight cores (13%) have CS centroids greater than $\theta_{mb}/2$ away from the water maser position. UCH II regions are marked with a plus in the images. Some of the cores contain multiple UCH II regions (see Conti & Blum 2002, W49N region), but only the closest UCHH II region to the water maser peak is marked. Nearly half of the regions mapped (31, 49%) contain an UCH II region. The median distance between the CS centroid and UCH II regions was $8''$, less than one third of the beam FWHM and larger than the average pointing uncertainty. The peak CS emission is directly associated with the UCH II region in

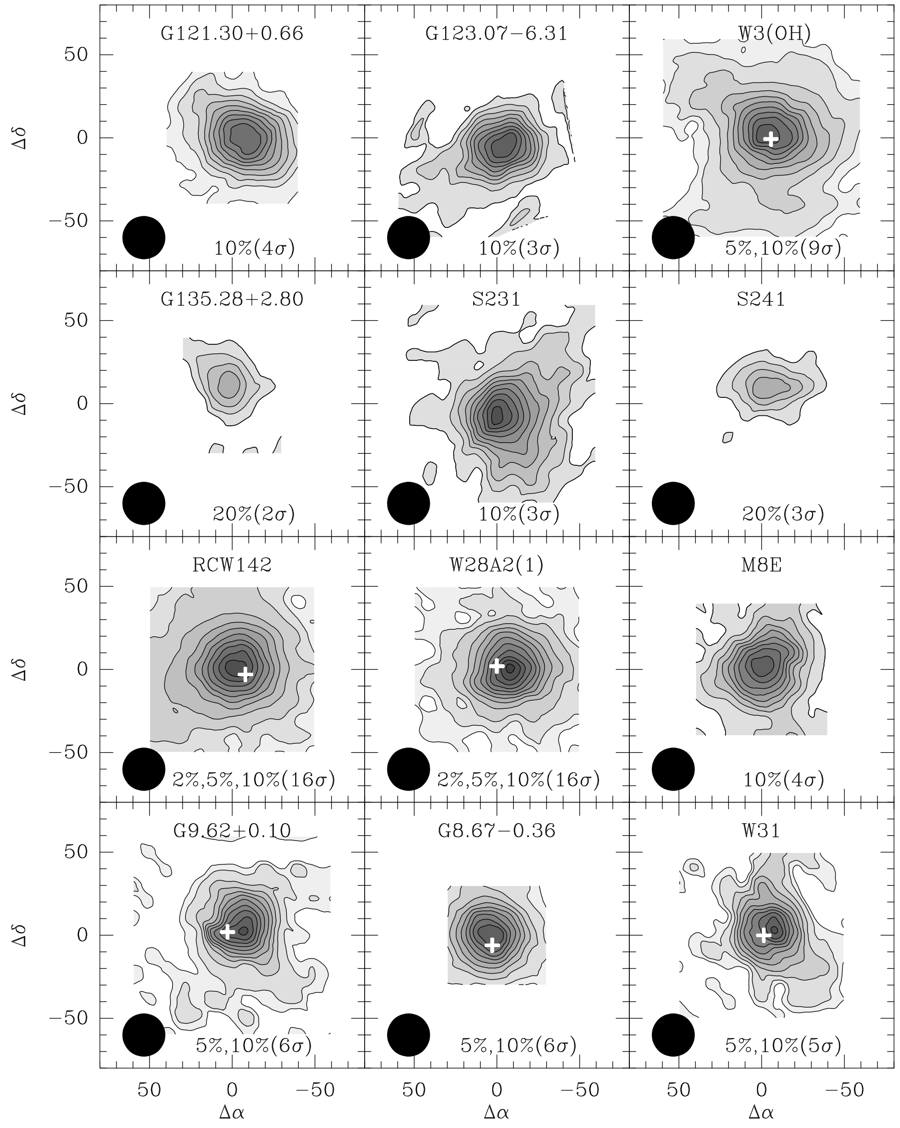

Figure 5.2 Contour maps of CS $J = 5 \rightarrow 4$ integrated intensity for isolated cores. The beam is shown in the lower left corner. The contour levels are indicated at the bottom of each panel. For instance, $5\%, 10\%(5\sigma)$ means the first contour is 5% the peak intensity, the next contour is 10% the peak intensity, and the contour interval is 10% or 5σ. The plus sign marks the location of an UCH II region. The water maser is at (0,0).

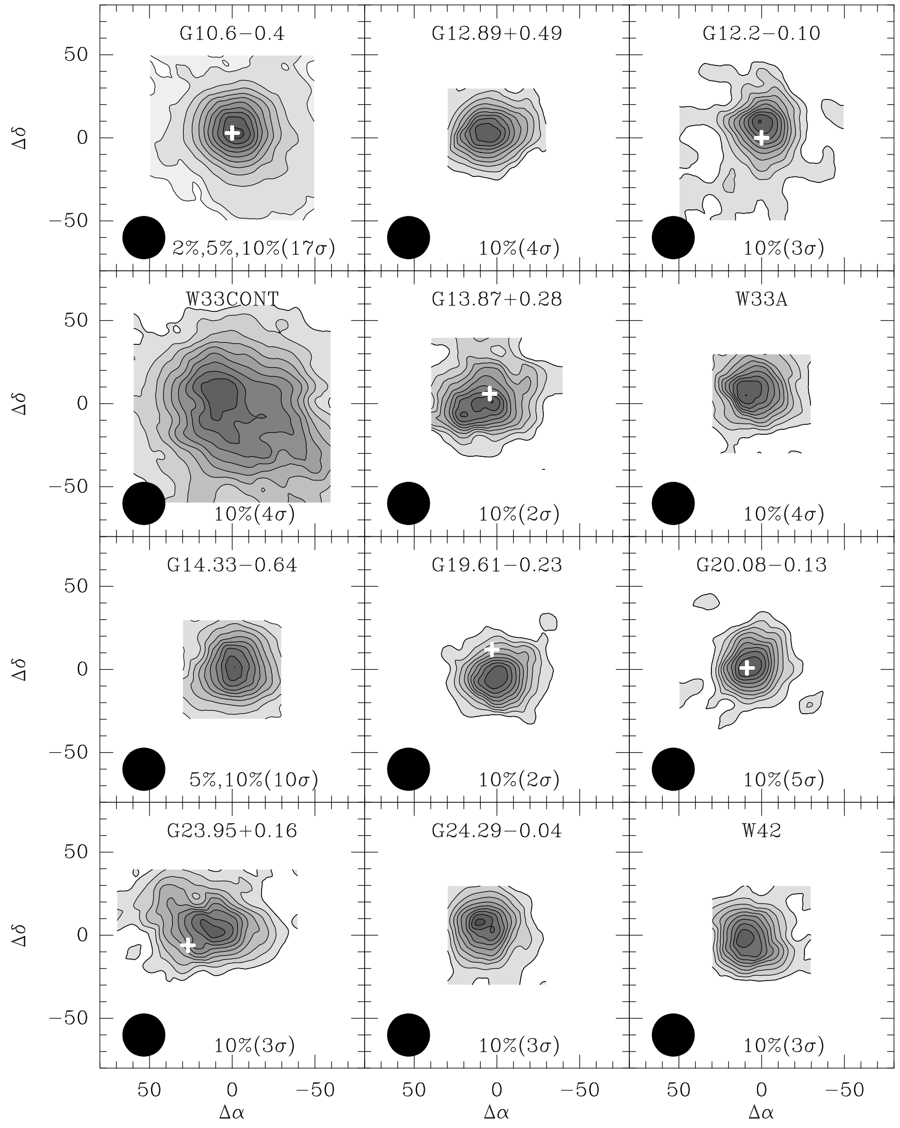

Figure 5.3 Contour maps of CS $J = 5 \rightarrow 4$ integrated intensity for isolated cores. The beam is shown in the lower left corner. The contour levels are indicated at the bottom of each panel. For instance, $5\%, 10\%(5\sigma)$ means the first contour is 5% the peak intensity, the next contour is 10% the peak intensity, and the contour interval is 10% or 5σ. The plus sign marks the location of an UCH II region. The water maser is at (0,0).

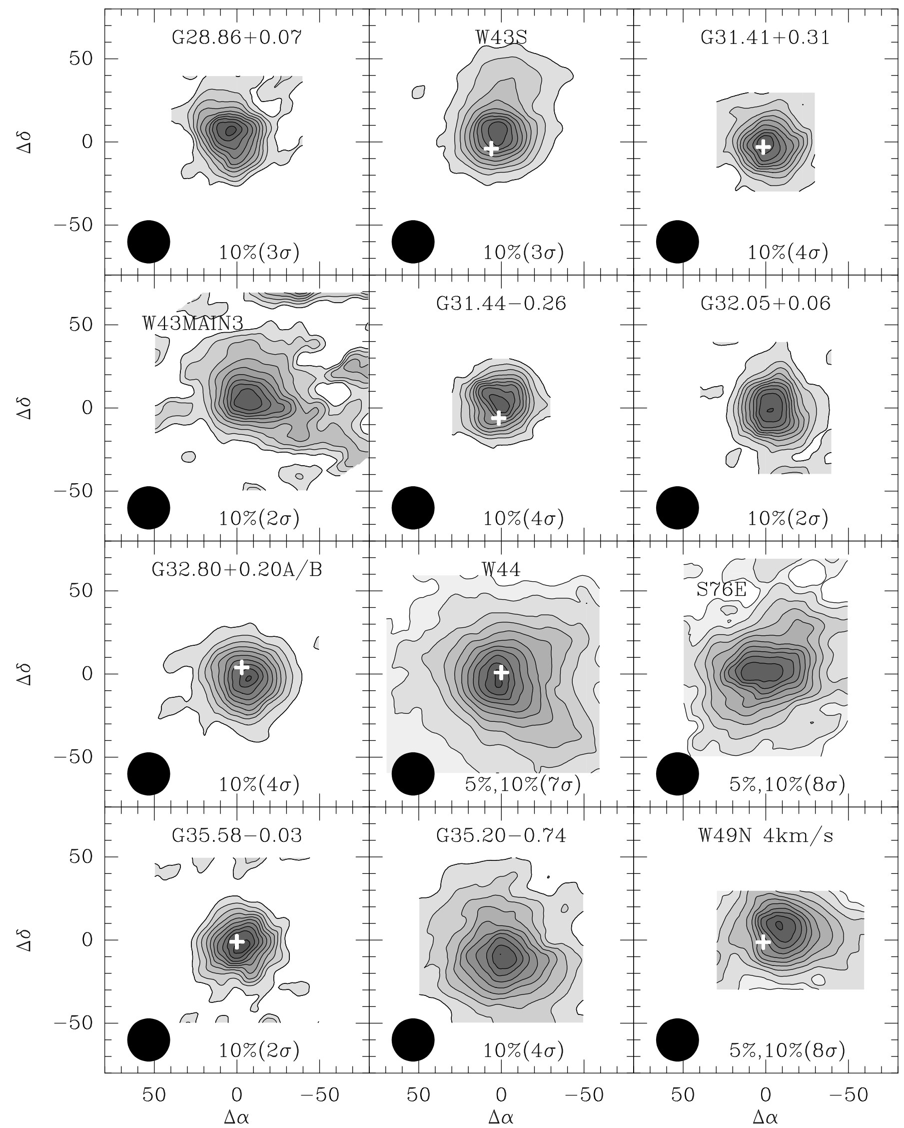

Figure 5.4 Contour maps of CS $J = 5 \rightarrow 4$ integrated intensity for isolated cores. The beam is shown in the lower left corner. The contour levels are indicated at the bottom of each panel. For instance, $5\%, 10\%(5\sigma)$ means the first contour is 5% the peak intensity, the next contour is 10% the peak intensity, and the contour interval is 10% or 5σ. The plus sign marks the location of an UCH II region. The water maser is at (0,0).

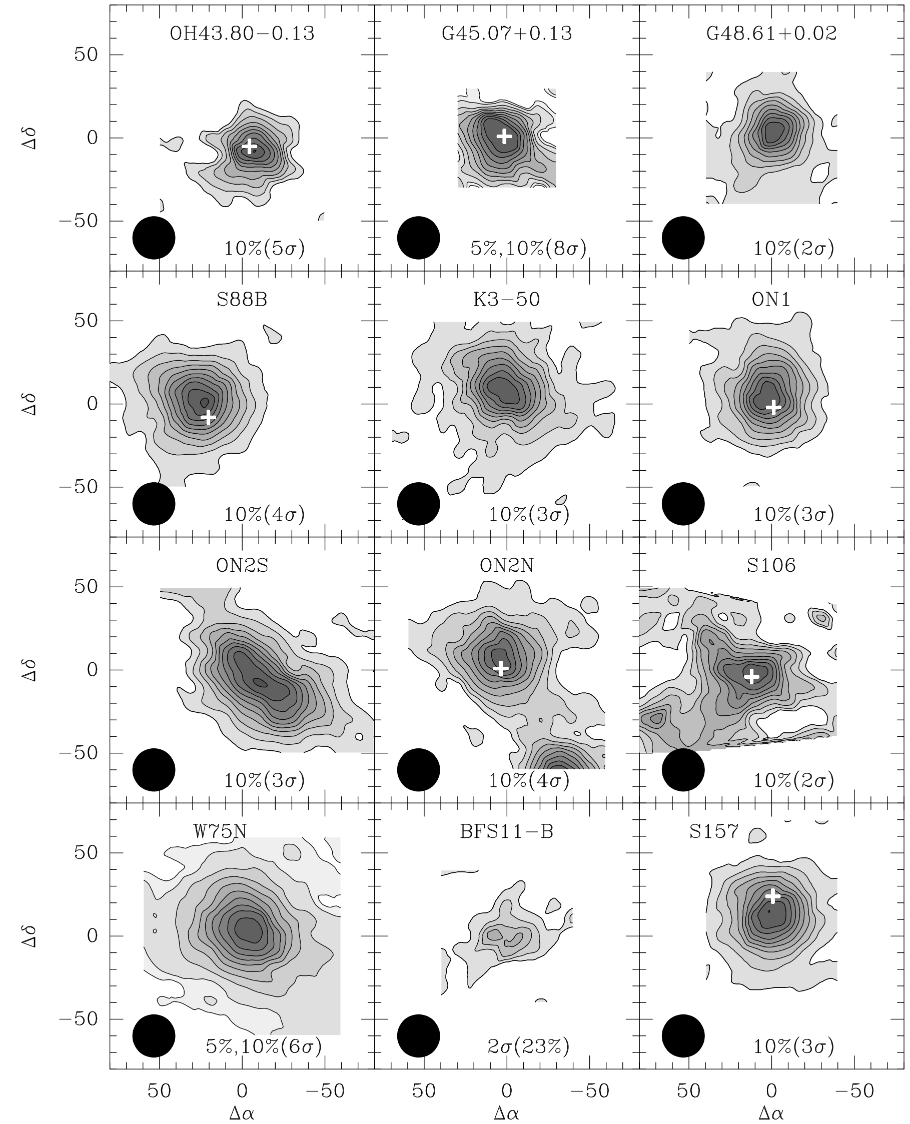

Figure 5.5 Contour maps of CS $J = 5 \rightarrow 4$ integrated intensity for isolated cores. The beam is shown in the lower left corner. The contour levels are indicated at the bottom of each panel. For instance, $5\%, 10\%(5\sigma)$ means the first contour is 5% the peak intensity, the next contour is 10% the peak intensity, and the contour interval is 10% or 5σ. The plus sign marks the location of an UCH II region. The water maser is at (0,0).

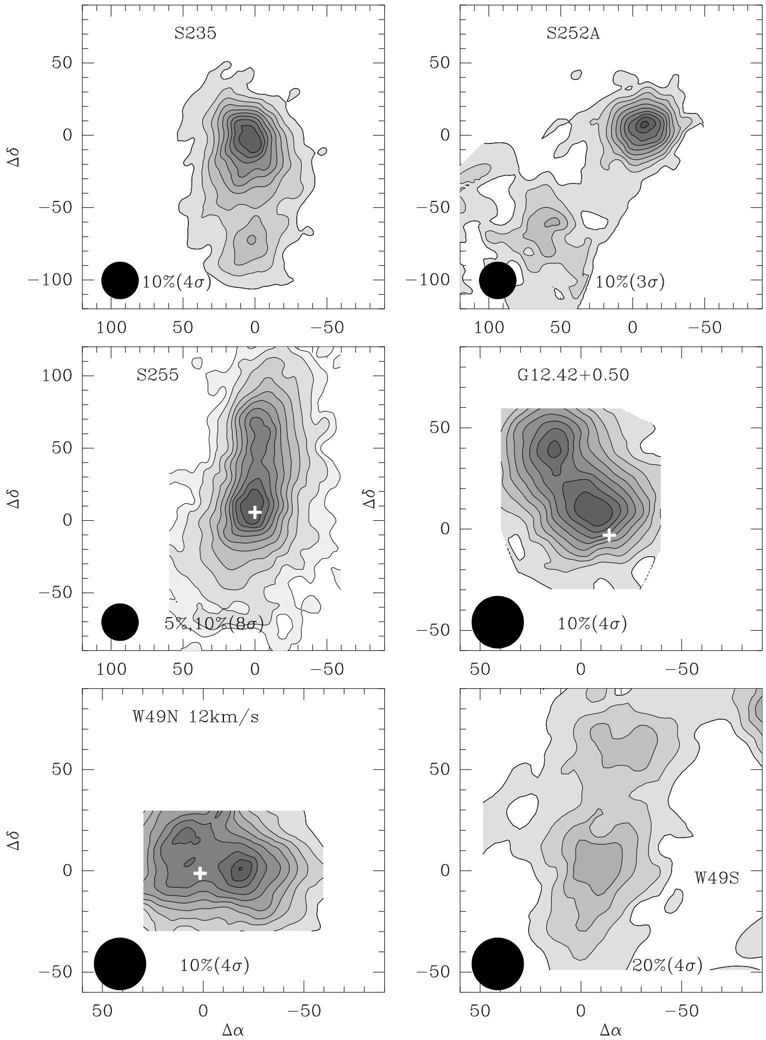

Figure 5.6 Contour maps of CS $J = 5 \rightarrow 4$ integrated intensity for multiple cores. The beam is shown in the lower left corner. The contour levels are indicated at the bottom of each panel. For instance, $5\%, 10\%(5\sigma)$ means the first contour is 5% the peak intensity, the next contour is 10% the peak intensity, and the contour interval is 10% or 5σ. The plus sign marks the location of an UCH II region. The water maser is at (0,0).

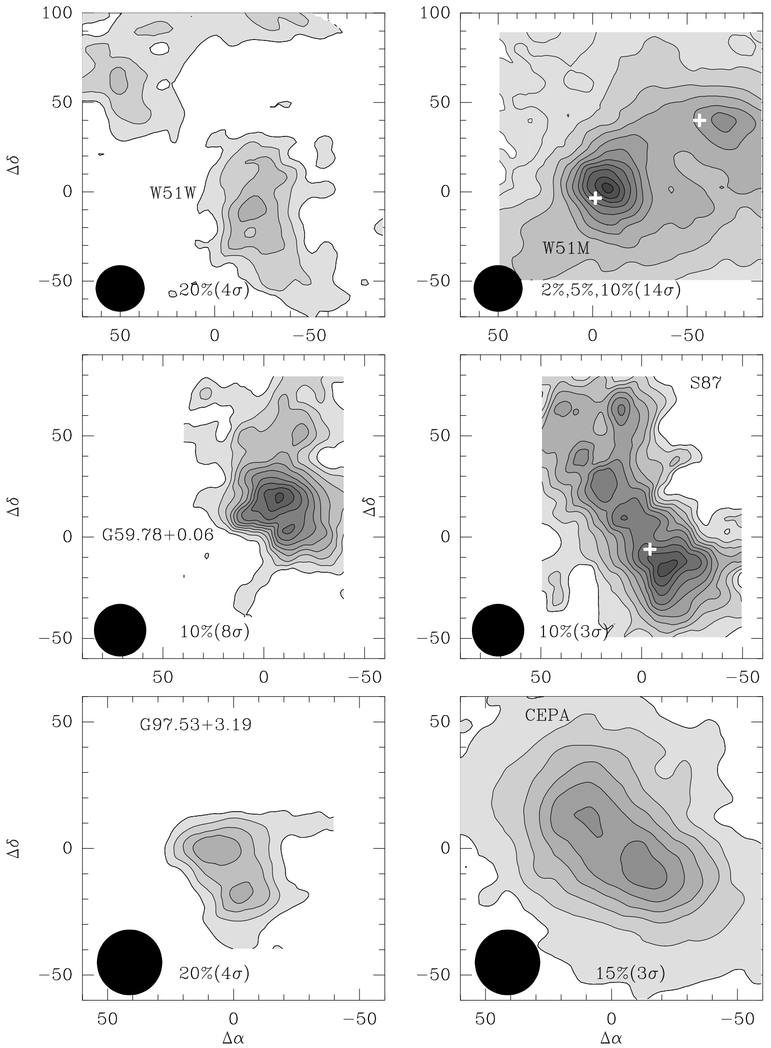

Figure 5.7 Contour maps of CS $J = 5 \rightarrow 4$ integrated intensity for multiple cores. The beam is shown in the lower left corner. The contour levels are indicated at the bottom of each panel. For instance, $5\%, 10\%(5\sigma)$ means the first contour is 5% the peak intensity, the next contour is 10% the peak intensity, and the contour interval is 10% or 5σ. The plus sign marks the location of an UCH II region. The water maser is at (0,0).

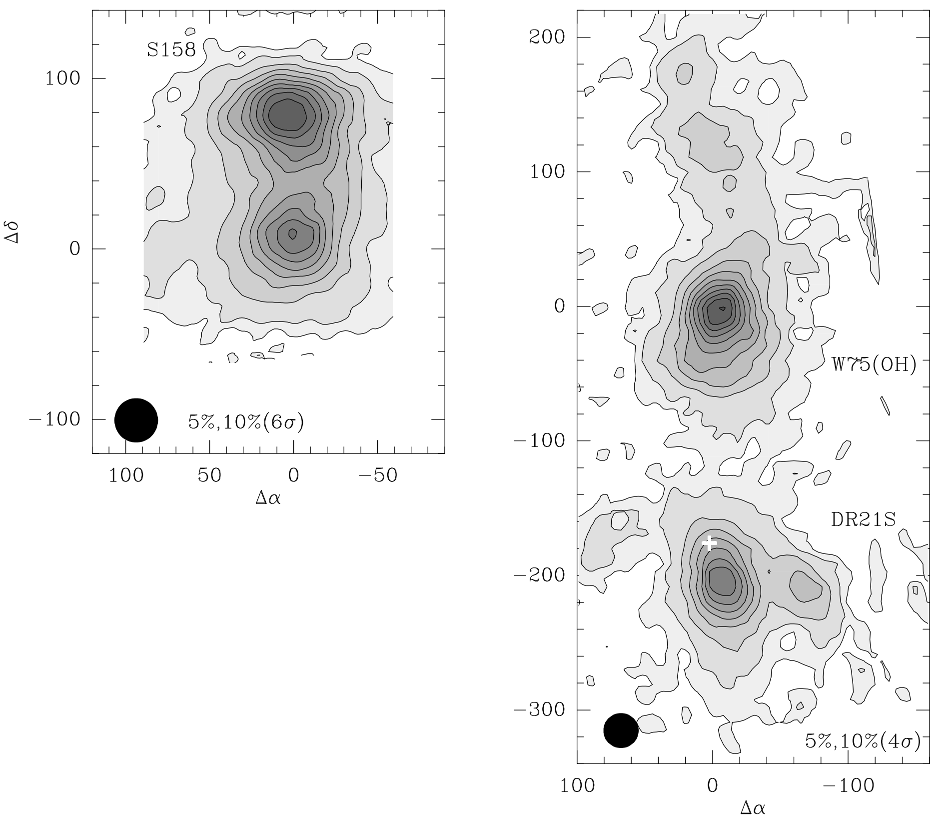

Figure 5.8 Contour maps of CS $J = 5 \rightarrow 4$ integrated intensity for multiple cores. The beam is shown in the lower left corner. The contour levels are indicated at the bottom of each panel. For instance, $5\%, 10\%(5\sigma)$ means the first contour is 5% the peak intensity, the next contour is 10% the peak intensity, and the contour interval is 10% or 5σ. The plus sign marks the location of an UCH II region. The water maser is at (0,0).

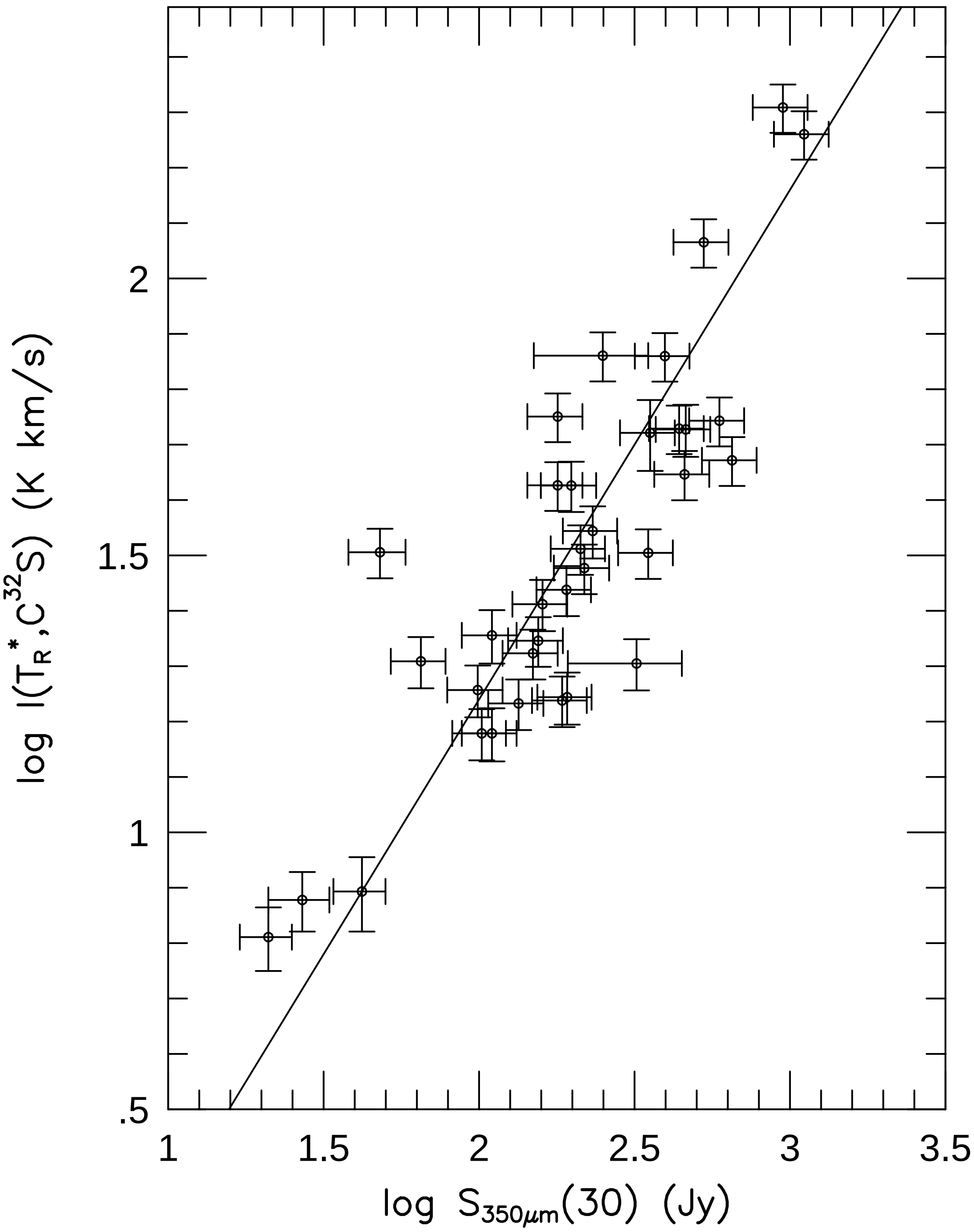

Figure 5.9 The logarithm of the peak CS 5-4 integrated intensity vs. the logarithm of the 350 μm flux density in a 30$''$ aperture (Mueller et al. 2002). The solid line indicates the best fit relation: $\log I(T_R^*) = (-0.60 \pm 0.01) + (0.92 \pm 0.05) \log S_{350\mu\mathrm{m}}$.

twenty-seven (90%) of those cores while four UCH II regions are more than $\theta_{mb}/2$ away from the CS peak. The dense gas traced by CS $J = 5 \rightarrow 4$ emission is clearly associated with water maser emission and often associated with an UCH II region.

The majority of cores (46) are isolated within the regions mapped ($\pm$1.3 pm from the water maser position for the average map size). Seventeen cores (27%) have companions (see Figures 5.6, 5.7, & 5.8) with a median separation of 0.93 pc. Three cores have more than 2 distinct companions within the mapped region (S87, W51W, W75(OH)).

Spectra towards the W49N region (also denoted W49A North) display two blended velocity components. The CS $J = 5 \rightarrow 4$ lines clearly show a peak near 4 km s^{-1} and 12 km s^{-1} in all spectra in the map. There is considerable debate in the literature over the correct interpretation of the two velocity components: are there multiple clouds (see Serabyn et al. 1993) or is this purely an optical depth effect (see Dickel et al. 1999)? Since the two components are also observed in the C^{34}S and ^{13}CS isotopomers, we shall analyze W49N as two separate clouds with the caveat that this region is very complicated. The integrated intensity for two-component Gaussian fits to the spectra are shown in Figures 5.4 and 5.6.

The integrated intensities for C^{34}S $J = 5 \rightarrow 4$ and ^{13}CS $J = 5 \rightarrow 4$ observations are listed in Tables 5.6–5.8. Fifty-six cores were observed in the C^{34}S $J = 5 \rightarrow 4$ transition with forty-nine cores detected. Seven cores were not detected to an average $3\sigma(T_A^*)$ baseline of 300 mK (G135.28+2.80, S241, S252A, G24.49$-$0.04, S106, BFS11$-$B, S157). The average integrated intensity ($I(T_R^*)$) is 6.5 ± 7.5 K km s^{-1} with a median of 4.0 K km s^{-1}, both values a factor of 10 lower than the corresponding values for CS $J = 5 \rightarrow 4$. Nine of the strongest cores were also observed in ^{13}CS $J = 5 \rightarrow 4$. All of the cores were detected. The average ratio between the integrated intensity of C^{34}S $J = 5 \rightarrow 4$ and ^{13}CS $J = 5 \rightarrow 4$ is 2.6, consistent with the observed interstellar isotope ratio between ^{34}S and ^{13}C (Wilson & Rood 1994).

TABLE 5.6
OBSERVED LINE PARAMETERS

Source	I(T_R^*, CS)[a] ($\mathrm{K\ km\ s^{-1}}$)	Δv($C^{32}S$) ($\mathrm{km\ s^{-1}}$)	I(T_R^*, $C^{34}S$)[a] ($\mathrm{K\ km\ s^{-1}}$)	Δv($C^{34}S$) ($\mathrm{km\ s^{-1}}$)
G121.30+0.66	22.2 (2.3)	3.46 (0.13)	1.5 (0.2)	4.23 (0.39)
G123.07-6.31	25.8 (2.7)	4.49 (0.13)	1.1 (0.2)	4.89 (0.45)
W3(OH)	72.4 (7.3)	5.92 (0.13)	6.3 (0.7)	5.80 (0.18)
G135.28+2.80	6.5 (0.8)	3.46 (0.13)	...	...
S231	27.4 (2.8)	3.89 (0.13)	1.6 (0.2)	2.48 (0.19)
S235	32.0 (3.3)	2.68 (0.12)	2.9 (0.4)	2.09 (0.18)
S241	7.5 (0.9)	2.63 (0.14)	...	...
S252A	17.1 (1.8)	3.11 (0.12)	...	...
S255	47.8 (4.8)	3.12 (0.12)	...	...
RCW142	116 (12)	6.00 (0.13)	26.2 (2.7)	5.60 (0.17)
W28A2(1)	204 (20)	6.85 (0.15)	23.2 (2.3)	5.91 (0.15)
M8E	32.5 (3.3)	3.12 (0.12)	4.7 (0.5)	2.23 (0.15)
G9.62+0.10	55.4 (5.6)	7.26 (0.19)	16.0 (1.6)	7.33 (0.38)
G8.67-0.36	47.0 (4.8)	5.43 (0.15)	5.6 (0.6)	5.08 (0.27)
W31	55.9 (5.7)	11.11 (0.26)	7.3 (0.8)	8.56 (0.31)
G10.6-0.4	182 (18)	7.04 (0.13)	29.8 (3.0)	6.72 (0.14)
G12.42+0.50	24.8 (3.5)	3.13 (0.13)	...	...
G12.89+0.49	30.0 (3.1)	5.09 (0.13)	5.4 (0.5)	3.78 (0.14)
G12.2-0.1	35.0 (3.8)	8.01 (0.22)	4.2 (0.4)	7.06 (0.22)
W33cont	122 (13)	6.49 (0.14)	21.1 (2.1)	5.13 (0.13)
G13.87+0.28	17.5 (1.9)	4.15 (0.18)	2.7 (0.3)	2.50 (0.21)
W33A	32.0 (3.3)	4.96 (0.18)	2.3 (0.3)	3.22 (0.27)
G14.33-0.64	53.6 (5.4)	4.97 (0.14)	4.5 (0.5)	2.74 (0.14)
G19.61-0.23	53.4 (5.8)	8.97 (0.23)	3.2 (0.4)	6.50 (0.30)
G20.08-0.13	26.7 (2.7)	8.20 (0.16)	4.5 (0.5)	8.39 (0.46)
G23.95+0.16	18.1 (1.9)	3.01 (0.13)	3.2 (0.4)	2.39 (0.25)
G24.49-0.04	17.3 (1.8)	4.43 (0.18)	...	...
W42	35.7 (3.7)	8.42 (0.19)	8.7 (0.9)	5.44 (0.13)
G28.86+0.07	16.3 (1.7)	5.34 (0.15)	2.5 (0.3)	3.17 (0.19)
W43S	52.6 (7.7)	5.01 (0.13)	8.0 (0.8)	3.97 (0.13)
G31.41+0.31	44.3 (4.5)	5.89 (0.24)	7.7 (0.8)	5.86 (0.20)

[a] Peak position.

Table 5.7

Observed Line Parameters Continued

Source	I(T_R^*, CS)[a] (K km s^{-1})	Δv($C^{32}S$) (km s^{-1})	I(T_R^*, $C^{34}S$)[a] (K km s^{-1})	Δv($C^{34}S$) (km s^{-1})
W43Main3	37.5 (4.1)	9.68 (0.12)	7.4 (0.8)	6.82 (0.23)
G31.44-0.26	22.7 (2.3)	5.22 (0.14)	2.0 (0.2)	3.80 (0.38)
G32.05+0.06	14.6 (1.5)	8.04 (0.18)	1.9 (0.2)	4.54 (0.59)
G32.80+0.20A/B	28.1 (2.9)	8.04 (0.14)	1.7 (0.3)	5.16 (0.74)
W44	107 (11)	5.92 (0.12)	21.8 (2.2)	5.04 (0.51)
S76E	56.3 (5.7)	3.70 (0.12)	...	...
G35.58-0.03	22.7 (2.5)	5.01 (0.18)	2.2 (0.4)	6.56 (0.52)
G35.20-0.74	31.8 (3.3)	6.49 (0.13)	1.9 (0.2)	8.45 (0.71)
W49N 4 km s^{-1}	103 (11)	9.79 (1.38)	2.2 (0.2)	9.80 (0.94)
W49N 12 km s^{-1}	63.4 (6.6)	9.54 (1.38)	3.0 (0.7)	5.60 (0.94)
W49S	27.3 (3.0)	8.32 (0.15)	1.9 (0.2)	7.56 (0.44)
OH43.80-0.13	28.8 (2.9)	7.55 (0.23)	1.0 (0.1)	4.12 (0.30)
G45.07+0.13	42.3 (4.3)	6.08 (0.16)	7.8 (0.8)	6.10 (0.21)
G48.61+0.02	15.1 (1.6)	5.00 (0.17)	0.4 (0.1)	2.34 (0.24)
W51W	29.1 (3.3)	3.82 (0.14)	4.2 (2.0)	3.39 (0.28)
W51M	230 (23)	10.95 (0.13)	26.7 (2.7)	8.96 (0.18)
G59.78+0.06	17.4 (1.9)	3.20 (0.15)	0.6 (0.1)	1.11 (0.19)
S87	28.6 (3.0)	2.49 (0.16)	...	...
S88B	21.1 (2.2)	3.06 (0.13)	1.3 (0.1)	2.35 (0.18)
K3-50	25.2 (2.7)	8.07 (0.15)	1.4 (0.2)	7.61 (0.56)
ON1	20.2 (2.1)	4.68 (0.13)	2.0 (0.3)	4.51 (0.24)
ON2S	42.3 (4.4)	4.63 (0.13)	1.9 (0.2)	3.65 (0.18)
ON2N	37.4 (3.8)	4.71 (0.13)	3.2 (0.3)	3.78 (0.10)
S106	15.1 (1.7)	4.70 (0.17)	...	...
W75N	76.3 (7.7)	4.60 (0.12)	6.8 (0.7)	4.15 (0.15)
DR21S	75.5 (7.6)	5.66 (0.15)	7.0 (0.7)	4.94 (0.15)
W75(OH)	91.6 (9.2)	5.48 (0.12)	4.0 (0.4)	5.44 (0.18)
G97.53+3.19	11.8 (1.3)	6.76 (0.31)	...	...
CepA	20.2 (2.2)	4.07 (0.16)	...	...
BFS11-B	7.8 (1.2)	3.14 (0.18)	...	...
S158	72.5 (7.4)	5.65 (0.12)	5.2 (0.6)	4.39 (0.16)
S157	20.4 (2.2)	3.51 (0.13)	...	...

[a] Peak position.

TABLE 5.8
OBSERVED ^{13}CS LINE PARAMETERS

Source	I(T_R^*, ^{13}CS)[a] (K km s^{-1})	Δv(^{13}CS) (km s^{-1})
W3(OH)	2.5 (0.3)	4.92 (0.25)
S235	0.5 (0.2)	2.32 (0.30)
RCW142	12.8 (1.3)	5.52 (0.14)
W28A2(1)	8.9 (0.9)	5.28 (0.16)
G10.6-0.4	17.1 (1.7)	6.43 (0.13)
W33cont	10.8 (1.0)	4.72 (0.14)
W44	7.6 (0.8)	4.72 (0.14)
W49N 4 km s^{-1}	1.4 (0.2)	9.14 (1.77)
W49N 12 km s^{-1}	3.8 (0.4)	7.38 (1.77)
W51M	19.2 (1.9)	8.03 (0.19)

[a]Peak position.

5.4 Analysis

5.4.1 Core Size & Aspect Ratio

Previous studies (e.g., van der Tak et al. 2000, Hatchell et al. 2000, Beuther et al. 2002) and our modeling of the dust continuum emission (Mueller et al. 2002) indicate that the distribution of density is well fitted by a power law, $n(r) \propto r^{-p}$. Since power laws have no intrinsic size scale, assigning a size to such distributions can be highly misleading. Following long tradition, we will calculate a nominal radius for each source from a Gaussian deconvolution of the beam, and we will use this radius for calculation of masses. We caution that this radius should be viewed strictly as a fiducial radius, with no physical significance. We discuss later the likely corrections to masses, etc. that result from continuation of power laws to larger scales.

The angular extent of each map at the half power level was determined by finding the area within the contour at half I_{peak}, $A_{1/2}$, and calculating the angular radius of a circle with the same area. The nominal core radius, R_{CS}, was determined by deconvolving the telescope beam (θ_{mb}) assuming both are Gaussians:

$$R_{CS} = D \left(\frac{A_{1/2}}{\pi} - \frac{\theta_{mb}^2}{4} \right)^{1/2} , \tag{5.3}$$

where D is the distance to the core. Similarly, the deconvolved core size, θ_{dec}, is found from

$$\theta_{dec} = \left(\frac{2A_{1/2}}{\pi} - \theta_{mb}^2 \right)^{1/2} . \tag{5.4}$$

The core radius and uncertainty are listed in Tables 5.9 and 5.10. The quoted uncertainty in core radius is derived from the uncertainty in area of the core ($A_{1/2}$) and the uncertainty in the main beam FWHM, assumed to be 10% of θ_{mb}. The distance uncertainty actually dominates the uncertainty in R_{CS}, but it is ignored in this analysis since σ_D is difficult to determine. Since the distance may be uncertain to at least 50%, the core radius would be uncertain to the same factor.

Almost all (57) of the cores have clearly defined values for R_{CS}. The remainder (6 cores) have multiple peaks too close together to allow unambiguous determination of a FWHM angular size (see Tables 5.9 and 5.10). This sample of 57 cores provides the sample for the statistical analysis in the rest of the paper. The majority of cores (36, 63%) have *deconvolved* sizes that are larger than the main beam FWHM, indicating that they are well resolved (Figure 5.10). The dashed line in Figure 5.10 indicates the R_{CS} at each distance for which the deconvolved source size equals the FWHM beamsize. The largest core was W49S with $R_{CS} = 1.53$ pc, while the smallest cores were S252A and G121.30+0.66, with $R_{CS} = 0.10$ pc.

The average over the sample is $R_{CS} = 0.37 \pm 0.26$ pc while the median core size is 0.32 pc. The distribution of $\log R_{CS}$ is peaked for core sizes near the mean and median values (Figure 5.11). For a source at the median distance of the sample, 4.0 kpc, $R_{CS} < 0.19$ pc would fail our criterion ($\theta_{dec} \geq \theta_{mb}$) for being well-resolved.

Table 5.9

Observed Properties

Source	Centroid ($''$, $''$)	R_{CS} (pc)	$(a/b)_{obs}$	PA (°)
G121.30+0.66	(−10,0)	0.10 (0.01)	1.5	55
G123.07-6.31	(−10,0)	0.14 (0.01)	1.7	110
W3(OH)	(0,+10)	0.18 (0.01)	1.4	60
G135.28+2.80	(0,+10)	0.10 (0.09)	1.5	50
S231	(0,−10)	0.17 (0.01)	1.2	135
S235	(0,0)	0.15 (0.01)	M	...
	(0,-70)	...	M	...
S241	(0,+10)	0.23 (0.05)	1.7	90
S252A	(−10,+10)	0.10 (0.01)	1.2	135
	(+60,−60)	...	M	...
S255	(0,0)	...	M	...
RCW142	(0,0)	0.14 (0.01)	1.2	120
W28A2(1)	(−10,0)	0.15 (0.04)	1.1	125
M8E	(0,0)	0.14 (0.01)	1.3	115
G9.62+0.10	(−10,+10)	0.33 (0.01)	1.3	35
G8.67-0.36	(0,+10)	0.26 (0.01)	1.2	35
W31	(−10,+10)	0.67 (0.04)	1.6	0
G10.6-0.4	(0,+10)	0.41 (0.01)	1.0	45
G12.42+0.50	(0,0)	...	M	...
	(+10,+40)	...	M	...
G12.89+0.49	(0,0)	0.19 (0.01)	1.3	115
G12.2-0.1	(0,+10)	0.65 (0.08)	1.2	25
W33cont	(+10,+10)	0.75 (0.02)	1.0	...
G13.87+0.28	(0,0)	0.33 (0.03)	1.2	120
W33A	(+10,+10)	0.26 (0.01)	1.0	...
G14.33-0.64	(0,0)	0.17 (0.01)	1.1	140
G19.61-0.23	(0,0)	0.20 (0.02)	1.2	140
G20.08-0.13	(+10,0)	0.15 (0.01)	1.1	150
G23.95+0.16	(+10,0)	0.45 (0.03)	1.3	55
G24.49-0.04	(−10,+10)	0.17 (0.01)	1.0	...
W42	(−10,0)	0.49 (0.04)	1.0	...
G28.86+0.07	(0,+10)	0.47 (0.02)	1.3	25
W43S	(0,+10)	0.46 (0.03)	1.4	160
G31.41+0.31	(0,0)	0.36 (0.02)	1.1	90

[a] M = Multiple cores.

TABLE 5.10

OBSERVED PROPERTIES CONT.

Source	Centroid ($''$, $''$)	R_{CS} (pc)	$(a/b)_{obs}$	PA ($^\circ$)
W43Main3	(0,0)	0.52 (0.05)	1.5	60
G31.44-0.26	(0,0)	0.52 (0.03)	1.0	...
G32.05+0.06	(0,0)	0.48 (0.02)	1.1	40
G32.80+0.20A/B	(−10,0)	0.96 (0.06)	1.1	55
W44	(0,0)	0.37 (0.01)	1.2	45
S76E	(0,0)	0.20 (0.01)	1.6	130
G35.58-0.03	(0,0)	0.20 (0.02)	1.1	140
G35.20-0.74	(0,−10)	0.30 (0.02)	1.4	35
W49N 4 km s^{-1}	(−10,0)	1.41 (0.04)	...	...
W49N 12km s^{-1}	(−20,0)	...	M	...
	(+10,+20)	...	M	...
W49S	(0,0)	1.53 (0.13)	M	...
	(−20,+60)	...	M	...
OH43.80-0.13	(0,−10)	0.11 (0.01)	1.4	125
G45.07+0.13	(0,0)	0.48 (0.02)	...	...
G48.61+0.02	(0,0)	0.54 (0.06)	1.3	145
W51W	(−20,0)	0.64 (0.08)	1.6	110
W51M	(0,0)	0.50 (0.01)	M	...
	(−70,+40)	...	M	...
G59.78+0.06	(−10,+20)	0.18 (0.01)	M	...
S87	(0,0)	...	M	...
	(+10,+60)	...	M	...
S88B	(+20,0)	0.16 (0.01)	1.0	...
K3-50	(0,+10)	0.71 (0.05)	1.3	50
ON1	(0,0)	0.43 (0.03)	1.0	..
ON2S	(−10,−10)	0.61 (0.02)	1.8	55
ON2N	(0,0)	0.41 (0.02)	1.2	40
S106	(+10,0)	0.37 (0.06)	...	...
W75N	(0,0)	0.27 (0.01)	1.5	70
DR21S	(0,0)	0.27 (0.01)	M	...
	(−60,0)	...	M	...
W75(OH)	(0,0)	0.29 (0.01)	1.5	60
G97.53+3.19	(+10,0)	...	M	...
	(0,−20)	...	M	...
CepA	(−10,−10)	...	M	...
	(+10,+10)	...	M	...
BFS11-B	(0,0)	0.12 (0.03)	...	...
S158	(0,0)	0.32 (0.01)	M	...
	(0,+80)	...	M	...
S157	(0,+10)	0.19 (0.01)	1.0	...

[a] M = Multiple cores.

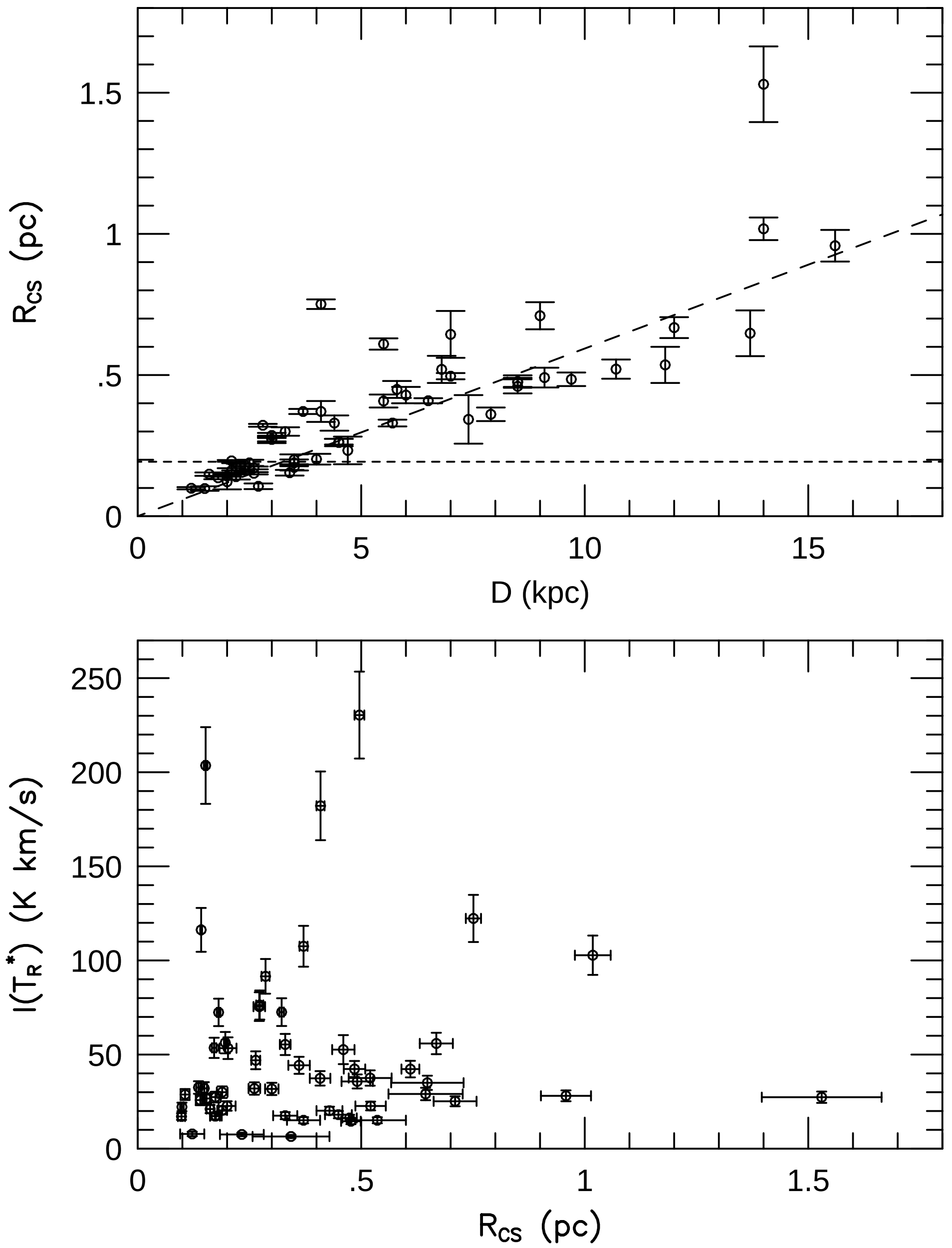

Figure 5.10 Plot of core size vs. distance (upper panel) and integrated intensity vs. R_{CS} (lower panel). The dashed line in the upper panel shows the size of a core with a deconvolved size equal to the beamsize while the horizontal dashed line marked the source size with a deconvolved source size equal to the beam for the median distance of the sample. No correlation is observed between integrated intensity and R_{CS}.

The median distance bias is shown as a horizontal dotted line in Figure 5.10. The average over the sample is smaller than the average core radius of 0.5 ± 0.4 pc determined in Paper II for the 25 cores with cross-scans. This difference is almost certainly caused by our having mapped some of the weaker sources.

The process of finding a FWHM size might vary with the intensity of the core, introducing a bias into the size distribution. The integrated intensity is plotted against R_{CS} in Figure 10 for 57 cores. There is no observed correlation ($r = 0.07$) between CS intensity and core radius over a wide range in both variables.

The 350 μm dust continuum from twenty-four sources from our survey were modeled with a radiative transfer code by Mueller et al. (2002). The best fit power law index, $p = -\log n / \log r$, is listed in Tables 5.11 and 5.12. Convolving a power law intensity distribution with a Gaussian beam pattern should result in deconvolved core sizes that are somewhat larger than θ_{mb} (e.g. Terebey et al 1993). Flatter power laws produce larger deconvolved source sizes than steeper power laws. This correlation was observed towards a sample of low mass cores observed at 850 μm with SCUBA (Shirley et al. 2000, Young et al. 2002). A weak correlation ($r = -0.55$) is observed between the best fit power law index and the deconvolved source size determined from our CS maps (Figure 5.12). This correlation is likely real since the observations were made with two different instruments, SHARC (Hunter et al. 1996) and the CSO 230 GHz receiver, with different beam sizes ($14''$ and $24\farcs5$ respectively). For power law density distributions, the deconvolved source size may be used as a rough guess of p if the correlation is calibrated.

Aspect ratios for each core were determined from the ratio of major to minor axis for the 20% peak contour (Tables 5.9 and 5.10). The 20% peak contour is less susceptible to smoothing by the beam and is well detected for the entire sample ($\langle \sigma_{20\%} \rangle = 10\sigma_I$). The distribution of aspect ratios (Figure 5.11) is strongly peaked towards low ($(a/b)_{obs} < 1.4$) aspect ratios indicating that the observed contours are

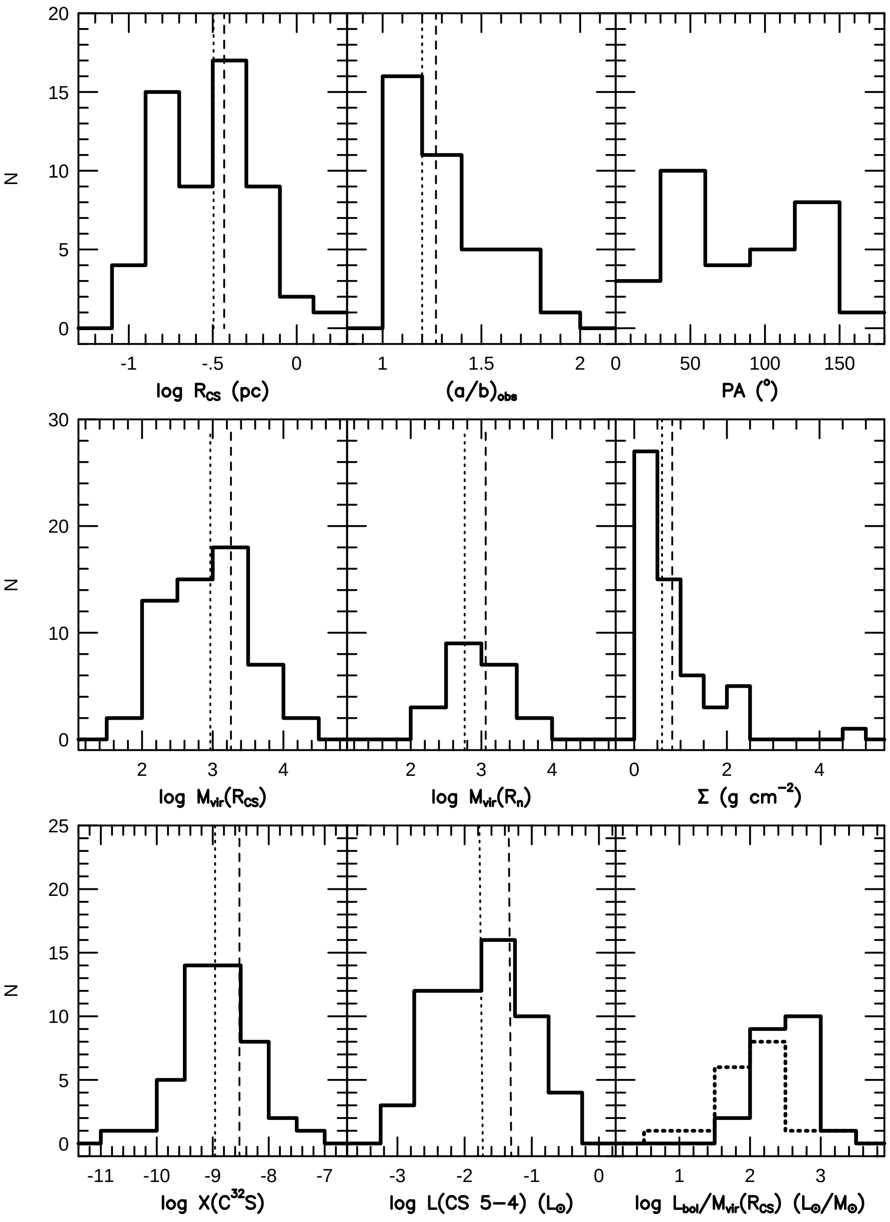

Figure 5.11 Histograms of R_{CS}, $(a/b)_{obs}$, major axis position angle, M_{vir}, Σ, CS abundance, CS $J = 5 \rightarrow 4$ luminosity, and L_{bol}/M_{vir}. The mean (dashed line) and median (dotted line) of each distribution are plotted. There are two histograms plotted for L_{bol}/M_{vir}: The solid histogram is sources with UCH II regions while the dashed histogram is sources without UCH II regions.

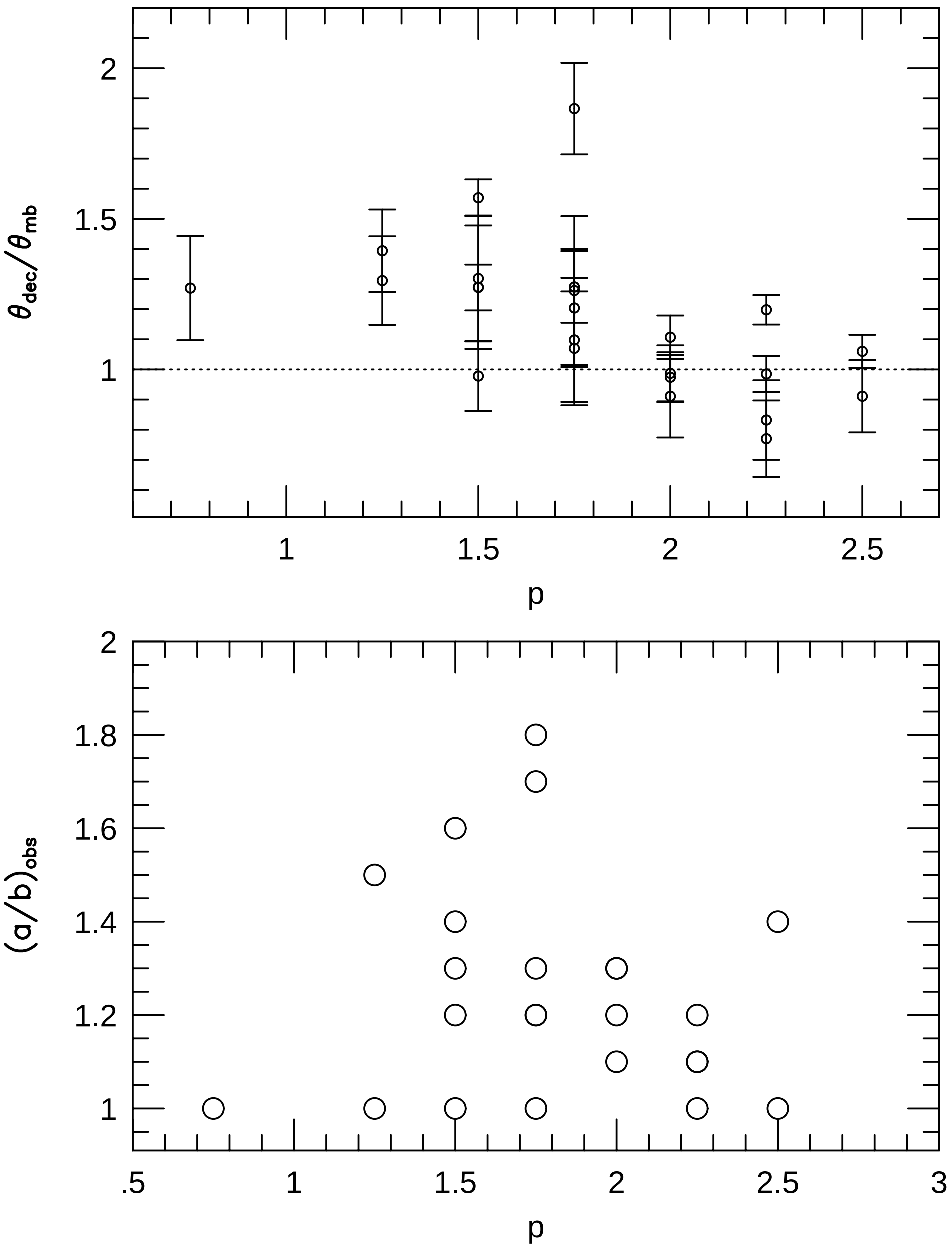

Figure 5.12 The aspect ratio is compared to the best fit power law density index determined by Mueller et al. 2002. (lower panel) and the deconvolved source size (θ_{dec}; upper panel). No correlation between aspect ratio and p is observed while a weak correlation is observed between p and θ_{dec}/θ_{mb}.

consistent with circular symmetry. The mean aspect ratio is 1.26 ± 0.22 while the largest observed aspect ratio is 1.8 (ON2S). The cores are observed in projection, making $(a/b)_{obs}$ a lower limit to the actual aspect ratio. The position angle of the major axis, measured counter-clockwise from north, is listed in Tables 5.9 and 5.10. The histogram of position angles for cores with $(a/b)_{obs} \geq 1.2$ is plotted in Figure 5.11. There is no bias in the core elongation observed along the scan direction of the OTF map (90°), indicating that the aspect ratios are unaffected by any beam smearing from the OTF method.

Young et al. (2002) report a correlation between $(a/b)_{obs}$ and p toward low-mass cores; flatter power laws ($p \sim 1$) are associated with more elongated cores. Using the p values from Mueller et al. (2002) and the CS aspect ratios, we find no evidence for a correlation in this sample (Figure 5.12). It is necessary to use the CS data to determine the aspect ratio since Mueller et al. were unable to determine reliable aspect ratios because of the effects of chopping.

5.4.2 Linewidth-Size Relationship

The FWHM linewidth, Δv, for each core was determined from a Gaussian fit to a spectrum produced by convolving the data to an effective size corresponding to the half-power contour. The average linewidth for the sample of 63 cores was $\Delta v = 5.6 \pm 2.2$ km s^{-1}. A few cores show evidence for self-absorption and other optical depth effects. For a Gaussian line shape, the broadening due to optical depth can be expressed by

$$\frac{\Delta v}{\Delta v_o} = \frac{1}{\sqrt{\ln 2}} \sqrt{\ln \frac{\tau}{\ln \frac{2}{1+\exp(-\tau)}}}\,, \tag{5.5}$$

where Δv_o is the optically thin linewidth (Phillips et al. 1979). We can use the $C^{34}S$ $J = 5 \rightarrow 4$ linewidth to test optical depth effects. The CS to $C^{34}S$ linewidth ratio for 49 cores was 1.3 ± 0.4 corresponding to an average optical depth of $\tau = 1.7$ (Figure 5.13). Therefore, $\Delta v(C^{34}S)$ should be used when possible in calculations sensitive to the linewidth. We checked the optical depth of $C^{34}S$ by observing ^{13}CS $J = 5 \rightarrow 4$ towards nine of the brightest cores. The $C^{34}S$ linewidths are consistent with being optically thin for all but 3 cores (Figure 5.13).

The linewidth-size relationship for 51 cores using $\Delta v(C^{34}S)$ is plotted in Figure 5.14. The data were fitted with a least-squares method, including statistical errors in both quantities to give $\log\Delta v(C^{34}S) = (0.86 \pm 0.01) + (0.28 \pm 0.01)\log R_{CS}$. For comparison, a fit using robust estimation gives a consistent slope, $\log\Delta v(C^{34}S) = 0.82 + (0.28)\log R_{CS}$. The linear correlation coefficient is low ($r = 0.37$). However, the more important point is that the linewidths are all much larger at a given radius that those found in either low-mass or "high-mass" regions by Caselli & Myers (1995). For the average core size in our sample, the average $C^{34}S$ linewidth is 4 times larger than the "high-mass" prediction and 5 times larger than the low-mass prediction of Caselli & Myers (1995). This point, already made in PaperII, is strengthened by the larger sample and fully sampled maps presented here. Note that the "high-mass" regions of Caselli et al. are considerably less massive than those studied here. Extension of the linewidth-size relation found in previous studies to regions of massive star formation would be very misleading.

We attribute the large linewidths to turbulent motions. Outflows are apparent in line wings for some sources, but they are unlikely to broaden the FWHM linewidth, except by stirring up turbulence. Our regions are at least four times more turbulent than regions involved in lower mass star formation (see Mardones et al. 1997, Gregersen et al. 1997). Based on comparison of power-law models using dust emission, Mueller et al. (2002) found that these cores were also about 100 times denser on average than the low mass sample.

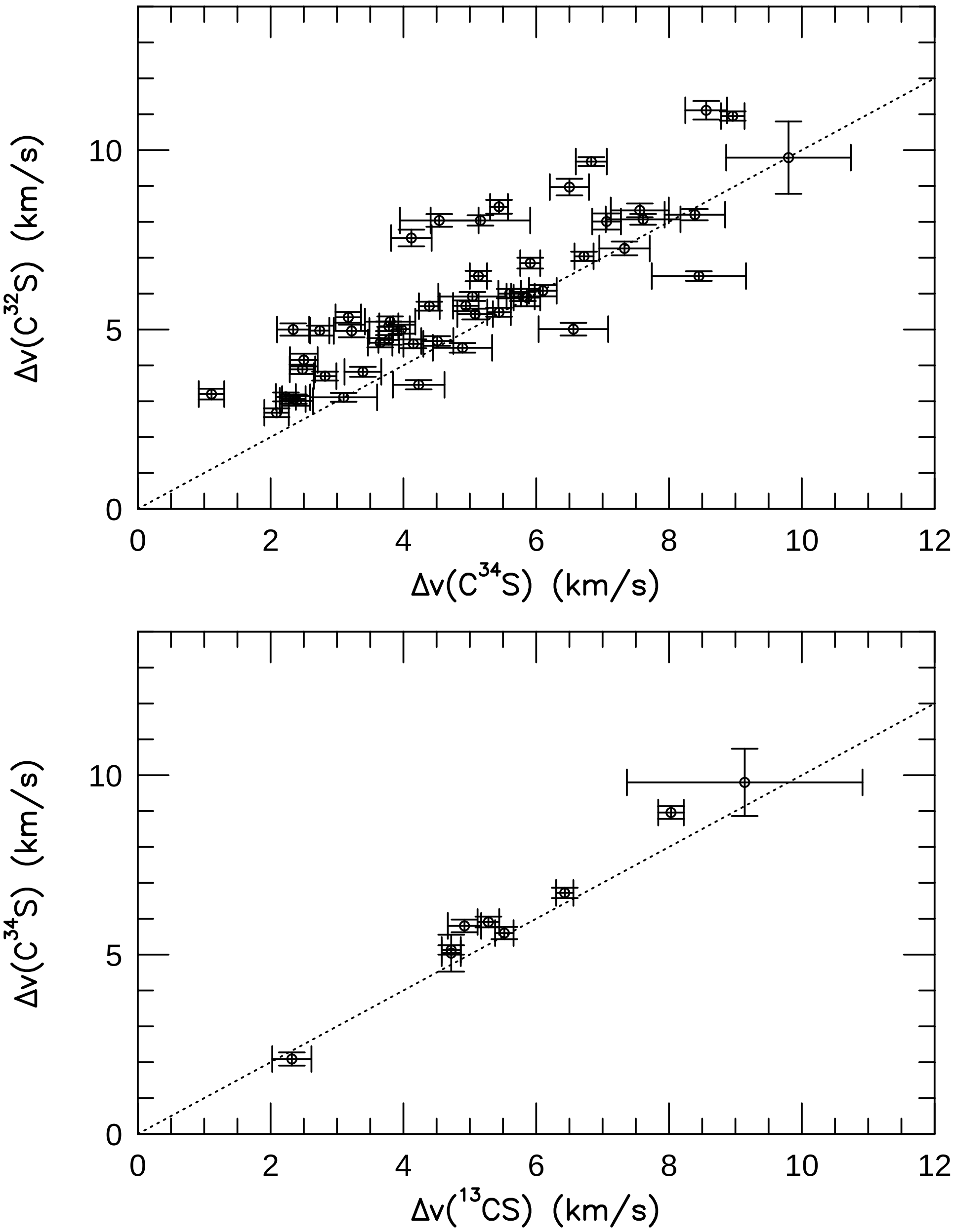

Figure 5.13 The upper panel shows the CS linewidth compared with $C^{34}S$ linewidth. For the subsample of cores mapped in both CS and $C^{34}S$, the CS linewidth is broader on average. The lower panel shows the $C^{34}S$ and ^{13}CS linewidths.

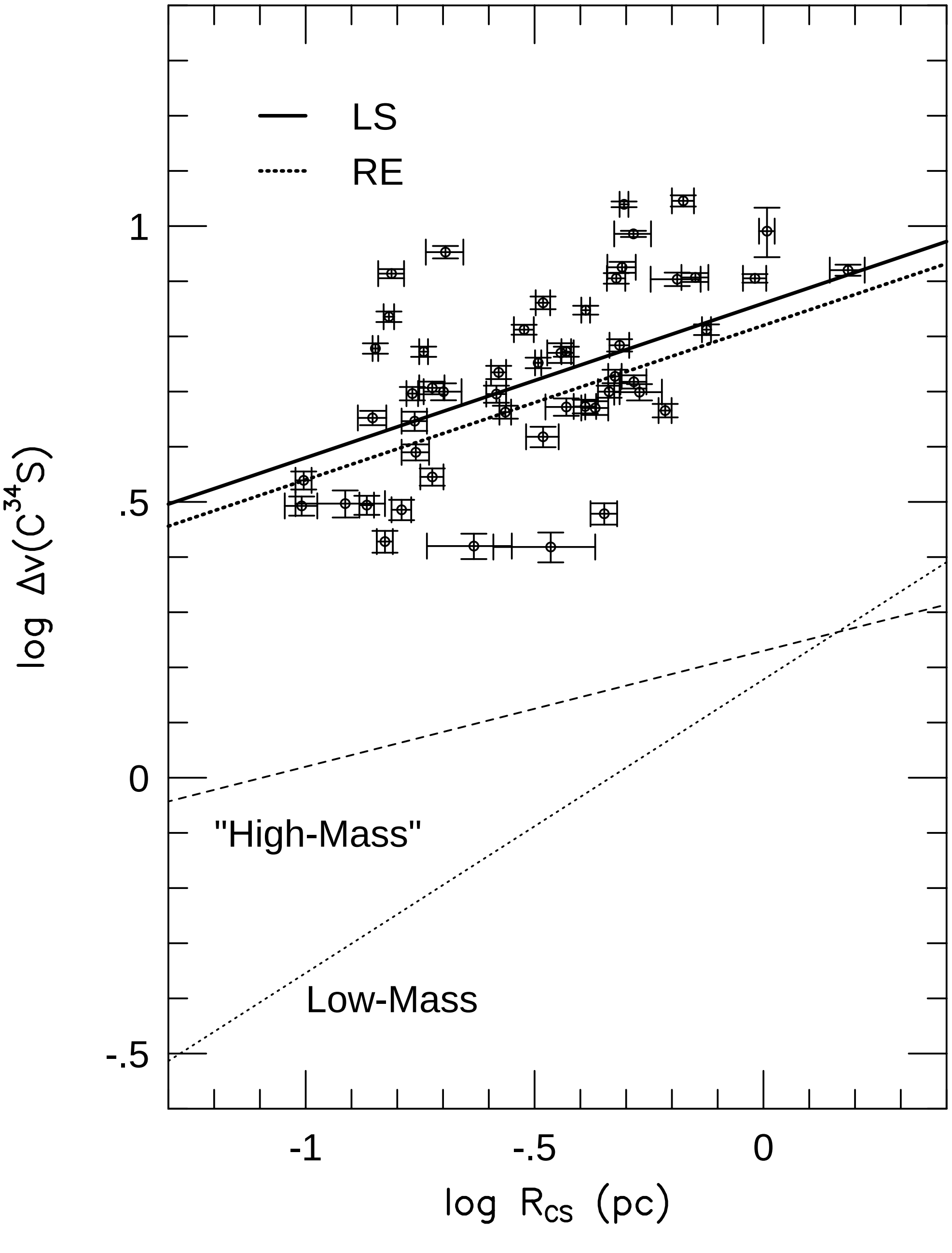

Figure 5.14 The linewidth-size relationship using CS linewidths. The extrapolated linewidth-size relationships for low and high mass regions are labeled. The least squares fit and robust estimation for our sample are shown.

5.4.3 Virial Mass

The virial mass for a homoeoidal ellipsoid (concentric ellipsoids of revolution with equal aspect ratios) is given by

$$M_{vir}(R) = \frac{5R\Delta v^2}{8a_1a_2G\ln 2} \approx 209\,\frac{(R/1\mathrm{pc})\,(\Delta v/1\mathrm{kms}^{-1})^2}{a_1a_2}\ \mathrm{M}_\odot \ ; \qquad (5.6)$$

$$a_1 = \frac{1-p/3}{1-2p/5}\ ,\ \ p < 2.5 \qquad (5.7)$$

where a_1 is the correction for a power law density distribution and a_2 is the correction for a non-spherical shape (Bertoldi & McKee 1992). For aspect ratios less than 2, $a_2 \sim 1$ and can be ignored for our sample. The equation in Bertoldi and McKee uses an rms velocity; we have converted to the observable (Δv) under the assumption that turbulent broadening dominates thermal broadening; this is a very safe assumption for these sources, but it fails for lines of light species in very quiescent regions (see Shirley et al. 2002b).

There are several corrections used in calculating the virial mass. Since the CS linewidth was found to be optically thick in some cores, we use the $C^{34}S$ linewidth when it was observed. The remaining cores (7) are corrected using the average ratio of $C^{34}S$ to CS linewidth for the sample (§5.4.2). We use the density power law index, p, from Mueller et al. (2002) for the cores common to each sample (21) and use the average $p = 1.77$ for the remaining cores. Finally we must choose a radius within which to calculate the virial mass. Initially we use R_{CS}. However, since a power law density distribution has no characteristic size, we also calculate virial masses using R_n, the radius at which the density of the dust models drops to 10^4 cm^{-3} (Mueller et al. 2002). This density corresponds to the density of the ambient molecular cloud at the edge of a core based on a detailed study of molecular clouds in our galaxy (Allers et al. 2002). The average $R_n = 0.40$ pc is only slightly larger than the average R_{CS}.

The distributions of virial masses are peaked near 1000 $\mathrm{M}_\odot$, for either definition of the cloud radius (Figure 5.11). Only cores for which all the corrections could be made (22) are included in the $M_{vir}(R_n)$ histogram. We are probably biased against cores with masses less than about 10^3 $M_\odot$ because they will tend to be too small to resolve at the average distance of sources in our sample (5.3 kpc). Consequently, the peaked histograms and the average values given below should be taken only as representative of this particular sample.

The mean virial mass using R_{CS} is 1810 ± 2810 $M_\odot$ and the median mass is 920 $M_\odot$ for the full sample of 57 cores. The large dispersion about the mean mass partially results from the mass of W49N, which is 8 times higher than the average mass; therefore, the median is a better indicator of the typical virial mass for this sample. The mean virial mass using R_n is 1180 ± 1080 $M_\odot$ and the median mass is 610 $M_\odot$ using the subsample of 21 cores that were modeled by Mueller et al (2002). The virial mass using corrections for $\langle p \rangle$ and $\langle \Delta v(C^{34}S)/\Delta v(C^{32}S) \rangle$ is 2.3 times smaller than the mass calculated using Δv and assuming a constant density envelope.

The virial mass may be compared to the mass derived from models of the dust continuum emission at 350 μm, denoted $M_{dust}(R_{CS})$ (Mueller et al. 2002), for the sources in common. The average ratio of virial mass to dust-determined mass ($\langle M_{vir}/M_{dust} \rangle$) is 3.4 ± 3.3 and the median ratio is 2.2 for 21 sources with virial mass corrections, $C^{34}S$ linewidths, and dust models (see Figure 5.15). Given the many sources of uncertainty in deriving virial and dust-determined masses (distance, dust opacity, etc.), the agreement is good. The agreement suggests that the assumptions used in deriving the virial mass and the choice of Ossenkopf & Henning (OH5, 1994) opacities for the dust are sensible, and that virial masses provide a good mass estimate.

Since the regions we are studying are forming massive stars, we can compare the virial mass to regions that have formed high mass stars, namely OB associations.

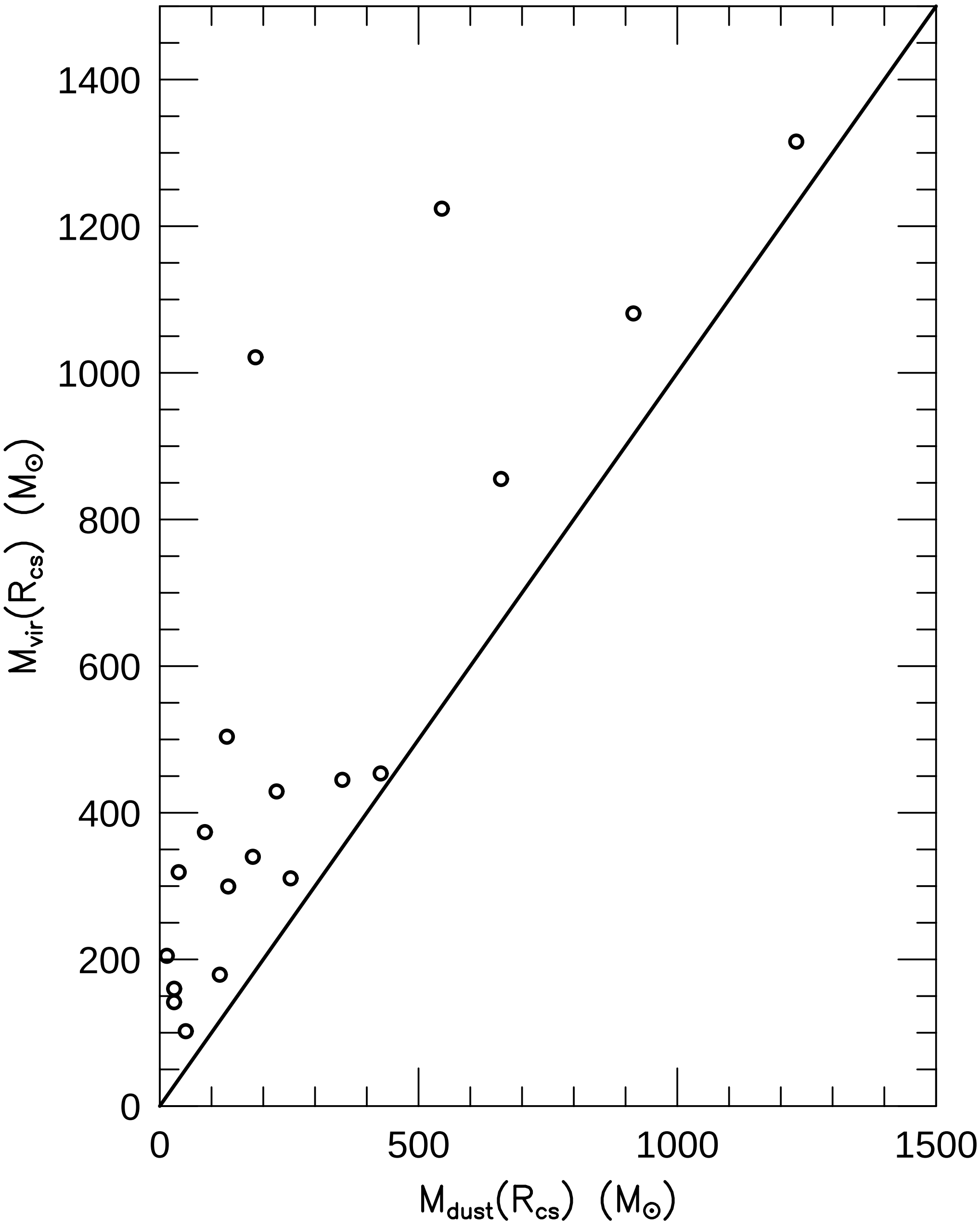

Figure 5.15 The virial mass and mass derived from dust continuum emission correlate well, but $M_{vir} > M_{dust}$.

Matzner (2002) calculated a mean mass per association of 440 $M_\odot$ based on the Galactic H II region luminosity function of McKee & Williams (1997). This mass is roughly 50% the median virial mass calculated using R_{CS}, and 75% of the virial mass calculated using R_n. If the regions traced by water maser emission and CS $J = 5 \rightarrow 4$ emission are forming new OB associations, then the star formation efficiency of the gas traced by high-J CS emission is high ($\sim 50\%$).

5.4.4 The Mass Spectrum

Because all these cores have masses greater than those of individual stars, they are destined to form clusters or associations. The cumulative mass spectrum of dense cores should then be directly related to the cumulative distribution of the *total* mass of stars in clusters or OB associations ($M_\star(tot)$). Using the model of McKee and Williams (1997), the cumulative distribution of $M_\star(tot)$ in OB associations is proportional to $M_\star(tot)^{-1}$. The mass function of our cores may be related less directly to the initial mass function of stars *within* those clusters and associations (the usual IMF). Stars above about 5 $M_\odot$ roughly follow a power-law mass spectrum ($N(> M) \propto M^\Gamma$, with Γ often assumed to be -1.35 (Salpeter 1955). Massey et al. (1995) find $\Gamma = -1.1 \pm 0.1$(standard deviation of the mean) for 13 OB associations. In contrast to these slopes, molecular clouds as a whole have a flatter distribution. Mass spectra with Γ of -0.6 to -0.7 have been observed for molecular clouds (see Scoville & Sanders 1987), as well as the large clumps within clouds (Blitz 1993, Williams et al. 2000, Kramer at al. 1998). Studies of cores forming low-mass stars in Ophiuchus reveal a steeper mass spectrum, $\Gamma = -1.5$ (Motte, André, & Neri 1998, Johnstone 2000), and a study in Serpens finds $\Gamma = -1.1$ (Testi & Sargent 1998). These slopes begin to resemble the slope of the the IMF for massive stars, but they mostly apply to lower mass regions where the stellar IMF actually turns over (Scalo 1998, Meyer et al. 2000).

TABLE 5.11
DERIVED PROPERTIES

Source	p	$M(R_{CS})^{a}$ ($M_\odot$)	$M(R_n)^{a}$ ($M_\odot$)	Σ (g cm^{-2})	X(CS) (10^{-9})	$L(\mathrm{CS})^{b}$ (10^{-2} $L_\odot$)	L_{bol}/M_{vir} ($L_\odot/M_\odot$)
G121.30+0.66	1.25	320	1870	2.16	0.03	0.10	3
G123.07-6.31	1.75	500	1640	1.72	...	0.28	12
W3(OH)	1.50	1020	3550	2.08	0.27	1.15	93
G135.28+2.80	...	210	...	0.12	1.39	0.60	269
S231	1.50	180	490	0.40	1.81	0.40	73
S235	...	100	...	0.29	0.37	0.30	98
S241	...	140	...	0.18	...	0.30	91
S252A	1.75	140	350	0.99	...	0.09	45
RCW142	2.25	370	610	1.23	5.29	1.19	153
W28A2(1)	2.25	450	1280	1.29	16.4	2.85	450
M8E	1.75	100	200	0.37	7.23	0.29	166
G9.62+0.10	2.00	2230	3930	1.37	3.15	3.68	157
G8.67-0.36	2.00	860	1890	0.82	...	1.97	152
W31	...	7300	...	1.09	3.60	15.9	...
G10.6-0.4	2.50	2750	...	1.10	12.7	17.2	334
G12.89+0.49	2.00	340	470	0.63	0.83	0.71	115
G12.2-0.1	...	4810	...	0.77	1.48	11.3	114
W33cont	...	2950	...	0.35	0.85	22.7	...
G13.87+0.28	1.75	310	350	0.19	2.53	0.92	419
W33A	1.50	454	1260	0.44	...	1.33	220
G14.33-0.64	2.00	160	450	0.37	3.30	0.85	621
G19.61-0.23	...	1270	...	2.08	0.64	1.55	141
G20.08-0.13	...	1610	...	4.56	0.15	0.51	...
G23.95+0.16	1.50	430	270	0.14	...	1.72	443
G24.49-0.04	2.25	300	450	0.67	1.05	0.38	164
W42	...	2160	...	0.60	1.64	5.66	...
G28.86+0.07	...	710	...	0.21	1.95	2.33	...
W43S	2.50	1080	...	0.34	1.08	7.31	1480
G31.41+0.31	2.25	1040	2090	0.53	0.69	4.62	221

[a] M refers to M_{vir}

[b] CS $J = 5 \rightarrow 4$

Table 5.12

Derived Properties Continued

Source	p	$M(R_{CS})$[a] ($M_\odot$)	$M(R_n)$[a] ($M_\odot$)	Σ (g cm^{-2})	$X(CS)$ (10^{-9})	L(CS)[b] (10^{-2} $L_\odot$)	L_{bol}/M_{vir} ($L_\odot/M_\odot$)
W43Main3	...	3610	...	0.89	...	4.84	...
G31.44-0.26	...	1120	...	0.28	0.76	4.56	...
G32.05+0.06	...	1470	...	0.43	1.55	2.09	...
G32.80+0.20[c]	...	3800	...	0.28	2.10	14.8	...
W44	...	1400	...	0.68	1.20	5.95	214
S76E	1.50	240	...	0.41	4.07	0.90	118
G35.58-0.03	...	1280	...	2.15	0.40	0.56	33
G35.20-0.74	...	3200	...	2.37	0.45	1.22	...
W49N 4km s^{-1}	...	14570	...	0.94	2.76	52.8	...
W49S	...	13030	...	0.37	2.48	17.9	...
OH43.80-0.13	...	270	...	1.59	0.73	0.32	...
G45.07+0.13	...	2690	...	0.77	0.95	7.14	446
G48.61+0.02	...	440	...	0.10	4.24	3.50	2290
W51W	...	1100	...	0.18	35.9	3.81	...
W51M	...	5930	...	1.61	3.59	28.7	472
G59.78+0.06	...	30	...	0.07	7.41	0.25	...
S88B	1.25	160	220	0.41	0.55	0.26	562
K3-50	...	6130	...	0.81	0.07	5.92	343
ON1	1.75	1320	2230	0.48	...	1.87	114
ON2S	1.75	1220	700	0.22	0.47	6.02	302
ON2N	...	870	...	0.35	...	3.04	...
S106	...	720	...	0.35	...	0.88	692
W75N	...	700	...	0.63	0.25	2.41	...
DR21S	...	990	...	0.90	0.16	1.78	506
W75(OH)	...	1260	...	1.03	0.39	2.30	40
BFS11-B	...	110	...	0.48	...	0.07	66
S158	...	200	...	0.60	0.41	2.83	206
S157	0.75	920	450	0.39	0.12	0.35	141

[a] M refers to M_{vir}

[b] CS $J = 5 \rightarrow 4$

[c] G32.80+0.20A/B

The cumulative mass spectrum of cores, based on the corrected virial masses, is shown in Figure 5.18. The mass spectrum is clearly incomplete below about 1000 $M_\odot$. The spectrum for $M_{vir} \geq 1000$ $M_\odot$ was fitted using least squares and robust estimation (Figure 5.16), with resulting $\Gamma = -0.91 \pm 0.17$ and $\Gamma = -0.95$, respectively. A $\Gamma = -0.8$ to -1.1 is consistent within the uncertainties of the fit. The mass function of dense cores is similar to that of $M_\star(tot)$ in the model of McKee and Williams (1997). It is also within the range of the values for the IMF of stars within OB associations (Massey et al. 1995). The similarity of our value for Γ to that of the IMF of stars within clusters suggests that the fragmentation process keeps nearly the same mass spectrum.

Our values of Γ are slightly higher than found by other studies towards high mass star forming regions that used probes that trace lower densities. Kramer et al. (1998) find $\Gamma = 0.6$ to 0.8 for CO clumps within seven high mass star forming clouds. A CS $J = 2 \rightarrow 1$ survey towards fifty-five dense cores containing water masers found $\Gamma = 0.6 \pm 0.3$ (Zinchencko et al. 1998).

5.4.5 Surface Density, Pressure, and Confinement of UCH II Regions

McKee and Tan (2002a,b) have emphasized the importance of the surface density of a molecular core (which they call a clump) in the stellar mass accretion rate ($dm_*/dt \propto \Sigma^{0.75}$) and the time to form a star ($t_{*f} \propto \Sigma^{-0.75}$). Based on the results in Paper II, they assumed $\Sigma = 1.0$ gm cm^{-2}.

The surface density of the core can be calculated from

$$\Sigma = \frac{M_{vir}(R_{CS})}{\pi {R_{CS}}^2} \approx 0.665 \, \frac{(M_{vir}/1.0 \times 10^4 \mathrm{M_\odot})}{(R_{CS}/1\mathrm{pc})^2} \ \mathrm{gm\ cm^{-2}} \ . \tag{5.8}$$

The average over the sample with well-determined sizes is $\Sigma = 0.82 \pm 0.78$ gm cm^{-2} with a median of 0.60 gm cm^{-2}. The median surface density corresponds to 2870 $M_\odot$ pc^{-2}. There is a wide range of surface densities from 0.07 gm cm^{-2} (G58.78+0.06)

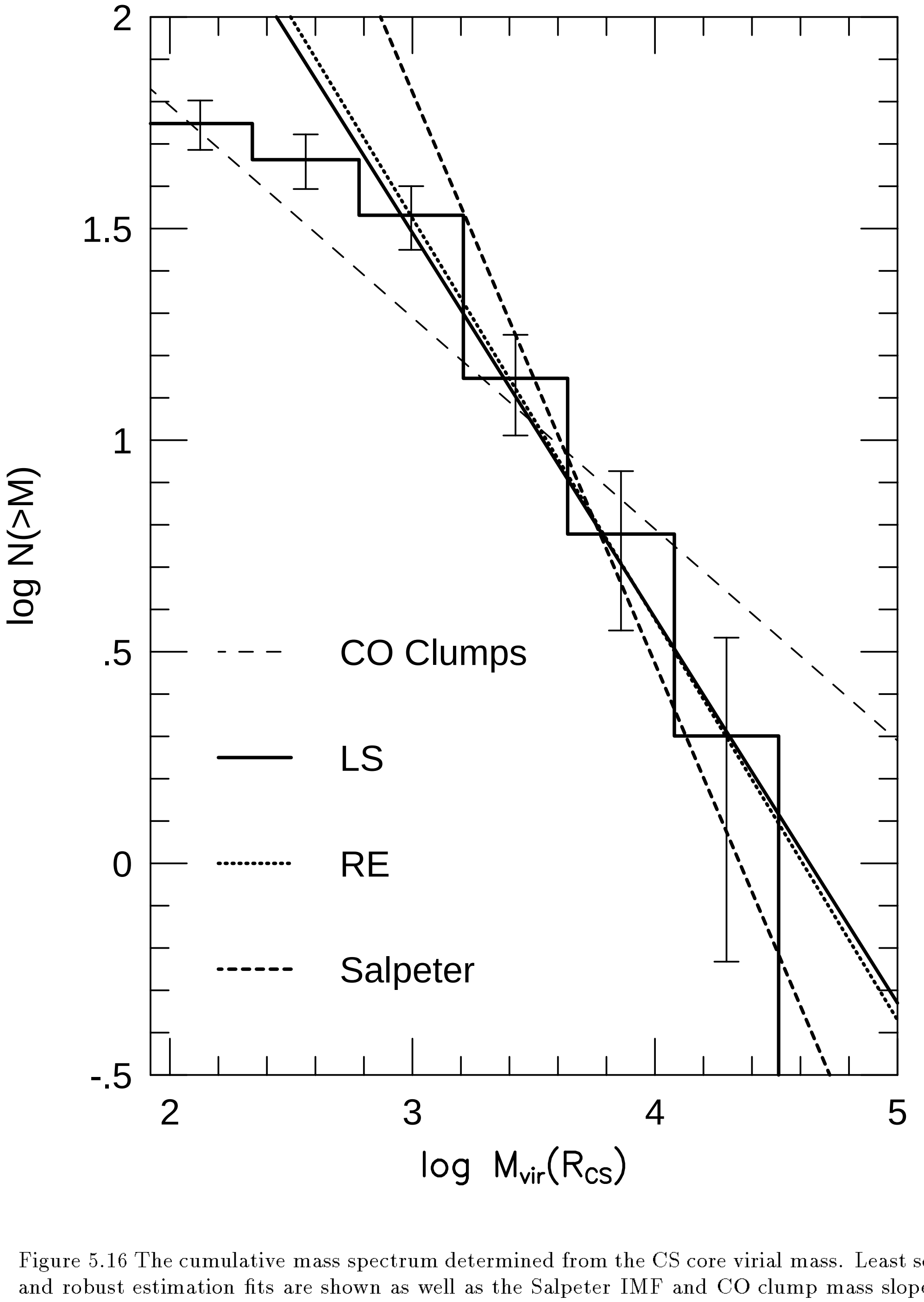

Figure 5.16 The cumulative mass spectrum determined from the CS core virial mass. Least squares and robust estimation fits are shown as well as the Salpeter IMF and CO clump mass slope.

to 4.6 gm cm^{-2} (G20.08$-$0.13). While the distribution is sharply peaked for $\Sigma < 1$ gm cm^{-2}, a few cores (6) have surface densities greater than 2 gm cm^{-2} (Figure 5.11). The median surface density would imply a decrease in the mass accretion rate and increase in the star formation time for the accretion models of McKee & Tan (2002a,b) by a factor of 2/3. The picture of McKee & Tan would imply that cores with higher Σ should have a higher star formation rate. Then one might expect the luminosity to correlate with Σ. We see no correlation (r = -0.06) in our data, but the range of Σ is small.

The large surface densities and linewidths also translate into high pressures, both thermal and turbulent. Using equation A6 from McKee & Tan (2002),

$$\langle \bar{P}/k \rangle \approx 4.25 \times 10^8 \, (\Sigma/1\mathrm{gm\,cm^{-2}})^2 \ \mathrm{Kcm^{-3}} \quad , \tag{5.9}$$

we compute a mean pressure for each of our cores with a known surface density. The average over these cores is $\langle \bar{P}/k \rangle = (5.4 \pm 12.6) \times 10^8$ Kcm^{-3}, with a median value of 1.5×10^8 Kcm^{-3}. The distribution is highly skewed by the core with very high surface density, so the median is more representative.

These high pressures may have some bearing on the issue of confinement of UCH II regions. Simple considerations suggest that the thermal pressure of an UCH II with $T_e = 10^4$ K and $n_e = 10^4$ cm^{-3} could be balanced by the median pressure in these cores. The pressure would be even higher close to the center of the cores. Mueller et al. (2002) found a median density over 1.4×10^7 cm^{-3} at the fiducial radius of 1000 AU, and a median temperature of 260 K, leading to a thermal pressure of 4×10^9 Kcm^{-3}. Including turbulent pressure raises this to about 1.5×10^{10} Kcm^{-3}, comparable to those in the newly discovered hypercompact H II regions, which have sizes on the order of 1000 AU (e.g., Kurtz & Franco 2002).

While the issues surrounding UCH II regions are complicated (see Kurtz et al. 2000 for a review), our data do generally agree with the idea that turbulent pressure in the surrounding molecular gas may affect the evolution of H II regions (Xie et al.

1996). Xie et al. have suggested an anticorrelation between the turbulent linewidth and the size of an UCH II region for a sample of eight sources. We do not find strong evidence for an anticorrelation (r = −0.29) between $\Delta v(C^{34}S)$ (r = −0.12) or $\langle \bar{P}/k \rangle$ (r = −0.29) and UCH II region sizes (Tables 5.3 and 5.4); however, the linewidth and mean pressure determined from CS $J = 5 \rightarrow 4$ observations with a large beamsize is probably not the best tracer of the gas that may be directly associated with confinement of the UCH II region.

5.4.6 Filling Factor and CS abundance

The constant density volume filling factor was calculated by taking the ratio of the constant density virial mass ($p = 0$) to the mass calculated from the volume density. The volume density was taken to be the best fit density from the LVG models, n_{lvg}, using multiple transitions of CS and $C^{34}S$ (Paper II),

$$f_{\rm v}(p=0) = \frac{M_{vir}(R_{CS}; p=0)}{\frac{4}{3}\pi\mu m_H n_{lvg} {R_{CS}}^3} \approx 0.042 \, \frac{(M_{vir}/1.0\times10^4{\rm M}_\odot)}{(n_{lvg}/1.0\times10^6{\rm cm}^{-3})\,(R_{CS}/1{\rm pc})^3} \; . \tag{5.10}$$

The average filling factor of a subsample of 42 cores was 0.46 ± 0.72 with a median of 0.13. Paper II found an average filling factor of 0.33 ± 0.59, consistent with the mean of our sample. However, $f_{\rm v}(p=0)$ underestimates the filling factor when there is a density gradient. The LVG models of Paper II assume a constant density envelope; therefore, n_{lvg} represents an average density that is strongly weighted toward the denser gas. Using the power law models of Mueller et al (2002) with a density gradient, the mean n_{lvg} corresponds to the density at a radius of 7300 ± 5200 AU or about 0.1 times the average R_{CS}. Detailed models of sources will allow us to determine $f_{\rm v}$ more accurately, but this comparison suggests that the average core is not highly clumped in the sense of being mostly empty space with a small volume filling factor of very dense clumps probed by the CS emission.

In a similar way, we can compare the mass calculated from the CS column density to the virial mass to constrain the CS abundance,

$$X(CS) = \frac{\mu m_H N_{lvg} \pi {R_{CS}}^2}{M_{vir}(R_{CS})} \approx 5.75 \times 10^{-10} \frac{(N_{lvg}/1.0 \times 10^{14}\mathrm{cm}^{-2})\,(R_{CS}/1\mathrm{pc})^2}{(M_{vir}/1.0 \times 10^4 \mathrm{M}_\odot)} \quad . \tag{5.11}$$

The column density was determined from the LVG models of multiple transitions of CS lines (Paper II). The resulting mean value of X(CS)= $(3.0 \pm 5.9) \times 10^{-9}$ with a median value of 1.1×10^{-9}, with a distribution (Figure 5.11) highly skewed by large abundances in G10.6−0.4 ($X(CS)$ = 1.3×10^{-8}), in W28A2(1) ($X(CS)$ = 1.6×10^{-8}), and in W51 ($X(CS) = 3.6 \times 10^{-8}$). The mean and median are three times higher than those used in Paper II.

5.4.7 Luminosity of CS

The luminosity of CS $J = 5 \rightarrow 4$ emission was calculated from

$$L(\mathrm{CS54}) \approx 1.05 \times 10^{-5} \left(\frac{D}{1\mathrm{kpc}}\right)^2 \left(\frac{\Omega_{source} + \Omega_{beam}}{\Omega_{beam}}\right) \left(\frac{\int T_R^* dv}{1\mathrm{Kkm\ s}^{-1}}\right) \mathrm{L}_\odot \quad , \tag{5.12}$$

using the deconvolved source size and assuming that the source is described by a Gaussian brightness distribution (Paper II). The average CS(5–4) luminosity is $(5.0 \pm 8.8) \times 10^{-2}$ $\mathrm{L}_\odot$ for the sample of 57 cores, similar to the average CS(5–4) luminosity from Paper II (4.0×10^{-2}). The distribution of CS luminosities is strongly peaked with a tail of high luminosity sources (Figure 5.11). The median L(CS54) is 1.9×10^{-2} $\mathrm{L}_\odot$, lower than the average luminosity from Paper II, because our sample has included more of the less luminous cores. The total L(CS54) for our subsample of 57 cores is 2.85 $\mathrm{L}_\odot$.

By estimating the number of star forming cores emitting CS we can estimate the total galactic L(CS54). The latest update to the Arcetri H_2O maser catalog (Valdettaro et al. 2001) indicates 410 regions that have IRAS colors indicative of star formation. Paper II had a detection rate of 75% towards a subset of that sample. Also correcting for the unobserved portion of the Galaxy in the Arcetri survey, roughly 1/3 of the sky, we find that there are roughly 460 cores detectable in the CS $J = 5 \rightarrow 4$ line emitting in our Galaxy. We add the total luminosity from our subsample to the mean L(CS54) for the remaining CS $J = 5 \rightarrow 4$ emitting clouds ($460 - 57 = 403$) to find a galactic luminosity, L_{gal}(CS54), of 23 L$_\odot$. If the median L(CS54) is used, L_{gal}(CS54) $\approx$ 11 L$_\odot$. If the detection rate is 100% and the average L(CS54) is used, then L_{gal} has an upper limit of 31 L$_\odot$. Another estimate is to assume that the CS cores not observed in our survey have a similar distribution in L(CS54). The total luminosity is multiplied by the ratio of unobserved to observed CS emitting clouds (460/57) to find $L_{gal}(CS54) \approx 23$ L$_\odot$. Therefore, the total galactic L(CS54) is likely between $11 - 31$ L$_\odot$ with a value most likely near 20 L$_\odot$. Assuming that CS $J = 5 \rightarrow 4$ emission is confined to dense cores within molecular clouds (see Helfer & Blitz 1997), this estimate of the galactic L(CS54) is probably complete. This is consistent with previous estimates of the galactic luminosity from Paper II and is well below the CS luminosities of nearby starburst galaxies (see Table 8 in Paper II).

5.4.8 Star Formation Rate per Unit Mass

The ratio of bolometric luminosity to virial mass is roughly proportional to the star formation rate per unit mass. The bolometric luminosity is calculated from fluxes collected in Table 2 of Mueller et al. (2002). The average L_{bol}/M_{vir} ratio is 314 ± 416 L$_\odot$/M$_\odot$, ranging from 3 to 2290 L$_\odot$/M$_\odot$ for a subsample of 40 cores with sufficient flux information to calculate L_{bol}. This average is somewhat higher than those computed for our subsample with masses from dust emission (136 ± 100) and from the sample of Beuther et al. (2002) (120 ± 90), once similar assumptions about dust opacity are made (Mueller et al. 2002). We can compare to the values in Paper II after correcting the Paper II virial mass for density gradients and optically thick CS linewidths to find $L_{bol}/M_{vir} = 440 \pm 100$ L$_\odot$/M$_\odot$. The L_{bol}/M_{vir} ratio was higher for Paper II due to a bias towards the most luminous high mass star forming regions.

Sridharan et al. (2002) found that their sample of sources with low radio continuum emission had a systematically lower L_{bol}/M_{vir} than did a sample of regions with UCH II regions (Hunter et al. 2000). They interpreted this difference as an evolutionary effect: the sources without well-developed H II regions were younger and had yet to reach their full luminosity. Our sample provides a good check of this hypothesis because it was chosen without regard for the presence of an H II region, but slightly more than half (22, 55%) of the cores in the L_{bol}/M_{vir} distribution do contain UCH II regions. The L_{bol}/M_{vir} ratio for cores with UCH II regions is higher ($\langle L_{bol}/M_{vir}\rangle = 362 \pm 316$ L$_\odot$/M$_\odot$, $\mu_{1/2} = 278$ L$_\odot$/M$_\odot$) than for cores without ($\langle L_{bol}/M_{vir}\rangle = 257 \pm 516$ L$_\odot$/M$_\odot$, $\mu_{1/2} = 117$ L$_\odot$/M$_\odot$). The distributions of both subsamples are plotted in Figure 5.11. Thus, our data provide some support for the interpretation by Sridharan et al. (2002), but the difference is not great and the overlap of the two samples is substantial. If we use the median values, the L_{bol}/M_{vir} for cores with UCH II regions is 2.4 times that for the sample without, similar to the enhancement of the sample of H II regions studied by Hunter et al. (2000) over than studied by Sridharan et al. (2002), according to the analysis of those samples by Mueller et al. (2002).

All these ratios are much higher than the L_{bol}/M_{vir} for molecular clouds, as traced by CO generally (0.4L$_\odot$/M$_\odot$; Bronfman et al. 2000) or the enhanced value for molecular clouds with bright H II regions (4L$_\odot$/M$_\odot$; Mooney & Solomon 1988). The dispersion in this ratio is also less than that for studies using CO, again indicating that the dense cores are the relevant entities for the study of massive star formation. This result agrees with studies of HCN toward galaxies that show a tight, linear relation between far-infrared luminosity and luminosity of HCN emission (Solomon, Downes, & Radford 1992; Gao & Solomon 2002). Those authors argue that the global star formation rate per unit mass depends on the fraction of molecular gas in a dense phase. We see the same trend in dense cores in our Galaxy, suggesting that studies of these dense cores may provide information on conditions in galaxies with intense star formation.

A strong correlation ($r = 0.75$) between bolometric luminosity and virial mass is observed for our sample of cores (Figure 5.17), $\log L_{bol} = 1.70 + 1.19 \log M_{vir}$. The corresponding trend for CO clumps is shown as a dashed line with slightly flatter slope. There is no trend in L_{bol}/M_{vir} versus M_{vir} over two orders of magnitude in virial mass (Figure 5.17). This result is very similar to the lack of correlation seen for CO clumps over four order of magnitude in mass (see Evans 1991), except that the dispersion in L_{bol}/M_{vir} for the CS cores in this survey is a factor of 6 smaller than for CO clumps. In the dense cores within molecular clouds, the star formation rate per unit mass does not depend on the mass of the core.

Because the luminosity is strongly affected by the most massive star [$L \propto M_\star^\alpha$ with $\alpha \sim 3.5$ up to $M_\star \sim 60$ $M_\odot$ (Scalo 1986)], the linear relation between luminosity and mass and modest dispersion about the relation suggests that the mass of the most massive star is closely related to the mass of the core, with a relation that approximates $M_\star(max) \sim {M_{vir}}^{1/3.5}$. Because the mass of the most massive star must be subject to strong statistical fluctuations, the dispersion in L_{bol}/M_{vir} is surprisingly small; a factor of 2 change in the mass of the most massive star will cause a change of a factor of 11 in luminosity, about the dispersion that we observe. Sridharan et al. (2002) make a similar conclusion based on their sample of source without UCH II regions.

5.4.9 Galactic Trends

The core size, linewidth, virial mass, surface density, CS abundance, and luminosity-to-mass ratio are plotted versus galactic radius in Figure 5.18. The large spike in

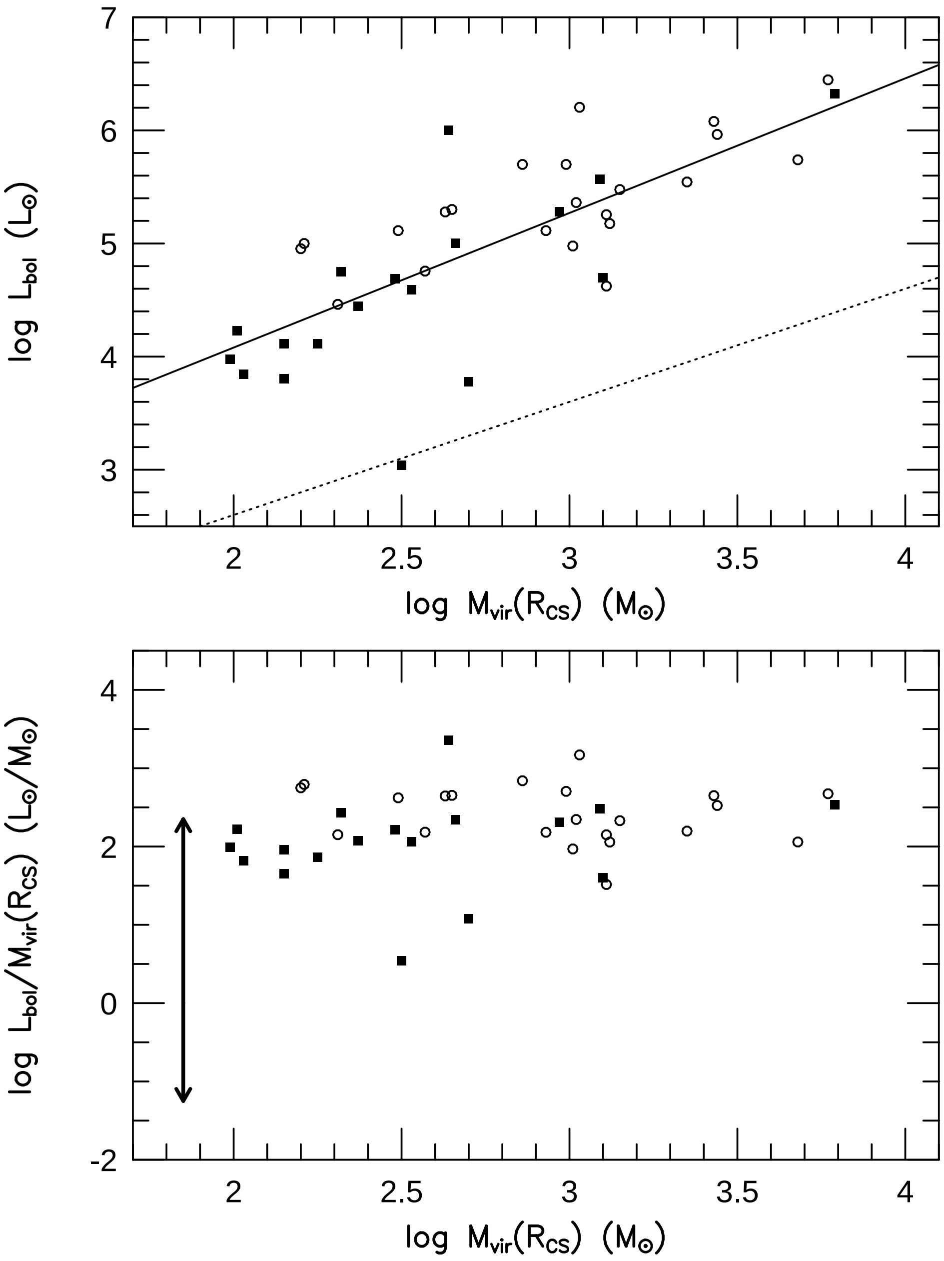

Figure 5.17 The top panel plots L_{bol} vs. M_{vir} and the bottom panel plots L_{bol}/M_{vir} vs. the M_{vir}. Source with UCH II regions are plotted as circles while sources without UCH II regions are plotted as filled squares. The dotted line in the top panel is the relationship derived for CO clumps while the solid line is a least squares fit. L_{bol}/M_{vir} is proportional to the star formation rate per unit mass. The range of L_{bol}/M_{vir} for CO clumps is shown as a double arrow at the left of the bottom panel. The dispersion observed towards CS cores is roughly 6 times smaller than the equivalent relationship for CO clumps (Evans 1991).

core sizes near $D_g = 10$ kpc is due to the massive cores observed towards the W49 and G32.80+0.20 star forming regions. There is little evidence for a trend in core size ($r = -0.01$) or linewidth ($r = -0.14$). There may be weak anticorrelations of surface density ($r = -0.20$), virial mass ($r = -0.26$), and luminosity-to-mass ratio ($r = -0.26$) with D_g. The strongest, but still weak, correlation is between log CS abundance and galactocentric radius ($r = -0.32$). These results mostly agree with previous CS surveys, which found few trends with galactocentric distance (e.g., Zinchencko 1995, Zinchencko et al. 1998). In particular, Zinchenko et al. (1998) also noted a weak correlation ($r = -0.35$) of L/M with D_g.

Zinchenko et al. (1998) found that the most significant correlation in their sample was a decrease of mean density with D_g. Their mean densities were obtained from the CS column densities, determined from the CS $J = 2-1$ line, assuming an abundance of CS that is constant with D_g. In contrast, we find no evidence for a decrease in the density determined from the LVG modeling in Paper II with D_g ($r = -0.03$). We do see an anticorrelation in CS abundance with D_g at about the same level of significance as the correlation Zinchenko et al. found in mean density. A decrease in abundance could have introduced an artificial decrease in their mean densities because they assumed a constant abundance. A decrease in abundance of CS could be caused by many factors, but a simple explanation would be a Galactic gradient in sulfur abundance, as has been found by Rudolph et al. (1997).

5.5 Conclusions

We have mapped 63 high mass star forming cores associated with water masers in CS $J = 5 \rightarrow 4$. The source size, aspect ratio, virial mass, surface density, CS(5–4) luminosity, and L_{bol}/M_{vir} ratio were calculated. A statistical summary of all calculated quantities is shown in Table 5.13. Typically, smaller average sizes and masses are found compared to results from Paper II due to the inclusion of weaker

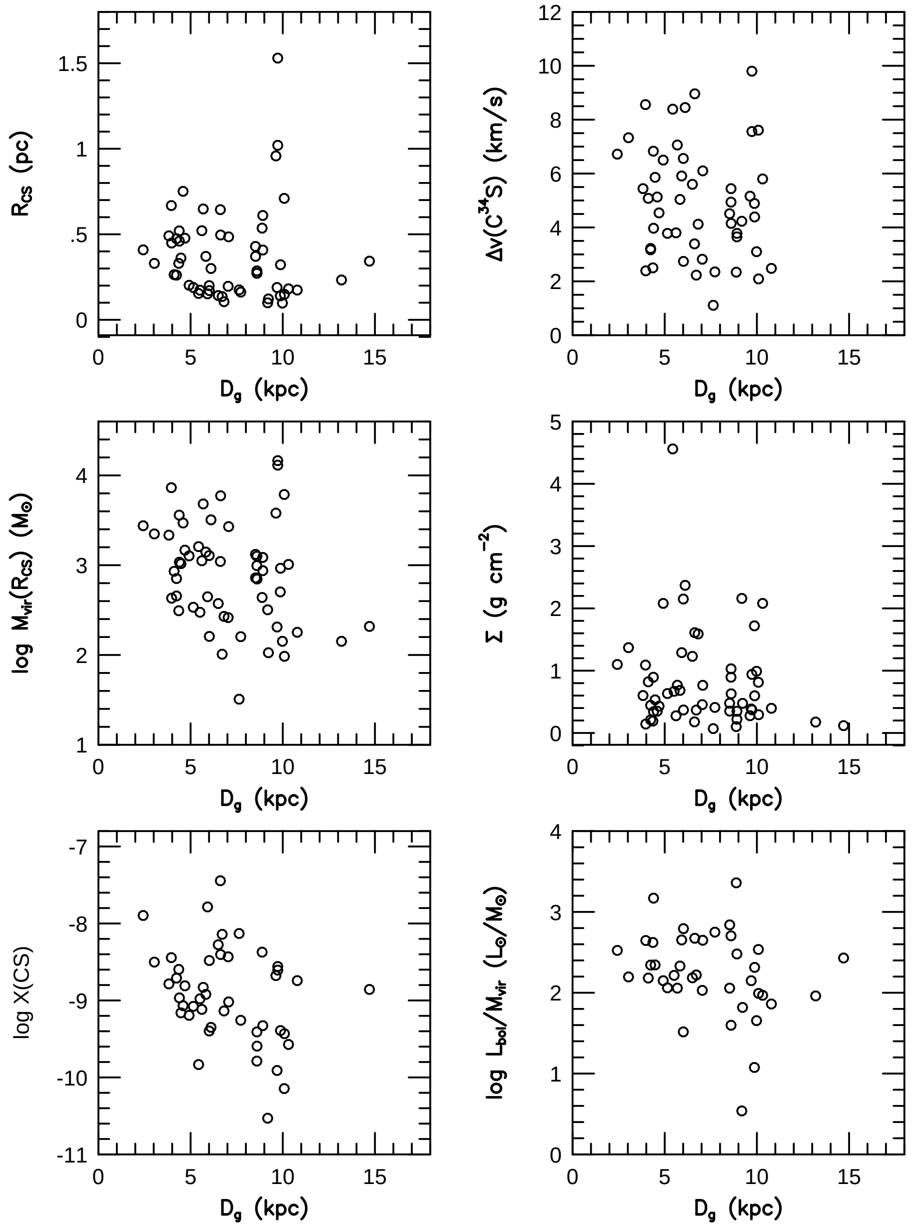

Figure 5.18 Plot of R_{CS}, $\Delta v(C^{34}S)$, M_{vir}, Σ, $X(CS)$, and $\mathrm{L}_{bol}/\mathrm{M}_{vir}$ versus galactocentric distance. Only the CS abundance shows a weak correlation with galactocentric distance.

TABLE 5.13
STATISTICAL SUMMARY

Source Property	N	Mean	Std. Dev.	Mean Dev.[a]	$\mu_{1/2}$	Median Dev.[b]	Skewness[c]	Units
D	63	5.3	3.7	3.0	4.0	2.8	1.1	kpc
D_g	63	7.2	2.6	2.2	6.8	2.2	0.5	kpc
$I_{peak}(T_R^*$, CS)	63	47.2	44.7	30.1	31.8	26.6	2.4	K km s^{-1}
$(S/N)_{peak}$	63	50	40	27	40	25	2.4	
$I_{peak}(T_R^*$, $C^{34}S$)	49	6.5	7.5	5.2	4.0	5.0	1.9	K km s^{-1}
R_{CS}	57	0.37	0.26	0.19	0.32	0.19	2.0	pc
Δv	63	5.6	2.2	1.8	5.1	1.6	0.7	km s^{-1}
$\Delta v(C^{34}S)$	51	5.0	2.0	1.7	4.9	1.6	0.4	km s^{-1}
$\Delta v(^{13}CS)$	9	5.7	2.0	1.5	5.3	1.4	0.3	km s^{-1}
$(a/b)_{obs}$	47	1.27	0.22	0.18	1.20	0.18	0.6	
$M_{vir}(R_{CS})$	57	1810	2810	1750	920	1450	3.1	$M_\odot$
$M_{vir}(R_n)$	21	1180	1080	870	610	760	1.3	$M_\odot$
$\Sigma(R_{CS})$	57	0.82	0.78	0.55	0.60	0.51	2.4	g cm^{-2}
$f_v(p=0)$	42	0.46	0.72	0.49	0.13	0.39	2.4	
X(CS)	46	3.0	5.9	3.1	1.1	2.5	4.4	10^{-9}
L(CS54)	57	5.0	8.8	5.2	1.9	4.3	3.6	10^{-2} $L_\odot$
$L_{bol}/M_{vir}(R_{CS})$	40	314	416	248	165	218	3.4	$L_\odot/M_\odot$
$\langle \bar{P}/k \rangle$	57	5.4	12.6	6.3	1.5	4.9	5.4	10^8 K cm^{-3}

[a] Mean Deviation $= \frac{1}{N}\sum_i |x_i - <x>|$

[b] Median Deviation $= \frac{1}{N}\sum_i |x_i - \mu_{1/2}(x)|$

[c] Skewness $= \sum_i \frac{(x_i - <x>)^3}{(N-1)\sigma^3}$

sources.

Our main conclusions are as follows:

(1) A strong correlation is observed between the integrated intensity of the CS $J = 5 \rightarrow 4$ line and continuum flux observed at 350 μm (Mueller et al. 2002) indicating that high-J CS emission is an excellent tracer of dense gas in high mass star forming cores.

(2) The median size 0.32 pc. While a power law density profile does not have a characteristic size, the median FWHM size is comparable to the core size from dust emission (R_n) determined by Mueller et al. (2002), based on setting the outer radius at the point where the density drops of 10^4 cm^{-3}.

(3) Most of the core aspect ratios are consistent with spherical symmetry. No trend is seen in aspect ratio with p, the exponent in the power law density distribution.

(4) A weak trend between deconvolved source size and p is observed, as expected for power laws.

(5) There is a weak correlation between linewidth and size that is consistent with $\Delta v \propto {R_{CS}}^{0.3}$. The linewidths of the cores in this sample are much larger than would be predicted from the usual size-linewidth relation, indicative of high turbulence.

(6) The median virial mass is 920 M$_\odot$ after corrections for C^{34}S linewidth and p. On average, the virial mass is 2 to 3 times larger than the mass calculated from 350 μm dust emission toward the same region.

(7) The cumulative mass spectrum is steeper ($\Gamma = -0.8$ to -1.1) than studies of molecular clouds as a whole and clumps within those clouds. It is flatter than the Salpeter IMF, but similar to that of the IMF of OB associations and the distribution of total masses of stars in OB associations.

(8) The median pressure of the sample is 1.5×10^8 K cm^{-3}. The high pressure

may mitigate the long standing lifetime problem for confinement of Ultra-Compact H II regions.

(9) The L_{bol}/M_{vir} ratio is about two orders of magnitude higher than estimates made from tracers of lower density gas (CO) and has a smaller dispersion, indicating that dense cores traced by submillimeter continuum and high-J CS emission are the relevant entities for assessing the star formation rate per unit mass. The L_{bol}/M_{vir} ratio is 2.4 times larger for cores with UCH II regions compared to cores without UCH II regions.

(10) A strong correlation is observed between luminosity and virial mass. This result combined with the low dispersion in L_{bol}/M_{vir} indicates that the mass of the most massive star is likely related to the mass of the core.

(11) No trends in size, mass, or L_{bol}/M_{vir} with galactocentric radius are apparent. A weak decrease in CS abundance with galactocentric distance is observed.

Acknowledgments

We are grateful to the staff of the CSO for excellent assistance. We are very grateful to Richard Chamberlin for assistance with beam information and to Jeong-Eun Lee for help compiling the CSO efficiencies and pointing measurements. We thank C. McKee, J. Tan, and P. Solomon for helpful discussions. This work was supported by NSF Grant AST-9988230 and the State of Texas.

Chapter 6

Thesis Conclusions

Optically thin dust continuum emission is an excellent tracer of mass in the outer envelopes of low-mass (Shirley et al. 2000; §2) and high-mass protostars (Mueller et al 2002). Submillimeter bolometer array cameras (Holland et al. 1999, Hunter et al. 1996) have revolutionized our ability to map the earliest phases of star formation. The methods for analyzing the dust continuum emission in this thesis are complementary to other methods, such as near-infrared extinction mapping (e.g., Alves et al. 1999), that probe the outer envelope. Submillimeter dust continuum emission has the advantage of being able to probe the innermost regions of the envelope on scales where near-infrared extinction maps are deprived of background sources.

Radiative transfer models of the dust continuum are necessary to understand the temperature and density structure of the envelope because short wavelength radiation is optically thick in deeply embedded cores and heating from the ISRF becomes important, especially in low-mass star forming cores (§4.2). It is crucial to characterize accurately the observing method and convolve the radiative transfer models with the observed beam shape and simulate chopping (§3.2).

The temperature distributions of low-mass and high-mass cores is very different. Low-mass cores are colder in the outer envelope and have temperature profiles that rise towards the outer boundary of the core due to heating from the ISRF. Single power law temperature profiles are not good approximations to the temperature structure. The dust temperature drops below 20 K in the outer envelopes of both low-mass and high-mass cores, resulting in failure of the Rayleigh-Jeans approximation (§4.2).

The shapes of the density distributions of low-mass and high-mass star forming cores are surprisingly similar, but the density is 2 orders of magnitude higher in high-mass cores. Single power law models, $n(r) = n(r_f)(r/r_f)^{-p}$, provide good fits to the outer envelopes of low-mass (10^3 to 10^4 AU) and high-mass (10^4 to 10^5 AU) star forming cores with average power law indices, $p = -d\log n/d\log r$, of $\langle p\rangle = 1.6 \pm 0.4$ (Shirley et al. 2002a, Young et al. 2002) and $\langle p\rangle = 1.8 \pm 0.4$ (Mueller et al. 2002) respectively. Elongated low-mass cores ($a/b > 1.5$) have lower values of the power index, $p \sim 1.0$ (Shirley et al. 2002a, Young et al. 2002); if they are excluded from the low-mass sample, then the $\langle p\rangle$ rises to 1.8 ± 0.4.

The average p for both low-mass and high-mass regions is inconsistent with theoretical models that predict low values ($p \sim 1$), such as the logatropic sphere (McLaughlin & Pudritz 1997). The inside-out collapse models of Shu (1977) with infall models taken from previous modeling of molecular line emission (e.g., B335, Choi et al. 1995) were found to be inconsistent with the submillimeter emission. The submillimeter data require the infall radii to be within the central beam (§3.3). Our results suggest a re-analysis of the molecular line emission from collapse models are needed.

Uncertainties in the models are $\Delta p \approx \pm 0.2$ if the effects of disks, outflows, and geometrical asymmetries are ignored. Inclusion of the flux from a disk may increase our total uncertainty to $\Delta p \approx \ ^{-0.6}_{+0.2}$ in the most pessimistic case (§3.5.5). The dispersion in the power law indices is slightly larger than the modeling uncertainty, suggesting that theoretical models of star formation should predict a range in p.

However, a firmer conclusion awaits submillimeter interferometric observations to constrain the flux contribution from a compact component (e.g., a disk) within the central beam of bolometer camera maps. Three dimensional radiative transfer modeling is just becoming available and is needed to analyze the effects of asymmetries in the core geometry.

The CS $J = 5 \rightarrow 4$ transition is another excellent tracer of the mass in outer envelopes of high-mass star forming cores. The CS $J = 5 \rightarrow 4$ molecular line intensity is strongly correlated with submillimeter dust continuum emission (§5.3). The CS $J = 5 \rightarrow 4$ mapping survey towards cores associated with water masers provides a sample from which the physical conditions of the deeply embedded phase of high-mass star formation are determined. The typical high-mass star forming region in the Galaxy has a size of 0.37 pc, a mass of dense gas of 1000 $M_\odot$, and a luminosity to mass ratio of 150 $L_\odot/M_\odot$. The linewidths indicate that these regions are very turbulent while the surface densities indicate high pressures, $\langle \bar{P}/k \rangle \sim 1.5 \times 10^8$ K cm^{-3} that result in large predictions for protostellar accretion rates (in an accretion formation scenario, McKee & Tan 2002b). The high pressure we find in molecular gas may provide an explination for the long-standing lifetime problem for ultra-Compact H II regions, by providing external confinement.

Since the average distance of the high-mass regions in the CS survey is 30 times that of cores in the low-mass continuum survey, our understanding of the structure of the high-mass cores is limited by 30 times worse resolution. Dust continuum studies of high-mass cores also suffer from the uncertainties within the central beam such as the effects of H II regions and fragmentation. Submillimeter interferometers will revolutionize our understanding of these regions.

Studies of chemistry, dynamics, and initial conditions of star formation have been severely limited by simplistic assumptions about the temperature or density structure of the core. Those problems can now be re-analyzed using more realistic density and temperature structures derived from radiative transfer modeling of the dust continuum emission of low-mass and high-mass regions. A survey of the chemical and dynamical state of low-mass star forming regions is currently underway (Lee et al. 2002b) that utilizes the modeling results from Evans et al. (2001) and Shirley et al. (2002a). Interferometric observations of the millimeter continuum will help resolve uncertainties within the central beam of low-mass cores (Shirley et al. 2002d). A study of high-mass regions using multiple transitions of the CS molecule and its isotopes (Knez et al. 2002a) will increase our understanding of the structure of high-mass cores, building upon the results from the CS survey and dust continuum observations and modeling results from Mueller et al (2002).

Appendix A

Appendix

A.1 Optically Thin Dust Continuum Emission

We start with the equation of radiative transfer for pure emission,

$$\frac{dI_\nu}{ds} = j_\nu(s) \quad , \tag{A.1}$$

where j_ν is the monochromatic emission coefficient (erg cm^{-3}s^{-1} ster^{-1} Hz^{-1}). Equation (A.1) is valid at long wavelengths where absorption and scattering are negligible. Kirchoff's Law relates the emission coefficient to the monochromatic absorption coefficient, α_ν for dust grains at temperature T$_d$,

$$j_\nu(s) = \alpha_\nu(s) B_\nu[T_d(s)] \quad , \tag{A.2}$$

where $B_\nu[T_d(s)]$ is the Planck function with dust temperature varying along the line-of-sight. The absorption coefficient is directly proportional to the differential optical depth along the line-of-sight,

$$d\tau = \alpha_\nu(s) ds \quad . \tag{A.3}$$

The equation of radiative transfer then becomes

$$\frac{dI_\nu}{d\tau} = B_\nu[T_d(s)] \quad . \tag{A.4}$$

We write the optical depth in term of the dust opacity along the line-of-sight,

$$d\tau = \kappa_\nu(s)\rho(s)ds \ , \tag{A.5}$$

where ρ is the mass density of gas (gm cm^{-3}) and κ_ν is the mass opacity of dust per gram of gas (cm^2 gm^{-1}). The mass opacity is also given by

$$\kappa_\nu = \frac{\pi a^2 Q_\nu^{abs}}{m_d}\left(\frac{M_g}{M_d}\right)^{-1} \ , \tag{A.6}$$

where a is the grain radius, Q_ν^{abs} is the grain absorption coefficient, m_d is the mass of a dust grain, and M_g/M_d is the gas-to-dust ratio. A gas-to-dust ratio of 100 is assumed throughout this thesis. A change in the gas-to-dust ratio will manifest itself as a change in the opacity with this interpretation.

We solve the equation of radiative transfer for the specific intensity along the line-of-sight,

$$I_\nu = \int_s B_\nu[T_d(s)]\kappa_\nu(s)\rho(s)ds \ . \tag{A.7}$$

Since previous studies of star forming regions characterize the density in terms of the number density of particles (e.g., LVG models), we switch from mass density to number density,

$$\rho(s) = \mu m_H n(s) \ , \tag{A.8}$$

where $\mu \approx 2.29$ is the mean molecular mass of gas, m_H is the mass of a hydrogen atom, and n is the number density of gas particles ($n = n(\mathrm{H_2}) + \mathrm{n(He)} + \ldots$). Substituting, we find for the integrated intensity,

$$I_\nu = \mu m_H \int_s B_\nu[T_d(s)]\kappa_\nu(s)n(s)ds \ . \tag{A.9}$$

In general, this equation must be solved numerically.

In the case of a spherical shell, we can change variables from an integration along the line-of-sight to integration along the radius of the shell,

$$r = \sqrt{s^2 + b^2} \ , \tag{A.10}$$

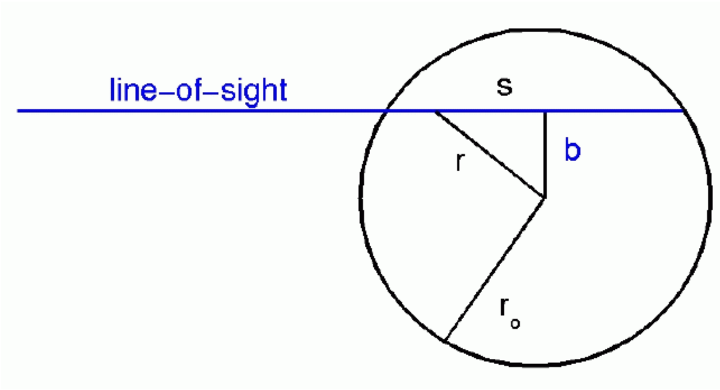

Figure A.1 Spherical geometry of dusty envelope.

where b is the impact parameter of the line-of-sight (Figure 1).

The integrated intensity at impact parameter, b, is

$$I_\nu(b) = 2\mu m_H \int_b^{r_o} B_\nu[T_d(r)]\kappa_\nu(r)n(r)\frac{r}{\sqrt{r^2-b^2}}dr \tag{A.11}$$

$$= \frac{4h\mu m_H \nu^3}{c^2}\int_b^{r_o} \frac{\kappa_\nu(r)n(r)}{\exp[h\nu/kT_d(r)]-1}\,\frac{r}{\sqrt{r^2-b^2}}dr \tag{A.12}$$

This equation has an analytical solution if several assumption are made. If we assume we are in the Rayleigh-Jeans limit, $T_d(r) \gg h\nu/k \;\forall\; r \in [r_i, r_o]$, then we have,

$$I_\nu(b) = \frac{4h\mu m_H \nu^2}{c^2}\int_b^{r_o} T_d(r)\kappa_\nu(r)n(r)\frac{r}{\sqrt{r^2-b^2}}dr \tag{A.13}$$

Let us assume that the temperature and density follow single power laws for radii $r \in [r_i, r_o]$,

$$T_d(r) = T_d(r_f)\left(\frac{r}{r_f}\right)^{-q}, \tag{A.14}$$

$$n(r) = n(r_f)\left(\frac{r}{r_f}\right)^{-p}, \tag{A.15}$$

such that r_f is a fiducial radius and $q = -d\log T/d\log r$ and $p = -d\log n/d\log r$ are the power law indices. If we also assume that the dust opacity remains constant throughout the envelope ($\kappa_\nu(r) = \kappa_\nu \ \forall \ r \in [r_i, r_o]$), then we have,

$$I_\nu(b) = \frac{4h\nu^2 kT_d(r_f)\mu m_H n(r_f)\kappa_\nu r_f^{q+p}}{c^2} \int_b^{r_o} \frac{r^{1-q+p}}{\sqrt{r^2 - b^2}} dr \quad . \tag{A.16}$$

If we make the variable transformation, $x = r/b$, then

$$I_\nu(b) = \frac{4h\nu^2 kT_d(r_f)\mu m_H n(r_f)\kappa_\nu r_f^{q+p}}{c^2} b^{1-q+p} \int_1^{r_o/b} \frac{x^{1-q+p}}{\sqrt{x^2 - 1}} dx \quad . \tag{A.17}$$

Defining $m = q + p - 1$; then, if $r_o \gg b$,

$$I_\nu \propto b^{-m} \quad . \tag{A.18}$$

Therefore, the specific intensity at impact parameter b is a power law. While this general trend is true, the specific intensity integral (A.9) must be solved numerically if any of the assumption fail: (1) $T_d <\sim 2h\nu/k$; (2) $T_d(r)$ or $n(r)$ depart from single power laws; (3) The dust opacity varies with radius; (4) $b \sim r_o$.

A.2 Column Density

Assume an isothermal dust shell emitting optically thin radiation with constant dust opacity. The integrated intensity is given by

$$\begin{aligned} I_\nu &= \int_s B_\nu(T_d)\kappa_\nu \rho(s) ds & \text{(A.19)} \\ &= B_\nu(T_d)\mu m_{\rm H}\kappa_\nu \int_s n(s) ds & \text{(A.20)} \\ &= B_\nu(T_d)\mu m_{\rm H}\kappa_\nu N \quad , & \text{(A.21)} \end{aligned}$$

where N is the gas column density (cm^{-2}). The flux density observed within an aperture, θ_{ap}, is given by,

$$\begin{aligned} S_\nu &= \int_{\rm aperture} I_\nu d\Omega & \text{(A.22)} \\ &= \langle I_\nu \rangle \Omega_{ap} & \text{(A.23)} \\ &= B_\nu(T_d)\mu m_{\rm H}\kappa_\nu N \Omega_{ap} \quad , & \text{(A.24)} \end{aligned}$$

where Ω_{ap} is the solid angle of the aperture. Solving for the column density gives,

$$N = \frac{S_\nu}{B_\nu(T_d)\mu m_{\rm H}\kappa_\nu\Omega_{ap}} \quad . \tag{A.25}$$

A.3 Mass Within a Sphere

We shall derive the mass observed within an aperture, θ_{ap}, using the same assumptions and technique as for the derivation of column density. The integrated intensity is given by

$$I_\nu = B_\nu(T_d)\kappa_\nu m_d N_d \quad , \tag{A.26}$$

where we have substituted $\rho(s) = m_d n_d(s)$ in Equation (A.19) and N_d is the column density of dust. The flux density observed within θ_{ap}, is now given by,

$$\begin{aligned} S_\nu &= B_\nu(T_d)\kappa_\nu m_d N_d \Omega_{ap} && \text{(A.27)} \\ &= B_\nu(T_d)\kappa_\nu m_d N_d \frac{\pi R^2}{D^2} \quad , && \text{(A.28)} \end{aligned}$$

where $\Omega_{ap} = \pi\theta_{ap}^2/4$ for $\Omega_{ap} \gg \Omega_{mb}$, D is the distance to the source, and $R = D\theta_{ap}/2$ is the radius of the aperture. The total mass of dust grains within the aperture is given by

$$M_d = m_d N_d \pi R^2 \quad . \tag{A.29}$$

Substituting and solving for the mass gives,

$$M(T_d) = \frac{S_\nu D^2}{B_\nu(T_d)\kappa_\nu} \tag{A.30}$$

If κ_ν is expressed in term of the mass opacity per gram of gas, then the mass is the total gas mass.

A.4 Characteristic Isothermal Temperature

Typically, we measure the mass from the submillimeter flux density and assume an isothermal temperature; however, the temperature can vary along the line-of-sight.

We can characterize an isothermal temperature, T_{iso}, if we determine the mass from radiative transfer modeling of the source. For a model density distribution, the envelope mass is given by

$$M_{env} = \mu m_H \int_0^R n(r) 4\pi r^2 dr \tag{A.31}$$

If we substitute this mass in Equation (A.30), then we find the isothermal temperature that characterizes the envelope,

$$T_{iso} = \frac{h\nu}{k} \left[\ln \left(\frac{2h\nu^3 M_{env} \kappa_\nu}{S_\nu D^2 c^2} \right) + 1 \right]^{-1} \quad . \tag{A.32}$$

Bibliography

Abergel, J. P. B., et al. 1998, in ASP vol. 132, Star Formation with the Infrared Space Observatory, ed. J. L. Yun & R. Liseau (Provo:BYU), 220

Adams, F. C., Lada, C. J., & Shu, F. H. 1987, ApJ, 312, 788

Adams, F. C. 1991, ApJ, 382, 544

Allers, K. N., Jaffe, D. T., Evans, N. J., II, Plume, R., & van Dishoeck, E. F. 2002, in prep

Alves, J., Lada, C. J., Lada, E. A. 1999, ApJ, 515, 265

Alves, J. F., Lada, C. J., & Lada, E. A. 2001, Nature, 409, 159

André, P., Ward-Thompson, D., & Barsony, M. 1993, ApJ, 406, 122

André, P., Ward-Thompson, D., & Motte, F. 1996, A&A, 314, 625

André, P., Ward-Thompson, D., & Barsony, M. 2000, In Protostars and Planets IV, ed. V. Mannings, A. Boss, S. Russell. (Tucson:Univ. Arizona), in press.

Anglada, G., Estalella, R., Pastor, J., Rodríguez, & Haschick, A. D. 1996, ApJ, 463, 205

Aspin, C., Sandell, G. 1994, A&A, 288, 803

Bachiller, R., Martin-Pintado, J., Tafalla, M., Cernicharo, J., & Lazareff, B. 1990, A&A, 231, 174

Bachiller, R., André, P., & Cabrit, S. 1991b, A&A, 214, L43

Bachiller, R., Martin-Pintado, J., & Planesas, P. 1991a, A&A, 251, 639

Bachiller, R., Terebey, S., Jarret, T., Martin-Pintado, J., Beichman, C., & van Buren, D. 1994, ApJ, 437, 296

Bachiller, R., Guilloteau, S., Dutrey, A., Planesas, P., & Martin-Pintado, J. 1995 A&A, 299, 857

Bachiller, R., & Perez Gutierrez, M. 1997, ApJ, 487, L93

Barsony, M., Ward-Thompson, D., André, P., & O'Linger, J. 1998, ApJ, 509, 733

Basu, S. & Mouschovias, T. Ch. 1995, ApJ, 453, 271

Beichman, C. A., Myers, P. C., Emerson, J. P., Harris, S., Mathieu, R., Benson, P. J., Jennings, R. E. 1986, ApJ, 307, 337

Bence, S. J., Padman, R., Isaak, K. G., Wiedner, M. C., & Wright, G. S. 1998, MNRAS, 299, 965

Benson, P. J., & Myers, P. C. 1989, ApJS, 71, 89

Benson, P. J., Caselli, P. & Myers, P. C. 1998, ApJ, 506, 743

Bertoldi, F., & McKee, C. F. 1992, ApJ, 395, 140

Beuther, H., Schilke, P., Menten, K. M., Motte, F., Sridharan, T. K., & Wyrowski, R. 2001, ApJ, 566, 945

Black, J. H. 1994, ASP Conf. Ser. 58: The First Symposium on the Infrared Cirrus and Diffuse Interstellar Clouds, 355

Blitz, L., Fich, M., & Stark, A.A. 1982, ApJS, 49 183

Blitz, L. 1993, in Protostars & Planets III, ed. Levy, E. H. & Lunine, J. I., 125

Bok, B. J., & Reilly, E. F. 1947, ApJ, 105, 255

Bonnell, I. A., Bate, M. R., Clarke, C. J., & Pringle, J. E. 1997, MNRAS, 285, 201

Bonnell, I. A., Bate, M. R., Zinnecker, H. 1998, MNRAS, 298, 93

Bontemps, S., Andre, P., Terebey, S. & Cabrit, S. 1996, A&A, 311, 858

Boss, A. 1998, ApJ, 501, L77

Brand, J., Blitz, L. 1993, A&A, 275, 67

Braz, M.A., & Epchtein, N. 1983, A& A, 54, 167

Bronfman, L., Casassus, S., May, J., & Nyman, L.-Å. 2000, A&A, 358, 521

Butner, H. M., Evans, N. J., II, Lester, D. F., Levreault, R. M., & Strom, S. E. 1991, ApJ, 376, 636

Butner, H. M., Evans N. J. II, Lester, D. F., Levreault, R. M., Strom, S. E. 1991, ApJ 376, 636.

Carpenter, J. M. 2000, AJ, 120, 3139

Caselli, P., & Myers. P. C. 1995, ApJ, 446, 665

Černis, K. 1990, Ap&SS, 166, 315

Cesaroni, R., Palagi, F., Felli, M., Catarzi, M., Comoretto, G., DiFranco, S., Giovanardi, G., & Palla F. 1988, A& AS, 76, 445

Chandler, C. J., & Richer, J. S. 2000, ApJ, 530, 851

Chapin, E. 1998, Submillimetre Sky Opacity Calibration at the James Clerk Maxwell Telescope, Physics Co-op Work Term Report

Chen, H. Myers, P. C., Ladd, E. F., & Wood, D. O. S. 1995, ApJ, 445,377

Chernin, L. M. 1995, ApJL , 400, L97

Chini, R., Kreysa, E., Mezger, P. G., & Gemuend, H. -P. 1986, A& A, 154, L8

Churchwell, E., Wolfire, M. G., & Wood, D. O. S. 1990, ApJ, 354, 247

Ciolek, G. E., & Königl, A. 1998, ApJ, 504, 257

Ciolek, G. E., & Basu, S. 2000, ApJ, 529, 925

Clemens, D. P., & Barvainis R. 1988, ApJS, 68, 257

Combes, F. 1991, ARA&A, 29, 195

Conti, P. S., & Blum, R. D. 2002, ApJ, 564, 827

Cunningham, C. R., Gear, W. K., Duncan, W. D., Hastings, P. R., Holland, W. S. 1994, Proc. SPIE 2198, 638

Dame, T. M., & Thaddeus, P. 1985, ApJ, 297, 751

Davidson, J. A., & Jaffe, D. T. 1984, ApJ, 277, L13

Davidson, J. A. 1987, ApJ, 315, 602

de Geus, E., Bronfman, L., & Thaddeus, P. 1990, A&A, 231, 137

Dickel, H. R., Williams, J. A., Upham, D. E., Welch, W. J., Wright, M. C. H., Wilson, T. L., & Mauersberger, R. 1999, ApJS, 125, 413

Draine, B. T., & Lee, H. M. 1984, ApJ, 285, 89

Doty, S. D., & Leung C. M. 1994, ApJ, 424, 729

Downes, D., Wilson, T.L., Bieging, J., & Wink, J. 1980, A& A, 91, 186

Egan, M. P., Leung, C. M., & Spagna, G. F., 1988, Comput. Physics Comm., 48, 271

Eiroa, C., Miranda, L. F., Anglada, G., Estalella, R., & Torrelles, J. M. 1994, A&A, 283, 973.

Elias, J. 1978, ApJ, 224, 453

Elmegreen, B. G. 1985, in Protostars and Planets II, ed. D. C. Black & M. S. Matthews (Tucson: University of Arizona Press), 33

Evans, N. J., II 1991, in Frontiers of Stellar Evolution McDonald Observatory 50^{th} Anniversary, ASP. Conference Series, ed. D. L. Lambert, Vol. 20, 45

Evans, N. J., Rawlings, J. M. C., Shirley, Y. L., & Mundy, L. G. 2001, ApJ, 557, 193

Evans, N. J., Shirley, Y. L., Mueller, K. M., & Knez, C. 2002, in Hot Star Workshop III: The Earliest Phases of Massive Star Birth, ASP Conference Series, Vol. xxx, 2002, ed. P. A. Crowther

Fich, M. Blitz, L., Stark, A. A. 1989, ApJ, 342, 272

Field, G. B. 1978, in Protostars and Planets, ed. T. Gehrels (Tucson: Unviersity of Arizona Press), 243

Foster, P. N., Chevalier, R. A. 1993, ApJ, 416, 303

Frerking, M. A., Langer, W. D., & Wilson, R. W. 1987, ApJ, 313, 320

Fuller G. A., Lada, E. A., Masson, C. R., & Myers, P. C. 1995, 453, 754

Galli, D., & Shu, F. H. 1993, ApJ, 417, 220

Galli D., & Shu F. 1993, ApJ, 417, 243

Gao, Y., & Solomon, P. M. 2002, ApJ, submitted

Gee, G., Griffin, M. J., Cunningham, T., Emerson, J. P., Ade, P. A. R., & Caroff, L. J., 1985, MNRAS, 215, 15

Genzel, R. & Downes, D. 1977, A& AS, 30 145

Giannini, T., Nisini, B., & Lorenzetti, D. 2001, ApJ, 555, 40

Gilmore, G. 2001, in Galaxy Disks and Disk Galaxies, ASP Conference Series, Vol. 230, ed. G. José, Funes, S. J., & Enrico, M. C., 3

Girart, J. M., Acord, J.M.P. 2001, ApJL, 551, L63

Goldsmith, P. F., Snell, R. L., Hemeon-Heyer, M., Langer, W. D. 1984, ApJ, 286, 599

Goodman, A. A., Benson, P. J., Fuller, G. A., & Myers, P. C. 1993, ApJ, 406,528

Gregersen, E. M. 1998, PhD Dissertation, The University of Texas at Austin

Gregersen, E. M., & Evans, N. J., II 2000, ApJ, in press

Gregersen, E. M., Evans, N. J., II, Zhou, S., & Choi, M. 1997, ApJ, 484, 256

Gregersen, E. M., Evans, N. J., Mardones, D. M., & Myers, P. C. 2000 ApJ, in press (astro-ph/9912175)

Gueth, F., Guilloteau, S., Dutrey, A., Bachiller, R. 1997, A&A, 323, 943

Harvey, D.W.A., Wilner, D. J., Lada, C. J., Myers, P. C., Alves, J. F., & Chen, H. 2001, 563, 903

Harris, S., & Wynn-Williams, C. G. 1976, MNRAS, 174, 649

Harvey, P. M., Smith, B. J., Di Francesco, J., & Colome, C. 1998, ApJ, 499, 294

Hatchell, J., Fuller, G. A., Millar, T. J., Thompson, M. A., & MacDonald. G. H. 2000, A&A, 357, 637

Helfer, T. T., & Blitz, L. 1997, ApJ, 478, 233

Helfer, T. T., et al. 2001, Ap&SS, 276, 1131

Henriksen, R., André, P., & Bontemps, S. 1997, A & A, 323, 549

Herbig, G. H., & Jones, B. F. 1983, AJ, 88, 1040

Heyer, M. H., & Graham, J. A. 1989, PASP, 101, 816

Hilton, J. & Lahulla, J. F. 1995, A&AS, 113, 325

Hirano, N., Hayashi, S. S., Umemoto, T., & Ukita, N. 1998, ApJ, 504, 334

Hodapp, K.-W., 1994, ApJS, 94, 615

Hofner, P., Kurtz, S., Churchwell, E., Walmsley, C. M., & Cesaroni , R. 1996, ApJ, 460, 359

Hogerheijde, M. R., & Sandell G. 2000, ApJ, 534, 880

Holland et al. 1999, MNRAS 303, 659

Hollenbach, D. J., Takahashi, T., & Tielens, A. G. G. M. 1991, ApJ, 377, 192

Huard, T. L., Sandell, G. & Weintraub, D. A. 1999, ApJ, 526, 833

Hunter, T. R., Benford, D. J., Serabyn, E. 1996, PASP 108, 1042 reference Hunter, T. R., Churchwell, E., Watson, C., Cox, P., Benford, D. J., & Roelfsema, P. R. 2000, AJ, 119, 2711

Jenness, T., & Lightfoot, J.F. 1997, SURF - SCUBA User Reduction Facility ver. 1.1 User's Manual

Johnstone, D. & Bally, J. 1999, ApJ, 510, L49

Johnstone, D., Wilson, C. D., Moriarty-Schieven, G., Joncas, G., Smith, G., Gregersen, E., & Fich, Michel 2000, ApJ, 545, 327

Jørgensen, J. K., Schöier, F. L., & van Dishoeck, E. F. 2002, A&A, in press

Juvela, M. 1996, A& ASS, 118, 191

Keene, J., et al. 1983, ApJ, 274, L43

Kenyon, S., Hartmann, L., Strom, K., Strom, S. 1990, ApJ, 99, 869

Klessen, R. 2001, ApJ, 556, 837

Knez, C., Shirley, Y. L., Evans II, N. J., & Mueller, K. E. 2002b, ApJ, in prep

Knez, C., Shirley, Y. L., Evans, N. J., II, & Mueller, K. E., 2002a, in Hot Star Workshop III: The Earliest Phases of Massive Star Birth, ed. P. A. Crowther, ASP conf. series, in press.

Kramer, C., Stutzki, J., Rohrig, R., & Corneliussen, U. 1998, ApJ, 329, 429

Kooi, J. 1998, CSO Sidecab Optics, Problems and Solutions, CSO Technical Memo, July 1998

Kramer, C., Stutzki, J., Rohrig, R., Corneliussen, U. 1998, A&A, 329, 249

Kurtz, S., Cesaroni, R., Churchwell, E., Hofner, P., & Walmsley, C. M. 2000, Protostars and Planets IV, 299

Kurtz, S., Churchwell, E., Wood, D.O.S. 1994, ApJS, 91, 659

Kurtz, S. & Franco, J. 2002, Revista Mexicana de Astronomia y Astrofisica Conference Series, 12, 16

Kutner, M. L., & Ulich, B. L. 1981, ApJ, 250, 341

Lada, C. J. 1987, in IAU Symp. 115, Star Formation Regions, ed. M Peimbert & J. Jugaku (Dordrecht:Reidel), 1

Lada, C. J. 1991, in The Physics of Star Formation and Early Stellar Evolution, ed. C. J. Lada, & N. D. Kylafis (Dordrecht: Kluwer), 329

Lada, C. J., Alves, J., Lada, E. A. 1999, ApJ, 512, 250

Ladd, E. F., et al. 1991, ApJ, 366, L203

Ladd, E. F., et al. 1991, 382, 555

Larson, R. B. 1969, MNRAS, 145, 271

Larson, R. B. 1995, MNRAS, 272, 213

Larsson, B. 1998, ASP Conf. Ser. 132: Star Formation with the Infrared Space Observatory, ed. J. L. Yun & R. Liseau (Provo:BYU), 382

Launhardt, R., & Henning, Th. 1997, A&A, 326, 329

Lee, C. W., & Myers, P. C. 1999, ApJS, 123, 233

Lee, C. W., Myers, P. C.,& Tafalla, M. 1999, ApJ, 526, 788

Lee, J.-E., Young, C. H., Shirley, Y. L., Mueller, K. E., & Evans, N. J., II 2002, in Hot Star Workshop III: The Earliest Phases of Massive Star Birth, ed. P. A. Crowther, ASP conf. series, in press.

Li, Z., & Shu, F. H. 1996, ApJ 472, 211

Liseau, R., Sandell, G., & Knee, L. B. G. 1988, A&A, 192, 153

Looney, L. W., Mundy, L. G., & Welch, W. J. 2000, ApJ, in press (astro-ph/9908301)

MacLeod, J., Avery, L., Harris, A., Tacconi, L. & Schuster, K. 1994, JCMT Newsletter No. 3, 46

Mangum, J. G., Emerson, D. T., & Greisen, E. W. 2000, in Imaging at Radio through Submillimeter Wavelengths, ASP Conference Series, 217, 179

Mardones, D., Myers, P. C., Tafalla, M., Wilner, D. J., Bachiller, R., & Garay, G. 1997, ApJ, 489, 719

Mathis, J. S., Mezger, P. G., & Panagia, N. 1983, A&A, 128, 212

Matzner, C. D. 2002, ApJ, 566, 302

McKee, C. F., Tan, J. C. 2002, Nature, 416, 59

McKee, C. F. & Williams, J. P. 1997, ApJ, 476, 144

McLaughlin, D. E., & Pudritz, R. E. 1997, ApJ, 476, 750

Men'shchikov A. B., & Henning, Th. 1997, A&A 318, 879

Mestel, L. 1985 in Protostars and Planets II, ed. D. C. Black, & M. S. Matthews, 320

Mooney, T. J., & Solomon, P. M. 1988, ApJ, 334, 51

Motte, F. André, P., & Neri, R. 1998, A&A 336, 150

Motte, F., André P. 2001, A&A, 365, 440

Mueller, K. E., Shirley, Y. L., Evans, N. J., II, & Jacobson, H. R. 2002, ApJS, submitted

Mueller, K. E., Shirley, Y. L., Evans, N. J., II, & Jacobson, H. R. 2002, in Hot Star Workshop III: The Earliest Phases of Massive Star Birth, ed. P. A. Crowther, ASP conf. series, in press.

Murphy, D. C., Cohen, R., & May, J. 1986, A&A, 167, 234

Myers, P. C., & Benson, P. J. 1983, ApJ, 266 309

Myers, P. C., Fuller, G. A., Mathieu, R. D., Beichman, C. A., Benson, P. J., Schild, R. E., & Emerson, J. P. 1987, ApJ, 319, 340

Myers, P. C., & Ladd, E. F. 1993, ApJ, 413, L47

Myers, P. C., & Lazarian, A. 1998, ApJ, 507, L157

Nisini, B., et al. 1999, A&A, 350, 529

Ohashi, N., Hayashi, M., Ho, P. T. P., Momose, M., Tamura, M., Hirano, N., & Sargent, A. I. 1997, ApJ, 488, 317

OĹinger, J., Grace, W-C., Barsony, M., & Ward-Thompson, D. 1999, ApJ, 515, 696

Olmi, L., & Cesaroni, R. 1999, A&A, 352, 266

Ossenkopf, V., & Henning, Th. 1994, A & A, 291, 943

Palacios, J., & Eiroa, C. 1999, A&A, 346, 233

Park, Y.-S., Panis, J.-F., Ohashi, N., Choi, M., & Minh, Y. C. 2001, 542, 344

Parker, N. D., Padman, R., Scott, P. F., & Hills, R. E. 1988, MNRAS, 234, 67

Penzias, A. A., & Burrus, C. A. 1973, ARA& A, 11, 51

Pezutto, S. et al. 2001, accepted in MNRAS, (astroph/0111270)

Phillips, T. G., Huggins, P. J., Wannier, P. G., Scoville, N. Z. 1979, ApJ, 231, 720

Plume R., Jaffe, D. T., Evans, N. J. E. 1992, ApJS, 78, 505

Plume R., Jaffe, D. T., Evans, N. J. E., Martin-Pintado, J., Gomez-Gonzalez, J. 1997, ApJ, 476, 730

Rawlings, J.M.C., & Yates, J.A. 2001, MNRAS, 326, 1423

Reipurth, B. A., Chini, R., Krugel, E., Kreysa, E., & Sievers, A. 1993, A&A, 273, 221

Rudolph, A. L., Simpson, J. P., Haas, M. R., Erickson, E. F., & Fich, M. 1997, ApJ, 489, 94

Salpeter, E. E. 1955, ApJ, 121, 161

Scalo, J. M. 1986, Fund. Cos. Phys., 11, 1

Schweizer, F. 1976, ApJS, 31, 313

Scoville, N. Z., & Sanders, D. B. 1987, in Interstellar Processes, Eds. D. J. Hollenbach, & H. A. Thronson Jr. (Dordrecht:Kluwer), 21

Serabyn, E., Gusten, R., & Schulz, A. 1993, ApJ, 413, 571

Shirley, Y. L., Evans, N. J. E., Rawlings, J. M. C., & Gregersen, E. M. 2000, ApJS, 131, 249

Shirley, Y. L., Evans, N. J., II, & Rawlings J. M. C. 2002, ApJ, 575, 337

Shirley, Y. L., Evans, N. J., II, Mueller, K. E., Knez, C., & Jaffe, D. T. 2002, in Hot Star Workshop III: The Earliest Phases of Massive Star Birth, ed. P. A. Crowther, ASP conf. series, in press.

Shirley Y. L., Mueller, K. E., Young, C. H., Evans, N. J., II 2002, in Galactic Star Formation Across the Stellar Mass Spectrum, ed. J. M. De Buizer, APS conf. series, in press

Shirley, Y. L, Evans, N. J., II, Mueller, K. E., Knez, C., & Jaffe, D. T. 2002, ApJS, submitted

Shirley, Y. L., Evans, N. J., II, & Mundy, L. G. 2002d, ApJ, in prep

Shu, F. H. 1977, ApJ, 214, 488

Shu, F. H., Adams, F. C., & Lizano, S. 1987, ARA & A, 25, 23

Shu, F. , Najita, J. , Galli, D. , Ostriker, E. & Lizano, S. 1993, Protostars and Planets III, 3

Sievers, A. W., Mezger, P. G., Kreysa, E., Haslam, C. G. T., Lemke, R., Gordon, M. A. 1991, A&A, 251, 231

Solomon, P. M., Downes, D., & Radford, S. 1992, ApJ, 387, L55

Solomon, P.M., Rivolo, A.R., Barret, J., & Yahil, A. 1987, ApJ, 319,370

Sridharan, T. K., Beuther, H., Schilke, P., Menten, K. M., & Wyrowski, F. 2002, ApJ, 566, 931

Straižys, V. Černis, K., Kazlauskas, A., & Meištas, E. 1992, Baltic Astr., 1, 149

Terebey, S., Shu, F. H., & Cassen, P. 1984, ApJ, 286, 529

Terebey, S. Chandler, C. J., & André, P. 1993, ApJ, 414, 759

Tomita, Y., Saito, T., Ohtani, H. 1979, PASJ, 31, 407

Valdettaro, R., et al. 2001, A&A, 368, 845

Val'tts, I. E., Ellingsen, S. P., Slysh, V. I., Kalenskii, S. V., O trupcek, R., & Larionov, G. M. 2000, MNRAS, 317, 315

van der Tak, F. F. S., van Dishoeck, E. F., Evans, N. J., II, Bakker, E. J. & Blake, G. A. 1999, ApJ, 522, 991

van der Tak, F. F. S., van Dishoeck, E. F., Evans, N. J., II, & Blake, G. A. 2000, ApJ, in press (astro-ph/0001527)

van Dishoeck, E. F. 1988, Rate Coefficients in Astrochemistry, T. J. Millar and D. A. Williams, Dordrect: Kluwer, 49

Vázques-Semadeni, E., Ostriker, E. C., Passot, T., Gamme, C. F., & Stone, J. M. 2000, in Protostars & Planets IV, ed. V. Mannings, A. P. Boss, & S. S. Russell (Tucson: University of Arizona Press), 3

Visser, A. E., Richer, J. S., Chandler, C. J., & Padman, R. 1998, MNRAS, 301, 585

Visser, A. E., Richer, J. S., & Chandler C. J. 2001, MNRAS, accepted

Walker, C. K., Adams, F. C., & Lada, C. J., 1990, ApJ, 349, 515

Walsh, A. J., Burton, M. G., Hyland, A. R., Robinson, G. 1998, MNRAS, 301, 640

Ward-Thompson, D., & André, P. 1999, in The Universe as seen by ISO, ESA SP-427, ed. P. Cox & M. F. Kessler (Noordwijk: ESA) 463

Ward-Thompson, D., Motte, F., & André, P. 1999, MNRAS, 305, 143

Ward-Thompson, D., Scott, P. F., Hills, R. E., & André, P. 1994, MNRAS, 268, 276

Ward-Thompson, André, P. H., Motte, F., 1998, in Star Formation with the Infrared Space Observatory, ASP vol. 132, ed. J. L. Yun & R. Liseau (Provo:BYU), 195

Wood, D. O. S, & Churchwell, E. 1989, ApJ, 340, 265

Wood, D.O.S., & Churchwell, E. 1987, ApJS, 69, 831

Williams, J. P. McKee, C. F. 1997, ApJ, 476, 166

Williams, J. P, Blitz, L., McKee, C. F. 2000, in Protostars & Planets IV, ed. Mannings, V., Boss, A. P., Russell, S. S., 97

Wilner, D.J., Welch, W.J., Forster, J.R. 1995, ApJ, 449, L73

Wilson, T. L., & Rood, R. 1994, ARA&A, 32, 191

Wink, J.E., Altenhoff, W.J., & Mezger, P.G. 1982, A& A, 108, 227

Xiang, D.-L., Turner, B. E. 1992, AcASn, 33, 87

Xie, T., Mundy, L. G., Vogel, S. N., & Hofner, P. 1996, ApJ, 473, L131

Young, C. H., Shirley, Y. L., Evans, N. J., II, & Rawlings, J. M. C. 2001, ApJS, submitted.

Yun, J. L., & Clemens, D. P. 1994, ApJS, 92, 145

Zhou, S., Evans, N. J., Koempe, C., & Walmsley, C. M. 1993, ApJ, 404, 232

Zhou, S. 1995, ApJ, 442, 685

Zhou, S., Evans, N. J., Wang, Y. 1996, ApJ, 406, 296

Zinchenko, I., Forsstroem, V., Lapinov, A., & Mattila, K. 1994, A&A, 288, 601

Zinchenko, I. 1995, A&A, 303, 554

Zinchenko, I., Mattila, K., & Toriseva, M. 1995, A& ASS, 111, 95

Zinchenko, I., Pirogov, L., & Toriseva, M. 1998, A& ASS, 133, 337

Vita

Yancy Shirley was born on April 8, 1974, the son of Len and Marilyn Shirley. Since that date corresponded to the day Hank Aaron broke Babe Ruth's home run record, he was very nearly named Homer. Thankfully, better judgment prevailed. Instead, he was named after a dapper riverboat gambler, Yancy Derringer, from the famous 1950s televison serial, The Yancy Derringer Show. At 7 lbs. 11 ounces with sandy blonde hair and brown eyes, he was an average baby in many respects. However, he quickly developed an extraordinary interest in astronomy, writing his first book (complete with crayon illustrations), "Planets Space", at age 5.

Yancy bought his first telescope at age 10, an 8-inch Meade Newtonian reflector (with generous supplemental funds from his parents). On its first night of use, Yancy found M57, the Ring Nebula, which quickly became his favorite Messier object. Yancy's father, Len, used to carry the telescope outside for him since it weight nearly 40 lbs. Yancy maintained a keen interest in astronomy throughout high school and was a member of the Indiana University at Kokomo Astronomy Club.

After graduating from Kokomo High School in 1992, Yancy attended the University of Arizona where he triple majored in Astronomy, Physics, and Applied Mathematics. After seeing a flier for the NASA Space Grant program, he applied and began working with Stephen M. Larson at the Lunar and Planetary Laboratory on a variety of projects studying comets and asteroids. On a tip from a friend

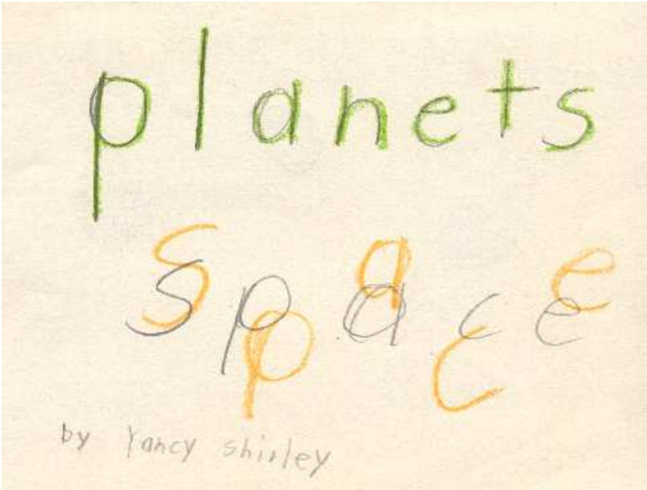

Figure A.2 The cover of Yancy's first book.

about a summer job opening in the lab of Dr. Christopher Walker, Yancy moved to Steward Observatory his junior year and began working on submillimeter receivers and studying star formation. Throughout college, Yancy never lost touch with amateur astronomy, maintaing a key to the 21-inch telescope in the courtyard of Steward Observatory. Yancy graduated in 1997 with a B.S. in Astronomy and Physics and a B.S. in Applied Mathematics.

Yancy began his graduate career in August, 1997 working with Dr. Neal J. Evans on various projects related to star formation. At some point during his graduate career, he lost touch with his amateur interests; however, professionally, he has used the largest submillimeter telescope in the world (JCMT, 15 meter) and spent over 100 nights on Mauna Kea.

Permanent Address:

This dissertation was typeset with $\LaTeX\,2_\varepsilon$[1] by the author.

[1] $\LaTeX\,2_\varepsilon$ is an extension of $\LaTeX$. $\LaTeX$ is a collection of macros for $\TeX$. $\TeX$ is a trademark of the American Mathematical Society. The macros used in formatting this dissertation were written by Dinesh Das, Department of Computer Sciences, The University of Texas at Austin, and extended by Bert Kay and James A. Bednar.